Multiphysics modeling of polymers and metals: Experimental and numerical investigations

Von der Fakultät für Bauingenieurwesen
der Rheinisch-Westfälischen Technischen Hochschule Aachen
zur Erlangung des akademischen Grades eines Doktors der Ingenieurwissenschaften
genehmigte Dissertation

vorgelegt von

Sebastian Felder, M. Sc.

Berichter*innen: Prof. Dr.-Ing. habil. Stefanie Reese
Prof. Dr.-Ing. habil. Alexander Lion

Tag der mündlichen Prüfung: 04.02.2022

"Wenn man so will
Bist du das Ziel einer langen Reise
Die Perfektion der besten Art und Weise
In stillen Momenten leise
Die Schaumkrone der Woge der Begeisterung
Bergauf, mein Antrieb und Schwung"
Ein Kompliment - Sportfreunde Stiller

Dedicated to my wife Lise who has always been my muse and emotional anchor. Furthermore, this dissertation is dedicated to my parents Birgit and Joachim, who gave me invaluable educational opportunities and unwavering trust.

Acknowledgements

The present dissertation is the result of my research and studies as a research assistant at the Institute of Applied Mechanics (IFAM) at the RWTH Aachen University. I would like to express my gratitude to all the people who contributed to the successful completion of this disertation. The English-speaking reader may forgive me my decision to write the following personal acknowledgements in German.

Mein großer Dank gilt zunächst der Betreuerin meiner Doktorarbeit, Frau Prof. Dr.-Ing. Stefanie Reese, die mir die Möglichkeit gab als wissenschaftlicher Mitarbeiter am IFAM zu forschen. Während meiner Zeit an ihrem Institut schätzte ich vor allem die großen individuellen Freiheiten und das damit einhergehende Vertrauen, das Sie mir entgegen brachte. Insbesondere im Zuge der Veröffentlichung meiner Ergebnisse war Sie mir stets eine sehr große und verlässliche Hilfe. Gerne erinnere ich mich an die interessanten fachlichen Diskussionen im Zuge dessen zurück.

Weiterhin gilt mein Dank Herrn Prof. Dr.-Ing. Alexander Lion, der sich einverstanden erklärt hat, als Zweitgutachter dieser Dissertation zu fungieren. Außerdem möchte ich Herrn Prof. Dr.-Ing. Martin Claßen dafür danken, dass er den Vorsitz der Promotionskommission übernommen hat.

Mein großer Dank gilt des Weiteren Prof. Dr.-Ing. Jaan Simon, der stets für eine großartige Gruppendynamik und fachlichen Austausch innerhalb seiner Arbeitsgruppe sorgte. Ich bin ihm sehr für seinen wertschätzenden Kommunikations- und Führungsstil dankbar und weiß unsere Zusammenarbeit, in der ich viel von seinem ausgeprägten strategischen sowie konzeptionellen Geschick profitieren konnte, sehr zu schätzen. Ein riesiges Dankeschön gilt außerdem meinem Freund Dr.-Ing. Tim Brepols. Es steht außer Frage, dass meine Forschung sehr von seinen wichtigen Impulsen profitierte und ich bin ihm zu tiefsten Dank für die zahllosen Gespräche verpflichtet, in denen er sich meinen fachlichen Fragen widmete. Weiterhin hatte ich das Glück einige sehr clevere und engagierte Studierende im Rahmen meiner Promotionszeit zu betreuen. Zu nennen sind hier explizit Ngoc Anh Vu, Greta Kloppenburg, Erik Prume, Nadir Kopic-Osmanovic und Timo Czarnecki. Ich habe sie stets als wichtige Sparringspartner begriffen, deren tatkräftige Hilfe meine Forschung wesentlich vorantrieb. In diesem Kontext ist auch Hagen Holthusen zu nennen. Weit über seine Masterarbeit hinaus stand er mir stets als Kollege und Freund mit seiner überdurchschnittlich ausgeprägten Kreativität und Problemlösungskompetenz zur Seite, wofür ich ihm sehr dankbar bin. Außerdem bin ich dem restlichen „A-Team“ und damit allen Kollegen und Kolleginnen am IFAM für die vielen großartigen, lehrreichen und humorvollen Momenten in den letzten Jahren dankbar. Zu gerne schwelge ich

in Erinnerungen an die vielen tollen Konferenzen, Mittagessen und Feierlichkeiten und freue mich sehr Teil dieses tollen Teams sein zu dürfen.

Großer Dank gilt des Weiteren meinen langjährigen Freunden außerhalb des Instituts: Julius Krieg, Robin Lamm und Björn Lang. Ich weiß ihr ehrliches Interesse an meiner doch recht abstrakten Arbeit enorm zu schätzen und bin sehr dankbar für die vielen wertvollen Gespräche auf der Suche nach Antworten darauf, was eine erfüllende berufliche Karriere und Leben eigentlich auszeichnen.

Große Dankbarkeit empfinde ich außerdem für die ständige Unterstützung meiner Familie. Besonders meinen Eltern Birgit und Joachim Felder danke ich dafür, mir diesen Bildungsweg ermöglicht und mir stets ihr unerschütterliches Vertrauen entgegengebracht zu haben. Es ist eine riesige Erleichterung, sie an meiner Seite zu wissen!

Abschließend gilt es dem wichtigsten Menschen in meinem Leben, meiner Frau Lise, zu danken. Seit Beginn meines Studiums hat sie es perfektioniert mich mit ihrem nie endenden Optimismus aus jeder emotionalen Vertiefung zu ziehen. Ich danke ihr für all die wichtigen Impulse abseits der Arbeit, die mein Leben unwahrscheinlich bereichern. Ich kann nicht in Worte fassen, wie sehr ich ihren liebevollen Umgang mit unserem Sohn Leo aber auch mit mir in dieser neuen Vaterrolle bewundere und bin unfassbar Stolz auf unsere junge Familie. Ich liebe dich und freue mich auf Alles was da noch kommt.

Sebastian Felder
Aachen, 2022

Summary

Due to the steadily increasing computing power of modern computers, numerical simulation is nowadays used in all engineering disciplines. For example, digital twins (i.e. the virtual representation of physical objects) are employed in the conception and development phase of products or processes to analyze, design and optimize them in advance. In particular, the finite element method (FEM) has established itself as a well-proven tool for the simulation of technical (coupled multiphysical) problems. However, the accuracy and reliability of the predictions made in the course of finite element analyses are essentially dependent on the underlying material models. Therefore, new models are still developed today, in order to represent increasingly complex phenomena and effects and to achieve predictions that are as close to reality as possible.

In particular, the modeling of the material behavior in the context of non-isothermal forming processes (e.g. warm and hot sheet metal forming and thermoforming of thermoplastics or glass) represents a complicated task. Here, the following challenges arise: In general, the materials are formed under large irreversible deformations. Consequently, only finite strain constitutive theories lead to reliable results. Furthermore, complex (time-dependent) inelastic deformation mechanisms occur. For most materials (such as metals and polymers), these irreversible processes lead to significant self-heating of the material, especially at higher forming rates. In addition, the temperature-dependent mechanical properties and the formation of residual stresses in the course of non-isothermal processes must be taken into account. Moreover, temperature dependent microstructural phase transformations occur in metals as well as in polymers during the cooling process, which have a significant influence on the effective properties of the manufactured components. Therefore, a complicated coupling of the mechanical quantities with the temperature and the corresponding phase transformations arises.

If damage and crack propagation are to be considered in the course of modeling, the complicating necessity to integrate non-local damage approaches arises, in order to exclude undesired mesh-dependent results. For gradient-extended damage concepts, this leads to the introduction of additional balance equations, which have to be solved in addition to the classical balances of energy and linear momentum.

The coupled modeling of these multiple physical phenomena is a challenging and relevant task, which still requires fundamental research. This cumulative dissertation aims to make a valuable contribution in this regards. The overarching objective of the current work is the development of coupled multiphysics modeling approaches for polymers and metals in order to enable more realistic simulations of the above-mentioned processes in the future.

Essentially, this work comprises a collection of published research articles by the author (and his co-authors), in the context of the aforementioned topic. In the introduction, the research-relevant questions are elaborated in detail. In addition, an up-to-date literature review is provided. The subsequent first two publications deal with the experimental investigation and modeling of semi-crystalline polymers. In the first paper, extensive experimental data regarding the mechanical behavior of semi-crystalline polyamide 6 is collected. Based on this data, a new isothermal continuum mechanical material model is developed. The underlying formulation is based on a coupled visco-hyperelastic, elasto-plastic approach in which nonlinear relaxation and strain hardening effects are considered. The temperature as well as the degree of crystallinity serve as constant input parameters, which significantly influence the effective material behavior.

In the second paper, a thermo-mechanically coupled extension of the former model is proposed. The degree of crystallinity is now treated as a non-constant internal variable, which is dependent on the temperature history. Thus, the processing induced microstructural crystallization kinetics and the corresponding (locally varying) changes in the macroscopic behavior can be represented. In addition, the heat generation due to irreversible deformation processes and exothermic crystal growth is derived from the energy balance. The predicted mechanical behavior, the heat of crystallization, as well as the self-heating due to large irreversible deformations show qualitatively and quantitatively a good agreement with experiments in three-dimensional structural examples.

The third and last article in this dissertation deals with the complex interplay between plastic deformations, damage processes and temperature, which occurs in metals during e.g. forming processes. To this end, a gradient-extended thermo-mechanically coupled constitutive framework is developed. The modeling of the mechanical behavior is based on the work of Brepols et al. [2020], where a two-surface damage plasticity approach is proposed. The heat generation of these dissipative processes are derived from the energy balance in a consistent manner. A fully implicit and monolithic algorithm is presented and discussed in detail for solving the three global solution fields (i.e. displacement, temperature, and nonlocal damage variable). In this way, mesh-objective descriptions of the complex interactions between the aforementioned phenomena can be resolved.

Zusammenfassung

Aufgrund der stetig wachsenden Rechenleistung moderner Computer werden numerische Simulationsmodelle heutzutage in allen Ingenieurdisziplinen eingesetzt. Digitale Zwillinge (d.h. die virtuelle Replikation physikalischer Objekte) werden beispielsweise in der Entwurfs- und Entwicklungsphase von Produkten oder Prozessen eingesetzt und ermöglichen diese im Vorfeld zu analysieren, auszulegen und zu optimieren. Zur Simulation technischer (gekoppelter multiphysikalischer) Probleme hat sich insbesondere die Finite-Elemente-Methode (FEM) etabliert. Die Güte von FEM-Analysen ist jedoch im Wesentlichen von den zugrundeliegenden Materialmodellen bestimmt. Bis heute werden daher neue konstitutive Modelle entwickelt, die immer komplexere Phänomene und Effekte abbilden, um möglichst realitätsnahe Vorhersagen zu erzielen.

So stellt die Simulation nicht-isothermer Umformprozesse (z.B. Warm- und Heißblechumformung, Thermoformen von thermoplastischen Kunststoffen oder Glas) bis heute eine anspruchsvolle Aufgabe dar. Dies lässt sich insbesondere auf die folgenden Herausforderungen bei der Werkstoffmodellierung zurückführen: Das eingesetzte Material erfährt im Zuge der Umformung große irreversible Verformungen, weshalb nur konstitutive Ansätze unter der Berücksichtigung großer Deformationen zu zuverlässigen Ergebnissen führen. Darüber hinaus treten komplexe (zeitabhängige) inelastische Deformationsmechanismen auf. Bei den meisten Werkstoffen (wie z.B. Metallen und Polymeren) führen diese irreversiblen Prozesse, insbesondere bei höheren Umformgeschwindigkeiten, zu einer signifikanten Eigenerwärmung des Materials. Außerdem müssen die temperaturabhängigen mechanischen Eigenschaften und die Ausbildung von Eigenspannungen berücksichtigt werden. Zudem treten sowohl bei Metallen als auch bei Polymeren mikrostrukturelle Phasenumwandlungen im Zuge der nichtisothermen Prozessführung auf, welche die effektiven Eigenschaften des resultierenden Bauteils maßgeblich beeinflussen. Insgesamt ergibt sich deshalb eine komplexe wechselseitige Kopplung der mechanischen Größen mit der Temperatur und den entsprechenden Phasentransformationen. Zur Modellierung von Materialschädigung und der Ausbreitung von Rissen müssen des Weiteren nicht-lokale Schädigungsansätze integriert werden, um netzunabhängige Ergebnisse zu gewährleisten. Dies führt bei gradientenerweiterten Schädigungsansätzen zu zusätzlichen Bilanzgleichungen, welche neben der klassischen Energie- und Impulsbilanz gelöst werden müssen.

Die gekoppelte Modellierung dieser vielfältigen physikalischen Phänomene ist ein herausforderndes und wichtiges Thema, für das weiterhin ein dringender Forschungsbedarf besteht. Die vorliegende kumulative Dissertation soll einen wertvollen Beitrag dazu leisten. Ziel dieser

Dissertation ist die Entwicklung multiphysikalischer Modellierungsansätze für Polymere und Metalle, um in Zukunft eine möglichst realitätsnahe Simulation der oben genannten Prozesse zu ermöglichen.

Im Wesentlichen umfasst diese Arbeit eine Zusammenstellung veröffentlichter Publikationen des Autors (und seiner Koautorinnen) im Kontext der genannten Thematik. In einer Einleitung erfolgt zu Beginn die detaillierte Ausführung der betrachteten Forschungsfragen. Außerdem wird ein aktueller Literaturüberblick gegeben. Die darauffolgenden ersten beiden Veröffentlichungen befassen sich in erster Linie mit der experimentellen Untersuchung und Modellierung teilkristalliner Polymere. In der ersten Arbeit werden zunächst umfängliche experimentelle Daten bezüglich des mechanischen Verhaltens von Polyamid 6 erhoben. Aufbauend auf diesen Erkenntnissen erfolgt die Entwicklung eines isothermen kontinuumsmechanischen Materialmodells. Die zugrundeliegende Formulierung basiert auf einem gekoppelten visko-hyperelastischen, elasto-plastischen Ansatz, bei dem nichtlineare Relaxations- und Verfestigungsprozesse berücksichtigt werden. Die Temperatur sowie der Kristallinitätsgrad dienen als konstante Eingangsparameter, die das effektive Materialverhalten beeinflussen.

In der zweiten Arbeit wird das Modell zu einer thermo-mechanisch gekoppelten Formulierung weiterentwickelt. Hierin dient der Kristallinitätsgrad nun als eine von der Temperaturgeschichte abhängige interne Variable. Der prozessabhängige Kristallisationsprozess und die korrespondierenden (lokal variierenden) Veränderungen des makroskopischen Verhaltens können somit abgebildet werden. Darüber hinaus wird aus der Energiebilanz die Wärmeentwicklung infolge irreversibler Deformationsprozesse und infolge des exothermen Kristallwachstums abgeleitet. Das vorhergesagte mechanische Verhalten, die Kristallisations- wärme sowie die Eigenerwärmung infolge großer Deformationen zeigen qualitativ und quantitativ eine gute Übereinstimmung mit den Experimenten.

Die dritte Arbeit befasst sich mit dem komplexen Zusammenspiel aus plastischen Verformungen, Schädigungsprozessen und der Temperatur, die im Zuge von Umformprozessen in Metallen auftreten. Dazu wird ein gradientenerweitertes, thermo-mechanisch gekoppeltes Konstitutivgesetz entwickelt. Das mechanische Verhalten wird basierend auf der Arbeit von Brepols et al. [2020] über einen „Zwei-Flächen“ Schädigungs-Plastizitätsansatz beschrieben. Die entsprechenden Rückkopplungen dieser dissipativen Prozesse auf das Temperaturfeld werden aus der Energiebilanz hergeleitet. Zur Lösung der drei globalen Lösungsfelder (Verschiebung, Temperatur und nicht-lokale Schädigungsvariable) wird ein impliziter und monolithischer Algorithmus implementiert und im Detail diskutiert. Auf diese Weise können die komplexen Wechselwirkungen zwischen den zuvor genannten Phänomenen netzunabhängig abgebildet werden.

Contents

1 Introduction

1.1 Motivation and research-relevant questions

With increasing computational resources, the integration of numerical simulation tools within all engineering disciplines is standard, nowadays. For example, during the design and development stage, digital twin prototypes are employed to optimize and refine the product before it is manufactured. The possibility to simulate the products' behavior, functionality and quality under every relevant aspect naturally reduces the number of physical prototypes and leads to lower costs, in addition. Regarding the simulation and analysis, the finite element method (FEM) is a well-established tool, which offers the ability to solve large-scale technical (coupled, multi-physics) problems in the fields of automotive, civil, medical, mechanical and aerospace engineering. Ultimately, the quality and significance of the prediction in the course of a FEM analysis depends essentially on the incorporated material models. Thus, to represent complex processes and materials under increasingly realistic conditions, a strong demand for sophisticated material models has emerged, which continues to drive the need for fundamental research until today.

In particular the modeling of non-isothermal forming processes (e.g. warm and hot sheet metal forming, thermoforming of thermoplastic polymers or glass) is a challenging task, until today. Independent of the employed material, the actual forming process usually follows the same sequence: To improve the formability of the material before processing, the workpiece (often in the form of a sheet) is heated to a specific temperature. Subsequently, the final shape of the part is imprinted by e.g. vacuum-forming, pressure-forming, or deep drawing. This offers the potential of components with complex geometries and a cost-effective mass production. However, process stability is often difficult to ensure. Thermal gradients, phase transformations, and resulting residual stresses can lead to component distortion or even defects. To avoid this, process parameters such as heating and cooling rates, mold geometry and positioning of the component usually have to be laboriously adjusted by trial and error. This often negates potential time and cost advantages. Thus, accurate process simulation tools are highly desirable.

From a modeling perspective, (non-isothermal) forming processes are in particular challenging for the following reasons. Typically, the material undergoes large strains and large rotations. Consequently, only finite strain constitutive theories lead to reliable results. In addition, complex (time-dependent) inelastic deformation mechanisms occur and must be captured during the forming stage. For most materials (especially metals and polymers) these irreversible processes induce material self-heating, leading to a change in the temperature, in particular at higher forming rates. Furthermore, the change in the mechanical properties and the formation of residual stresses due to thermal-contraction during supercooling must be addressed. Consequently, it must be accounted for strong thermo-mechanical coupling effects.

Next, to these advanced model requirements, which are far from being trivial, phase transformation must be considered in some cases. For example, during hot forming of metallic materials, the blank is austenitized at high temperatures above 900 °C prior to processing. Subsequently, deep drawing and quenching is performed simultaneously, which leads to a non diffusional martensitic transformation (see e.g. Merklein and Lechler [2006], Cui et al. [2012]). Equivalently, in the case of thermoforming of semi-crystalline polymers (SCP), the material is initially heated above the softening point, where the polymer is in a purely amorphous state. Due to the contact of the blank with the colder dies, supercooling of the amorphous phase triggers the formation of crystalline regimes during the solidification and forming process. Naturally, in both cases the resulting morphology of the underlying microstructure strongly influences the effective properties of the resulting part. Noteworthy, the aforementioned processes are driven by the temperature evolution and are in general cooling rate dependent. However, due to the exothermic nature of both transformation processes, back-coupling and a change in temperature is triggered, additionally. Conclusively, these interactions increase the complexity to a fully-coupled multiphysics problem, which requires sophisticated coupled multi-field modeling schemes.

Despite numerous phenomenological or physically based models in the literature, which describe for example the crystallization kinetics in SCP, the thermodynamically consistent incorporation of these theories into thermo-mechanically coupled frameworks is a challenging task. Furthermore, it remains the question on how to incorporate the information of the current state of the morphology into continuum mechanical models. For example, is it sufficient to consider only the crystal volume fraction as an additional (evolving) internal variable? Moreover, a general problem in this context is the systematic acquisition of comprehensive experimental data, in which both the influence of temperature and the properties of the microstructure (e.g. austenite / martensite volume fractions in metals or degree of crystallinity in SCP) on the effective material properties must be investigated for large inelastic deformations. Even if this

data were available, the question of how to systematically proceed with the material parameter identification and corresponding optimization procedure arises. In particular, in the context of SCP, these questions and problems seem to be worthwhile to be investigated, due to the very limited amount of studies dealing with all of the aforementioned points (simultaneously).

An additional interesting modeling aspect is related to the complex interaction between inelastic (e.g. plastic) deformation mechanisms and thermo-mechanical coupling effects, which eventually lead to crack initiation and propagation during forming. In fact, to predict and understand these interactions plays an important role in most metal manufacturing processes, where the formation of large quantities of plastic strain at relatively high strain rates can be observed. As alluded above, these irreversible deformations lead locally to high temperatures and thermal-softening, which accelerate strain localization and the onset and propagation of damage. These mechanisms emphasize the need of coupled thermo-damage-plasticity model formulations. While there are several established formulations available for thermo (visco-) plasticity at finite strains and brittle damage, the modeling of coupled damage and plasticity is the current subject in many ongoing studies.

Regarding damage, there exist many different approaches on how to capture the effects of microscopic damage mechanisms on the macroscopic response. For example, in the context of continuum damage mechanics, the nucleation, growth and coalescence of microvoids is accounted for in an averaged sense only, by introducing scalar- or tensor-valued internal variables. The stiffness, strength and other material properties are usually assumed to be functions of the damage variable, such that material softening can be modeled. However, today it is well-known that conventional local damage models lead in general to mesh-dependent, physically unreasonable results (shrinking damage zones and decreasing energy dissipation with increasing mesh sizes). Thus, different concepts were developed in the recent years to solve the aforementioned problem. In particular nonlocal integral-type or gradient-type formulations seem promising, to overcome the problematic mesh dependency by introducing internal material length scales. In most of the latter type of approaches, an additional nonlocal variable is introduced on the global level, whose evolution is governed by an additional partial differential equation and a set of boundary conditions. In this way, the evolution of damage on the integration point level is made dependent on the nonlocal damage variable and thus on the damage state of surrounding points, which is essentially the key to resolve the issue.

Only a very limited number of works are concerned with incorporating such advanced regularization techniques into thermo-mechanically coupled damage-plasticity formulations. Due to the gradient-extension, an additional balance equation must be solved next to the classical balance of linear momentum and the balance of energy, which rises several questions: From a

theoretical point of view, it is not clear how the complex interplay between displacement, temperature, and nonlocal damage field should be incorporated into the constitutive framework, such that thermodynamic consistency as well as the damage growth criterion (Wulfinghoff et al. [2017]) are always fulfilled. From a computational point of view it is also difficult to implement such a fully coupled multiphysical formulation in an efficient, yet accurate and fully implicit manner.

Conclusively, the considerations above reveal several open questions in the context of modeling non-isothermal forming processes, which still provide the need for fundamental research. Therefore, the aim of this dissertation is to develop thermo-mechanically coupled constitutive frameworks at finite strains for polymers and metals, in order to enable the simulation of processing under increasingly realistic conditions in the future.

This work is first of all concerned with the modeling of semi-crystalline polymers. In particular, the evolution and influence of the degree of crystallinity on the mechanical properties during forming and supercooling is experimentally and numerically investigated. The models underlying formulation is based on a coupled visco-hyperelastic elasto-plastic scheme, in which nonlinear relaxation and hardening processes are accounted for. In this way, new experimental insights and modeling approaches regarding the influence of both the temperature and the degree of crystallinity on the overall material response are generated.

Related to the issues and raised questions in the last part of the above section, this work is furthermore concerned with the derivation and implementation of a gradient-extended thermo-damage-plasticity theory at finite strains, in order to model metallic materials. This framework can be understood as the thermo-mechanical extension of the two-surface damage-plasticity approach by Brepols et al. [2020], in which both mechanisms are treated as distinct but coupled dissipative phenomena. In this way, complex interactions of e.g. material self-heating due to damage and plasticity, strain localization and accompanied thermal-softening can be captured. Furthermore, crack propagation and back-coupling effects on the material properties and the temperature field can be resolved mesh-insensitively.

1.2 State-of-the-art

To bring the aforementioned questions and issues in the context of previously published studies and to motivate this dissertation further, a review of the relevant literature is provided below. The focus is primarily on continuum mechanical approaches, which serve as the starting point for the solution schemes developed in this work. An overview of important contributions related to the modeling of polymeric and metallic materials is presented separately.

1.2.1 Modeling semi-crystalline polymers and the impact of temperature and temperature history

Semi-crystalline polymers (SCP) are a specific class of thermoplastic polymers. During cooling from the (unordered) amorphous melt, the polymer chains fold partly together and form ordered regions referred to as lamellae, which form quasi-spherical structures (spherulites). Thus, the microstructure of the solidified polymer is typically decomposed into three different phases, namely the crystalline phase as well as the soft and rigid amorphous phases (Wunderlich [2003]). Furthermore, in some SCP (for example Polyamide 6), the polymer chains within the crystalline phase arrange either in a fully extended (monoclinic) configuration, or in a twisted (hexagonal/ pseudohexagonal) configuration, referred to as α- and γ-form, respectively (see e.g. Fornes and Paul [2003]). The resulting crystal structure is in general dependent on the temperature history, applied stress, and presence of moisture (see e.g. Kyotani and Mitsuhashi [1972], Illers et al. [1972] and Gurato et al. [1974]). In general, the γ-form was found to be produced from rapid cooling ($\dot{\theta} < 8$ °C s^{-1}), whereas processes with low cooling rates lead to the formation of the α-form (Cavallo et al. [2011]).

From experimental studies regarding the mechanical behavior of SCP (see e.g. Ayoub et al. [2010], Barriere et al. [2019], and Qi et al. [2019]), it can be concluded that this class of material shows in general a complex inelastic behavior. The latter is characterized by large loading-rate dependent plastic deformations, strain hardening, as well as strain recovery, stress relaxation, and loading-unloading hysteresis loops. Molecular dynamic simulations (cf. e.g. Rottler [2009], Jatin et al. [2014], and Jabbari-Farouji et al. [2017]) helped to understand the microscopic mechanisms, which lead to visco-plastic behavior and the nonlinearity upon unloading. It was concluded that strain hardening is in general related to a limited number of possible network conformations upon loading. In addition, SCP (as most polymers) exhibit a significant Bauschinger-like effect upon unloading (cf. e.g. Anand et al. [2009], Krairi and Doghri [2014]). The microscopic nature of this phenomenon was discussed in the work of Chevalier et al. [2018], where it was concluded that the formation of back stresses during loading eventually lead to an early activation of Shear Transformation Zones (STZ) upon unloading.

During the last decades, numerous scientific contributions were concerned with the modeling of SCP. Many continuum mechanical frameworks for amorphous and semi-crystalline polymers are based on the approach for glassy polymers of Haward et al. [1968], who proposed an additive combination of the intermolecular and molecular network resistance, in order to obtain the total resistance to deformation. Based on this idea and the considerations of Boyce

et al. [2000], several phenomenological approaches followed: For amorphous polymers, see e.g. Anand et al. [2009] and Srivastava et al. [2010] and for semi-crystalline polymers e.g. van Dommelen et al. [2003], Ayoub et al. [2010], and Barriere et al. [2019]).

In earlier works, either (nonlinear) visco-elastic modeling strategies (cf. e.g. Lai et al. [2005] and Khan et al. [2006])) or visco-plastic formulations, mainly incorporating the concept of over-stress, were proposed (e.g Zeng et al. [2010], Drozdov [2011], Khan and Yeakle [2011], and Kästner et al. [2012]). However, more recent investigations (cf. Miled et al. [2011], Yu et al. [2016], Gudimetla and Doghri [2017], Praud et al. [2017], Qi et al. [2019], and Wang et al. [2019]) showed that coupled visco-elastic, visco-plastic models are crucial to accurately predict the complex deformation phenomena within amorphous and semi-crystalline polymers discussed above. Kinematic hardening approaches were proposed by e.g. Hasan and Boyce [1995], Anand et al. [2009], Krairi and Doghri [2014] and validated for cyclic-loading behavior (see e.g. Qi et al. [2019] for high density polyethylene).

Besides continuum mechanical modeling schemes on the macroscopic level, models at the micro-scale were employed, to obtain the effective material response of polymeric materials by either analytical or FE-based homogenization schemes (see e.g. Gueguen et al. [2010], Li and Shojaei [2012], Uchida and Tada [2013], Popa et al. [2014], and Alisafaei et al. [2016], to name a few). Other authors integrated microstructural aspects into their mathematical formulations, for example by considering the molecular chains network reorganization (Maurel-Pantel et al. [2015]). These approaches are typically characterized by a small number of parameters and less complex model formulations. However, the characterization of the microstructural constituents and the identification of the required physical data is in general rather difficult. This is in particular the case for semi-crystalline polymers, where the microstructure is decomposed into three different molecular arrangements (crystalline, soft and rigid amorphous phases). Consequently, employing multi-scale approaches inevitably leads to difficult choices regarding the geometry, the size, and the distribution of the aforementioned characteristic phases. Furthermore, assumptions regarding the individual mechanical behavior and properties of the distinct phases must be made, which are experimentally hardly accessible. This is in contrast to phenomenological models, where the (usually larger number of) required material parameters can be identified from conventional mechanical tests at the macro-scale.

As alluded in the motivation, the mechanical behavior of most polymers is highly dependent on thermal conditions. Early works related to the non-isothermal modeling of polymeric materials are Holzapfel and Simo [1996], Lion [1997*a*,*b*], where the latter two employed a multiplicative decomposition (cf. Kröner [1959] and Lee [1969]) of the deformation gradient to account for visco-elastic material behavior. Reese and Govindjee [1998*a*] followed this ap-

proach and proposed a thermo-mechanically coupled theory, where the free Helmholtz energy suggested by Chadwick and Hill [1974], Chadwick and Creasy [1984] was enhanced in order to account for a non-linear dependence of the material parameters on the temperature. In the work of Arruda et al. [1995], the influence of the loading-rate and adiabatic heating on the response of glassy polymers was studied. Reese [2003*a*] derived a continuum mechanical model of finite viscoelasticity from micro-mechanical considerations based on the transient network concept. In Lion et al. [2010, 2011], a concept was developed to describe the glass transition of semi-crystalline polymers. Later on, the same group developed a hybrid modeling approach for the specific free energy to capture the mechanical and caloric material properties under given pressure (Lion et al. [2014]). Ames et al. [2009] and Srivastava et al. [2010] suggested thermo-mechanically coupled formulations to capture the material self-heating of amorphous polymers under finite deformations.

Despite numerous contributions related to the isothermal modeling of semi-crystalline polymers, only a limited number of thermo-mechanically coupled works were proposed. In the more recent publications of Maurel-Pantel et al. [2015], Garcia-Gonzalez et al. [2018], and Li et al. [2019] the thermo-mechanical behavior of Polyamide 66 (PA66), Polyether ether ketone (PEEK), ultra-high-molecular-weight Polyethylene (UHMWPE), and HDPE, was investigated, respectively. In addition, a thermo-elastic-viscoplastic-damage model was introduced by Shen et al. [2019] for Polyamide 6. The impact and importance of the self-heating phenomenon was among others revealed by the works of Şerban et al. [2013] and El-Qoubaa and Othman [2016]. The same phenomena were investigated in the context of lifetime prediction of polymeric materials by Shojaei and Volgers [2017] and Katunin [2019]. In the work of Krairi et al. [2019] a non-isothermal, visco-elastic, visco-plastic theory was applied for PA 66 and Polypropylene, in the context of small strains. Furthermore, Lei et al. [2021] focused on the thermo-mechanical behavior of stretch-induced anisotropy within PEEK.

As alluded above, the effective thermo-mechanical behavior of SCP is strongly affected by the (process dependent) morphology of the underlying micro-structure (e.g. the degree of crystallinity, crystal configuration, and lamellae thickness etc.), see e.g. Jenkins [1992] and Ayoub et al. [2011]. In order to predict the evolution of the crystalline phase during processing (e.g. during cooling from the amorphous melt), several approaches were proposed over the past decades. The isothermal Avrami equation (Avrami [1939]) served as a starting point for numerous non-isothermal models (see e.g. Ozawa [1971], Nakamura et al. [1973], and Mubarak et al. [2001]), where non-isothermal crystallization and isothermal induction time were accounted for. Based on the enthalpy of fusion measured in differential scanning calorimetry (DSC) experiments, Goff et al. [2005], Zinet et al. [2010], and Kugele et al.

[2017] applied similar concepts, in order to account for the heat generation associated with the exothermic crystallization process. Lion and Johlitz [2016] developed a thermodynamically consistent model for describing the pressure- and temperature history-dependent melting and crystallization process, which takes into account the characteristic three phases within semi-crystalline thermoplastics. Noteworthy, in most of these works, the crystallization process and corresponding heat of fusion is modeled in the context of thermal problems only, where supercooling is considered as the main driving force and back-coupling effects on the thermo-mechanical behavior are not considered.

Only a limited number of constitutive models incorporate the effect of degree of crystallinity on the mechanical response. Different rules of mixture of the amorphous and crystalline regimes were studied by Dusunceli and Colak [2008] in a phenomenological approach. Ayoub et al. [2011] and Abdul-Hameed et al. [2014] suggested a two-phase representation of the microstructure. More recently, the significant dependence of ultra-high-molecular-weight polyethylene (UHMWPE) on the degree of crystallinity was investigated by Chen et al. [2019] at small strains. However, in all these works, the influence of varying constant degrees of crystallinity was investigated for only one specific temperature. More recently, the process-dependent behavior of semi-crystalline polymers under thermal and volumetric loads was investigated experimentally and modeled on a phenomenological and micromechanical basis in Mittermeier and Lion [2020]. Herein, a simplified small strain viscoelastic generalization of Hooke's law was employed.

From the above review, a considerable large progress regarding the experimental and numerical investigation of semi-crystalline polymers becomes apparent. However, most models are either limited by accounting for the impact of the temperature (e.g. Krairi et al. [2019], Shen et al. [2019]) or the process induced degree of crystallinity (e.g. Dusunceli and Colak [2008], Ayoub et al. [2011]) on the macroscopic response only. Furthermore, the published experimental data of the mechanical behavior is typically also limited to the investigation of the influence of the temperature or the underlying degree of crystallinity. In particular for Polyamide 6, there is no comprehensive experimental study (including cyclic loading and relaxation tests for large deformations) available, where both effects are investigated simultaneously over a large range of temperatures (spanning the glass transition temperature), at least to the author's knowledge. Clearly, investigating and modeling the coupling effects between degree of crystallinity and temperatures simultaneously is crucial, since the impact of varying crystal volume fractions on the overall mechanical response is strongly temperature dependent. Furthermore, in the context of forming processes, the morphology of the material's internal microstructure is not a material constant but dependent on the preceding processing

conditions and, in particular, the temperature history. Thus, the evolution of the degree of crystallinity should be incorporated, in addition. However, to the author's knowledge, there is no model available in the literature, which comprises all of the aforementioned features in a fully thermo-mechanically coupled constitutive framework at large strains.

1.2.2 Modeling the interplay between temperature, plasticity, and damage within metals

In contrast to polymeric materials, the microstructure of metals is characterized by a long-ranged ordered arrangement of the metal atoms into crystal structures. The three most common crystal structures are referred to as the body-centered cubic (bcc), face-centered cubic (fcc), and hexagonal close-packed (hcp) configuration. Noteworthy, phase transformations between different crystal arrangements occur in some metals depending on temperature and applied stresses.

As alluded above, in most metal forming processes, the material is shaped under the formation of large plastic strains at relatively high strain rates. The plastic deformations are related to two distinct deformation modes in the crystal lattice: dislocation movement on certain crystallographic planes (slip) as well as twinning (see e.g. Hirth and Lothe [1982] and Pokharel et al. [2014]). These irreversible processes lead to significant local heat accumulation (Miller et al. [1986]), accompanied by temperature-induced softening and additional plastic strain localization. Furthermore, plastic deformations are known to be the precursor to damage initiation, which is related to the nucleation, growth and coalescence of microvoids (cf. Hosokawa et al. [2013], Landron et al. [2013], Tekoğlu et al. [2015]). These complex coupling effects between dissipative deformation mechanisms (such as damage and plasticity) and the temperature were investigated and confirmed in different experimental studies for various metals at ambient temperatures (see among others Rusinek and Klepaczko [2009], Knysh and Korkolis [2015] and Bragov et al. [2019]) and motivated numerous modeling approaches over the last decades.

In the following, a brief overview of some fundamental thermo-mechanically coupled plasticity theories for metals is presented. These frameworks serve as the foundation for many modeling schemes, until today.Argyris and Doltsinis [1981] and Argyris et al. [1982] proposed models, which were restricted to adiabatic conditions. First, fully coupled finite strain formulations for metallic materials were, for example, proposed by Simo and Miehe [1992] and Wriggers et al. [1992], who investigated classical von Mises thermo-plasticity. Rosakis et al. [2000] numerically and experimentally assessed the rate of plastic work converted into

heating. Based on the proposed variational theory of Yang et al. [2006] and Stainier and Ortiz [2010], Canadija and Mosler [2011] developed a thermo-mechanically coupled framework, including kinematic hardening at finite strains.

Nowadays, it is well known that conventional 'local' plasticity theories lead to a pathological mesh dependency, in the context of finite element simulations, if localized inelastic deformations and structural softening occur. This non-physical behavior can be cured by incorporating internal length scales. The models are enhanced by nonlocal counterparts to the internal variables, which loosely speaking leads to a coupling between the local quantity and the associated spatial neighborhood. This can be e.g. achieved by gradient-extended models (for isothermal gradient crystal plasticity, see e.g. Gurtin [2008], Svendsen and Bargmann [2010], Wulfinghoff and Böhlke [2012], Klusemann and Yalçinkaya [2013], and Miehe [2014]) where the plastic length scale is associated with the microscopic lattice spacing. Alternatively, phenomenological gradient plasticity models determine the plastic length scale from experimental studies on the macroscale, see for example Gudmundson [2004], Reddy et al. [2008], Fleck and Willis [2009], Polizzotto [2009], Voyiadjis et al. [2010], Polizzotto [2014], and Miehe et al. [2014].

To capture plastic deformations in non-isothermal settings, regularized thermo-plasticity theories were introduced, more recently (cf. Forest and Aifantis [2010], Voyiadjis and Faghihi [2012]), where finite strains (Wcislo and Pamin [2017]) as well as micro-structure based size effects (Aldakheel and Miehe [2017]) were incorporated. For a detailed review paper on this topic, the interested reader is referred to Voyiadjis and Song [2019].

Besides plasticity, the modeling of damage has been of interest for many decades already. For most engineering purposes, a continuum mechanical approach is sufficient enough to predict the influence of damage on the material response.

Coupled damage models, which incorporate damage effects into the constitutive formulation can be subdivided into two groups: Micro-mechanically motivated models, which introduce the volume fraction of microvoids within the material through one or more internal variables. The material behavior is affected by the growth of the microvoids. Comprehensive knowledge of the earlier mentioned microstructural phenomena (nucleation, growth and coalescence of microvoids) is the basis for deriving the respective evolution equations. This class of models is based on the pioneering work of Gurson [1977] and the Gurson-Tvergaard-Needleman (GTN) model (Needleman and Tvergaard [1984]). Recent improvements incorporate e.g. the void size and the void shearing effect (among others, see Malcher and Mamiya [2014], Zhou et al. [2014], Jiang et al. [2016], Wu et al. [2019]).

Models related to the second group rely on the continuum damage mechanics (CDM) approach, where the material's microstructural behavior is approximated by internal variables

(scalar- or tensor-valued), which decrease the stiffness and / or the strength of the material. The earlier CDM models were based on a single-surface formulation (cf. Lemaitre [1984, 1985*a*,*b*]), allowing damage to develop only alongside evolving plastic deformations. This approach is widely employed until today and was further developed to capture e.g. crack-closure (Desmorat and Cantournet [2008]), finite strains (e.g. Badreddine et al. [2010, 2017]) or the influence of the Lode angle (e.g. Malcher and Mamiya [2014], Yue et al. [2019]). In contrast, two-surface approaches were introduced in the early works of e.g. Hansen and Schreyer [1994] and Zhu and Cescotto [1995], formulating damage and plasticity as two fully independent dissipative yet strongly interacting mechanisms. This conceptually very different method was applied in more recent works, in the context of small (Voyiadjis et al. [2011, 2012], Zhu et al. [2016]) and finite deformation theories (e.g. Vignjevic et al. [2012], Balieu and Kringos [2015], Brünig et al. [2014, 2018]).

Analogously to 'local' plasticity models, 'local' damage models (micromechanical and CDM based) lead to strong mesh-dependent results in simulations where material softening occurs (see e.g. Bažant et al. [1984], Cervera and Chiumenti [2006], Jirásek and Grassl [2008], de Borst et al. [2012]). Not only does the damage zone and corresponding energy dissipation shrink with finer meshes (see Bažant et al. [1984], de Borst et al. [1993]), but the location and the direction of propagation of the damage zone are also dependent on the mesh structure and element types (cf. Cervera and Chiumenti [2006] and Jirásek and Grassl [2008]). Thus, to acquire reliable, mesh-independent results, one possible solution is to introduce an additional 'nonlocal' damage variable into the formulation, similarly as in the context of 'nonlocal' plasticity models. This can be achieved e.g. through integral-type formulations (Bažant and Jirásek [2002]), explicit (Comi [1999]) or implicit gradient-type formulations. The present work focuses on the latter, in which the evolution of the global 'nonlocal' variable is governed by an additional partial differential equation and a set of boundary conditions. A modified Gurson-type coupled plasticity-damage model was proposed by Miehe, Kienle, Aldakheel and Teichtmeister [2016] and Aldakheel et al. [2018], where damage is captured by employing the conceptually very similar phase field of fracture approach.

In the context of CDM approaches, Papadioti et al. [2019] developed a theory where the failure criterion by Bai and Wierzbicki [2008] was combined with the implicit gradient damage-plasticity model by Engelen et al. [2002]. A fundamental contribution was made by Forest [2009, 2016], who introduced the so-called micromorphic approach, which can be considered as a very general blueprint for deriving implicit gradient-type formulations (see e.g. Saanouni and Hamed [2013]). Based on the work of Forest, Brepols et al. [2017, 2018, 2020] published gradient-extended two-surface damage-plasticity theories. A conceptually similar regularized

multi-surface formulation was developed by Kiefer et al. [2018]. Furthermore, coupled crystal plasticity and micromorphic gradient-extended damage models were proposed by e.g. Aslan, Cordero, Gaubert and Forest [2011] and Aslan, Quilici and Forest [2011]. Ultimately, recent models combine gradient damage with gradient plasticity, see e.g. Dimitrijevic and Hackl [2011] and Lodygowski et al. [2011], or the works of Miehe, Aldakheel and Raina [2016], Miehe, Teichtmeister and Aldakheel [2016], and Dittmann et al. [2018], where the phase field of fracture method is employed.

Despite the aforementioned strong coupling phenomena between plasticity, damage, and temperature, most of the above gradient-extended damage-plasticity theories were derived under the assumption of isothermal conditions only. Regarding regularized thermo-brittle theories, Sicsic et al. [2014] suggested the first phase field based method, which was extended by Miehe et al. [2015]. However, the number of regularized models capturing thermo-mechanically coupled damage and plasticity is very limited, until today. A thermo-mechanically coupled gradient-damage constitutive framework was proposed by Sarkar et al. [2020] in the context of small strains. One of the few contributions with the aforementioned characteristics in the context of finite deformations was proposed by Dittmann et al. [2020], which is based on the isothermal phase field theory by Dittmann et al. [2019]. Conclusively, due to this lack in regularized thermo-damage-plasticity models, an ongoing demand for further developments arises.

1.3 Outline of the dissertation

This cumulative dissertation is organized as follows. Chapter 2 and Chapter 3 are concerned with the experimental and numerical investigation of semi-crystalline Polyamide 6, to resolve some of the open questions discussed above. More precisely, in Chapter 2, a comprehensive experimental study is performed to investigate both, the influence of the degree of crystallinity and the temperature on the mechanical response of the polymer. To this end, various tensile experiments under monotonic and cyclic loading conditions as well as relaxation tests are conducted. This reveals new insights into the complex dependencies of the effective material properties on the temperature and degree of crystallinity. Based on this data, a continuum mechanical approach is proposed, which combines a nonlinear visco-elastic and elasto-plastic theory, where nonlinear isotropic and kinematic hardening as well as nonlinear relaxation behavior are accounted for. In this isothermal framework, the temperature as well as the degree of crystallinity serve as constant input parameters, which contribute to the overall constitutive behavior. In this way, the effect of the aforementioned factors on the loading-rate depen-

dent plastic deformations, strain hardening, strain recovery, stress relaxation, and loading-unloading hysteresis loops can be accurately predicted.

In Chapter 3, this model is further developed towards a fully thermo-mechanically coupled theory. The degree of crystallinity is now treated as a non-constant temperature history dependent internal variable to account for the process dependent evolution of the underlying microstructure and the corresponding variations in the mechanical behavior. To this end, the crystallization kinetics are modeled by means of a non-isothermal representation of the Avrami equation. The corresponding parameters are obtained from isothermal and non-isothermal differential scanning calorimetry experiments. Furthermore, from the energy balance, the heat release due to irreversible processes and exothermic crystal growth are derived. The predicted heat of crystallization is qualitatively in good agreement with experimental findings. It is concluded that the employed formulation is suitable to predict the crystallization process from a static relaxed melt, in transient, three-dimensional heat transfer problems. Furthermore, comparisons with infrared thermography measurements reveal accurate predictions of the material self-heating and accompanied thermal-softening during uniaxial tensile tests.

In the last Chapter 4, the above issues in the context of non-isothermal damage and plasticity modeling in metals are addressed. Based on the isothermal theory of Brepols et al. [2020], a thermo-mechanically coupled two-surface damage-plasticity theory is derived. The framework is valid for large deformations, thermodynamically consistent, and fulfills the damage growth criterion. To overcome the non-physical mesh-dependence of conventional 'local'theories discussed above, a gradient-extension based on the micromorphic approach of Forest [2009, 2016] is incorporated. Due to the additional degree of freedom related to the micromorphic extension, three fully coupled fields of global unknowns must be solved. To this end, the implementation of a fully implicit and monolithic solution scheme is presented and discussed in detail. The model's predictions (regarding e.g. local heat accumulation due to damage and plasticity, strain localization and thermal softening as well as crack propagation and back-coupling effects) are quantitatively and qualitatively in good agreement with experimental observations.

2 Article 1: Modeling the effect of temperature and degree of crystallinity on the mechanical response of Polyamide 6

This article was published as:

Felder, S., Vu, N.A., Reese, S. and Simon, J.-W. [2020], 'Modeling the effect of temperature and degree of crystallinity on the mechanical response of Polyamide 6 ', *Mechanics of Materials* **1**48, 103476.

Disclosure of the individual authors' contributions to the article:

S. Felder reviewed the relevant existing literature, derived and implemented the constitutive framework as a user-defined material model (UMAT) into the commercial Finite Element software *ABAQUS* / Standard, and wrote the article. The conceptual design of the experimental study was developed by S. Felder, in addition. Most experiments were conducted by N.A. Vu, who also performed the parameter fitting, implemented the corresponding optimization procedure, and carried out the structural computations. S. Reese and J.-W. Simon gave conceptual advice, contributed to the discussion of the results, read the article and gave valuable suggestions for improvement. All authors approved the publication of the final version of the manuscript.

2.1 Abstract

In the current work, an extensive experimental study is performed, to investigate the influence of both, the applied thermal conditions over a wide range of temperatures and the manufacturing process induced degree of crystallinity on the mechanical response of semi-crystalline polymers. To this end, large-strain tensile experiments with different loading procedures (i.e. monotonic, cyclic, and relaxation tests) are conducted on Polyamide 6 for different loading rates. The experimental data base provides new insights into the complex dependencies of the effective material properties on the aforementioned factors and serves as the foundation for the development of a continuum mechanical constitutive framework.

The phenomenological, isothermal model is developed in a reasonably general, thermodynamically consistent manner, to predict the strain rate, temperature and degree of crystallinity dependent large-deformation response of semi-crystalline polymers. A coupled nonlinear visco-elastic, elasto-plastic theory, incorporating nonlinear isotropic and kinematic hardening, is proposed to capture the complex material behavior (e.g. strain recovery and hysteresis loop after cyclic loading-unloading and nonlinear stress relaxation). A staggered characterization method is proposed, to identify a set of material parameters from the experimental data. Finally, validation studies demonstrate the great capabilities of the novel constitutive framework, to accurately predict the significant influence of the temperature and degree of crystallinity on the material response.

Nomenclature

a	Scalar quantity
$\boldsymbol{a}$	First order tensor
$\boldsymbol{A}$	Second order tensor
$\mathbb{A}$	Fourth order tensor
$\dot{(*)}$	Total derivative with respect to time
$(*)^T$	Transpose of a quantity
$(*)^{-1}$	Inverse of a quantity
tr$(*)$	Trace of a quantity
det$(*)$	Determinant of a quantity
sym$(*)$	Symmetric part of a quantity
dev$(*)$	Deviatoric part of a quantity
$\boldsymbol{A} : \boldsymbol{B}$	Scalar product of two tensors $\boldsymbol{A}$ and $\boldsymbol{B}$
$\omega_{(*)}$	Eigenvalue of a quantity
$\|\| * \|\|$	Frobenius norm of a tensor
$\|\| * \|\|_s$	Second norm of a tensor
$(*)_{1}$	Intermolecular quantity
$(*)_{2}$	Network quantity
$(*)_{e1}$	Intermolecular elastic quantity
$(*)_{e2}$	Network elastic quantity
$(*)_{i}$	Network inelastic quantity
$(*)_{n}$	Quantity from last converged time step
$(*)_{p}$	Intermolecular plastic quantity
$(*)_{pe}$	Intermolecular plastic elastic quantity
$(*)_{pi}$	Intermolecular plastic inelastic quantity
b and c	Kinematic hardening parameters
$\boldsymbol{B}$	Left Cauchy-Green deformation tensor
$\boldsymbol{C}$	Right Cauchy-Green deformation tensor
$\mathbb{C}$	Material tangent modulus
cc	Current configuration
$\boldsymbol{D}$	Symmetric part of velocity gradient
E	Young's modulus
$\boldsymbol{F}$	Deformation gradient
H	Isotropic hardening modulus
$\boldsymbol{I}$	Second order identity tensor
ic_{1a}	Intermediate plastic configuration
ic_{1b}	Intermediate configuration of kinematic hardening
ic_{2}	Inelastic intermediate configuration
J	Determinant of deformation gradient
K	Bulk modulus
$\boldsymbol{L}$	Velocity gradient
$\boldsymbol{M}$	Mandel stress tensor
rc	Reference configuration
R	Driving force of isotropic hardening
$\boldsymbol{S}$	Second Piola-Kirchhoff stress tensor
$\boldsymbol{u}$	Displacement vector
$\boldsymbol{U}$	Right stretch tensor
$\boldsymbol{W}$	Antisymmetric part of velocity gradient
$\boldsymbol{X}$	Back stress tensor in ic_{1a}
$\tilde{\boldsymbol{X}}$	Back stress tensor in rc
$\boldsymbol{Y}$	Stress like quantity: $\boldsymbol{Y} = \boldsymbol{C}\boldsymbol{S}_1 - \boldsymbol{C}_p\tilde{\boldsymbol{X}}$
$\boldsymbol{Y}_{kin}$	Stress like quantity: $\boldsymbol{Y}_{kin} = \boldsymbol{C}_p\tilde{\boldsymbol{X}}$
β	Isotropic hardening parameter
δ	Relaxation time function parameter
Δt	Time increment
θ	Temperature
κ	Accumulated plastic strain
λ_i	stretch in i-direction
Λ	Lamé constant
$\dot{\gamma}$	Plastic multiplier
μ	Shear modulus
ν	Poisson's ratio
$\boldsymbol{\xi}$	Set of internal variables
ρ_0	Density in rc
$\boldsymbol{\sigma}$	Cauchy stress tensor
σ_∞	Isotropic hardening parameter
σ_y	Initial yield stress
τ	Relaxation time
τ_0	Relaxation time function parameter
$\boldsymbol{\tau}$	Kirchhoff stress tensor
φ	Relaxation time function parameter
Φ	Yield function
χ	Absolute degree of crystallinity
ψ	Specific Helmholtz free energy
Ψ	Volumetric Helmholtz free energy

2.2 Introduction

Semi-crystalline thermoplastics represent an important class of engineering materials in a large range of industrial sectors, due to their potential of a cost-effective mass production and attractive mechanical properties such as high strength to weight ratio. In contrast to amorphous thermoplastics, semi-crystalline polymers (SCPs) partly crystallize during cooling from the melt. Depending on the manufacturing process (e.g. forming processes of continuous fiber reinforced SCPs, injection moulding etc.) and the preceding thermal treatment, applied stress, and presence of moisture, the crystallization kinetics can substantially differ (cf. Fornes and Paul [2003]). Naturally, the emerged morphology of the underlying microstructure (e.g. the degree of crystallinity, crystal configuration, and lamellae thickness etc.) has a significant influence on the mechanical behavior of SCPs (e.g. Jenkins [1992] and Ayoub et al. [2011]). Moreover, the material response is strongly affected by the temperature and the loading rate. Due to the growing demand for this type of materials, it is of high interest to identify, analyze, and predict the complex material and structural response of parts during and after processing.

Consequently, numerous computational models, aiming at reliably capturing the complex nonlinear behaviour of SCPs or SCP-based composites, were published during the last decades. In the pioneer modeling approach for glassy polymers of Haward et al. [1968], an additive decomposition of the total resistance to deformation into an intermolecular and molecular network resistance, was proposed. Based on the latter and the fundamental ideas of Boyce et al. [2000], several phenomenological models were developed for amorphous (e.g. Anand et al. [2009], Anand et al. [2009], and Srivastava et al. [2010]) and semi-crystalline polymers (e.g. van Dommelen et al. [2003], Ayoub et al. [2010], and Barriere et al. [2019]).

Within the class of phenomenological modeling approaches, several authors (e.g. Lai et al. [2005] and Khan et al. [2006]) proposed to govern the material deformation by reversible, (nonlinear) visco-elastic modeling strategies. In contrast, in other works (e.g Zeng et al. [2010], Drozdov [2011], Khan and Yeakle [2011], and Kästner et al. [2012] visco-plastic formulations, mainly based on the over-stress concept, were suggested to capture rate dependent irreversible deformations. However, to accurately predict the observed plastic behavior, as well as the strain recovery, stress relaxation, and loading-unloading hysteresis loop of amorphous and semi-crystalline polymers, coupled visco-elastic, visco-plastic models are crucial (cf. Miled et al. [2011], Yu et al. [2016], Gudimetla and Doghri [2017], Praud et al. [2017], and Wang et al. [2019]). In addition, to account for the Bauschinger-like effect upon unloading, kinematic hardening was incorporated in several constitutive frameworks (cf. e.g. Anand and Ames [2006], Anand et al. [2009], and Krairi and Doghri [2014]). Recently, Qi et al.

[2019] endeavored to improve these models and developed a small strain theory to capture the complex cyclic behavior of semi-crystalline high density Polyethylene (HDPE), where a parallel arrangement of elasto-plastic intermolecular and nonlinear visco-elastic network resistance was proposed.

Besides the phenomenological modeling approaches, multi-scale strategies were employed, by using either analytical or FE-based homogenization schemes, e.g. Gueguen et al. [2010], Li and Shojaei [2012], Uchida and Tada [2013], Popa et al. [2014], and Alisafaei et al. [2016] to name a few. In other physical approaches, aspects related to the microstructure were integrated into the mathematical framework, such as the molecular chains network reorganization (Maurel-Pantel et al. [2015]). Despite the usually small number of parameters and less complex model formulations for this class of constitutive frameworks, it is in general rather difficult to obtain the required physical or microstructural data from experimental observations. This is in contrast to phenomenological models, where the required material parameters can be identified from conventional mechanical tests.

As alluded above, the nonlinear mechanical behavior of semi-crystalline polymers is significantly depending on the thermal conditions. Despite the abundant literature on isothermal constitutive frameworks, only a limited number of researchers focused on thermo-mechanically coupled formulations. Recently, Maurel-Pantel et al. [2015], Garcia-Gonzalez et al. [2018], and Li et al. [2019] studied the thermo-mechanical coupling effects for Polyamide 66 (PA66), Polyether ether ketone (PEEK), ultra-high-molecular-weight Polyethylene (UHMWPE), and HDPE, respectively. In addition, Shen et al. [2019] introduced a thermo-elastic-viscoplastic-damage model for Polyamide 6. In the work of Shojaei and Volgers [2017], the significance of the self-heating phenomenon in the context of lifetime prediction of polymeric materials was revealed. Furthermore, Krairi et al. [2019] developed a non-isothermal, visco-elastic, visco-plastic small strain theory and applied it for PA 66 and Polypropylene.

Despite the significant influence of the composition of the underlying amorphous and crystalline regimes on the macroscopic response of SCPs, only a limited number of constitutive models account for this effect. Dusunceli and Colak [2008] investigated different rules of mixture of the amorphous and crystalline regimes in a phenomenological approach. A two-phase representation of the microstructure was chosen by Ayoub et al. [2011] and Abdul-Hameed et al. [2014] and further contributions were made by Ponçot et al. [2013] and Rozanski and Galeski [2013]. Recently, Chen et al. [2019] studied and modeled the significant dependence of the ratcheting behavior of UHMWPE on the degree of crystallinity at small strains. In all these works, the influence of the degree of crystallinity was investigated for only one specific temperature.

From the presented review above, a considerable large progress associated with the experimental and numerical analysis of semi-crystalline polymers is evident. However, in all these works, the impact of the temperature (e.g. Krairi et al. [2019], Shen et al. [2019]) and the process induced degree of crystallinity (e.g. Dusunceli and Colak [2008], Ayoub et al. [2011]) on the mechanical response was assessed individually and the corresponding models account for one of these quantities only. Consequently, the prediction of the material response for different process induced morphologies of the material's internal microstructure (e.g. the degree of crystallinity), in applications where the temperature varies over a wide range, remains a challenge, until today. To assess and predict the interplay and coupling effects between degree of crystallinity and temperatures is in particular crucial, since the influence of the crystalline regimes on the material properties is strongly temperature dependent and changes significantly above the glass transition temperature.

Thus, the ultimate objective of the current work is to study and evaluate the impact and interplay of all the aforementioned influences (strain rate, degree of crystallinity, and temperature) collectively. To this end, a new phenomenological constitutive model with the following features is developed:

- Thermodynamically consistent, 3D, finite strain theory (cf. Section 2.5).
- Including a coupled visco-elastic, plastic model formulation, comprising a nonlinear relaxation function as well as nonlinear isotropic and kinematic hardening.
- Accounting for a processing induced variation of the degree of crystallinity.
- Accounting for a wide range of temperatures, spanning the glass transition.

To the authors' knowledge, there is no model available for SCPs, which comprises all of theses features.

This novel isothermal theory is applied to model Polyamide 6. Despite the numerous experimental data published over the last decades, no comprehensive (true) stress-stretch data is available for Polyamide 6 over a wide range of temperatures, including large strains, different loading rates, and accounting for different degrees of crystallinity. In order to investigate the material behavior, different loading procedures (i.e. monotonic, cyclic, and relaxation tests) must be considered, in addition. In this work, data with the aforementioned features is generated, by conducting uniaxial tensile tests for *Ultramid B40*, kindly provided by BASF SE (see Section 2.3 and 2.4). In order to identify a set of material parameters, based on the experimental observations, a staggered calibration procedure is developed (cf. Section 2.6).

The model is implemented as an user material subroutine *UMAT* into the commercial FEM software *ABAQUS*/Standard (see Appendix 2.9). The capabilities of the model, to efficiently and accurately predict the three-dimensional material behavior for large deformations, different strain rates, temperatures, and degrees of crystallinity are verified in Section 2.7 and finally conclusions are drawn in Section 2.8.

2.3 Experimental investigation

2.3.1 Specimen preparation

As alluded above, the objective of the experimental investigations was to obtain true stress-stretch data for constant temperatures (under isothermal conditions), constant strain rates, and constant degrees of crystallinity. The tested tensile specimens were produced by injection moulding and the geometry and dimensions were in accordance with type 5A of ISO 527-2:2012.

The crystalline regimes of Polyamide 6 are either characterized by a fully extended (monoclinic) configuration of the polymer chains, referred to as α-form, or a twisted (hexagonal/ pseudohexagonal) configuration (γ-form) (see e.g. Fornes and Paul [2003]), which depend on the thermal conditions, applied stress, and presence of moisture. To study the influence of the crystallographic structure of the microstructure on the mechanical properties, two sets of specimens were annealed after processing, to alter the degree of crystallinity. The resulting total degree of crystallinity χ was determined by differential scanning calorimetry (DSC) analysis, utilizing the DSC 1 from *Mettler Toledo*. All samples were prepared by cutting the polymer into pieces significantly smaller than 1 mg. Subsequently, 5 mg of the polymer were filled in 40 μl tins for the DSC analysis, which was conducted under nitrogen atmosphere. The samples were heated up from room temperature 23.5 °C way above the melting point to 245 °C with 10 °C/min. Each testing procedure was repeated three times.

The recorded curves of heat flow over temperature are displayed in Figure 2.1. Noteworthy, the curves have been shifted vertically, in order to increase the readability. The heat absorption during the endothermic melting of the crystalline regime i.e. the change in specific enthalpy Δh_m, was computed by integrating the obtained specific heat flow curves over time. As it is common practice (cf. e.g. Zinet et al. [2010]), the absolute degree of crystallinity χ (based on mass) of the samples was obtained by

$$\chi = \frac{\Delta h_m}{\Delta h_f^{100}} \tag{2.1}$$

where Δh_f^{100} represents the specific fusion enthalpy of a hypothetical 100% crystalline material. For Polyamide 6, Illers [1978] reported a heat of fusion of $\Delta h_f^{100} = 241$ J/g and 239 J/g corresponding to the monoclinic and hexagonal form, respectively. In line with Fornes and Paul [2003], the average of these values, i.e. 240 J/g, was considered, in the current work.

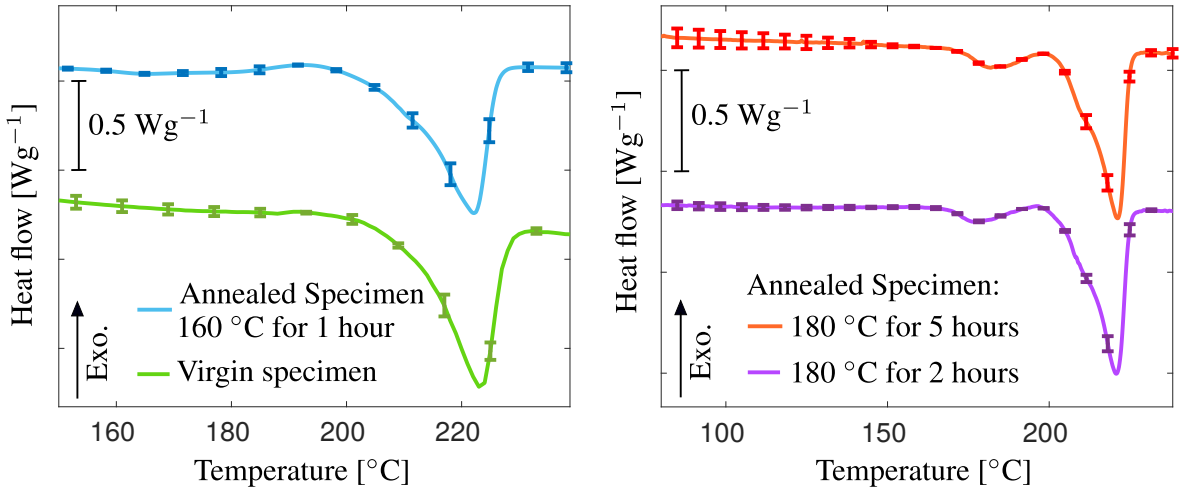

Figure 2.1: Experimental results of the DSC analysis. Left: Heat flow over temperature for a virgin specimen and a specimen annealed at 160 °C for 1 hour, revealing no traceable change of the degree of crystallinity ($\chi = 0.229 \pm 0.008$ vs. $\chi = 0.228 \pm 0.005$, respectively). Right: DSC trace for two specimens annealed at 180 °C for 2 hours and 5 hours, resulting in a change of the total degree of crystallinity ($\chi = 0.250 \pm 0.0057$ and $\chi = 0.281 \pm 0.0006$, respectively).

The DSC analysis for the virgin specimen resulted in a degree of crystallinity of $\chi = 0.229 \pm 0.008$. In addition, specimens which were annealed at 160 °C for 1 hour were investigated and revealed no traceable effect of the preceding thermal treatment on the measured degree of crystallinity ($\chi = 0.228 \pm 0.005$). The corresponding heat flow curves over temperature (provided on the left-hand side of Figure 2.1) exhibited a unique melting peak at $\theta_{\text{peak}} \approx 122$ °C in both cases. After Kyotani and Mitsuhashi [1972], this suggests the melting of a predominately α-crystal configuration. However, during injection molding, usually a small amount of non-spherulitic pseudohexagonal γ-form is present, close to the surface, according to Fornes and Paul [2003]. The faint exotherm pointing at 193 °C was also reported by several other authors (e.g. Khanna and Kuhn [1997] and Xie et al. [2009]) and is related to reorganization processes of unstable crystals. These experimental findings substantiated the assumption that the degree of crystallinity remained constant during the mechanical testing, especially at elevated temperatures above the glass transition, in the considered temperature range (20 °C - 160 °C).

To alter the degree of crystallinity, two sets of virgin specimens were annealed at 180 °C for 2 and 5 hours, respectively. The corresponding heat flow over temperature relations are provided on the right-hand side of Figure 2.1. In line with the results of Millot et al. [2015], a double endotherm was present upon heating of the samples. With increasing annealing time, the distance between the two endothermic peaks decreased (cf. Gurato et al. [1974]). This resulted in a constant major endotherm at $\theta_{\text{peak}} \approx 121$ °C, and minor once at $\theta_{\text{peak}} \approx 179$ °C and $\theta_{\text{peak}} \approx 185$ °C, for annealing times of 2 hours and 5 hours, respectively. These results suggest the melting of a small amount of γ-crystals followed by melting of the predominant α-form (cf. Kyotani and Mitsuhashi [1972] and Millot et al. [2015]). This annealing procedure led to a total degree of crystallinity of $\chi = 0.250 \pm 0.0057$ and $\chi = 0.281 \pm 0.0006$, for annealing times of 2 and 5 hours, respectively.

In the course of the current work, no differentiation between either crystal configurations (γ-phase and α-phase) nor morphology (lamella thickness) of the crystalline phase is made. In this way, the biphasic nature of the underlying microstructure is accounted for by introducing a single scalar variable χ, which represents the total crystal weight fraction. In summary, the following sets of specimens were obtained:

1. No annealing: $\chi \approx 0.23$
2. Annealing under vacuum for 2 hours at 180 °C: $\chi \approx 0.25$
3. Annealing under vacuum for 5 hours at 180 °C: $\chi \approx 0.28$

Noteworthy, all experiments were conducted for the first and third set of specimens to characterize the proposed constitutive framework (cf. Section 2.5), whereas the second set was utilized for model validation only, see Section 2.7.

2.3.2 Mechanical testing and experimental setup

Polyamide 6 is hydrophilic and the significant influence of water absorption in a humid environment on the mechanical properties was reported by several authors e.g. Ishisaka and Kawagoe [2004] and Miri et al. [2009]. In the context of thermoforming processes, the material behavior in a dried state is of particular interest. Consequently, all tested specimens were dried under vacuum at 100 °C for 48 hours, subsequently vacuum-sealed, and directly tested after unpacking.

The experimental setup is depicted in Figure 2.2. Tensile experiments were conducted by using a *Zwick Z005* universal testing machine. For the experiments above room temperature, a temperature furnace was incorporated into the test set up. In preceding investigations,

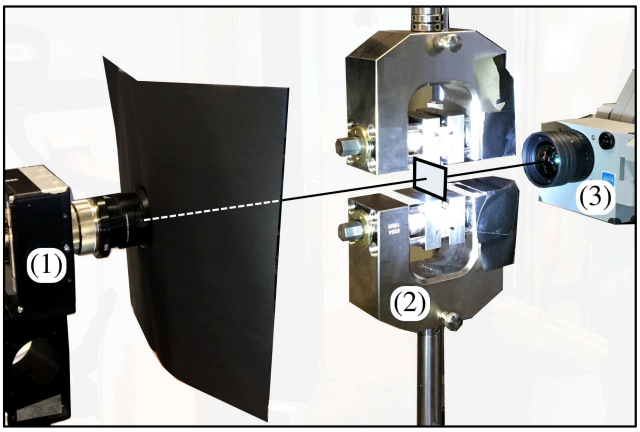

Figure 2.2: Experimental setup at room temperature: *ARAMIS* camera (1), *Zwick Z005* testing machine (2), *VarioCAM HD* infrared camera (3).

thermocouples within the specimens yielded the required heating time for an uniform temperature distribution within the sample. To obtain non-tactile displacement measurements in longitudinal and traversal direction at the surface of the specimen, a 2D *ARAMIS 4M* digital image correlation (DIC) system was employed during all experiments. To increase the accuracy and precision of these measurements, major attention was paid to achieve a perpendicular alignment of the camera to the specimen's surface. Simultaneous infrared thermography (IR) measurements were performed during the experiments at room temperature, by utilizing a *InfraTecVarioCAM HD* device (see Figure 2.2).

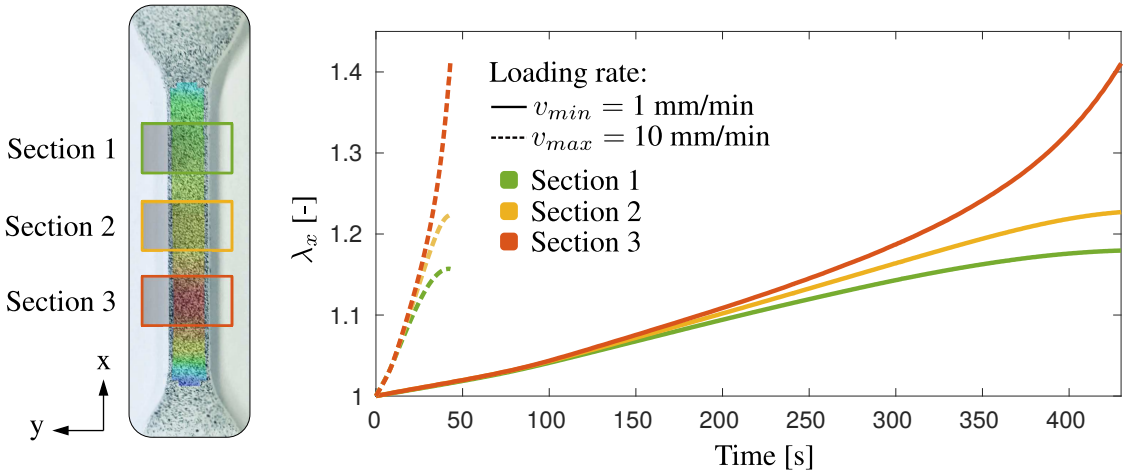

Figure 2.3: Representative DIC image and section concept (left). Evolution of stretch in longitudinal x-direction λ_x for different loading rates v and sections (right).

The loading rate was controlled by the cross head speed of the testing machine and two

different velocities ($v_{min} = 1$ mm/min and $v_{max} = 10$ mm/min) were prescribed. At moderate deformations, local necking occurred and a heterogeneous strain field, accompanied by non-constant strain rates, arose (see Figure 2.3). Noteworthy, the necking area was almost always located at the lower part of the specimen. To identify areas within the specimen exhibiting constant strain rates, the mean stretch in longitudinal x-direction λ_x over time, for three distinct sections was investigated for both loading velocities, see Figure 2.3. An almost constant stretch rate of $\dot{\lambda}_{x,min} \approx 0.0005$ s^{-1} and $\dot{\lambda}_{x,max} \approx 0.0058$ s^{-1} for v_{min} and v_{max}, respectively, was observed for section 2. Moreover, strain induced crystallization was present in the local necking regime, leading to an evolution of the crystallographic structure during the tests. Accordingly, evaluating section 2 was also favorable in order to investigate the material response for constant degrees of crystallinity. Consequently, the true stress-stretch relation obtained from the stretch field corresponding to this homogeneously deformed area was evaluated for each experiment.

Noteworthy, injection molding usually leads, to a certain extend, to the orientation of the molecular chains in the flow direction. This results in a material anisotropy, which was reported by e.g. Fujiyama et al. [1977]. This effect was not further investigated, by e.g. evaluating the tensile properties in transversal direction, in addition. However, additional measurements of the out-of-plane stretch λ_z revealed that the stretch in transversal direction λ_y and λ_z evolved equally. Thus a transversely isotropic material behavior was concluded.

Each loading procedure was conducted over a wide range of temperatures, below and above the glass transition temperature ($\theta_g \approx 80$ °C) at 23 $\pm$ 1.0 °C, 50 $\pm$ 1.0 °C, 120 $\pm$ 1.0 °C, and 160 $\pm$ 1.0 °C. Due to the small deviation of the material response for different specimens (indicated by the error bars in the corresponding stress over stretch data in e.g. Figure 2.6), each procedure was only repeated 3 times.

2.4 Experimental results

To obtain insights into the fundamental deformation processes during the tensile experiments, cyclic loading-unloading-recovery experiments were performed. During this cyclic loading procedure, the specimen was first subjected to displacement controlled loading and subsequently unloaded until the force equaled zero. In the last step, the force was held constant for a sufficiently long time, to distinguish between time-independent and time-dependent remaining deformations. In Figure 2.4, the true (Cauchy) stress over stretch and stretch over time relation is presented for this loading procedure at room temperature for $\dot{\lambda}_{x,max}$ and $\chi = 0.23$.

The data revealed three distinct deformation regimes:

1. In the elastic regime, no remaining stretch was present after unloading to zero force.

2. In the visco-hyperelastic regime, some remaining deformations were detected after unloading. However, in the recovery step, these were dissolved and the undeformed initial configuration was obtained at the end ($\lambda_x \approx 1$), as depicted in Figure 2.4 on the right hand side.

3. In the visco-hyperelastic-plastic regime, the stretch value after unloading converged towards an equilibrium, where some irreversible plastic deformations remained.

Furthermore, constant initial slopes upon loading ascertained an undamaged material, in the considered deformation range. After the plastic regime was reached, the recovery step after unloading was omitted and the specimen was directly subjected to loading, for the sake of a less time-consuming experimental procedure.

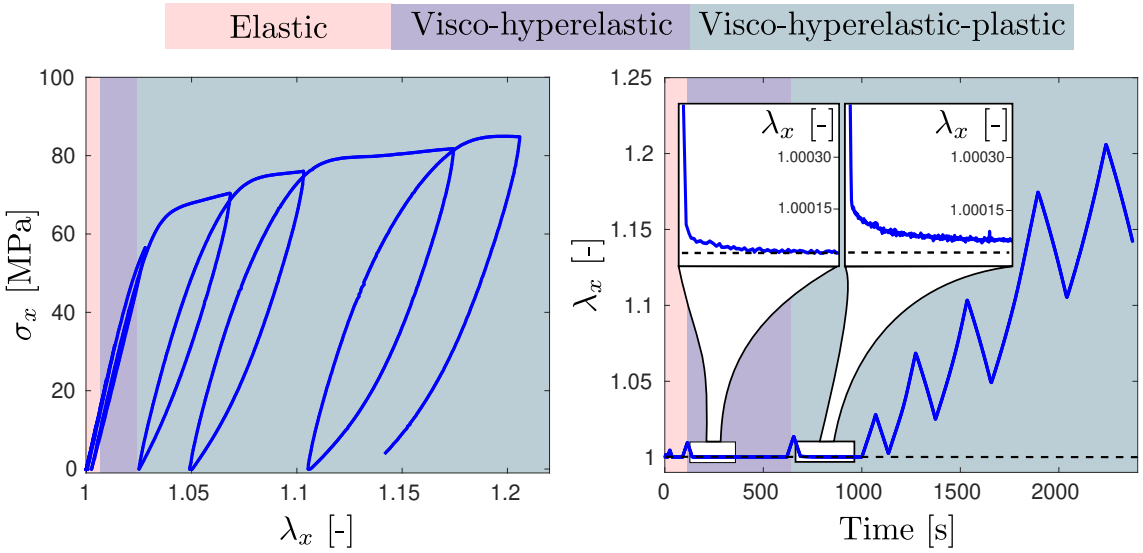

Figure 2.4: Cyclic loading-unloading-recovery experiments at room temperature for $\dot{\lambda}_x \approx 0.0058\ \mathrm{s}^{-1}$ and $\chi = 0.23$.

In this work, the initial yield stress was determined from the average of the maximum stress of the first load cycle within the plastic regime and the maximum stress of the preceding load cycle (results see Figure 2.5). Due to the small increase of the maximum stretch for the load cycles within the visco-elastic regime, the difference between the maximum stresses of consecutive load cycles was small as well. Consequently, this identification procedure led to acceptable uncertainties in the determination of the yield stress (difference between maximum stress of first load cycle in the plastic regime and maximum stress of preceding load cycle), highlighted as error bars in Figure 2.5. It should be emphasized that this approach

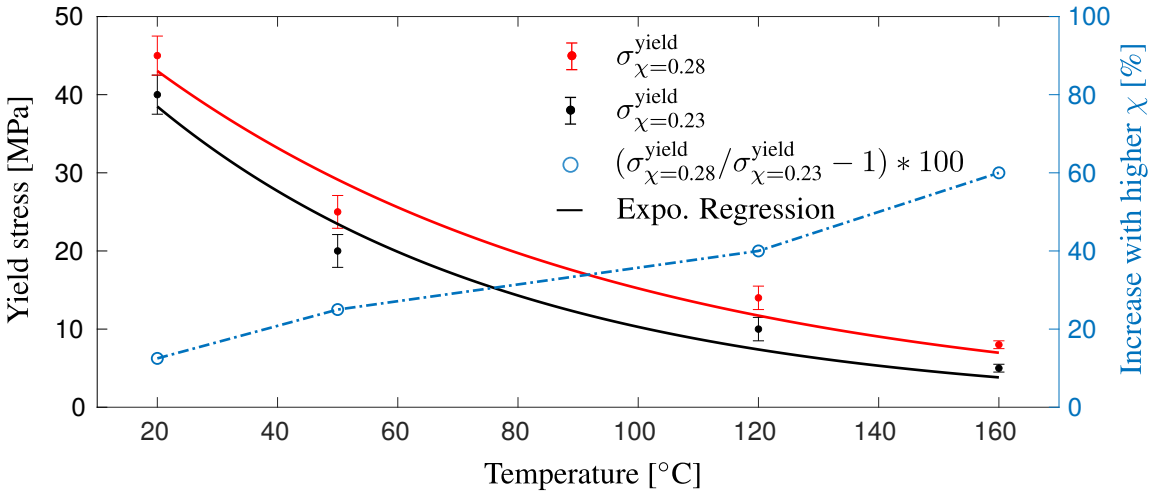

Figure 2.5: Yield stress σ^{yield} for the investigated temperatures and degrees of crystallinity. The increase for a higher degree of crystallinity is highlighted, in addition. The exponential trend line is of the form $\sigma^{\text{yield}} = \mathrm{C}_1 \exp(-\mathrm{C}_2\,\theta)$, where the parameters $C_1 = 53.5247$, 55.8121 and $C_2 = 0.0165$, 0.0130 were fitted for $\chi = 0.23$ and $\chi = 0.28$, respectively.

was in contrast to most identification procedures presented in the literature. It is common practice to estimate the initial yield stress from monotonic tensile tests only. To this end, the intersection of the initial slope of the stress stretch curve and the hardening slope (e.g Şerban et al. [2013]) or the peak in the engineering stress-stretch relation (e.g. Rae et al. [2007]) are considered. Among others, El-Qoubaa and Othman [2016] determined the yield stress for semi-crystalline PEEK at higher temperatures from cyclic loading procedures, without introducing an additional recovery step. However, from the provided data for Polyamide 6 in this study, it is obvious that these identification schemes would lead to less accurate values for the onset of plastic flow.

Monotonic tensile tests were conducted until rupture of the specimen occurred or a maximum stretch of $\lambda_x = 1.20$ was reached. The true (Cauchy) stress σ_x over stretch relation is presented in Figure 2.6 for various fixed temperatures, loading rates, and degrees of crystallinity. The observed influence of the temperature on the material response is in line with several studies (Shan et al. [2007], Maurel-Pantel et al. [2015], and Parodi et al. [2018] to name a few). As the temperatures increased, the Young's modulus of the material decreased exponentially, as shown in Figure 2.7. Furthermore, at higher temperatures a more gradual roll-over to yielding was observed, the yield strength decreased (nearly exponentially cf. Figure 2.5), and the amount of strain-hardening diminished. Noteworthy, the displayed exponential regressions (cf. Figures 2.5 and 2.7) provide only a trend and must be treated with

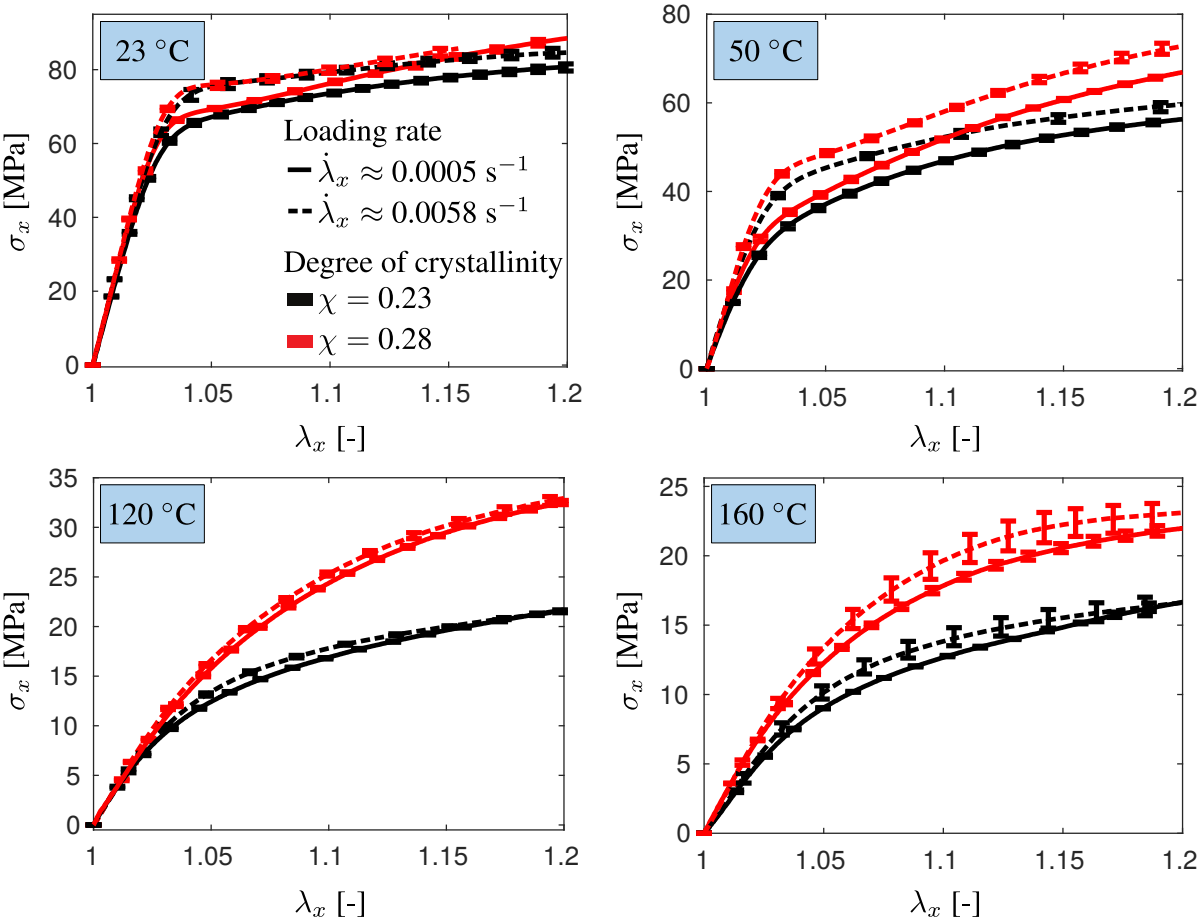

Figure 2.6: Monotonic tensile tests at various temperatures, degrees of crystallinity χ and loading rates $\dot{\lambda}_x$.

care, since not enough data is provided close to the glass transition temperature $\theta_g \approx 80$ °C, where sudden changes of the material properties might occur.

A clear dependency of the material properties on the morphology of the underlying microstructure was evident from the presented data. With increasing degree of crystallinity, an increase of the initial stiffness, hardening, and yield stress was observed, which has been also reported by Ayoub et al. [2011] above the glass transition temperature for polyethylene. The influence of the degree of crystallinity was more pronounced at temperatures above the glass transition regime and increased significantly at 160 °C, in particular for the yield stress (cf. Figures 2.5 and 2.7). Above the glass transition, the chain mobility within the amorphous phase increased significantly and the resistance to deformation, provided by the additional crystalline structures, was thus more prominent. Interestingly, the influence of the degree of crystallinity on the stiffness was the highest at 160 °C (cf. Figure 2.7), whereas the hardening behavior was most effected at 120 °C.

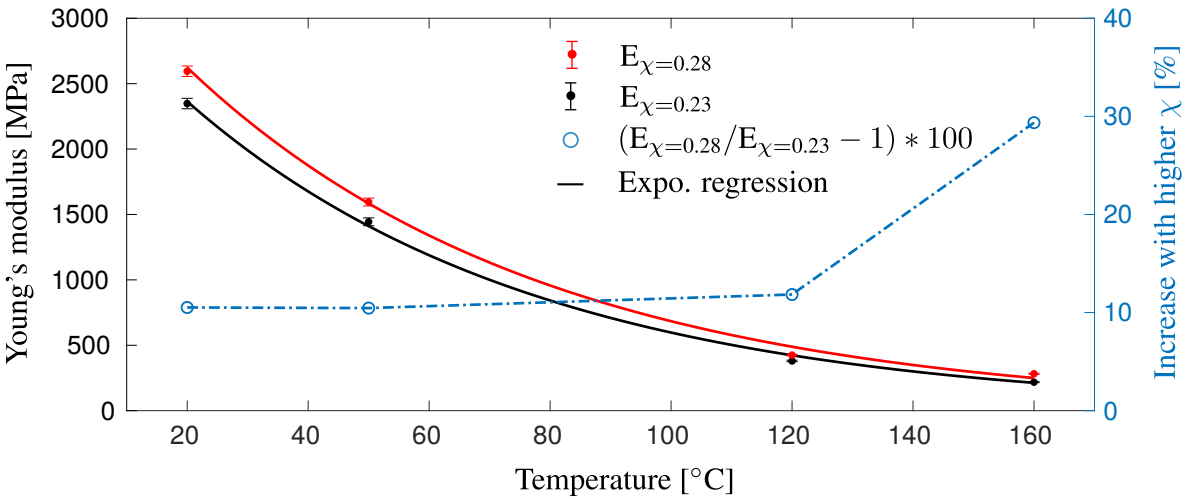

Figure 2.7: Young's modulus E for the investigated temperatures and degrees of crystallinity. The increase for a higher degree of crystallinity is highlighted, in addition. The exponential trend line is of the form $E = C_1 \exp(-C_2\,\theta)$, where the parameters $C_1 = 3334$, 3670 and $C_2 = 0.0172$, 0.0168 were fitted for $\chi = 0.23$ and $\chi = 0.28$, respectively.

Concomitant with the observation of an initially elastic material response, the initial stiffness appeared to be relatively strain rate independent (cf. Figure 2.6).Shan et al. [2007] reported that the sensitivity of the yield stress with increasing loading rates was logarithmic for Polyamide 6 and that the influence became more and more negligible at temperatures above the glass transition temperature. These observations corresponded with the authors findings, in particular since the considered strain rates were limited to one decade only. This is in contrast to the shape of the stress stretch curves, in particular below the glass transition. For increasing loading velocities, an increase of hardening accompanied by a loss in ductility was detected (cf. Ayoub et al. [2011], Şerban et al. [2013], and El-Qoubaa and Othman [2016], for other semi-crystalline polymers). In line with the results of e.g. Shan et al. [2007], the influence of the strain rate on both the shape of the stress stretch curves and the yield stress decreased at temperatures above the glass transition. This behavior can be attributed to the fact that at higher temperatures, the material behavior was mostly dominated by the crystalline regimes, as alluded above. Interestingly, at a temperature of 120 °C, the effect of the loading rate was slightly less pronounced, compared to a temperature of 160 °C.

At higher loading speeds, the hardening behavior became more complicated. The slope of the stress-stretch curves decreased for higher strain rates, after moderate stretch levels of $\lambda_x \approx 1.05$ (see Figure 2.6). At higher temperatures (e.g. 120 °C and 160 °C), this eventually led to an intersection of the curves for $\dot{\lambda}_{x,min}$ and $\dot{\lambda}_{x,max}$. This behavior can be traced

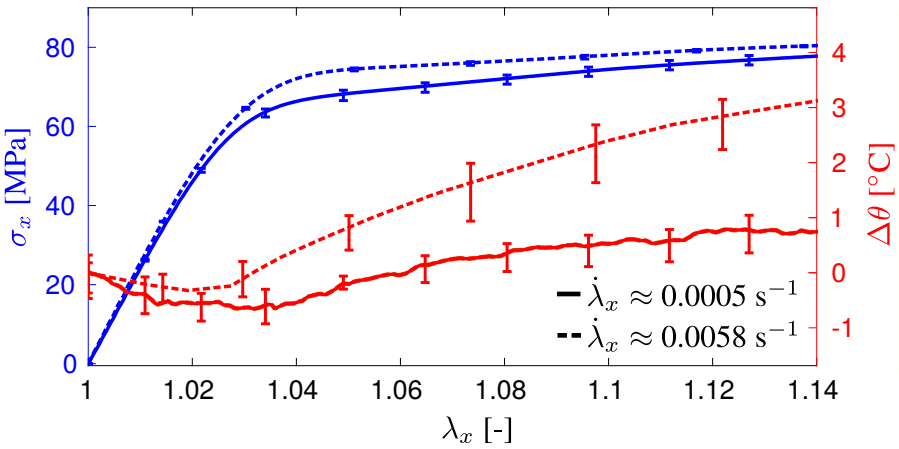

Figure 2.8: Investigation of material self-heating, indicating the change in temperature $\Delta\theta$ for an ambient temperature of 23 °C and $\chi = 0.23$.

back to the self-heating of the material due to dissipative effects (cf. Maurel-Pantel et al. [2015] and Mohagheghian et al. [2015]). At higher loading speeds, strain induced hardening competed with self-heating induced thermal-softening. To investigate this effect in the current experimental study, infrared thermography (IR) was employed. In Figure 2.8, the average temperature of section 2 (cf. Figure 2.3) is plotted over the stretch in longitudinal direction for $\dot{\lambda}_{x,min}$ and $\dot{\lambda}_{x,max}$ at room temperature. Noteworthy, the temperature resolution of the employed infrared camera (*InfraTec VarioCAM HD*) is 0.08 °C, whereas the measurement accuracy is ± 2 °C. Consequently, comparatively large error bars arose for the measured temperatures. Nevertheless, a clear trend was visible from the provided data, indicating a temperature increase due to irreversible deformation processes at higher loading rates. For the sake of a better comparison, the temperature curves were shifted vertically to the same starting temperature. Interestingly, a small initial decrease of the temperature, referred to as thermoelastic effect, was present. The latter phenomenon was already described by Moreau et al. [2005] and Maurel-Pantel et al. [2015] in the context of amorphous (PMMA and PC) and semi-crystalline (PA 66) polymers, respectively.

To provide additional insights into the time dependent material behavior, relaxation tests were performed for all considered temperatures. The objective was to investigate the stress relaxation under homogeneous states of tension, at different deformation stages, i.e. in the visco-hyperelastic and visco-hyperelastic-plastic regime. Stepwise relaxation experiments after loading with $\dot{\lambda}_{x,max}$ were performed, to investigate the short-term relaxation behavior ($t_{\text{relax}} \approx 300$ s) at different stretch levels. In addition, separate specimens were loaded with $\dot{\lambda}_{x,min}$ to investigate the long-term relaxation behavior ($t_{\text{relax}} \approx 1200$ s) at different stretch levels. Exemplary results are provided for 120 °C for both loading procedures, in Figure 2.9.

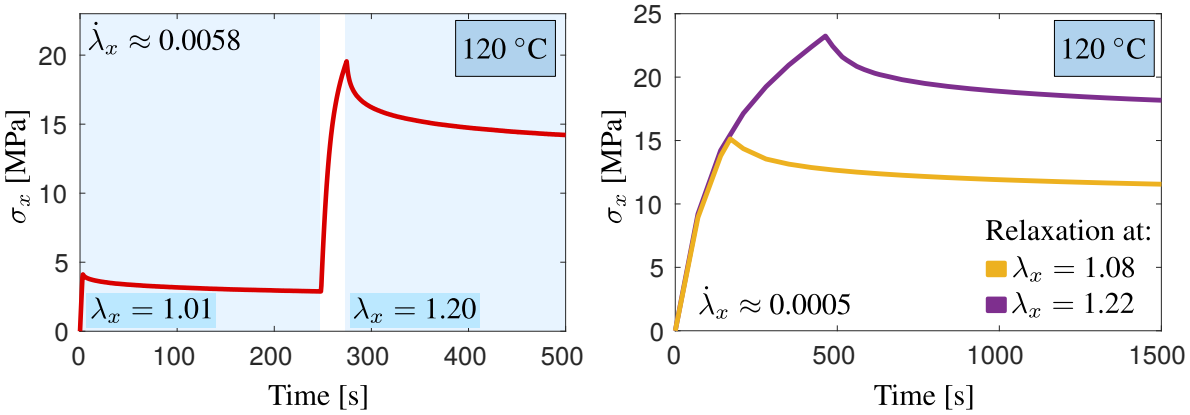

Figure 2.9: Exemplary results for stepwise (short-term) relaxation (left) and long-term relaxation (right) experiments at 120 °C and for $\chi = 0.23$.

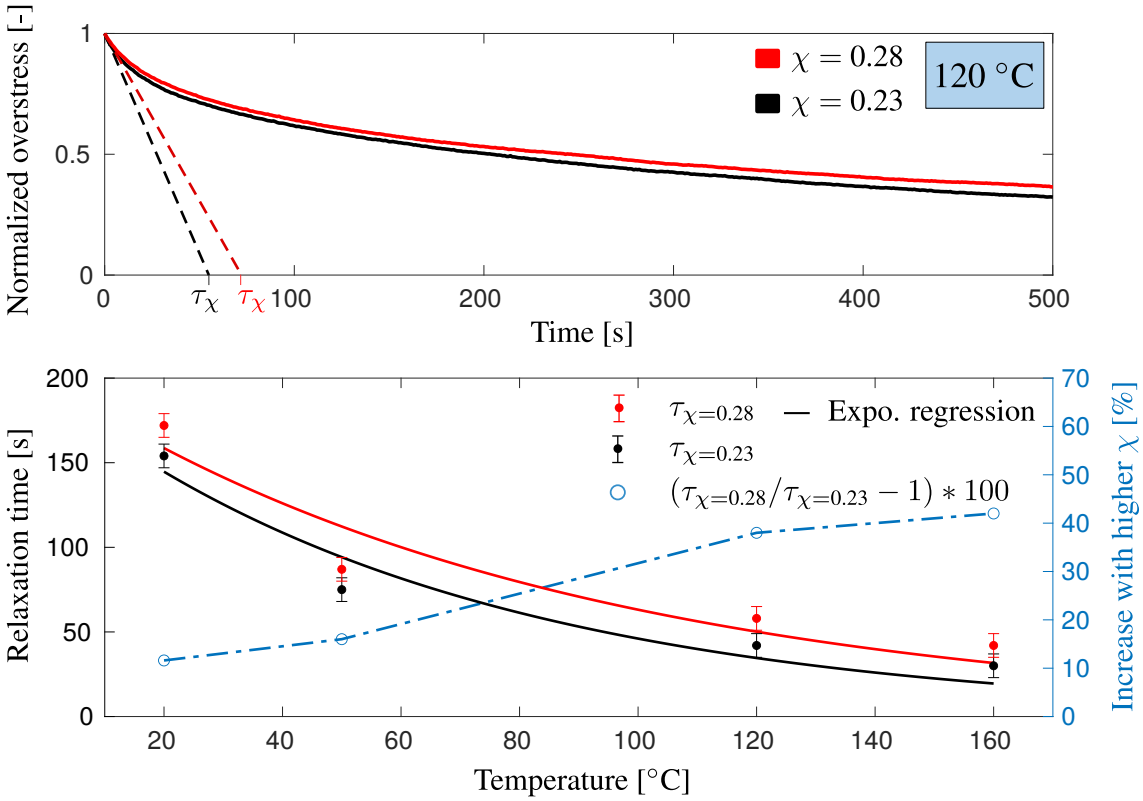

Figure 2.10: Top: Zoom-in on normalized overstress over time curve for a stretch level of $\lambda_x = 1.01$ at 120 °C, highlighting the identification procedure for the relaxation time τ at the beginning of the relaxation step.
Bottom: Relaxation time τ for the investigated temperatures and degrees of crystallinity. The increase for a higher degree of crystallinity is highlighted, in addition. The exponential trend line is of the form $\tau = \mathrm{C}_1 \exp(-\mathrm{C}_2\,\theta)$, where the parameters $C_1 = 192.6$, 199.7 and $C_2 = 0.0143$, 0.0152 were fitted for $\chi = 0.23$ and $\chi = 0.28$, respectively.

To obtain first insights regarding the effect of temperature and degree of crystallinity on the relaxation behavior, the long-term stress relaxation at the smallest stretch level (i.e. at a stretch level of $\lambda_x = 1.01$) was investigated in more detail. To this end, the normalized overstress $\sigma_{\text{over}}(t) = (\sigma(t) - \sigma_{\text{end}})/(\sigma_{\text{max}} - \sigma_{\text{end}})$, which is defined by the (maximum) stress level σ_{max} at the beginning of the relaxation step and the stress level at the termination point of the relaxation step σ_{end}, was plotted over time. From the intersection of the tangent of the normalized overstress curve at the beginning of the relaxation step and the horizontal axis, the initial relaxation time τ was estimated. This procedure is illustrated exemplary for a temperature of 120 °C, in the top of Figure 2.10. The values for τ for different temperatures and varying degrees of crystallinity are provided in the bottom of Figure 2.10.

With increasing temperature the ability to relax stresses increased significantly corresponding to a decrease of the relaxation time. With increasing degree of crystallinity, the relaxation time increased and the impact of the degree of crystallinity was more significant at higher temperatures, concomitant with the results for the Young's modulus and yield stress. Furthermore, with increasing stress and stretch level, the ability to relax stresses increased significantly. This influence became more evident, by applying a post-processing scheme to the experimental data, which was originally proposed by Amin et al. [2006]. The latter indicated a complex, nonlinear dependency of the relaxation time based on the aforementioned factors and will be discussed in detail in Section 2.6.

In summary, the experimental study revealed the following major findings regarding the effect of crystallinity and temperature on the material response of Polyamide 6:

- In general, coupled visco-elastic, visco-plastic material behavior at large strains was observed (cf. Figure 2.4).
- With increasing strain rates, an increase of the yield stress and hardening, accompanied with self-heating induced thermal-softening, occurred (cf. Figure 2.6 and Figure 2.8).
- An increase of the initial stiffness (cf. Figure 2.7), hardening, yield stress (cf. Figure 2.5), and relaxation time (cf. Figure 2.9) was observed, with increasing degree of crystallinity.
- With increasing temperature, the Young's modulus (cf. Figure 2.7), yield strength (cf. Figure 2.5) and relaxation time (cf. Figure 2.9) decreased nonlinearly, a more gradual roll-over to yielding was observed, and the amount of strain-hardening diminished. Furthermore, the effect of the degree of crystallinity on the mechanical response increased nonlinearly.

2.5 Material model formulation

The experimental findings imply that in general a finite strain, coupled visco-elastic, elasto-plastic theory, which incorporates nonlinear relaxation behavior and strain hardening, is required to accurately predict the mechanical behavior of semi-crystalline Polyamide 6. Thus, a suitable constitutive framework, which is able to capture the material response under isothermal conditions at various temperatures and different degrees of crystallinity, is derived in a thermodynamically consistent manner. To this end, a continuum-mechanical, phenomenological modeling approach is chosen. To provide a better understanding of the modeling strategy, a schematic illustration by means of an one dimensional rheological model is shown in Figure 2.11.

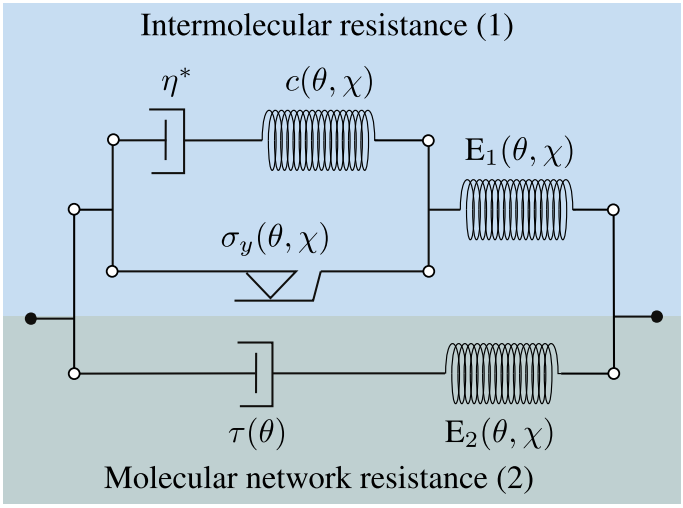

Figure 2.11: Schematic 1D representation of the constitutive model.

In line with the works of e.g. Boyce et al. [2000], Ahzi et al. [2003], Srivastava et al. [2010], and Ayoub et al. [2011], a parallel arrangement of an intermolecular resistance and a network resistance is chosen. In the following, properties associated with the intermolecular and network resistance will be denoted by index 1 and 2, respectively. The network resistance is captured by means of a Maxwell element with stiffness E_2 and a nonlinear function of the relaxation time τ, to account for the molecular orientation and relaxation. The intermolecular resistance is an elasto-plastic model with stiffness E_1 and yield stress σ_y. Several studies, e.g. Hasan and Boyce [1995] and Anand et al. [2009], revealed a significant Bauschinger-like effect for polymers upon unloading. Despite the lack of cyclic tension-compression data in the current work, nonlinear kinematic hardening of Armstrong-Frederick type is already incorporated in the model formulation, to capture this phenomenon accordingly. To this end,

the friction element of the plastic model is connected in parallel with an additional spring with stiffness c and a dashpot. The 'pseudo'-viscosity parameter η^* of the dashpot is given by $\eta^* = c/\dot{\gamma}b$, where b is a dimensionless parameter and $\dot{\gamma}$ the plastic multiplier. With this arrangement, the elastic, visco-hyperelastic, and visco-hyperelastic-plastic deformation regimes, observed in cyclic experiments (cf. chapter 2.4), can be captured accordingly.

In order to account for the dependence of the material properties on the temperature θ and the degree of crystallinity χ, the material parameters are functions of both quantities. Isothermal conditions ($\dot{\theta} = 0$) and no evolution of the crystalline phase ($\dot{\chi} = 0$) are considered. Consequently, the set of material parameters is determined beforehand from the prescribed degree of crystallinity and temperature and remains constant throughout the computational procedure. Based on the experimental results, the intermolecular resistance increases for a higher degree of crystallinity, resulting in an increase of stiffness, hardening, and yield stress. In contrast, the relaxation time τ is assumed to be independent of the degree of crystallinity. Noteworthy, due to the lack of experimental tensile test data in transversal direction, isotropic material behavior is assumed, despite the potential processing induced anisotropy, briefly addressed in Section 2.3.

2.5.1 Kinematics

For the 3D continuum mechanical extension of the presented rheological model to finite strains, the kinematic relations are introduced. The classical multiplicative decomposition of the total deformation gradient, $\boldsymbol{F} = \boldsymbol{F}_{e1}\boldsymbol{F}_p$, into an elastic $\boldsymbol{F}_{e1}$ and plastic part $\boldsymbol{F}_p$ is employed for the elasto-plastic model (cf. Eckart [1948], Kröner [1959], and Lee [1969]). In order to account for nonlinear kinematic hardening, the plastic deformation gradient, $\boldsymbol{F}_p = \boldsymbol{F}_{pe}\boldsymbol{F}_{pi}$, is multiplicatively decomposed in addition (cf. Dettmer and Reese [2004]), which is physically motivated by Lion [2000]. Resulting from these splits, the intermediate plastic configuration ic_{1a} and the so-called intermediate configuration of kinematic hardening ic_{1b} are introduced.

Analogously, the kinematic relations for the viscous model are based on a multiplicative split of the total deformation gradient, $\boldsymbol{F} = \boldsymbol{F}_{e2}\boldsymbol{F}_i$, into an elastic $\boldsymbol{F}_{e2}$ and an inelastic part $\boldsymbol{F}_i$. This decomposition results in the inelastic intermediate configuration ic_2 and is in line with the works of e.g. Sidoroff [1974], Lubliner [1985], and Reese and Govindjee [1998*b*].

2.5.2 Helmholtz free energy

The specific Helmholtz free energy ψ is depending on the elastic right Cauchy-Green deformation tensors $\boldsymbol{C}_{e1}$, $\boldsymbol{C}_{e2}$, and $\boldsymbol{C}_{pe}$

$$\boldsymbol{C}_{e1} = \boldsymbol{F}_{e1}^T \boldsymbol{F}_{e1} = \boldsymbol{F}_p^{-T} \boldsymbol{C} \boldsymbol{F}_p^{-1}, \;\; \boldsymbol{C}_{e2} = \boldsymbol{F}_{e2}^T \boldsymbol{F}_{e2} = \boldsymbol{F}_i^{-T} \boldsymbol{C} \boldsymbol{F}_i^{-1}, \;\; \boldsymbol{C}_{pe} = \boldsymbol{F}_{pe}^T \boldsymbol{F}_{pe} = \boldsymbol{F}_{pi}^{-T} \boldsymbol{C}_p \boldsymbol{F}_{pi}^{-1} \tag{2.2}$$

based on the principle of material frame invariance. Here, $\boldsymbol{C} = \boldsymbol{F}^T \boldsymbol{F}$ is the right Cauchy-Green tensor and $\boldsymbol{C}_p = \boldsymbol{F}_p^T \boldsymbol{F}_p$ represents the plastic right Cauchy-Green tensor. Concomitant with the proposed modeling strategy, the total specific Helmholtz free energy

$$\begin{aligned} \psi &= \psi_1(\boldsymbol{C}_{e1}, \boldsymbol{C}_{pe}, \kappa, \chi, \theta) + \psi_2(\boldsymbol{C}_{e2}, \chi, \theta) \\ \psi_1 &= \psi_{e1}(\boldsymbol{C}_{e1}, \chi, \theta) + \psi_{kin}(\boldsymbol{C}_{pe}, \chi, \theta) + \psi_{iso}(\kappa, \chi, \theta) \end{aligned} \tag{2.3}$$

is additively decomposed. The contributions of the intermolecular and network resistance are denoted by ψ_1 and ψ_2, respectively. In the above expression the energy associated with the elasto-plastic model is the sum of the following contributions: an energy related to intermolecular reactions ψ_{e1}, a defect-energy associated with plastic deformations ψ_{kin}, which allows to phenomenological account for the Bauschinger-like phenomena, and the stored energy due to isotropic hardening ψ_{iso}, which is depending on the accumulated plastic strain κ. Noteworthy, it is assumed that ψ_{e1}, ψ_{e2}, and ψ_{kin} are isotropic functions of $\boldsymbol{C}_{e1}$, $\boldsymbol{C}_{e2}$, and $\boldsymbol{C}_{pe}$, respectively.

2.5.3 Derivation based on the Clausius-Duhem inequality

The constitutive equations are derived in a thermodynamically consistent manner from the second law of thermodynamics

$$\boldsymbol{S} : \frac{1}{2} \dot{\boldsymbol{C}} - \rho_0 \dot{\psi} \geq 0 \tag{2.4}$$

which is expressed by means of the Clausius-Duhem inequality for isothermal processes, with respect to the reference configuration. Here, the second Piola-Kirchhoff stress tensor $\boldsymbol{S}$ and the density in the reference configuration ρ_0 are introduced. This expression needs to be fulfilled for arbitrary processes. The inequality (2.4) is reformulated by inserting the total time derivative of the specific Helmholtz free energy (2.3). After several mathematical operations this results in

$$(\boldsymbol{S} - \boldsymbol{S}_1 - \boldsymbol{S}_2) : \frac{1}{2} \dot{\boldsymbol{C}} + \boldsymbol{M}_2 : \boldsymbol{D}_i + \left(\boldsymbol{M}_1 - \bar{\boldsymbol{X}}\right) : \boldsymbol{D}_p + \boldsymbol{M}_{kin} : \boldsymbol{D}_{pi} + R\,\dot{\kappa} \geq 0 \tag{2.5}$$

wherein $\boldsymbol{D}_{(*)} = \mathrm{sym}\,(\boldsymbol{L}_{(*)})$ refers to the symmetric part of the velocity gradient $\boldsymbol{L}_{(*)} = \dot{\boldsymbol{F}}_{(*)}\boldsymbol{F}_{(*)}^{-1}$, with $(*) = i, p, pi$. In the inequality (2.5), the following stress quantities were introduced: The second Piola-Kirchhoff stress tensors

$$\boldsymbol{S}_1 = 2\,\rho_0\,\boldsymbol{F}_p^{-1}\frac{\partial\psi_{e1}}{\partial\boldsymbol{C}_{e1}}\boldsymbol{F}_p^{-T}, \quad \boldsymbol{S}_2 = 2\,\rho_0\,\boldsymbol{F}_i^{-1}\frac{\partial\psi_2}{\partial\boldsymbol{C}_{e2}}\boldsymbol{F}_i^{-T} \tag{2.6}$$

corresponding to the intermolecular and molecular network resistance, respectively. Furthermore, the symmetric stress tensors of Mandel-type

$$\boldsymbol{M}_1 = 2\,\rho_0\,\boldsymbol{C}_{e1}\frac{\partial\psi_{e1}}{\partial\boldsymbol{C}_{e1}}, \quad \boldsymbol{M}_{kin} = 2\,\rho_0\,\boldsymbol{C}_{pe}\frac{\partial\psi_{kin}}{\partial\boldsymbol{C}_{pe}}, \quad \boldsymbol{M}_2 = 2\,\rho_0\,\boldsymbol{C}_{e2}\frac{\partial\psi_2}{\partial\boldsymbol{C}_{e2}} \tag{2.7}$$

as well as the back stress tensor $\bar{\boldsymbol{X}}$ and the stress-like driving force of isotropic hardening R

$$\bar{\boldsymbol{X}} = 2\,\rho_0\,\boldsymbol{F}_{pe}\frac{\partial\psi_{kin}}{\partial\boldsymbol{C}_{pe}}\boldsymbol{F}_{pe}^T, \quad R = -\rho_0\,\frac{\partial\psi_{iso}}{\partial\kappa} \tag{2.8}$$

are defined.

Following the standard arguments of Coleman and Noll [1961], the total second Piola-Kirchhoff stress tensor is defined by

$$\boldsymbol{S} = \boldsymbol{S}_1 + \boldsymbol{S}_2 \tag{2.9}$$

Based on the remaining inequality, a set of evolution equations, which ensures the non-negativeness of the internal dissipation caused by plastic and viscous effects, is derived.

Due to the lack of experimental data, no pressure dependence, nor tension-compression asymmetry of the onset of yielding is considered, in the current framework. Consequently, a yield function of von Mises type

$$\Phi = ||\mathrm{dev}(\boldsymbol{M}_1) - \mathrm{dev}(\bar{\boldsymbol{X}})|| - \sqrt{\frac{2}{3}}\,(\sigma_y - R) \tag{2.10}$$

is assumed. Here, the deviatoric part of a quantity is denoted by $\mathrm{dev}(*)$ and $||*||$ is the Frobenius norm. As alluded in Section 2.4, the initial yield stress $\sigma_y(\theta, \chi)$ is depending on the total degree of crystallinity and temperature. A function for the latter quantity is discussed in Section 2.6. The associative plastic flow rule and the evolution equations for kinematic and

isotropic hardening read

$$\boldsymbol{D}_p = \dot{\gamma}\,\frac{\partial \Phi}{\partial \boldsymbol{M}_1} = \dot{\gamma}\,\frac{\mathrm{dev}(\boldsymbol{M}_1) - \mathrm{dev}(\bar{\boldsymbol{X}})}{||\mathrm{dev}(\boldsymbol{M}_1) - \mathrm{dev}(\bar{\boldsymbol{X}})||} \tag{2.11}$$

$$\boldsymbol{D}_{pi} = \dot{\gamma}\,\frac{b}{c}\,\mathrm{dev}(\boldsymbol{M}_{kin}) \tag{2.12}$$

$$\dot{\kappa} = \dot{\gamma}\,\frac{\partial \Phi}{\partial R} = \sqrt{\frac{2}{3}}\,\dot{\gamma} \tag{2.13}$$

in line with the proposed theories of Dettmer and Reese [2004] and Vladimirov et al. [2008]. In the latter expression the constants $b(\theta, \chi)$ and $c(\theta, \chi)$ are related to kinematic hardening (cf. Armstrong and Frederick [1966]) and the plastic multiplier $\dot{\gamma}$ is determined from the Kuhn-Tucker conditions $\Phi \leq 0$, $\dot{\gamma} \geq 0$, and $\Phi\,\dot{\gamma} = 0$.

In accordance with the work of Reese and Govindjee [1998*b*], the evolution of the inelastic deformation within the molecular network reads

$$\boldsymbol{D}_i = \frac{1}{2\,\tau\,\mu_2}\left(\boldsymbol{M}_2 - \frac{1}{3}\,\mathrm{tr}\,(\boldsymbol{M}_2)\,\boldsymbol{I}\right) + \frac{1}{9\,\tau\,K_2}\,\mathrm{tr}\,(\boldsymbol{M}_2)\,\boldsymbol{I} \tag{2.14}$$

The bulk modulus and shear modulus, corresponding to the molecular network resistance, are denoted by $K_2(\theta, \chi)$ and $\mu_2(\theta, \chi)$, respectively. Furthermore, the relaxation time $\tau(\boldsymbol{S}_2, \boldsymbol{C}, \theta)$ is introduced, which must be larger than zero. Based on the relaxation data discussed in Section 2.4, τ is assumed to be a function of the overstress $\boldsymbol{S}_2$, the deformation, and the temperature. The explicit function is proposed in Section 2.6.

This set of evolution equations fulfills the remaining inequality (2.5). For the elasto-plastic model this was already shown by Vladimirov et al. [2008], and will not be further discussed here. The thermodynamic consistency of the evolution equation of the inelastic deformation is discussed in the work of Reese and Govindjee [1998*b*].

2.5.4 Model representation in the reference configuration

The derivation of the constitutive equations was performed with respect to the intermediate configurations, for convenience. However, the numerical implementation of the constitutive equations is carried out with respect to the reference configuration. Consequently, tensorial pull back operation of the associated stress quantities $\boldsymbol{M}_1$, $\boldsymbol{M}_2$, $\bar{\boldsymbol{X}}$, and $\boldsymbol{M}_{kin}$ are applied to obtain the alternative model representation, provided in Table 2.1. To this end, the back stress tensor in the reference configuration $\tilde{\boldsymbol{X}}$ and the asymmetric stress like quantities $\boldsymbol{Y}$ and $\boldsymbol{Y}_{kin}$ are introduced. It should be emphasized that all tensor valued internal variables, i.e. $\boldsymbol{C}_p, \boldsymbol{C}_{pi}$

and $\boldsymbol{C}_i$, are symmetric, which reduces the computational costs. In addition, the plastic and inelastic spins remain undetermined.

Intermolecular resistance	Molecular network resistance
Stresses $\boldsymbol{S}_1 = 2\,\rho_0\,\boldsymbol{F}_p^{-1}\dfrac{\partial\psi_{e1}}{\partial\boldsymbol{C}_{e1}}\boldsymbol{F}_p^{-T},$ $\tilde{\boldsymbol{X}} = 2\,\rho_0\,\boldsymbol{F}_{pi}^{-1}\dfrac{\partial\psi_{kin}}{\partial\boldsymbol{C}_{pe}}\boldsymbol{F}_{pi}^{-T},$ $\boldsymbol{Y} = \boldsymbol{C}\,\boldsymbol{S}_1 - \boldsymbol{C}_p\tilde{\boldsymbol{X}}, \quad \boldsymbol{Y}_{kin} = \boldsymbol{C}_p\tilde{\boldsymbol{X}}$ $R = -\rho_0\,\dfrac{\partial\psi_{iso}}{\partial\kappa}$	**Stress** $\boldsymbol{S}_2 = 2\,\rho_0\,\boldsymbol{F}_i^{-1}\dfrac{\partial\psi_2}{\partial\boldsymbol{C}_{e2}}\boldsymbol{F}_i^{-T}$
Evolution equations $\dot{\boldsymbol{C}}_p = 2\,\dot\gamma\,\dfrac{\mathrm{dev}(\boldsymbol{Y})\boldsymbol{C}_p}{\sqrt{\mathrm{dev}(\boldsymbol{Y}) : \mathrm{dev}(\boldsymbol{Y})^T}},$ $\dot{\boldsymbol{C}}_{pi} = 2\,\dot\gamma\,\dfrac{b}{c}\,\mathrm{dev}\,(\boldsymbol{Y}_{kin})\,\boldsymbol{C}_{pi}, \quad \dot\kappa = \sqrt{\dfrac{2}{3}}\,\dot\gamma$	**Evolution equation** $\dot{\boldsymbol{C}}_i = \left(\dfrac{1}{\tau\,\mu_2}\,\mathrm{dev}\,(\boldsymbol{C}\boldsymbol{S}_2) + \dfrac{2}{9\,\tau\,K_2}\,\mathrm{tr}\,(\boldsymbol{C}\boldsymbol{S}_2)\boldsymbol{I}\right)\boldsymbol{C}_i$
Yield function $\Phi = \sqrt{\mathrm{dev}(\boldsymbol{Y}) : \mathrm{dev}(\boldsymbol{Y})^T} - \sqrt{\dfrac{2}{3}}\,(\sigma_y - R)$	
Kuhn-Tucker conditions $\Phi \le 0$, $\dot\gamma \ge 0$, and $\Phi\,\dot\gamma = 0$	
Second Piola-Kirchhoff stress $\boldsymbol{S} = \boldsymbol{S}_1 + \boldsymbol{S}_2$	

Table 2.1: Constitutive equations with respect to the reference configuration.

2.5.5 Specific choices for energy terms

The relations for the thermodynamic driving forces are derived in a completely general manner, up to now. In this way, the proposed framework offers great flexibility regarding the particular choices of the volumetric energy terms Ψ, which are introduced in this section.

The energy contributions associated with the intermolecular resistance belong to a Neo-Hookean material with combined linear and nonlinear isotropic hardening of Voce type (Voce

[1955]) and nonlinear kinematic hardening of Armstrong-Frederick type:

$$\Psi_{e1} = \frac{\mu_1}{2}\left(\text{tr}\left(\boldsymbol{C}_{e1}\right) - 3\right) - \mu_1 \ln(J_{e1}) + \frac{\Lambda_1}{4}\left(J_{e1}^2 - 1 - 2\,\ln(J_{e1})\right) \tag{2.15}$$

$$\Psi_{kin} = \frac{c}{2}\left(\text{tr}\left(\boldsymbol{C}_{pe}\right) - 3\right) - c\,\ln(J_{pe}) \tag{2.16}$$

$$\Psi_{iso} = (\sigma_\infty - \sigma_y)\left(\kappa + \frac{\exp\left(-\beta\,\kappa\right)}{\beta}\right) + \frac{1}{2}\,H\,\kappa^2 \tag{2.17}$$

Here, $J_{e1} = \det\left(\boldsymbol{F}_{e1}\right) = \sqrt{\det\left(\boldsymbol{C}_{e1}\right)}$ and $J_{pe} = \det\left(\boldsymbol{F}_{pe}\right) = \sqrt{\det\left(\boldsymbol{C}_{pe}\right)}$ holds. In the expression above, $\mu_1(\theta,\chi)$, $\Lambda_1(\theta,\chi)$, $\sigma_\infty(\theta,\chi)$, $\beta(\theta,\chi)$, and $H(\theta,\chi)$ represent the Lamé constants and isotropic hardening parameters, respectively. Based on the chosen energy contributions, $\boldsymbol{S}_1$, $\tilde{\boldsymbol{X}}$, and R are derived from the relations provided in Table 2.1

$$\boldsymbol{S}_1 = \mu_1\left(\boldsymbol{C}_p^{-1} - \boldsymbol{C}^{-1}\right) + \frac{\Lambda_1}{2}\left(\det\left(\boldsymbol{C}\right) - 1\right)\boldsymbol{C}^{-1} \tag{2.18}$$

$$\tilde{\boldsymbol{X}} = c\left(\boldsymbol{C}_{pi}^{-1} - \boldsymbol{C}_p^{-1}\right) \tag{2.19}$$

$$R = -(\sigma_\infty - \sigma_y)\left(1 - \exp(-\beta\kappa)\right) - H\,\kappa \tag{2.20}$$

Noteworthy, the model's plastic incompressibility (i.e. $\det(\boldsymbol{C}_p) = 1$) has been taken into account in Equation 2.18. The elastic energy contribution of the molecular network resistances is of Neo-Hookean type

$$\Psi_2 = \frac{\mu_2}{2}\left(\text{tr}\left(\boldsymbol{C}_{e2}\right) - 3\right) - \mu_2 \ln(J_{e2}) + \frac{\Lambda_2}{4}\left(J_{e2}^2 - 1 - 2\ln(J_{e2})\right) \tag{2.21}$$

Here, $\mu_2(\theta)$ and $\Lambda_2(\theta)$ are the Lamé constants corresponding to the molecular network resistance and $J_{e2} = \det\left(\boldsymbol{F}_{e2}\right) = \sqrt{\det\left(\boldsymbol{C}_{e2}\right)}$ holds. Based on this choice of the energy, $\boldsymbol{S}_2$ is defined by

$$\boldsymbol{S}_2 = \mu_2\left(\boldsymbol{C}_i^{-1} - \boldsymbol{C}^{-1}\right) + \frac{\Lambda_2}{2}\left(\frac{\det\left(\boldsymbol{C}\right)}{\det\left(\boldsymbol{C}_i\right)} - 1\right)\boldsymbol{C}^{-1} \tag{2.22}$$

The material model is implemented as an user material subroutine *UMAT* into the commercial FEM software *ABAQUS*/Standard. For details regarding the numerical implementation, the reader is referred to the Appendix 2.9.

2.6 Characterization of model parameters

In the following section, the material parameter identification scheme, which is based on the experimental data presented in Section 2.4, is discussed. Nonlinear optimization strategies are

often accompanied by the uncertainty, whether the obtained solution corresponds to a local or global minimum. In order to reduce this uncertainty, a staggered characterization method is proposed. The latter was successively applied to obtain a set of material parameters for each considered temperature.

2.6.1 Elastic constants

In the first identification step, the elastic parameters were identified based on the instantaneous, elastic response of the material during monotonic loading. Since a parallel arrangement of the intermolecular and molecular network resistances was chosen, the corresponding Poisson's ratio of both contributions were assumed to be equal, i.e. $\nu_1 = \nu_2$ holds. With the DIC data at hand, the Poisson's ratio of the uniformly deformed section 2 (cf. Figure 2.3) was calculated from the negative ratio of the average transversal and longitudinal strain $\nu = -\ln(\lambda_y)/\ln(\lambda_x)$. Noteworthy, the standard deviation for the computed strain fields was found to be the highest in the elastic regime. In the small deformation regime, vibrations and noise have a more significant impact on the strain accuracy and precision, and the results for the Poisson's ratio showed a significant variation (cf. Sutton et al. [2009]). From the experimental data no clear trend of the Poisson's ratio for different degrees of crystallinity and temperatures was evident, and consequently a constant value was assumed. It should be emphasized that the predicted lateral contraction was in good agreement with the experimental data for all considered cases (cf. Section 2.7).

The experimentally determined Young's modulus $E^{\mathrm{Exp}}(\chi)$ was obtained from the initial slope of the stress-stretch relation for different degrees of crystallinity. For simplicity, only the stiffness of the intermolecular resistance was assumed to depend linearly on χ, i.e.

$$E^{\mathrm{Exp}}(\theta, \chi) = E_1(\chi, \theta) + E_2(\theta) \tag{2.23}$$

holds. From the experimentally identified $E^{\mathrm{Exp}}(\chi)$, $E_{1,0}$ and E_2 were obtained analytically in a straight forward manner from equation (2.23).

2.6.2 Nonlinear relaxation function

With the governed elastic constants, the function of the relaxation time τ was determined from the stepwise (short-) relaxation test data (cf. Section 2.4). The long-term relaxation test data was used for model validation only (see Section 2.7). Based on the experimental results, the relaxation time was assumed to be a function of the current overstress $\boldsymbol{\sigma}_2$, the deforma-

tion, and the temperature. To identify the constitutive relation for the relaxation time from the experimental relaxation test data, a modified version of the post processing scheme, proposed by Amin et al. [2006], was applied. In the developed strategy by Amin et al. [2006], one-dimensional stress and strain data was utilized, based on the assumption of material incompressibility, to identify the function for the viscosity parameter, which was subsequently generalized for the three-dimensional case. In contrast, in the current work, the recorded three-dimensional deformation data, in terms of the deformation gradient $\boldsymbol{F}$ and the true stress tensor $\boldsymbol{\sigma}$, served as the input data to obtain the evolution of the relaxation time. During the relaxation steps within the experiments, a constant displacement was prescribed ($\boldsymbol{F} = \text{const.}$) and the stress relaxation was recorded over time, see Figure 2.12.

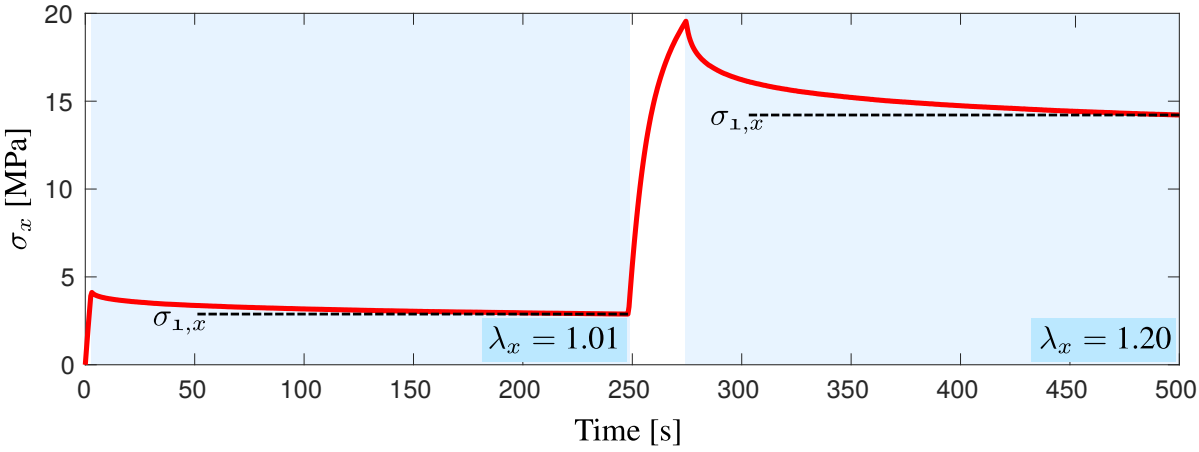

Figure 2.12: Stress relaxation at $\lambda_x = 1.01$ and $\lambda_x = 1.20$ at 120 °C for $\chi = 0.23$ and corresponding equilibrium stress $\sigma_{1,x}$.

At the termination point of the relaxation steps, stress equilibrium was assumed. Based on the proposed constitutive model, the remaining recorded stress corresponded to the constant contribution of the intermolecular resistance, as depicted in Figure 2.12. As a result, the stress relaxation within the molecular network resistance was governed by $\boldsymbol{\sigma}_2(t) = \boldsymbol{\sigma}(t) - \boldsymbol{\sigma}_1$. In the case of uniaxial tension, the applied loading direction coincided with the direction of principal stretch λ_x. Consequently, the coordinate system introduced in Figure 2.3 corresponded to the eigensystem of $\boldsymbol{F}$, $\boldsymbol{\sigma}$, and $\boldsymbol{\sigma}_2$. The corresponding coefficient matrices read:

$$\mathbf{F}_{ij} = \begin{pmatrix} \lambda_x & 0 & 0 \\ 0 & \lambda_y & 0 \\ 0 & 0 & \lambda_z \end{pmatrix}, \quad (\boldsymbol{\sigma}_2(t))_{ij} = \begin{pmatrix} \sigma_x(t) - \sigma_{1,x} & 0 & 0 \\ 0 & 0 & 0 \\ 0 & 0 & 0 \end{pmatrix} \tag{2.24}$$

With this input data at hand, the evolution of the second Piola-Kirchhoff stress tensor

$\boldsymbol{S}_2(t) = J\,\boldsymbol{F}^{-1}\boldsymbol{\sigma}_2(t)\boldsymbol{F}^{-t}$ was governed. Next, equation (2.22) was solved for the inelastic right Cauchy-Green tensor $\boldsymbol{C}_i$, for each experimental time step. Subsequently, the exponential map algorithm was applied for the numerical time integration of the evolution equation of the inelastic deformation (cf. Table 2.1).

$$\boldsymbol{C}_i = \exp\left(\Delta t\left(\frac{1}{\tau\,\mu_2}\mathrm{dev}\left(\boldsymbol{C}\boldsymbol{S}_2\right) + \frac{2}{9\,\tau\,K_2}\mathrm{tr}\left(\boldsymbol{C}\boldsymbol{S}_2\right)\boldsymbol{I}\right)\right)\boldsymbol{C}_{i,n} \tag{2.25}$$

Noteworthy, in this special case, all tensor valued quantities in equation (2.25) commute and the coefficient matrices with respect to the same set of eigenvectors were determined from the preceding evaluation of the experimental data for each time step. Consequently, equation (2.25) can be rewritten in terms of a system of three scalar-valued equations. Finally, the evolution of the relaxation time $\tau(t)$ was determined by solving the first scalar-valued equation for τ for each experimental time step.

In Figure 2.13, the results of this post processing procedure are depicted for some selected relaxation tests at different relaxation stretch levels and temperatures. As already reported by Amin et al. [2006], this treatment of the experimental data produced some scattering due to noise, especially at time steps close to the equilibrium state (i.e. for small overstress values). Despite this scatter, a linear trend for the relaxation time and overstress was evident at low stretches $\lambda_x \approx 1.01$. In contrast, at higher stretch levels, a non-linear relation emerged for all considered temperatures. Furthermore, a significant decrease of the relaxation time with increasing temperature was observed, due to the higher chain mobility within the amorphous regime, in particular above the glass transition temperature. These findings suggested the necessity of introducing a nonlinear dependence of the relaxation time on the relaxation stretch level, the overstress, and the temperature.

Therefore, a slightly modified relation for the relaxation time

$$\tau = \tau_0\,||\boldsymbol{C}||_s^{\varphi}\exp\left(||\boldsymbol{\sigma}_2||_s\right)^{-\delta} \tag{2.26}$$

compared to the proposed power-law type constitutive equation for the viscosity, originally proposed by Amin et al. [2006], was considered. Here, $||*||_s$ is the second norm of a tensor (i.e. $||*||_s = \sqrt{\omega_{\max}}$ holds, where $\omega_{\max}$ is the maximum eigenvalue of $(*)^T(*)$). In expression (2.26), the temperature dependent material parameters $\tau_0(\theta)$, $\varphi(\theta)$, and $\delta(\theta)$ were introduced. The latter were identified successively for each temperature, by simultaneously minimizing the least-square residuals (defined as the difference between the observed experimental data and fitted model response) for different stretch levels. To this end, the Trust-region algorithm, provided as an intrinsic functions in the commercial software *MATLAB*, was employed.

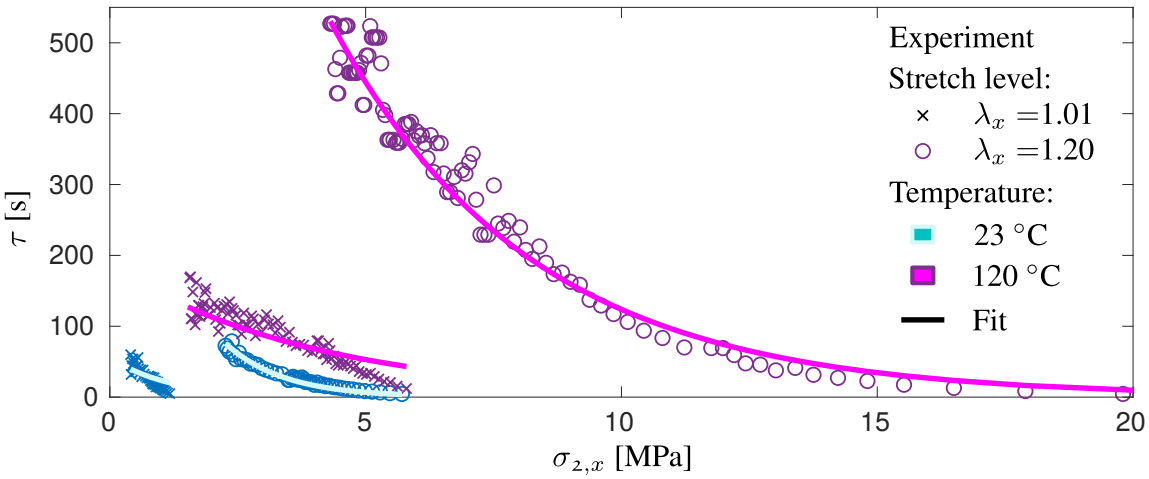

Figure 2.13: Relaxation time-overstress relation for different stretch levels and temperatures: Post processed experimental data and corresponding fit.

The parameter $\tau_0(\theta)$ corresponds to the relaxation time at low stretch $||\boldsymbol{C}||_s \approx 1.0$ and overstress levels $||\boldsymbol{\sigma}_2||_s \approx 0$. Consequently, good initial guesses were obtained for $\tau_0(\theta)$, from the presented data in Figure 2.10 and the identified values for $\tau_0(\theta)$ were very close to this experimental data. This was in contrast to the remaining parameters $\varphi(\theta)$ and $\delta(\theta)$, which do not allow for a physical interpretation. In order to minimize the uncertainty whether the obtained solution of the optimization procedure corresponded to a global or local minimum, different initial values were chosen successively for $\varphi(\theta)$ and $\delta(\theta)$. The corresponding fit for two selected temperatures is provided in Figure 2.13. The proposed function (2.26) led to accurate fits for the nonlinear evolution at higher stretch levels. Only in the small strain regime ($\lambda_x \approx 1.01$), a comparatively weaker fit was achieved due to the linear trend in the experimental data. To improve this fit, a more complex relation with additional parameters could be introduced. However, it should be emphasized that the visco-elastic behavior and stress relaxation was generally well captured (cg. Section 2.7) with the proposed function (2.26) and the identified set of parameters.

2.6.3 Plastic parameters

In the final characterization step, the parameters related to the plastic deformation behavior were identified. The initial yield stress was determined from the cyclic loading-unloading-recovery test data and a linear dependency on the degree of crystallinity was presumed $\sigma_y = \chi\, \sigma_{y,0}(\theta)$. Due to the lack of tension-compression data, the kinematic hardening response of the model was neglected throughout the following computational examples. Thus,

only the isotropic hardening parameters (i.e. $\beta(\theta,\chi)$, $\sigma_\infty(\theta,\chi)$, $H(\theta,\chi)$) were identified. To this end, based on the monotonic tensile test data for different degrees of crystallinity, a non-linear multiple curve fitting procedure, employing the Trust-region algorithm in *MATLAB*, was performed.

2.6.4 Fitting results

Based on this staggered identification scheme, a set of material parameters was identified successively for each temperature (see Table 2.2). It should be emphasized that no lower or upper bounds were prescribed during the curve fitting procedures for the relaxation time or hardening parameters. Nevertheless, most of the identified parameters followed a clear trend (e.g. decreasing τ_0, φ etc., for decreasing temperatures). However, as discussed in Section 2.4, at 120 °C a less pronounced rate dependency, compared to 50 °C and 160 °C, and a more gradual roll-over to linear hardening at higher degrees of crystallinity was observed. Concomitant with these experimental results, the corresponding identified parameters σ_∞, α, and δ exhibited a jump at this temperature cf. (Table 2.2).

Function	Parameter at:	23 °C	50 °C	120 °C	160 °C
$E_1 = \chi\, E_{1,0}(\theta)$	$E_{1,0}$ [MPa]	7610	4398	1051	901
$E_2 = E_2(\theta)$	E_2 [MPa]	1210	703	201	103
$\nu_1 = \nu_2$	ν_1 [-]	0.35	0.35	0.35	0.35
$\sigma_y = \chi\, \sigma_{y,0}(\theta)$	$\sigma_{y,0}$ [MPa]	71	49	30	14
$\beta = \chi\, \beta_0(\theta)$	β_0 [-]	2317	1614	227	240
$H = \chi\, H_0(\theta)$	H_0 [MPa]	333	819	214	150
$\sigma_\infty = \chi^{\alpha(\theta)}\, \sigma_{\infty,0}(\theta)$	$\sigma_{\infty,0}$ [MPa]	68	57	1252	234
	α [-]	0.188	0.575	3.061	2.088
$\tau = \tau_0\, \|\|\boldsymbol{C}\|\|_s^{\varphi} \exp\left(\|\|\boldsymbol{\sigma}_2\|\|_s\right)^{-\delta}$	τ_0 [s]	156	71	48	31
	φ [-]	4.80	2.50	2.38	2.24
	δ [-]	0.211	0.221	0.714	0.517

Table 2.2: Set of mechanical parameters at different temperatures.

As alluded in Section 2.4, material self-heating ($\dot{\theta} \gg 0$) at higher loading rates lead to non-isothermal conditions when stretch levels of $\lambda_x \approx 1.05$ were exceeded. Consequently, the proposed isothermal model was only fitted up to this stretch level for $\dot{\lambda}_{x,max}$. Naturally, the stress prediction of the constitutive model at higher rates lead to an over-prediction of the experimental records, exceeding $\lambda_x \approx 1.05$. It is important to emphasize that with this approach a set of

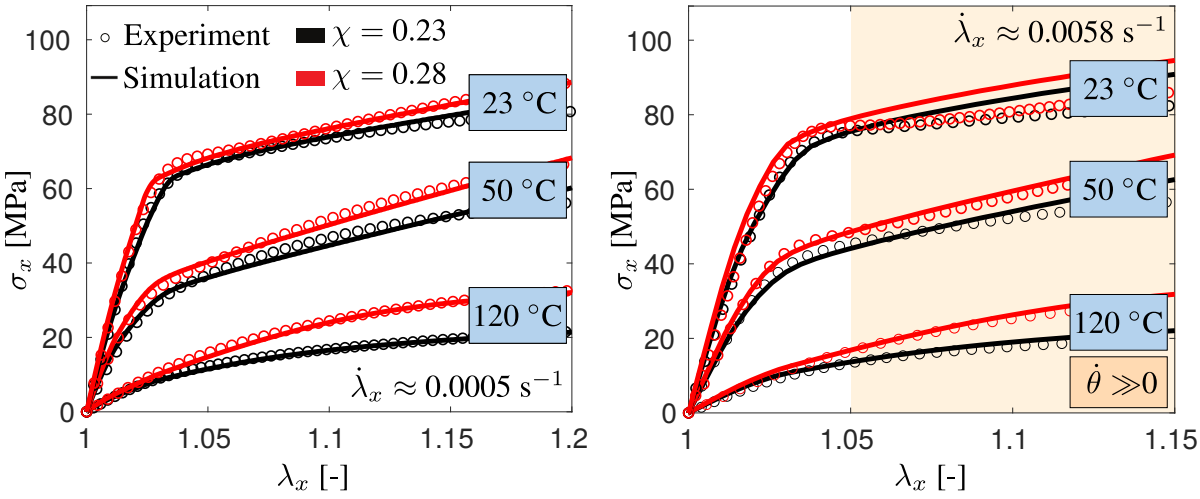

Figure 2.14: Monotonic, uniaxial extension - Experimental data and corresponding model response.

isothermal parameters was determined in a successive manner for each considered temperature (see Table 2.2), which serves as a fundamental input for an upcoming thermo-mechanically coupled model formulation. The corresponding model response for some monotonic tensile tests at different loading rates and for varying temperatures and degrees of crystallinity is depicted in Figure 2.14.

2.7 Model validation

In order to validate the proposed constitutive framework and the identified set of parameters, experimental data, which was not used for the model calibration (cf. Section 2.6), was compared to the corresponding model response.

2.7.1 Single element tests

In a first validation step, the model response for cyclic loading conditions was investigated for different temperatures and degrees of crystallinity. During these uniaxial tensile experiments, homogeneous stretch and stress fields arose in the considered sections (cf. Section 2.3). Consequently, a single element test was considered. To this end, the stress in longitudinal x-direction, obtained from the experimental data as a function of time, was prescribed as a traction boundary condition. Lateral contraction was unhindered and the predicted stretches in longitudinal (λ_x) and transversal (λ_y) direction were compared with the experimental data for all temperatures (see Figure 2.15).

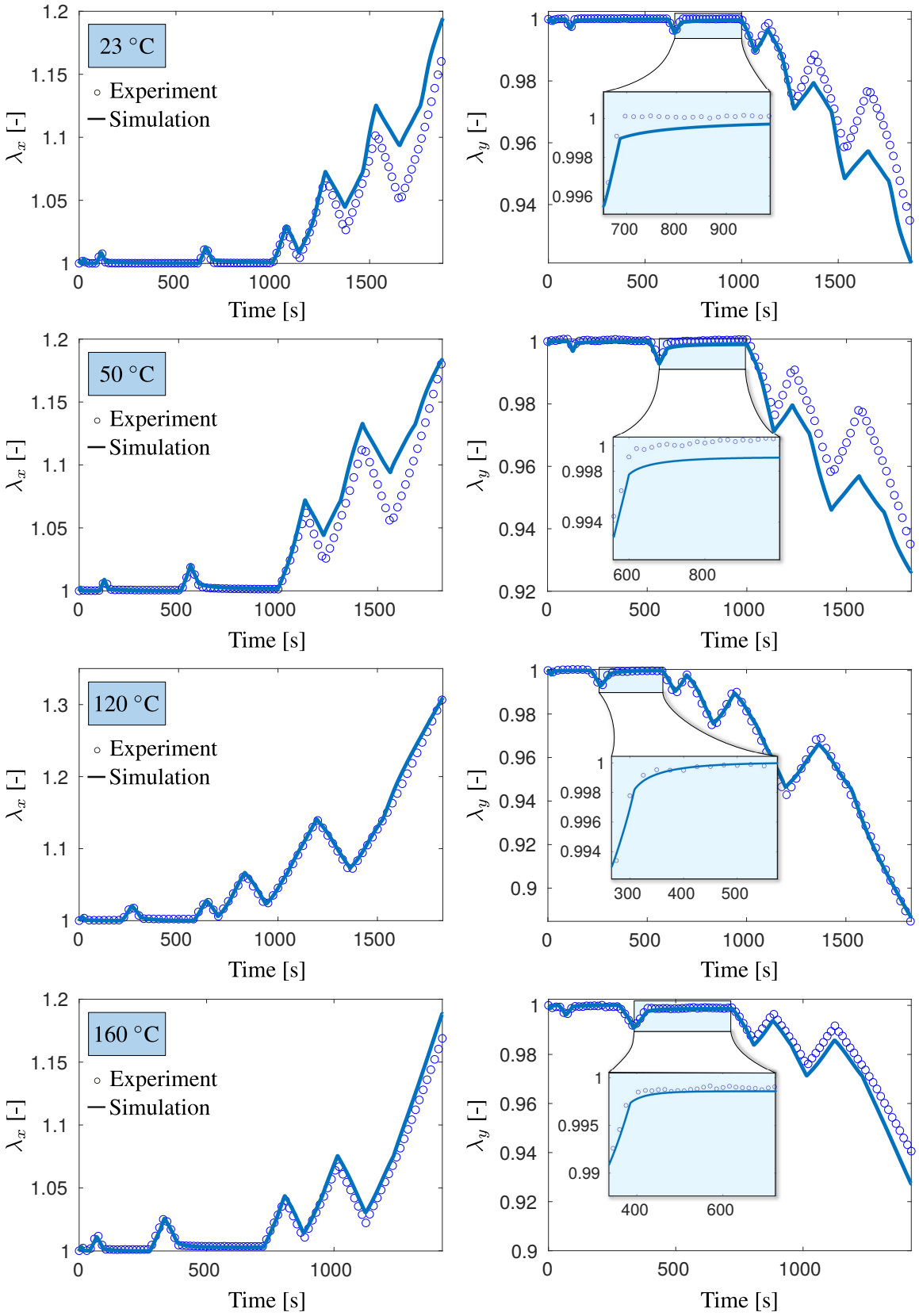

Figure 2.15: Cyclic loading at various temperatures for $\dot{\lambda}_{x,min} \approx 0.0005\ \mathrm{s}^{-1}$ and $\chi = 0.23$. Experimental data for the stretch in longitudinal λ_x and transversal direction λ_y and corresponding model predictions.

The complex deformation response of Polyamide 6 under cyclic loading conditions (e.g. plastic flow, strain recovery and hysteresis loop, cf. Section 2.4) could be captured by the proposed model for all considered temperatures. The model predictions were less accurate for temperatures below the glass transition point (i.e. at 23 °C and 50 °C). Especially at stretch levels in longitudinal direction exceeding 1.10, a significant mismatch between the predicted λ_x upon unloading and the experimental data arose. From the close-ups on the recovery steps, provided in Figure 2.15, it was evident that the predicted stretch values after unloading converged too slowly towards an overestimated equilibrium stretch at 23 °C and 50 °C. Consequently, the estimated relaxation time at small stretch levels seemed to be too high, while the yield strength was underestimated. This was in strong contrast to the results at 120 °C and 160 °C, where the model predictions were in very good agreement with the experimental data up to stretch levels of $\lambda_x = 1.30$. In addition, the transversal deformation was captured well, emphasizing the model capabilities to predict the three dimensional material response.

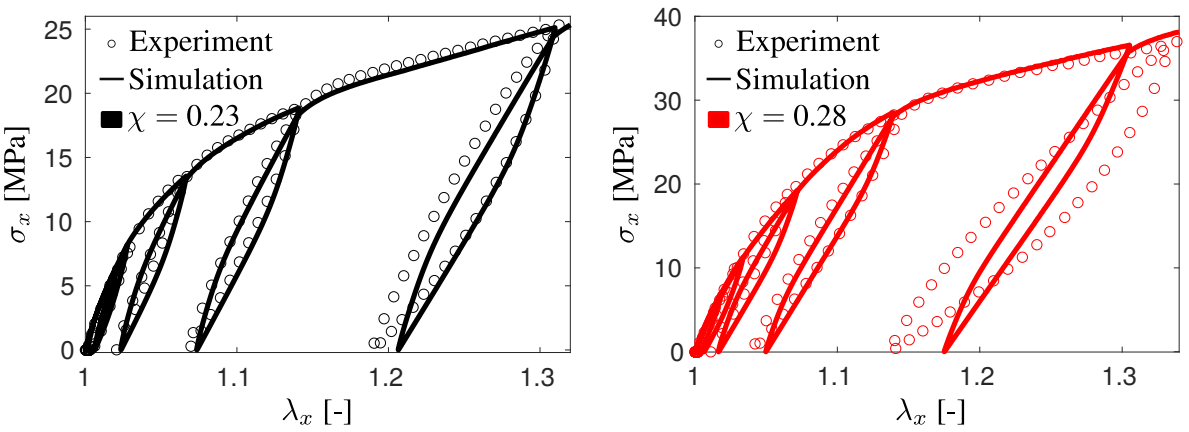

Figure 2.16: Cyclic loading response for different degrees of crystallinity χ for $\dot{\lambda}_x \approx 0.0005$ s^{-1} at 120 °C - Experimental stress-stretch data and corresponding model predictions.

Furthermore, the model response for cyclic loading conditions was assessed for $\chi = 0.28$ at 120 °C (see Figure 2.16). The loading and unloading paths were captured accurately. However, exceeding higher stretch levels $\lambda_x > 1.28$, a mismatch between experimental data and model prediction, regarding the loading and unloading paths, arose for $\chi = 0.28$.

To confirm the capabilities of the proposed framework to predict the material behavior for degrees of crystallinity in the range of $0.23 < \chi < 0.28$, a third set of specimens with a crystal volume fraction of 25.5 % was tested. Since the influence of the crystalline regimes on the material properties was more pronounced at temperatures above the glass transition (cf. Section 2.4), monotonic tensile tests were conducted at 160 °C with this set of specimens. In

the corresponding single element test, the stretch in longitudinal x-direction, obtained from the experimental data as a function of time, was prescribed as a displacement boundary condition. The lateral contraction was unhindered. The model predictions regarding the yield onset, hardening, rate dependency, and transversal deformation corresponded well to the experimental data, see Figure 2.17.

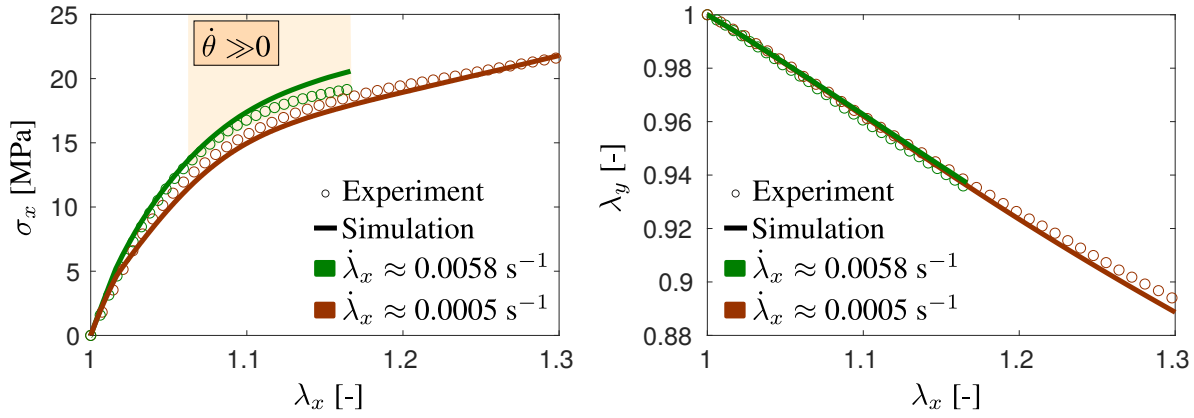

Figure 2.17: Monotonic loading at 160 °C for different loading rates and $\chi = 0.255$ - Experimental stress-stretch data in longitudinal x-direction (left), evolution of transversal stretch λ_y (right), and corresponding model predictions.

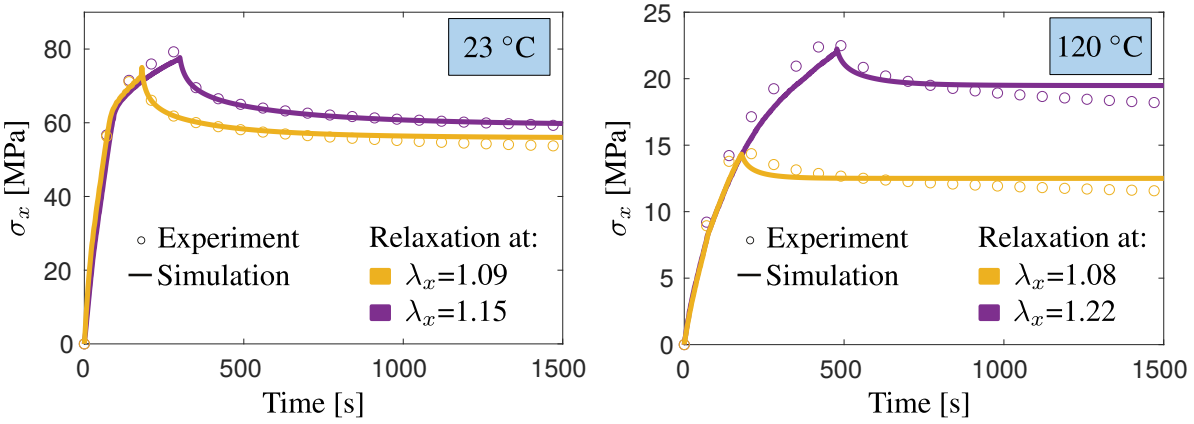

Figure 2.18: Long-term stress-relaxation at different stretch levels and temperatures with a preceding loading rate of $\dot{\lambda}_x \approx 0.0005$ s^{-1} and $\chi = 0.23$ - Experimental stress σ_x over time data and corresponding model predictions.

Finally, the prediction of the stress-relaxation was investigated. To this end, the longitudinal stretch-data λ_x, corresponding to the long-term relaxation experiments (cf. Section 2.4), served as a displacement boundary condition in the corresponding single element tests. Subsequently, the predicted stresses were compared to the experimental data as depicted in

Figure 2.18. It should be emphasized that the relaxation function was fitted to the post-processed short-term, stepwise relaxation test data (cf. Section 2.6). In the latter experiments, the specimens were loaded with $\dot{\lambda}_x \approx 0.0058$ s^{-1} to stretch levels of $\lambda_x = 1.01$ and $\lambda_x = 1.20$. Therefore, it is remarkable that the predicted long-term relaxation behavior, after a preceding loading with $\dot{\lambda}_x \approx 0.0005$ s^{-1} to stretch levels of $\lambda_x = 1.09$, 1.08 and 1.22 was in good agreement with the experimental observation. Interestingly, the model predictions were in better agreement at room temperature. This finding was in contrast to the conclusions drawn from the cyclic-loading validation experiments, where the visco-elastic behavior was predicted less accurately at 23 °C and 50 °C.

2.7.2 Structural validation example

To asses the capabilities of the proposed constitutive framework to capture the material response in multi-axial stress-states, a structural validation experiment was conducted, in addition. To this end, Polyamide 6 (*Ultramid B40*) samples with a circular hole were investigated under uniform tension. For this purpose, specimens (type 5A of ISO 527-2:2012) with a degree of crystallinity of $\chi = 0.23$ were modified by carefully drilling a circular hole with a diameter of 1 mm in the center of the gauge area. The specimen geometry is shown in Figure 2.19.

Prior to testing, the specimens were dried under vacuum at 100 °C for 48 hours. The loading rate was controlled by the cross head speed of the Zwick Z005 universal testing machine and a velocity of $v = 5$ mm/min was prescribed. During uniaxial extension of the specimens, a heterogeneous strain field arose close to the circular hole. The latter was detected by non-tactile displacement measurements at the surface of the specimen, by employing a 2D ARAMIS 4M digital image correlation (DIC) system. ARAMIS detects the deformation of the specimen by subdividing the individual camera images into various rectangular facets. With decreasing facet size the accuracy of the strain computation decreases. A compromise between accuracy of the strain computation (large facet size) and approximation of the measurement area along the circular hole (small facet size) was achieved by choosing a facet size of 14 x 14 pixel. The resulting DIC measurement area is highlighted in light green in Figure 2.19. The experiment was repeated 3 times. The small scatter of the recorded force data (cf. error bars in Figure 2.19) and the symmetric strain fields (cf. Figures 2.20) indicated a precise specimen preparation and reproducible measurement method.

Due to the symmetry of the considered problem, only one eighth of the specimen was modeled. The model dimensions were obtained from accurate measurements ($\pm$ 0.005 mm) of the specimen prior to testing. The length in longitudinal x-direction corresponded to the

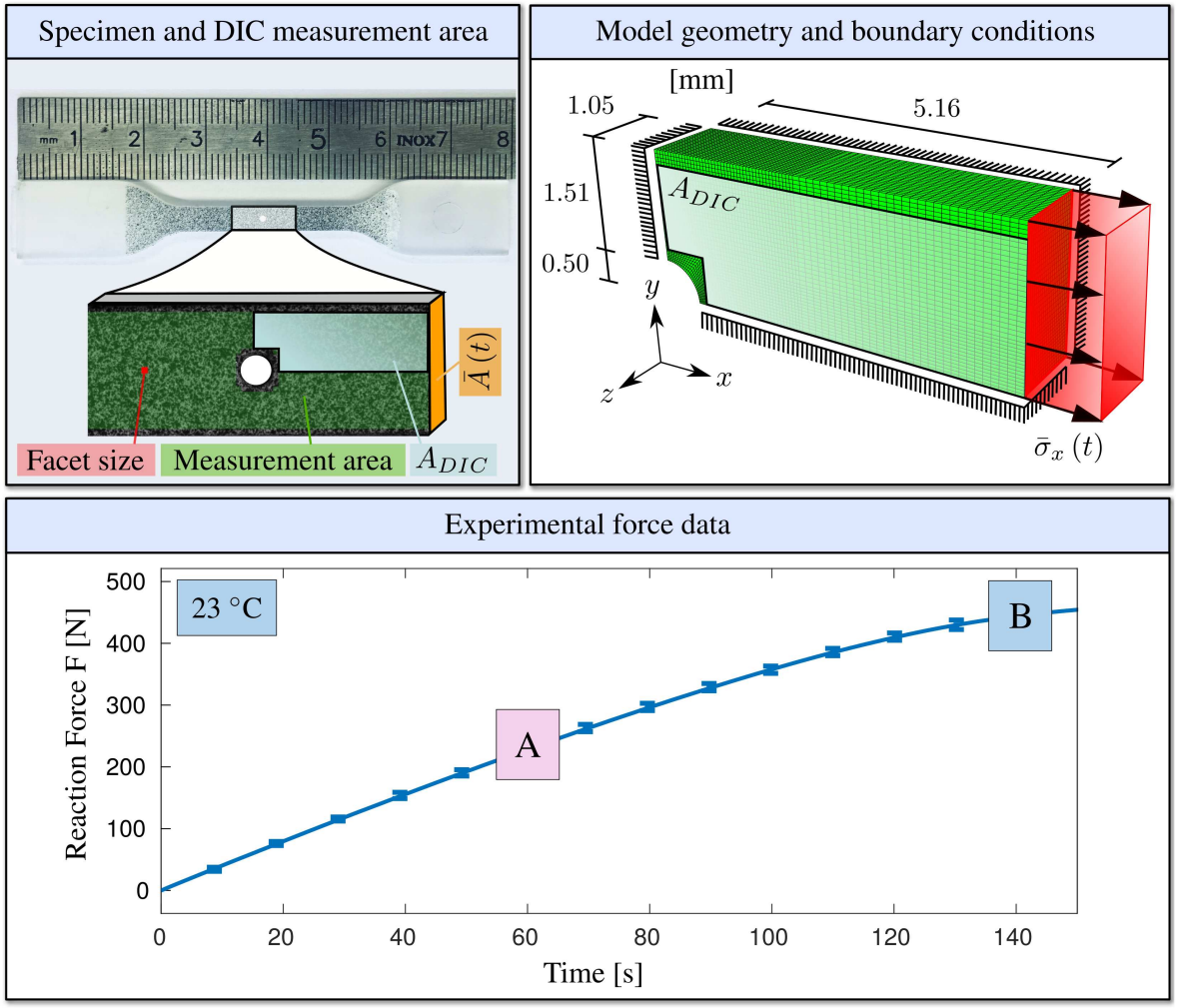

Figure 2.19: Geometry of specimen with circular hole, DIC measurement area, and Finite element model with boundary conditions (top). Recorded force data (bottom).

length of the ARAMIS measurement area. At the boundary of this area ($x = 5.16$ mm), a homogeneous strain field arose (cf. Figure 2.20). Therefore, the evolution of the cross section $\bar{A}(t)$ at the boundary of the measurement area (see. Figure 2.19) could be computed from the initial cross section A_0 and the measured mean stretch in transversal y-direction $\bar{\lambda}_y(t)$ in this section by $\bar{A}(t) = \bar{\lambda}_y(t)^2\, A_0$.

Consequently, the evolution of the true stress in longitudinal x-direction $\bar{\sigma}_x(t)$ at the boundary of the measurement area (see Figure 2.19) was computed from the measured force data $F(t)$ and the deformed cross section by

$$\bar{\sigma}_x(t) = \frac{F\,(t)}{\bar{\lambda}_y(t)^2\, A_0} \tag{2.27}$$

and served as a traction boundary condition for the finite element model. The latter was discretized by eight-node solid elements (C3D8) available in ABAQUS/Standard. The corresponding (converged) mesh is visualized in Figure 2.19.

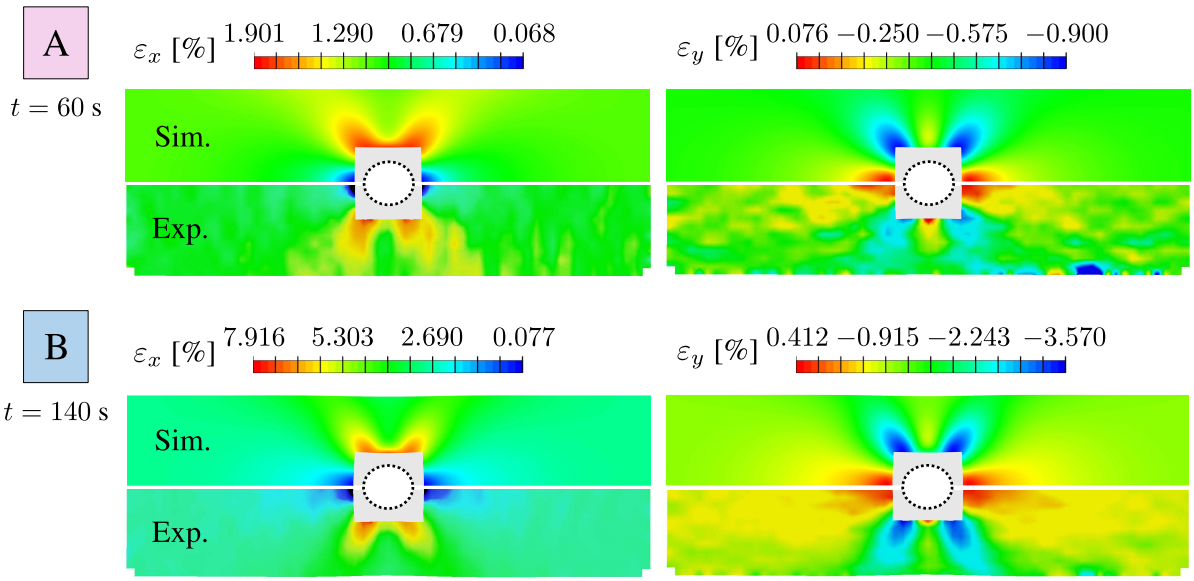

Figure 2.20: Engineering strain contour plots for two different time steps - Experimental data (Exp.) and corresponding model response (Sim.). Only the strain fields in the area A_{DIC} are compared (cf. Figure 2.19). The predicted strains in the light-gray area close to the hole are not provided, since no experimental strain data was accessible due to the chosen facet size (cf. discussion above).

In Figure 2.20, the engineering strain contours, obtained from both the finite element simulation and the DIC images are shown for the time steps A ($t = 60$ s) and B ($t = 140$ s), which are highlighted in the force-time relation in Figure 2.19. For the sake of a perspicuous comparison, only the strain fields in the DIC measurement area A_{DIC} (see Figure 2.20) are shown for the FEM model. The predicted strain fields in longitudinal and transversal direction were in very good agreement with the experimental records. Considering the development of a multi-axial strain field close to the hole, these results were in particular remarkable, since the model parameters were obtained from uniaxial tensile tests only. It is instructive to point out that the large variation of the corresponding strain rates was well captured by the model, in addition.

2.8 Conclusion

In this work, a phenomenological continuum model for semi-crystalline polymers was proposed to analyze, predict, and optimize the material and structural response of semi-crystalline polymers. To capture the complex mechanical response of this class of materials, a visco-elastic, elasto-plastic material model was derived in a thermodynamically consistent manner. A nonlinear relation for the relaxation time, as well as nonlinear isotropic and kinematic hardening were incorporated in the constitutive framework. In this novel finite-strain theory, the temperature and degree of crystallinity serve as input parameters, to predict the complex interplay between the process induced biphasic nature of the underlying microstructure and the applied thermal conditions on the overall material response.

An extensive experimental study was performed, to obtain a (true) stress-stretch data base for Polyamide 6 over a wide range of temperatures, including large strains, different loading rates, and degrees of crystallinity. It was accounted for three degrees of crystallinity in the range of $\chi = 0.23$ to $\chi = 0.28$ and the considered strain rates were limited to one decade. In order to investigate the visco-elastic, elasto-plastic behavior, different loading procedures (i.e. monotonic, cyclic, and relaxation tests) were considered. The study provided important insights into the complex dependencies of the effective material properties on the aforementioned factors. In this way, the presented results will serve as a starting point for more comprehensive experimental investigations in the future, where a wider range of loading rates and degrees of crystallinity should be considered. The provided results, discussed in Section 2.4, will help to reduce the number of experiments, by indicating which influences must be investigated more extensively in which temperature regime.

Based on the obtained experimental results, a staggered model parameter identification procedure was developed, to minimize the uncertainty during the applied nonlinear optimization strategies. The latter was successively applied to obtain a set of material parameters for each considered temperature.

Simultaneous infrared thermography measurements revealed significant material self-heating at higher loading rates, already at moderate stretch levels. The corresponding temperature increase lead to thermal softening and a reduction of the hardening slopes. An important conclusion was therefore to fit the isothermal model only in the range of constant temperatures. Consequently, the model overestimated the stress response for higher loading rates at higher stretch levels. To obtain accurate results in dynamic loading conditions, where dissipative effects lead to important local temperature increases, thermo-mechanical coupling must be taken into account, in the future. To this end, the set of material parameters at different temperatures

will provide an important foundation.

The performed validation studies demonstrated the great capabilities of the proposed framework to accurately predict the significant influence of the temperature and degree of crystallinity on the effective material properties. Particular attention was paid on investigating the three dimensional model predictions regarding the cyclic loading-unloading behavior and corresponding hysteresis loop, as well as the strain recovery, and the stress relaxation under uniform deformation. Furthermore, a structural validation experiment revealed the promising potential of the model to accurately predict the material response for multi-axial stress-states. However, to improve the model predictions for more complex loading scenarios, additional experiments should be conducted in the future. To this end, experimental studies regarding the material response under shear-, compression- and combined loading procedures are required. Based on these results, a yield criterion, accounting for the underlying microstructure and tension compression asymmetry, can be proposed. Moreover, combined tension-compression experiments are necessary to characterize the (nonlinear) kinematic hardening, which is already incorporated in the current constitutive framework. It is important to emphasize that these modifications can be incorporated in a straight forward manner, without changing the algorithmic solution scheme nor the implemented numerical approximation procedures for the required tangent moduli.

Acknowledgments: Financial support of the projects RE 1057/41-1 by the German Science Foundation (DFG) is gratefully acknowledged. Furthermore, the authors are grateful for the provision of *Ultramid B40* by BASF SE and for the production and corresponding DSC analysis of the tensile specimens by the “Institut für Textiltechnik” (ITA) of RWTH Aachen University.

2.9 Appendix

The material model is implemented as an user material subroutine *UMAT* into the commercial FEM software *ABAQUS*/Standard. During the numerical FE-solution scheme, the subroutine is called at each Gaussian integration point. In the course of solving nonlinear boundary value problem at large strains, the deformation gradient $\boldsymbol{F}$ and a vector containing all internal variables $\boldsymbol{\xi_n}$ of the last converged time step serves as an input. As alluded above, the degree of crystallinity χ and temperature θ serve as additional constant input parameters, to determine the set of material parameters (cf. Table 2.2). The required output is the Cauchy stress tensor $\boldsymbol{\sigma}$ (`STRESS`) and material tangent modulus $\mathbb{C}^{\boldsymbol{\sigma}}$ (`DDSDDE`), see equation 2.36. The algorithmic implementation is discussed in the following section.

The algorithmic treatment of the constitutive equations, related to the elasto-plastic model, is based on the proposed strategy of Vladimirov et al. [2008], which is revised briefly. The starting point is an alternative representation of the evolution equations presented in Table 2.1:

$$\dot{\boldsymbol{C}}_p = \dot{\gamma}\ \underbrace{2\frac{\mathrm{dev}(\boldsymbol{Y})\,\boldsymbol{C}_p}{\sqrt{\mathrm{dev}(\boldsymbol{Y}) : \mathrm{dev}(\boldsymbol{Y})^T}}}_{\boldsymbol{T}} = \dot{\gamma}\,\boldsymbol{T}(\boldsymbol{C},\boldsymbol{C}_p,\boldsymbol{C}_{pi})\boldsymbol{C}_p^{-1}\boldsymbol{C}_p \tag{2.28}$$

$$\dot{\boldsymbol{C}}_{pi} = \dot{\gamma}\ \underbrace{2\,\frac{b}{c}\,\mathrm{dev}\,(\boldsymbol{Y}_{kin})\,\boldsymbol{C}_{pi}}_{\boldsymbol{T}_{kin}} = \dot{\gamma}\,\boldsymbol{T}_{kin}(\boldsymbol{C},\boldsymbol{C}_p,\boldsymbol{C}_{pi})\boldsymbol{C}_{pi}^{-1}\boldsymbol{C}_{pi} \tag{2.29}$$

The unconditional stable and first-order accurate exponential map algorithm, which maintains the plastic incompressibility requirement, is applied

$$\boldsymbol{C}_p = \exp\left(\Delta\gamma\,\boldsymbol{T}\,\boldsymbol{C}_p^{-1}\right)\boldsymbol{C}_{p,n} \tag{2.30}$$

$$\boldsymbol{C}_{pi} = \exp\left(\Delta\gamma\,\boldsymbol{T}_{kin}\,\boldsymbol{C}_{pi}^{-1}\right)\boldsymbol{C}_{pi,n} \tag{2.31}$$

for the implicit numerical time integration of the set of evolution equations. The tensor valued functions $\boldsymbol{T}$ and $\boldsymbol{T}_{kin}$ are symmetric, since $\dot{\boldsymbol{C}}_p$ and $\dot{\boldsymbol{C}}_{pi}$ are symmetric. However, the quantities $\boldsymbol{T}\boldsymbol{C}_p^{-1}$ and $\boldsymbol{T}_{kin}\boldsymbol{C}_{pi}^{-1}$ are asymmetric. Thus, no closed-form expression for the exponential function of these arguments is available and a truncated series representation would be required. To overcome this, Reese and Christ [2008] and Vladimirov et al. [2008] utilized a modified ansatz originally proposed by Dettmer and Reese [2004]. In addition, this method a priori guarantees the symmetry of the tensorial internal variables $\boldsymbol{C}_p$ and $\boldsymbol{C}_{pi}$. To this end, equation (2.30) and (2.31) are multiplied from the right by $\boldsymbol{C}_{p,n}^{-1}\boldsymbol{C}_p$ and $\boldsymbol{C}_{pi,n}^{-1}\boldsymbol{C}_{pi}$, respectively and the series representation of the subsequently performed exponential mapping is

exploited. This leads to the final form of the discretized evolution equations, here summarized in a residuum format

$$\boldsymbol{r}_1 = -\left(\boldsymbol{U}_{p,n}\,\boldsymbol{U}_{p,n}\right)^{-1} + \boldsymbol{U}_p^{-1}\exp\left(\Delta\gamma\,\boldsymbol{U}_p^{-1}\,\boldsymbol{T}\,\boldsymbol{U}_p^{-1}\right)\boldsymbol{U}_p^{-1} = \boldsymbol{0} \tag{2.32}$$

$$\boldsymbol{r}_2 = -\left(\boldsymbol{U}_{pi,n}\,\boldsymbol{U}_{pi,n}\right)^{-1} + \boldsymbol{U}_{pi}^{-1}\exp\left(\Delta\gamma\,\boldsymbol{U}_{pi}^{-1}\,\boldsymbol{T}_{kin}\,\boldsymbol{U}_{pi}^{-1}\right)\boldsymbol{U}_{pi}^{-1} = \boldsymbol{0} \tag{2.33}$$

which need to be solved together with the yield function

$$r_3 = \Phi = \sqrt{\mathrm{dev}(\boldsymbol{Y}) : \mathrm{dev}(\boldsymbol{Y})^T} - \sqrt{\frac{2}{3}}\left(\sigma_y - R\left(\kappa\right)\right) = 0. \tag{2.34}$$

In the expression above, the relations $\Delta\gamma = \Delta t\,\dot{\gamma}$, $\boldsymbol{U}_p = \sqrt{\boldsymbol{C}_p}$ and $\boldsymbol{U}_{pi} = \sqrt{\boldsymbol{C}_{pi}}$ are introduced. The scalar evolution equation for the accumulated plastic strain is discretized by means of the classical backward Euler integration algorithm $\kappa = \kappa_n + \sqrt{(2/3)}\,\Delta\gamma$. The latter is already incorporated into the expression of the yield function. Due to the symmetry of the internal variables, a system of only 13 nonlinear scalar equations has to be solved by means of the Newton-Raphson-scheme for $\boldsymbol{U}_p^{-1}$, $\boldsymbol{U}_{pi}^{-1}$ and $\Delta\gamma$. After convergence is achieved, the required Cauchy stress corresponding to the intermolecular response $\boldsymbol{\sigma}_1 = 1/J\,\boldsymbol{F}\boldsymbol{S}_1\boldsymbol{F}^T$ is computed.

The evolution equation corresponding to the inelastic deformation is expressed in terms of the elastic left deformation tensor $\boldsymbol{B}_{e2} = \boldsymbol{F}_{e2}\boldsymbol{F}_{e2}^T$ and the Kirchhoff stress tensor $\boldsymbol{\tau}_2 = \boldsymbol{F}\boldsymbol{S}_2\boldsymbol{F}^T$, cf. Reese and Govindjee [1998*b*]. Subsequently applying the exponential mapping yields

$$\boldsymbol{B}_{e2} = \exp\left(-\Delta t\left(\frac{1}{\tau\,\mu_2}\mathrm{dev}\left(\boldsymbol{\tau}_2\right) + \frac{2}{9\,\tau\,K_2}\mathrm{tr}\left(\boldsymbol{\tau}_2\right)\boldsymbol{I}\right)\right)\boldsymbol{B}_{e2,trial} \tag{2.35}$$

In the expression above, $\boldsymbol{B}_{e2,trial} = \boldsymbol{F}\,\boldsymbol{C}_{i,n}^{-1}\,\boldsymbol{F}^T$ results from an initial trial step, where the inelastic deformation is assumed to be frozen in ($\dot{\boldsymbol{C}}_{i,trial}^{-1} = \boldsymbol{0}$). Since the argument within the exponential function is a symmetric quantity, the exponential mapping can be evaluated in closed form. Furthermore, equation (2.35) can be expressed with respect to the principal axes (cf. Reese and Govindjee [1998*b*]). The resulting system of only three scalar-valued implicit equations is solved by means of a local Newton-Raphson-scheme for the eigenvalues of $\boldsymbol{B}_{e2}$. Conclusively, the total Cauchy stress $\boldsymbol{\sigma} = \boldsymbol{\sigma}_1 + \boldsymbol{\sigma}_2$ is computed from the contributions of both models.

The material tangent modulus $\mathbb{C}^{\boldsymbol{\sigma}} = 1/J\,\mathbb{C}^{\boldsymbol{\tau}}$ (`DDSDDE`), is related to the tangent modulus tensor $\mathbb{C}^{\boldsymbol{\tau}}$ for the Jaumann rate of the Kirchhoff stress $\boldsymbol{\tau}$ (cf. Stein and Sagar [2008]). The

linearized incremental form of the latter reads

$$\Delta\boldsymbol{\tau} - \Delta\boldsymbol{W}\boldsymbol{\tau} - \boldsymbol{\tau}\Delta\boldsymbol{W}^T = \mathbb{C}^{\boldsymbol{\tau}}\Delta\boldsymbol{D} \tag{2.36}$$

where $\Delta\boldsymbol{D}$ and $\Delta\boldsymbol{W}$ are the incremental symmetric and antisymmetric parts of the incremental spatial velocity gradient $\Delta\boldsymbol{L}$. In the course of the current work, $\mathbb{C}^{\boldsymbol{\tau}}$ is approximated numerically. To reduce the computational costs, an algorithm proposed by Sun et al. [2008] is applied, which is based on a more systematic treatment of the topic by Miehe [1996]. In this procedure only 6 successive perturbations of the deformation gradient and thus only six additional stress computations are required. For all considered nonlinear initial boundary-value problems, this method resulted in a nearly quadratic rate of convergence of the global Newton-Raphson procedure.

3 Article 2: Incorporating crystallinity distributions into a thermo-mechanically coupled constitutive model for semi-crystalline polymers

This article was published as:

Felder, S., Holthusen, H., Hesseler, S., Pohlkemper, F., Gries, T., Simon, J.-W., and Reese, S. [2020], 'Incorporating crystallinity distributions into a thermo-mechanically coupled constitutive model for semi-crystalline polymers', *International Journal of Plasticity* **1**35, 102751.

Disclosure of the individual authors' contributions to the article:

S. Felder reviewed the relevant existing literature, derived the constitutive framework, implemented the material model as a user-defined material model (UMAT and UMATHT) into the commercial Finite Element software *ABAQUS* / Standard, carried out all computational examples, and wrote the article. H. Holthusen gave conceptual advice, implemented parts of the material routine, fitted the parameters corresponding to the crystallization kinetics model and implemented the corresponding optimization procedure. S. Hesseler and F. Pohlkemper carried out the differential scanning calorimetry (DSC) experiments and contributed to the discussion of the results. T. Gries, J.-W. Simon, and S. Reese gave conceptual advice, contributed to the discussion of the results, read the article and gave valuable suggestions for improvement. All authors approved the publication of the final version of the manuscript.

3.1 Abstract

Thermoplastic polymers (TP) are well-suited for thermoforming and injection moulding processes. Semi-crystalline polymers (SCP) are a specific class of TPs, which partly crystallize after cooling from the melt. During thermoforming processes, SCPs are subjected to large deformations and thermal loadings and show strong thermo-mechanical coupling effects. In addition, the evolution of the crystalline phase influences the macroscopic material response significantly. Due to these complex dependencies, a demand for computational models arises, to analyze, predict, and optimize the complex material and structural behavior of parts during these processes.

To this end, a finite strain, thermo-mechanically coupled constitutive framework is derived in a thermodynamically consistent manner for SCPs. In the continuum model, a visco-hyperelastic network resistance and an elasto-plastic intermolecular resistance are introduced, where non-linear isotropic and kinematic hardening as well as non-linear relaxation behavior are considered. To account for the dependence of the material response on the degree of crystallinity, the crystallization kinetics during cooling from the melt are captured by means of a non-isothermal representation of the Avrami equation. Furthermore, the heat generation, associated with irreversible processes and exothermic crystal growth, is derived in a thermodynamically consistent manner.

Uniaxial tensile test data for different temperatures, loading rates, and degrees of crystallinity, as well as isothermal and non-isothermal differential scanning calorimetry (DSC) data for Polyamide 6 is utilized to calibrate the model in a stepwise parameter identification scheme. The model response is discussed and reveals the promising potential of this new approach to efficiently and accurately predict this class of materials in the future.

Nomenclature

a	Scalar quantity
$\boldsymbol{a}$	First order tensor
$\boldsymbol{A}$	Second order tensor
$\mathbb{A}$	Fourth order tensor
$\dot{(*)}$	Total derivative with respect to time
$(*)^T$	Transpose of a quantity
$(*)^{-1}$	Inverse of a quantity
tr$(*)$	Trace of a quantity
det$(*)$	Determinant of a quantity
sym$(*)$	Symmetric part of a quantity
dev$(*)$	Deviatoric part of a quantity
grad$(*)$	Gradient of a quantity with respect to cc
Grad$(*)$	Gradient of a quantity with respect to rc
$\bar{(*)}$	Isochoric part of a quantity
$\boldsymbol{A} : \boldsymbol{B}$	Scalar product of two tensors $\boldsymbol{A}$ and $\boldsymbol{B}$
$(*)_{1}$	Intermolecular quantity
$(*)_{2}$	Network quantity
$(*)_{e1}$	Intermolecular elastic quantity
$(*)_{e2}$	Network elastic quantity
$(*)_{i}$	Network inelastic quantity
$(*)_{j}$	Quantity from last converged time step
$(*)_{p}$	Intermolecular plastic quantity
$(*)_{pe}$	Intermolecular plastic elastic quantity
$(*)_{pi}$	Intermolecular plastic inelastic quantity
b and c	Kinematic hardening parameters
$\boldsymbol{B}$	Left Cauchy-Green deformation tensor
c_T	Specific heat capacity
$\boldsymbol{C}$	Right Cauchy-Green deformation tensor
cc	Current configuration
D	Nakamura-Ziabicki parameter
$\boldsymbol{D}$	Symmetric part of velocity gradient
e	Specific internal energy
E	Young's modulus
$\boldsymbol{F}$	Deformation gradient
H	Isotropic hardening modulus
$\boldsymbol{I}$	Second order identity tensor
ic_{1a}	Intermediate plastic configuration
ic_{1b}	Intermediate configuration of kinematic hardening
ic_{2}	Inelastic intermediate configuration
J	Determinant of deformation gradient
K	Bulk modulus
K_c	Non-isothermal crystal growth rate
K_{max}	Nakamura-Ziabicki parameter
$\boldsymbol{L}$	Velocity gradient
$\boldsymbol{M}$	Mandel stress tensor
n	Avrami exponent
$\boldsymbol{q}_0$	Heat flux in rc
$\boldsymbol{q}_t$	Heat flux in cc
rc	Reference configuration
r	Heat generation with respect to rc
r_t	Heat generation with respect to cc
R	Driving force of isotropic hardening
$\boldsymbol{S}$	Second Piola-Kirchhoff stress tensor
t_{end}	Time at the end of crystallisation
t_{on}	Time at the crystallisation onset
$\boldsymbol{u}$	Displacement vector
$\boldsymbol{U}$	Right stretch tensor
$\boldsymbol{X}$	Back stress tensor in ic_{1a}
$\tilde{\boldsymbol{X}}$	Back stress tensor in rc
$\boldsymbol{Y}$	Stress like quantity: $\boldsymbol{Y} = \boldsymbol{C}\boldsymbol{S}_{1} - \boldsymbol{C}_p\tilde{\boldsymbol{X}}$
$\boldsymbol{Y}_{kin}$	Stress like quantity: $\boldsymbol{Y}_{kin} = \boldsymbol{C}_p\tilde{\boldsymbol{X}}$
α_T	Coefficient of thermal expansion
β	Isotropic hardening parameter
$\dot{\gamma}$	Plastic multiplier
δ	Relaxation time function parameter
Δh_f^{100}	Fusion enthalpy of a 100% crystalline material
Δh_m	Fusion enthalpy
Δt	Time increment
η	Specific entropy
θ	Temperature
θ_0	Reference temperature
θ_{max}	Nakamura-Ziabicki parameter
θ_{on}	Crystallisation onset temperature
κ	Accumulated plastic strain
λ_i	stretch in i-direction
λ_m	Locking stretch parameter
λ_T	Heat conductivity
Λ	Lamé constant
μ	Shear modulus
ν	Poisson's ratio
$\boldsymbol{\xi}$	Set of internal variables
ρ_0	Density in rc
$\boldsymbol{\sigma}$	Cauchy stress tensor
σ_∞	Isotropic hardening parameter
σ_y	Initial yield stress
τ	Relaxation time
τ_0	Relaxation time function parameter
$\boldsymbol{\tau}$	Kirchhoff stress tensor
φ	Relaxation time function parameter
Φ	Yield function
χ	Absolute degree of crystallinity
χ_c	Relative degree of crystallinity
ψ	Specific Helmholtz free energy
Ψ	Volumetric Helmholtz free energy

3.2 Introduction

Thermoplastic polymers (TP) are an important class of engineering materials for many technically relevant applications. They are widely used in the automotive industry, due to their high strength to weight ratio and potential of a cost-effective mass production. In contrast to thermosets, TPs can be repeatedly reshaped after heating above the melting point and are thus well-suited for forming processes of continuous fiber reinforced TPs and injection moulding. A specific class of thermoplastics are semi-crystalline polymers (SCP), where the amorphous phase partly crystallizes after cooling from the melt. During this process, the polymer chains fold together and form ordered regions referred to as lamellae, which grow radially (under isotropic temperature distribution) and form quasi-spherical structures (spherulites). In the course of this work, semi-crystalline Polyamide 6 (PA6) is considered.

Over the past decades, multiple models were proposed to describe the crystallization kinetics in SCPs, which can substantially differ for different polymers. Based on the isothermal Avrami equation (Avrami [1939]), several non-isothermal models were developed, by e.g. Ozawa [1971], Nakamura et al. [1973], and Mubarak et al. [2001] to account for non-isothermal crystallization and isothermal induction time. To estimate the heat generation during the exothermic crystallization process Goff et al. [2005], Zinet et al. [2010] and Kugele et al. [2017] used similar approaches, based on the enthalpy of fusion measured in DSC experiments. However, in all these works the crystallization process and associated heat generation is studied in the context of (1D) thermal problems and thermo-mechanical coupling is not accounted for.

Naturally, the morphology of the underlying microstructure (i.e. the degree of crystallinity, crystal configuration, and lamellae thickness etc.) has a significant influence on the mechanical behavior of SCPs (Jenkins [1992] and Ayoub et al. [2011]). Furthermore, the mechanical response of semi-crystalline polymers is characterized by nonlinear, visco-plastic behavior, depending on the thermal conditions. In addition, thermo-mechanical coupling effects, i.e. significant material self-heating and associated thermal softening, are present at higher loading rates (cf. e.g. Şerban et al. [2013], El-Qoubaa and Othman [2016], and Krairi et al. [2019]).

Due to the complex, nonlinear deformation behavior of SCPs, it is of high interest to identify, analyze, and predict the complex material and structural response of parts during and after thermoforming processes. Accordingly, multiple computational models were proposed at the lamellae, the spherulite and the continuum level, over the past decades. Based on the work of Boyce et al. [2000], where the elementary deformation mechanisms are described by two parallel resistances, several phenomenological models were proposed (e.g. Srivas-

tava et al. [2010], Ayoub et al. [2010], and to name only a few). Drozdov and Gupta [2003] and van Dommelen et al. [2003] developed visco-plastic material models for different variants of polyethylene. The latter describe the plastic effects by means of a crystallographic slip (dislocation) within the crystalline phase. The J2 -plasticity model, is used by Bergström et al. [2003] for ultra-high molecular weight polyethylene. Gudimetla and Doghri [2017], Wang et al. [2019] and Praud et al. [2017] developed coupled visco-elastic and visco-plastic models in the context of amorphous and semi-crystalline polymers, respectively. Already at moderate stress levels, polymers exhibit a significant Bauschinger-like effect upon unloading. Consequently, some authors (e.g. Hasan and Boyce [1995], Anand et al. [2009]) incorporated kinematic hardening into the constitutive framework and Qi et al. [2019] investigated the cyclic-loading behavior of high density polyethylene.

Besides the phenomenological approaches, different modeling schemes were presented in the past, to model the microstructural constituents separately by employing either analytical or FE-based homogenization schemes, e.g. Li and Shojaei [2012], Uchida and Tada [2013], Popa et al. [2014], and Alisafaei et al. [2016] to name a few. These approaches are usually characterized by a smaller number of parameters and less complex model formulations. However, it is in general rather difficult to obtain the required physical or microstructural data from experimental observations. In particular, for semi-crystalline Polyamide 6 this is a challenging task, since the complex microstructure is characterized by different molecular arrangements. Depending on the thermal conditions, applied stress, and presence of moisture, the crystalline phases of PA6 are either characterized by a fully extended (monoclinic) configuration of the polymer chains, referred to as α-form, or a twisted (hexagonal/ pseudohexagonal) configuration (γ-form) (see e.g. Fornes and Paul [2003]). Furthermore, the crystallization process is accompanied by the creation of a so-called rigid amorphous phase, introduced by Wunderlich [2003]. When multi-scale approaches are employed, the choices regarding the geometry and the size of the representative microstructure as well as the distribution of the characteristic microstructural elements play a crucial role, in addition. These difficulties do not arise by employing phenomenological models, where the (usually larger number of) material parameters can be identified from conventional mechanical tests at the macroscopic scale.

Despite the numerous studies dealing with the prediction of the material behavior under isothermal conditions, only a limited number of works focus on thermo-mechanical coupling. In the context of amorphous polymers, Ames et al. [2009] and Srivastava et al. [2010] proposed thermo-mechanically coupled formulations to capture the material self-heating under large deformation. Contributions regarding the thermo-mechanically coupled modeling of SCPs where made by Maurel-Pantel et al. [2015], and Garcia-Gonzalez et al. [2018] for

PA66, PEEK, UHMWPE, and HDPE, respectively. In addition, Shen et al. [2019] introduced a thermo-elastic-viscoplastic-damage model for Polyamide 6.

Furthermore, only a limited number of works account for the influence of the material internal microstructure (such as crystal volume fraction) on the macroscopic response (e.g. Ponçot et al. [2013] and Rozanski and Galeski [2013]). In a phenomenological approach, different rules of mixture of the amorphous and crystalline phases were investigated by Dusunceli and Colak [2008] . Ayoub et al. [2011] and Abdul-Hameed et al. [2014] suggested a two-phase representation of the microstructure. In these models, the degree of crystallinity serves as a constant input parameter.

However, to accurately predict the mechanical behavior of SCPs in the context of forming processes, it is crucial to account for the morphology of the material internal microstructure based on the preceding thermal treatment. To the authors' knowledge, there is no model available in the literature, where crystallization kinetics are incorporated into a fully thermo-mechanically coupled constitutive framework at large strains. In this work, a reasonably general material model with these features is derived in a thermodynamically consistent manner (cf. chapter 3.4). A visco-hyperelastic model (based on the work of Reese and Govindjee [1998*b*]), where a nonlinear relation for the relaxation time is incorporated (Amin et al. [2006]), represents the network resistance of the polymer. Furthermore, an elasto-plastic intermolecular resistance is assumed. To capture the Bauschinger-like phenomena after unloading, nonlinear kinematic hardening of Frederick-Armstrong type is incorporated, in line with the work of Vladimirov et al. [2008]. In order to account for the underlying microstructure, the total degree of crystallinity χ is treated as an additional internal variable. Crystallization from a relaxed, static melt is assumed and the evolution of χ is modeled by means of a non-isothermal representation of the Avrami equation. The internal heat sources, due to the exothermic crystallization process as well as due to viscous and plastic effects are derived in a thermodynamically consistent manner as well.

Finally, this new theory is applied to model Polyamide 6 (*Ultramid B40* kindly provided by BASF). To this end, both, the crystallization kinetics and the (thermo-)mechanical response for different degrees of crystallinity, strain rates and temperatures, are investigated experimentally (cf. Section 3.3). Noteworthy, despite the numerous studies regarding the material properties of PA6, no such comprehensive experimental data base was available in the literature. The capabilities of the model, to accurately predict self-heating and accompanied thermal softening is verified in Section 3.8 based on infrared thermography measurements. A more complex structural example is discussed in the last paragraph and finally conclusions are drawn in Section 3.9.

3.3 Experimental observations

The proposed constitutive framework was motivated by experimental studies for Polyamide 6 (*Ultramid B40* kindly provided by BASF). The experimental procedures and results are discussed briefly in the following.

3.3.1 Crystallization kinetics

In order to investigate the crystallization kinetics of PA6 under isothermal and non-isothermal conditions, several differential scanning calorimetry (DSC) experiments were conducted. To this end, the DSC 1 from *Mettler Toledo* was utilized and all specimens were prepared by cutting polymer granulate into pieces significantly smaller than 1 mg. The DSC analyses were performed for 5 mg samples filled in 40 μl tins and conducted under nitrogen atmosphere. Noteworthy, each testing procedure was repeated three times. For the isothermal crystallization analysis, the polymer was heated up from room temperature 23.5 °C way above the melting point to 245 °C with 10 °C/min and subsequently rapidly cooled down with 100 °C/min to the target crystallization temperature (i.e. 192 °C, 194 °C, 196 °C, and 198 °C), where the temperature was held constant for 30 minutes. During the non-isothermal crystallization experiments, the samples were heated up in the same way and afterwards cooled down with constant cooling rates of 5 °C/min, 10 °C/min, 20 °C/min, 40 °C/min, 60 °C/min, and 100 °C/min. The recorded exothermic curves of heat flow over time and temperature for the non-isothermal experiments are displayed in Figure 3.1. Noteworthy, the curves have been shifted vertically, in order to increase the readability.

Integrating the obtained specific heat flow curves $\dot{h}(t)$ from the crystallization onset time t_{on} to the end time t_{end}, yielded the heat release during the exothermic reaction i.e. the change in specific enthalpy Δh_m during the whole crystallization process (see Figure 3.1). As it is common practice (cf. e.g. Zinet et al. [2010] and Kugele et al. [2017]), the absolute degree of crystallinity χ at the end of the crystallization process was calculated by

$$\chi(t_{end}) = \frac{\int_{t_{on}}^{t_{end}} \dot{h}(t)\, dt}{\Delta h_f^{100}} = \frac{\Delta h_m}{\Delta h_f^{100}} \tag{3.1}$$

where the specific fusion enthalpy of a hypothetical 100% crystalline material Δh_f^{100} was introduced. For Polyamide 6, Wunderlich [1976] suggested a value of $\Delta h_f^{100} = 230$ J/g, which is widely accepted until today. However, Illers [1978] reported a heat of fusion of 241 J/g and 239 J/g corresponding to the monoclinic and hexagonal form, respectively. In line

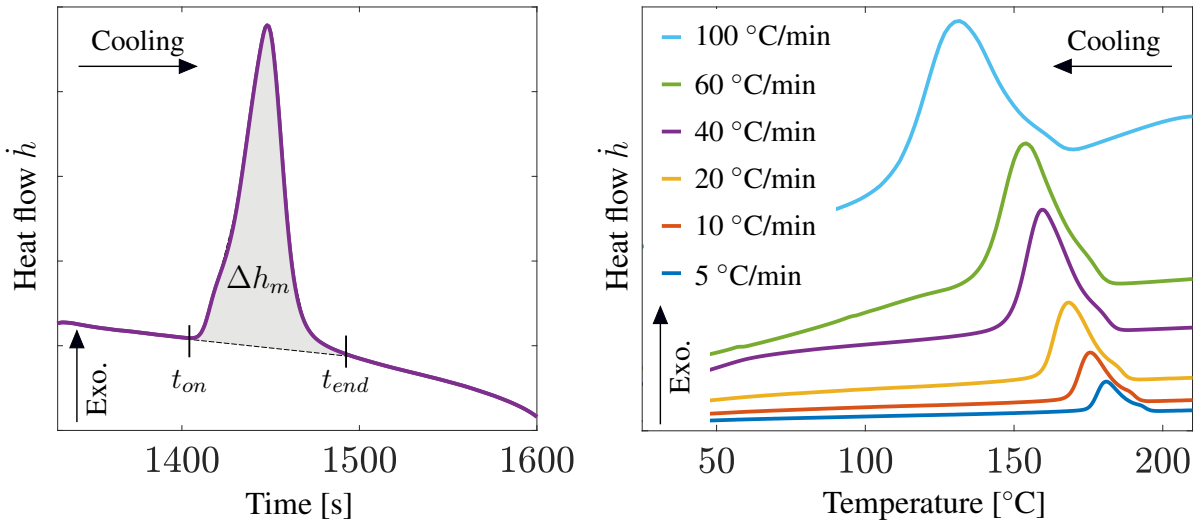

Figure 3.1: Representative example of the recorded heat flow $\dot{h}$ over time for 40 °C/min and corresponding t_{on}, t_{end}, and Δh_m (left). Non-isothermal DSC data for all considered cooling rates (right).

with Fornes and Paul [2003] the average of these values, i.e. 240 J/g, was considered, in the current work.

Based on these relations, the relative degree of crystallinity χ_c

$$\chi_c(t) = \frac{\int_{t_{on}}^{t} \dot{h}(t)\, dt}{\Delta h_m} \tag{3.2}$$

for arbitrary time steps was defined in the standard manner and lied consequently between zero (100% amorphous) and one (at the end of the crystallization process). From the latter expression and (3.1) the absolute degree of crystallinity as a function of time was defined by

$$\chi(t) = \frac{\int_{t_{on}}^{t} \dot{h}(t)\, dt}{\Delta h_f^{100}} = \chi_c(t)\, \frac{\Delta h_m}{\Delta h_f^{100}} \tag{3.3}$$

The experimental data revealed the typical crystallization kinetics characteristics for different thermal treatments. With increasing cooling rates, Δh_m and consequently also the total degree of crystallinity decreased. Furthermore, the onset temperature and the peak crystallization temperature were shifted to lower temperatures and the crystallization exotherm became wider, in line with the reported findings of e.g. Liu and Yang [2010].

3.3.2 Mechanical testing

To obtain insights into the complex material behavior at different temperatures and to study the effect of varying degrees of crystallinity tensile experiments were conducted. Monotonic, cyclic, and relaxation experiments were performed by a *Zwick Z005* universal testing machine with different loading rates at varying temperatures below and above the glass transition temperature ($\theta_g \approx 80$ °C) at 23 °C, 50 °C, 120 °C, and 160 °C. Dried specimens (type 5A in accordance with ISO 527-2:2012), which were produced by injection moulding were tested. To investigate the material response for different degrees of crystallinity, specimens with an initial degree of crystallinity of $\chi_I = 23$ % were annealed under vacuum for 5 hours at 180 °C. In this way, a second set of specimens with a higher degree of crystallinity ($\chi_{II} = 28$ %) was obtained. The loading procedure was controlled by the cross head speed and two different velocities ($v_{min} = 1$ mm/min and $v_{max} = 10$ mm/min) were prescribed. A heterogeneous strain distribution and non-constant strain rates arose at large strains, when necking of the specimen occurred. To evaluate the material response under constant loading rates, an *ARAMIS 4M* digital image correlation (DIC) system, which provides accurate non-tactile displacement measurements at the surface of the specimen, was utilized. With the DIC data at hand, regions of the specimen with a homogeneous strain field and an approximately constant stretch rate in longitudinal x-direction of $\dot{\lambda}_{x,min} = 0.03$ min^{-1} and $\dot{\lambda}_{x,max} = 0.35$ min^{-1} were evaluated to obtain the true stress (Cauchy stress σ_x) over stretch λ_x relation. Simultaneous infrared thermography (IR) (*VarioCAM HD* by textitInfraTec) measurements were performed during the monotonic tensile tests at room temperature. The average temperature of the considered section with approximately constant stretch rate was evaluated.

The true stress σ_x over stretch λ_x data from uniaxial tensile experiments at different temperatures and for varying loading rates $\dot{\lambda}$ and degrees of crystallinity χ, is depicted in Figure 3.2. With increasing degree of crystallinity, an increase of the initial stiffness, hardening, and yield stress was observed, which was also reported by several authors (e.g. Jenkins [1992] and Ayoub et al. [2011]).

Furthermore, for increasing strain rates, a loss in ductility and increase of yield stress and hardening was detected in line with the works of Rae et al. [2007], Şerban et al. [2013] and El-Qoubaa and Othman [2016]. This behavior becomes more complicated at higher loading speeds (v_{max}), where a significant temperature increase on the surface of the specimen, related to material self-heating, was observed, as depicted in Figure 3.3. At stretch levels exceeding $\lambda_x \approx 1.05$, the strain induced hardening competed with the self-heating induced thermal-softening (cf. Maurel-Pantel et al. [2015], Parodi et al. [2018]). In conjunction with these phenomena, the slopes of the stress-stretch relations, depicted in Figure 3.2 on the left

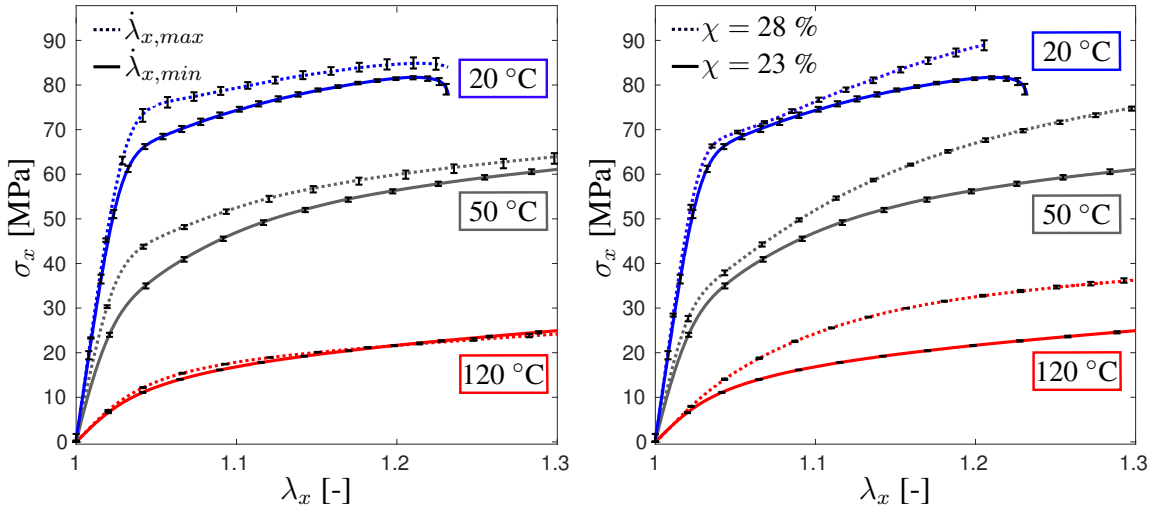

Figure 3.2: Monotonic, uniaxial tensile tests at various temperatures: Effect of loading rate ($\dot{\lambda}_{x,min} = 0.03$ min^{-1} vs. $\dot{\lambda}_{x,max} = 0.35$ min^{-1}) for $\chi = 23$ % (left). Effect of degree of crystallinity ($\chi = 23$ % vs. $\chi = 28$ %) for $\dot{\lambda}_{x,min}$ (right).

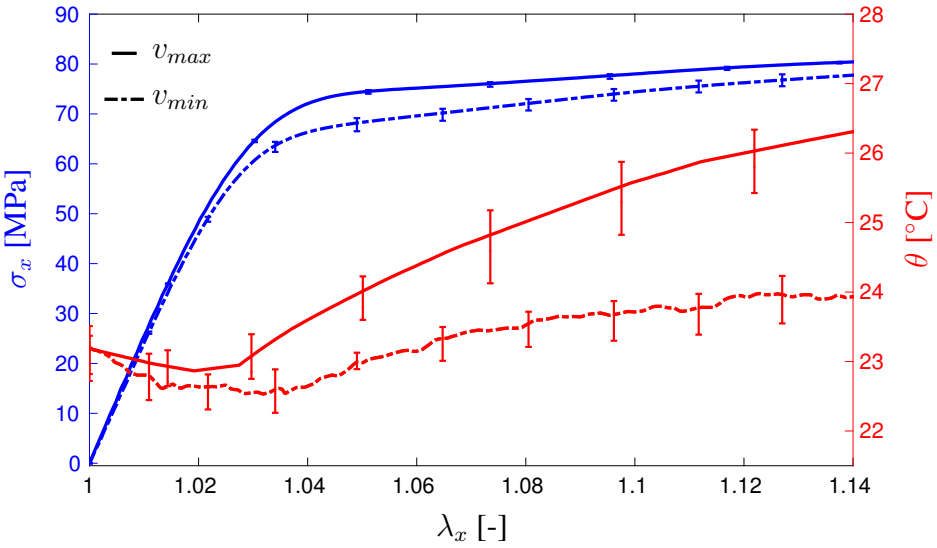

Figure 3.3: Investigation of material self-heating at room temperature for $\chi = 23$ %.

hand side, decrease for higher loading rates after moderate stretch levels of $\lambda_x \approx 1.05$.

In addition, uniaxial cyclic-loading-unloading-recovery tests revealed three distinct deformation stages of the considered PA6 (see Figure 3.4). In this cyclic experimental procedure, the specimen was first subjected to displacement controlled loading and afterwards unloaded until the force equaled zero. Subsequently, the force was held constant at zero for a sufficiently long time period, to allow for the remaining stretch to converge towards an equilibrium stage. In the elastic regime, the recorded stretch directly equaled 1 after unloading to zero force. In the visco-hyperelastic regime, some remaining stretch was detected after unloading, which converged towards 1 in the recovery step (see Figure 3.4 on the right hand side). In the visco-hyperelastic-plastic regime, the initial stretch value after unloading converged to some remaining plastic deformation in the recovery step.

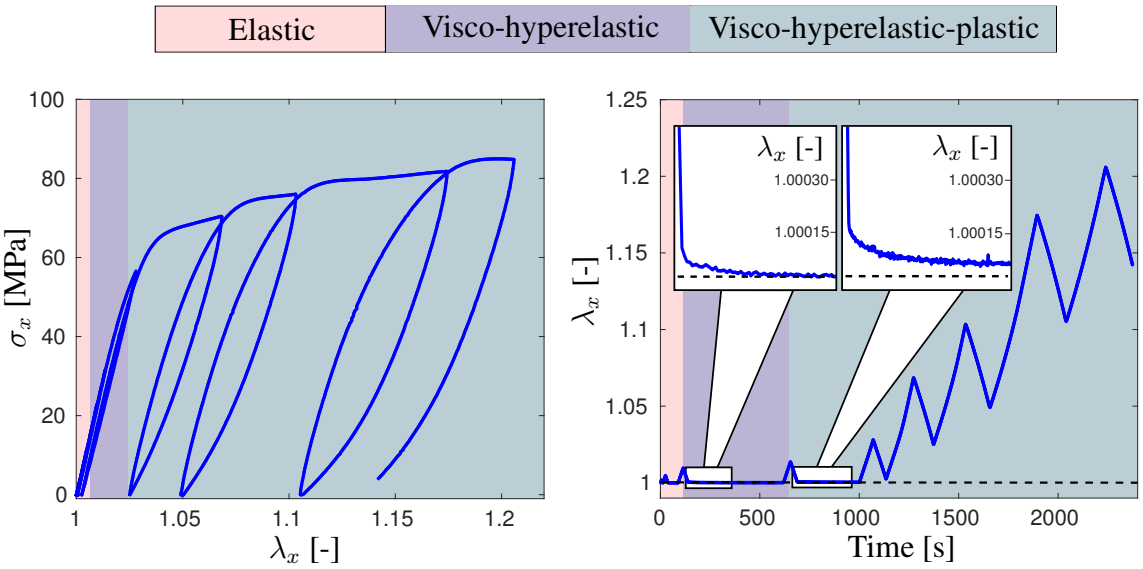

Figure 3.4: Cyclic-loading-unloading-recovery test at room temperature.

From this experimental data and the numerous preceding studies (referred to above), it is evident that SCPs show in general a complex inelastic behavior, especially under non-monotonic loading, characterized by strain recovery, stress relaxation, and loading-unloading hysteresis loop. Over the last decade, the nature of the underlying microscopic mechanisms related to the visco-plastic behavior and the large nonlinearity upon unloading were revealed e.g. throughout molecular dynamic simulations (e.g. Rottler [2009], Jatin et al. [2014], and Jabbari-Farouji et al. [2017]). It was concluded that strain hardening in polymeric materials is in general related to a limited number of possible network conformations upon loading. In the work of Chevalier et al. [2018], the physical origin of the prominent Bauschinger-like effect upon unloading (cf. e.g. Anand et al. [2009] and Krairi and Doghri [2014]) was explained by the

evolution of back stresses during the loading phase, which eventually lead to an early activation of Shear Transformation Zones (STZ) upon unloading.

3.4 Material model formulation

The objective of this work is the derivation of a constitutive theory, which allows for the prediction of the material behavior of semi-crystalline polymers under thermo-mechanical loading conditions. In addition, it is accounted for varying microstructural compositions of amorphous and crystalline phases, arising from different cooling conditions of the polymer melt. To this end, two decoupled processes are considered for simplicity:

I Supercooling of the polymer melt - crystallization from static relaxed melt: Thermo-chemically coupled problem ($\dot{\chi} \geq 0$ and $\boldsymbol{\sigma} = \mathbf{0}$).

II Thermo-mechanical behavior of solidified polymer: Thermo-mechanically coupled problem ($\dot{\chi} = 0$ and arbitrary $\boldsymbol{\sigma}$).

This split is based on the following considerations: Temperature induced, non-isothermal crystallization from a relaxed, static melt is assumed and consequently no initial orientation and stretching of the polymer molecules is present. Concomitant with these assumptions, the crystallization process is assumed to proceed under no volume constraints and stress-free conditions $\boldsymbol{\sigma} = \mathbf{0}$. The biphasic nature of the underlying microstructure is modeled in a continuum mechanical fashion, where the total degree of crystallinity is captured by introducing a single scalar internal variable χ. In this way, no differentiation between either crystal configurations (γ-phase and α-phase) nor morphology (lamella thickness) is made. Furthermore, the creation of the so-called rigid amorphous phase (cf. e.g. Wunderlich [2003] and Chen and Cebe [2007]), is not resolved either, for simplicity. In Section 3.4.5, a suitable evolution equation for the total degree of crystallinity is proposed. Solving the thermo-chemically coupled problem leads to an accurate prediction of the distribution and amount of crystalline phase for arbitrary thermal processing conditions and part geometries. To account for the influence of the emerged solidified microstructure on the macroscopic material properties, the resulting total degree of crystallinity χ serves as a constant input parameter ($\dot{\chi} = 0$) for the thermo-mechanically coupled model formulation.

To provide a better understanding of the thermo-mechanically coupled framework and the proposed Helmholtz free energy, a schematic illustration by means of a rheological model is shown in Figure 3.5. A decomposition into an intermolecular resistance and a network resistance, which is in line with the fundamental ideas described in the works of e.g. Boyce

et al. [2000], Ahzi et al. [2003], Srivastava et al. [2010] and Ayoub et al. [2011], is proposed. In the following, properties associated with the intermolecular and network resistance will be denoted by index 1 and 2, respectively. The network resistance is a visco-hyperelastic

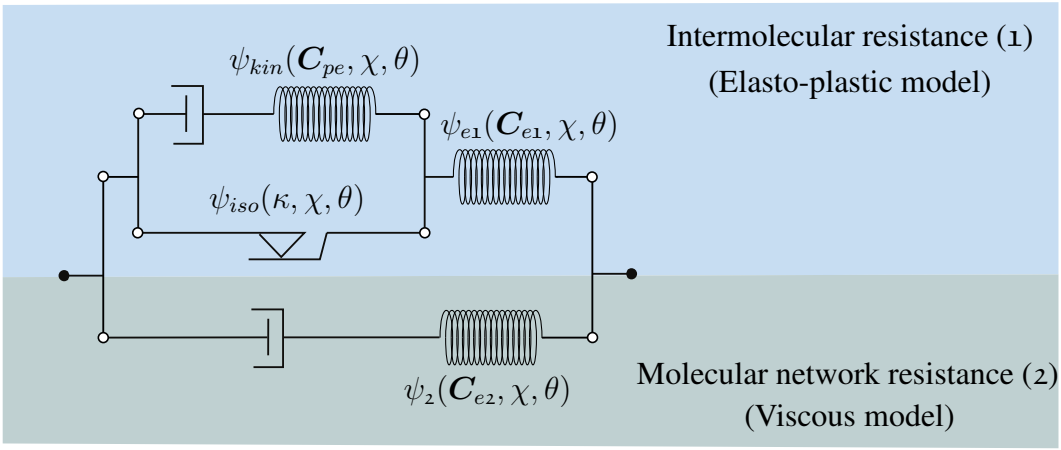

Figure 3.5: Schematic of the constitutive model.

model, to account for the molecular orientation and relaxation. The intermolecular resistance, an elasto-plastic model, is connected in parallel. In the latter, nonlinear kinematic hardening of Armstrong-Frederick type and nonlinear isotropic hardening are incorporated. With this modeling approach, the elastic, visco-hyperelastic, and visco-hyperelastic-plastic material response, observed in cyclic experiments (cf. chapter 3.3) can be captured accordingly.

3.4.1 Kinematics

For the continuum mechanical extension of the presented rheological model to finite strains, the kinematic relations are introduced first. These are based on several multiplicative decompositions of the total deformation gradient $\boldsymbol{F}$, which are shown in Figure 3.6. For the elasto-plastic model, the classical split of the deformation gradient, $\boldsymbol{F} = \boldsymbol{F}_{e1}\boldsymbol{F}_p$, into its elastic part $\boldsymbol{F}_{e1}$ and plastic part $\boldsymbol{F}_p$ is performed (cf. Eckart [1948], Kröner [1959], Lee [1969]). To account for nonlinear kinematic hardening, an additional split of the plastic deformation gradient $\boldsymbol{F_p} = \boldsymbol{F}_{pe}\boldsymbol{F}_{pi}$ is presented (see Dettmer and Reese [2004]), which is physically motivated (Lion [2000]). These decompositions result in the intermediate plastic configuration ic_{1a} and the so-called intermediate configuration of kinematic hardening ic_{1b}, depicted in Figure 3.6. For the viscous model the deformation gradient is decomposed into elastic and inelastic parts, $\boldsymbol{F} = \boldsymbol{F}_{e2}\boldsymbol{F}_i$, and the additional inelastic intermediate configuration ic_2 is introduced, in line with the work of e.g. Sidoroff [1974], Lubliner [1985], and Reese and Govindjee [1998*b*].

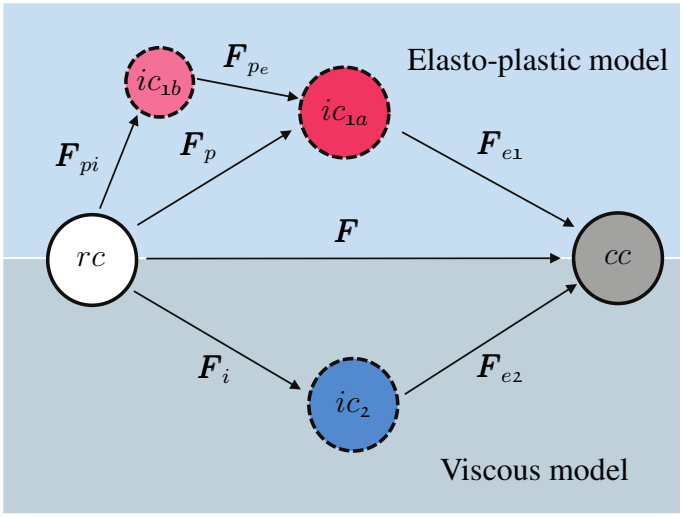

Figure 3.6: Multiplicative splits of the deformation gradient.

3.4.2 Helmholtz free energy

Concomitant with the preceding assumptions of two decoupled processes (I. Supercooling of the polymer melt and II. Thermo-mechanical behavior of solidified polymer) the total specific Helmholtz free energy is considered separately in an analogous fashion:

$$\text{I.} \quad \psi = \psi_\chi(\chi, \theta) + \psi_c(\theta) \tag{3.4}$$

$$\begin{aligned} \text{II.} \quad & \psi = \psi_1(\boldsymbol{C}_{e1}, \boldsymbol{C}_{pe}, \kappa, \chi, \theta) + \psi_2(\boldsymbol{C}_{e2}, \chi, \theta) + \psi_c(\theta), \\ & \text{with } \psi_1 = \psi_{e1}(\boldsymbol{C}_{e1}, \chi, \theta) + \psi_{kin}(\boldsymbol{C}_{pe}, \chi, \theta) + \psi_{iso}(\kappa, \chi, \theta) \end{aligned} \tag{3.5}$$

Here the specific free energy of crystallization, or chemical potential, is denoted by ψ_χ. In line with the fundamental thermodynamic considerations of Turnbull and Fisher [1949] and Mandelkern et al. [1954], phase transformation is initiated as soon as the corresponding free energy becomes negative. The specific form of this energy is discussed in Section 3.4.7. Furthermore, ψ_c is a caloric contribution related to the temperature-dependent specific heat of the material.

The free Helmholtz energy associated with the solidified polymer is additively decomposed into the contribution of the intermolecular ψ_1 and network resistance ψ_2 (see Figure 3.5). Here, ψ_{e1} represents an energy associated with intermolecular reactions and ψ_{kin} corresponds to a defect-energy associated with plastic deformations and allows to phenomenologically account for the Bauschinger-like phenomena. With increasing plastic deformations, an increasing resistance to plastic flow arises, due to the limited chain extensibility between entanglements and frictional interaction between the pendant side-groups (cf. Srivastava et al. [2010]). The stored

energy related to this phenomena is denoted by ψ_{iso}, which is a function of the accumulated plastic strain κ and allows to phenomenologically account for isotropic hardening.

To incorporate the influence of the temperature and the morphology of the microstructure on the material response, the energy contributions associated with the solidified polymer are functions of the temperature θ and total degree of crystallinity χ. The intermolecular resistance is assumed to increase for a higher degree of crystallinity, resulting in an increase of stiffness, hardening and yield stress, whereas all energy contributions decrease with an increase of temperature (cf. Section 3.3).

Based on the principle of material frame invariance, the Helmholtz free energy depends on the deformation only through the elastic right Cauchy-Green deformation tensors

$$\boldsymbol{C}_{e1} = \boldsymbol{F}_{e1}^T \boldsymbol{F}_{e1} = \boldsymbol{F}_p^{-T} \boldsymbol{C} \boldsymbol{F}_p^{-1} \tag{3.6}$$

$$\boldsymbol{C}_{pe} = \boldsymbol{F}_{pe}^T \boldsymbol{F}_{pe} = \boldsymbol{F}_{pi}^{-T} \boldsymbol{C}_p \boldsymbol{F}_{pi}^{-1} \tag{3.7}$$

$$\boldsymbol{C}_{e2} = \boldsymbol{F}_{e2}^T \boldsymbol{F}_{e2} = \boldsymbol{F}_i^{-T} \boldsymbol{C} \boldsymbol{F}_i^{-1} \tag{3.8}$$

where $\boldsymbol{C} = \boldsymbol{F}^T \boldsymbol{F}$ is the right Cauchy-Green tensor, $\boldsymbol{C}_p = \boldsymbol{F}_p^T \boldsymbol{F}_p$ the plastic right Cauchy-Green tensor and ψ_{e1}, ψ_{e2}, and ψ_{kin} are isotropic functions of $\boldsymbol{C}_{e1}$, $\boldsymbol{C}_{e2}$, and $\boldsymbol{C}_{pe}$, respectively.

3.4.3 Derivation based on the Clausius-Duhem inequality

In order to derive the constitutive equations in a thermodynamically consistent manner the Clausius-Duhem form of the entropy inequalities w.r.t. the reference configuration

$$\text{I} \quad -\rho_0(\dot{\psi} + \eta\dot{\theta}) - \frac{1}{\theta}\,\boldsymbol{q}_0 \cdot \text{Grad}(\theta) \geq 0 \tag{3.9}$$

$$\text{II} \quad \boldsymbol{S} : \frac{1}{2}\dot{\boldsymbol{C}} - \rho_0(\dot{\psi} + \eta\dot{\theta}) - \frac{1}{\theta}\,\boldsymbol{q}_0 \cdot \text{Grad}(\theta) \geq 0 \tag{3.10}$$

are evaluated separately for both considered processes. In the inequalities, the specific entropy is defined as η. The density and the heat flux w.r.t. the reference configuration are denoted with ρ_0 and $\boldsymbol{q}_0$, respectively. Furthermore, $\boldsymbol{S}$ is the second Piola-Kirchhoff stress. Differentiating the Helmholtz free energy (3.4) and (3.5) with respect to time and inserting it into (3.9) and

(3.10), respectively, yields

$$\begin{aligned}
\text{I} \quad & -\frac{1}{\theta}\,\boldsymbol{q}_0 \cdot \text{Grad}(\theta) - \rho_0 \left(\frac{\partial \psi}{\partial \theta} + \eta\right) \dot{\theta} - \rho_0 \,\frac{\partial \psi}{\partial \chi}\,\dot{\chi} \geq 0 \\
\text{II} \quad & \boldsymbol{S} : \frac{1}{2}\dot{\boldsymbol{C}} - \frac{1}{\theta}\,\boldsymbol{q}_0 \cdot \text{Grad}(\theta) - \rho_0 \left(\frac{\partial \psi}{\partial \theta} + \eta\right) \dot{\theta} \\
& - \rho_0 \left(\frac{\partial \psi}{\partial \boldsymbol{C}_{e1}} : \dot{\boldsymbol{C}}_{e1} + \frac{\partial \psi}{\partial \boldsymbol{C}_{pe}} : \dot{\boldsymbol{C}}_{pe} + \frac{\partial \psi}{\partial \kappa}\,\dot{\kappa} + \frac{\partial \psi}{\partial \boldsymbol{C}_{e2}} : \dot{\boldsymbol{C}}_{e2}\right) \geq 0
\end{aligned} \tag{3.11}$$

To reformulate the Clausius-Duhem inequality associated with the thermo-mechanically coupled process II, several stress quantities are introduced, in line with the works of e.g. Reese and Govindjee [1998*b*] and Vladimirov et al. [2008]. The second Piola-Kirchhoff stress tensor $\boldsymbol{S}_1$ and Mandel stress tensor $\boldsymbol{M}_1$ corresponding to the elasto-plastic model

$$\boldsymbol{S}_1 = 2\,\rho_0\,\boldsymbol{F}_p^{-1} \frac{\partial \psi_{e1}}{\partial \boldsymbol{C}_{e1}} \boldsymbol{F}_p^{-T}, \quad \boldsymbol{M}_1 = 2\,\rho_0\,\boldsymbol{C}_{e1} \frac{\partial \psi_{e1}}{\partial \boldsymbol{C}_{e1}} \tag{3.12}$$

are formulated w.r.t. the reference configuration and the plastic intermediate configuration ic_{1a}, respectively. Similarly,

$$\boldsymbol{S}_2 = 2\,\rho_0\,\boldsymbol{F}_i^{-1} \frac{\partial \psi_2}{\partial \boldsymbol{C}_{e2}} \boldsymbol{F}_i^{-T}, \quad \boldsymbol{M}_2 = 2\,\rho_0\,\boldsymbol{C}_{e2} \frac{\partial \psi_2}{\partial \boldsymbol{C}_{e2}} \tag{3.13}$$

are the second Piola-Kirchhoff stress tensor and Mandel stress tensor corresponding to the molecular network resistance, which are defined w.r.t. the reference and the inelastic intermediate state ic_2, respectively. In addition, the back stress $\boldsymbol{X}$ in the intermediate state ic_{1a}, the Mandel stress corresponding to kinematic hardening $\boldsymbol{M}_{kin}$ w.r.t. the intermediate configuration ic_{1b}, and the stress-like driving force of isotropic hardening R are defined as

$$\boldsymbol{X} = 2\,\rho_0\,\boldsymbol{F}_{pe} \frac{\partial \psi_{kin}}{\partial \boldsymbol{C}_{pe}} \boldsymbol{F}_{pe}^T, \quad \boldsymbol{M}_{kin} = 2\,\rho_0\,\boldsymbol{C}_{pe} \frac{\partial \psi_{kin}}{\partial \boldsymbol{C}_{pe}}, \quad R = -\rho_0\,\frac{\partial \psi_{iso}}{\partial \kappa} \tag{3.14}$$

After several mathematical transformations, the final forms of the Clausius-Duhem inequalities

$$\text{I} \quad -\frac{1}{\theta}\,\boldsymbol{q}_0 \cdot \text{Grad}(\theta) - \rho_0 \left(\frac{\partial \psi}{\partial \theta} + \eta\right) \dot{\theta} - \rho_0 \,\frac{\partial \psi}{\partial \chi}\,\dot{\chi} \geq 0 \tag{3.15}$$

$$\begin{aligned}
\text{II} \quad & (\boldsymbol{S} - \boldsymbol{S}_1 - \boldsymbol{S}_2) : \frac{1}{2}\dot{\boldsymbol{C}} - \frac{1}{\theta}\,\boldsymbol{q}_0 \cdot \text{Grad}(\theta) - \rho_0 \left(\frac{\partial \psi}{\partial \theta} + \eta\right) \dot{\theta} \\
& + \boldsymbol{M}_2 : \boldsymbol{D}_i + (\boldsymbol{M}_1 - \boldsymbol{X}) : \boldsymbol{D}_p + \boldsymbol{M}_{kin} : \boldsymbol{D}_{pi} + R\,\dot{\kappa} \geq 0
\end{aligned} \tag{3.16}$$

are derived, where $\boldsymbol{D}_{(*)} = \mathrm{sym}(\boldsymbol{L}_{(*)})$ denotes the symmetric part of the corresponding velocity gradient $\boldsymbol{L}_{(*)} = \dot{\boldsymbol{F}}_{(*)}\boldsymbol{F}_{(*)}^{-1}$, with $(*) = i, p, pi$. The above inequalities need to be fulfilled for arbitrary processes. By the standard arguments of Coleman and Noll [1961], the following relations for the total second Piola-Kirchhoff stress and entropy are given

$$\boldsymbol{S} = \boldsymbol{S}_1 + \boldsymbol{S}_2, \qquad \eta = -\frac{\partial \psi}{\partial \theta} \tag{3.17}$$

Both, the latter definition for the specific entropy and Fourier's law for the heat flux in isotropic materials

$$\boldsymbol{q}_0 = -J\, \lambda_T\, \boldsymbol{C}^{-1}\, \mathrm{Grad}(\theta) \tag{3.18}$$

w.r.t. the reference configuration, fulfill the thermodynamic restrictions for both processes I and II. In the expression above, $J = \det\boldsymbol{F}$ and $\lambda_T(\theta)$ denotes the temperature dependent heat conductivity.

3.4.4 Evolution Equations

To ensure the non-negativeness of the internal dissipation due to the recrystallization process from the melt (I) and caused by plastic and viscous effects (II), a set of evolution equations is presented, which fulfills the remaining parts of the inequalities (3.15) and (3.16).

3.4.4.1 Non-isothermal crystallization kinetics

In the current work, a non-isothermal representation of the well established isothermal Avrami equation (cf. Avrami [1939] and Avrami [1940]) is employed, to describe the crystallization process. As it is common practice, the validity of the Avrami approach was first examined by considering the classical double logarithmic form $\ln(-(\ln(1-\chi_c))$ of the experimentally determined relative degree of crystallinity $\chi_c(t)$ (cf. equation (3.2)). For all considered isothermal experiments, the plots of $\ln(-(\ln(1-\chi_c))$ over $\ln(t)$ yielded a straight line with slope n (see Appendix 3.10.2). Consequently, the applicability of the Avrami method for Polyamide 6 was confirmed, as already reported by e.g. Weng et al. [2003] and Sierra et al. [2006]. Noteworthy, n is referred to as the Avrami exponent and represents the nucleation mechanism and growth dimension, which is assumed to be temperature independent.

During supercooling of the melt, non-isothermal conditions arise in general and thus the isothermal Avrami equation is not valid to predict the relative degree of crystallinity χ_c. Among several works (Ozawa [1971], Jeziorny [1978], and Vázquez et al. [2000]), the non-

isothermal representation of the Avrami equation by means of the modified Nakamura-Ziabicki model (Nakamura et al. [1973]) was found to be the best suited model to capture the experimentally observed behavior for the considered Polyamide 6 (cf. chapter 3.7). Here, the model is represented by means of the evolution equation of the total degree of crystallinity

$$\dot{\chi} = n\, K_c\, (1 - \chi_c) \left(\int_{t_{on}}^{t} K_c\, dt \right)^{n-1} \frac{\Delta h_m}{\Delta h_f^{100}} \tag{3.19}$$

where non-isothermal conditions are taken into account, by integrating the temperature and cooling rate dependent crystal growth rate parameter K_c in time space. Consequently, $\dot{\chi}$ is a function of the temperature history. An empirical function for K_c, which is motivated by a Gaussian function

$$K_c = K_{max} \exp\left(-\frac{4 \ln(2)(\theta - \theta_{max})^2}{D^2} \right) \tag{3.20}$$

was proposed by Ziabicki [1976]. The Nakamura-Ziabicki crystallization parameters K_{max}, θ_{max} and D are in general dependent on the cooling rate $\dot{\theta}$ (Sierra et al. [2006]) and are governed from the non-isothermal DSC data, see Section 3.7.

Noteworthy, with this modified version of the Avrami theory, the influence of the pressure on the crystallization process is neglected, in line with the assumptions stated at the beginning of Section 3.4. For a more general but also more complex theory, the reader is referred to the work of e.g. Lion and Johlitz [2016], where the degree of crystallinity and the configuration of the amorphous phase are dependent on pressure and temperature. Furthermore, the impact of the degree of crystallinity on the shape of the glass-transition in DSC curves is not captured either. However, due the experimental data regarding the mechanical behavior of the material above and below the glass transition point (cf. Section 3.3), the identified set of mechanical parameters (see Section 3.7) accounts for the drastic change in the material properties during the glass transition.

3.4.4.2 Elasto-plastic model

In this work, neither tension-compression asymmetry nor pressure dependence is considered. A yield function of von Mises type

$$\Phi = ||\text{dev}(\boldsymbol{M}_1) - \text{dev}(\boldsymbol{X})|| - \sqrt{\frac{2}{3}}(\sigma_y - R) \tag{3.21}$$

is assumed, where dev$(*)$ denotes the deviatoric part of a quantity (i.e. dev$(\boldsymbol{A}) := \boldsymbol{A} - \frac{1}{3}\,\text{tr}(\boldsymbol{A})\boldsymbol{I}$ for $\boldsymbol{A}$ being a second-order tensor). The initial yield stress $\sigma_y(\theta, \chi)$ is in general

a function of the total degree of crystallinity and temperature and is provided in chapter 3.7. The plastic flow rule and the evolution equations for kinematic and isotropic hardening are

$$\boldsymbol{D}_p = \dot{\gamma}\,\frac{\partial \Phi}{\partial \boldsymbol{M}_1} = \dot{\gamma}\,\frac{\mathrm{dev}(\boldsymbol{M}_1) - \mathrm{dev}(\boldsymbol{X})}{||\mathrm{dev}(\boldsymbol{M}_1) - \mathrm{dev}(\boldsymbol{X})||} \tag{3.22}$$

$$\boldsymbol{D}_{pi} = \dot{\gamma}\,\frac{b}{c}\,\mathrm{dev}(\boldsymbol{M}_{kin}) \tag{3.23}$$

$$\dot{\kappa} = \dot{\gamma}\,\frac{\partial \Phi}{\partial R} = \sqrt{\frac{2}{3}}\dot{\gamma} \tag{3.24}$$

respectively (see Dettmer and Reese [2004] and Vladimirov et al. [2008]). The constants b and c are related to kinematic hardening in accordance with Armstrong and Frederick [1966]. In equation (3.22) - (3.24), $\dot{\gamma}$ represents the plastic multiplier and the usual Kuhn-Tucker conditions $\Phi \leq 0$, $\dot{\gamma} \geq 0$, and $\Phi\,\dot{\gamma} = 0$ complete the set of constitutive equations of the elasto-plastic model.

3.4.4.3 Viscous model

The evolution of the inelastic deformation within the network resistance is chosen in line with the work of Reese and Govindjee [1998*b*] and is given with respect to the inelastic intermediate configuration ic_2

$$\boldsymbol{D}_i = \frac{1}{2\tau\mu_2}\,\mathrm{dev}\,(\boldsymbol{M}_2) + \frac{1}{9\tau K_2}\,\mathrm{tr}\,(\boldsymbol{M}_2)\,\boldsymbol{I} \tag{3.25}$$

Here the bulk modulus $K_2(\theta)$ and shear modulus $\mu_2(\theta)$ corresponding to the molecular network resistance are introduced. The relaxation time $\tau(\boldsymbol{S}_2, \boldsymbol{C}, \theta, \chi)$ must be larger than zero and is in general a function of the overstress $\boldsymbol{S}_2$, the deformation, the temperature, and the degree of crystallinity. The explicit function is given in chapter 3.7. Noteworthy, this evolution equation is valid for large deformations and large perturbations away from thermodynamic equilibrium.

3.4.5 Thermodynamic consistency

It remains to show, that the chosen evolution equations fulfill in fact the inequalities (3.15) and (3.16). The inequality (3.15) reduces for the governed relations for the entropy (3.17) and heat flux (3.18) to $-\rho_0(\partial\psi_\chi/\partial\chi)\dot{\chi} \geq 0$. Since $\dot{\chi} \geq 0$ and the derivative of the energy term associated with transformation ψ_χ (cf. equation (3.26)) with respect to χ is negative, if $\theta < \theta_{on}$ (see Section 3.4.7), the remaining inequality is non-negative.

For the proof regarding the thermodynamic consistency of the the chosen evolution equa-

tions, corresponding to the elasto-plastic model, the reader is referred to Vladimirov et al. [2008]. Furthermore, the thermodynamic consistency of the evolution equation of the inelastic deformation can be shown in a straight forward way (cf. Reese and Govindjee [1998*b*]) and will not be further discussed here.

3.4.6 Representation in the reference configuration

For convenience the derivation of the material model was carried out in the intermediate configurations. For the numerical implementation, however, the constitutive framework is represented in the reference configuration. To this end, the tensorial pull back operation of the associated stress quantities $\boldsymbol{M}_1$, $\boldsymbol{M}_2$, $\boldsymbol{X}$, and $\boldsymbol{M}_{kin}$ as well as the relations $\dot{\boldsymbol{C}}_p = 2\,\boldsymbol{F}_p^T \boldsymbol{D}_p \boldsymbol{F}_p$ and $\dot{\boldsymbol{C}}_i = 2\,\boldsymbol{F}_i^T \boldsymbol{D}_i \boldsymbol{F}_i$ are applied, to obtain the alternative model representation, which is summarized in Table 3.1. Here, the back stress tensor in the reference configuration $\tilde{\boldsymbol{X}}$ and the stress-like quantities $\boldsymbol{Y}$ and $\boldsymbol{Y}_{kin}$ are introduced (cf. Vladimirov et al. [2008]). Noteworthy, $\boldsymbol{Y}$ and $\boldsymbol{Y}_{kin}$ are asymmetric tensors. The presented model includes only symmetric tensor-valued internal variables, i.e. $\boldsymbol{C}_p$, $\boldsymbol{C}_{pi}$, and $\boldsymbol{C}_i$, which is important from a computational point of view. The plastic and inelastic spins as well as the corresponding deformation gradients remain undetermined.

Table 3.1: Constitutive equations in reference configuration

Intermolecular resistance	**Molecular network resistance**
Stresses $\boldsymbol{S}_1 = 2\,\rho_0\,\boldsymbol{F}_p^{-1}\dfrac{\partial \psi_{e1}}{\partial \boldsymbol{C}_{e1}}\boldsymbol{F}_p^{-T}$, $\tilde{\boldsymbol{X}} = 2\,\rho_0\,\boldsymbol{F}_{pi}^{-1}\dfrac{\partial \psi_{kin}}{\partial \boldsymbol{C}_{pe}}\boldsymbol{F}_{pi}^{-T}$, $R = -\rho_0\,\dfrac{\partial \psi_{iso}}{\partial \kappa}$, $\boldsymbol{Y} = \boldsymbol{C}\boldsymbol{S}_1 - \boldsymbol{C}_p\tilde{\boldsymbol{X}}, \quad \boldsymbol{Y}_{kin} = \boldsymbol{C}_p\tilde{\boldsymbol{X}}$	Stress $\boldsymbol{S}_2 = 2\,\rho_0\,\boldsymbol{F}_i^{-1}\dfrac{\partial \psi_{e2}}{\partial \boldsymbol{C}_{e2}}\boldsymbol{F}_i^{-T}$
Evolution equations $\dot{\boldsymbol{C}}_p = 2\,\dot{\gamma}\,\dfrac{\mathrm{dev}(\boldsymbol{Y})\boldsymbol{C}_p}{\sqrt{\mathrm{dev}(\boldsymbol{Y}) : \mathrm{dev}(\boldsymbol{Y})^T}}$, $\dot{\boldsymbol{C}}_{pi} = 2\,\dot{\gamma}\,\dfrac{b}{c}\,\mathrm{dev}(\boldsymbol{Y}_{kin})\boldsymbol{C}_{pi}, \quad \dot{\kappa} = \sqrt{\dfrac{2}{3}}\,\dot{\gamma}$	Evolution equation $\dot{\boldsymbol{C}}_i = \left(\dfrac{1}{\tau\mu_2}\,\mathrm{dev}(\boldsymbol{C}\boldsymbol{S}_2) + \dfrac{2}{9\tau K_2}\,\mathrm{tr}\,(\boldsymbol{C}\boldsymbol{S}_2)\boldsymbol{I}\right)\boldsymbol{C}_i$
Yield function $\Phi = \sqrt{\mathrm{dev}(\boldsymbol{Y}) : \mathrm{dev}(\boldsymbol{Y})^T} - \sqrt{\dfrac{2}{3}}(\sigma_y - R)$	

3.4.7 Specific choices for free Helmholtz energy terms

3.4.7.1 Free energy of crystallization

The free energy associated with crystallization, or chemical potential

$$\psi_\chi = \Delta h_f^{100} \frac{\theta - \theta_{on}}{\theta_{on}} \chi \tag{3.26}$$

is chosen in line with the proposed function of Kelly et al. [2016] in the context of martensitic phase transformation. It determines the relative stability of the amorphous and crystalline phases. During the supercooling of the polymer melt, the crystallization process starts below the cooling rate dependent onset temperature θ_{on}. Consequently, phase transformation is initiated as soon as the corresponding free energy becomes negative, in line with the fundamental thermodynamic considerations of Turnbull and Fisher [1949] and Mandelkern et al. [1954]. Noteworthy, with this particular form, the non-negativeness of the remaining Clausius-Duhem inequality (3.15) is guaranteed, as alluded above. Furthermore, ψ_χ contributes in an important manner to the heat release due to crystallization in the balance of energy (cf. chapter 3.5).

3.4.7.2 Free energy of intermolecular resistance

Up to now, the relations for the thermodynamic driving forces are derived in a completely general manner. In this way, the proposed framework offers large flexibility regarding the particular choices of the energy terms. To conclude the constitutive framework, a set of energy terms per volume Ψ is specified in the following.

The energy contributions associated with the intermolecular resistance belong to a Neo-Hookean material with combined nonlinear isotropic hardening and nonlinear kinematic hardening of Armstrong-Frederick type. In addition, an elastic thermal expansion term is included.

$$\begin{aligned} \Psi_{e1} =& \frac{\mu_1}{2} \left(\text{tr}(\boldsymbol{C}_{e1}) - 3\right) - \mu_1 \ln(J_{e1}) + \frac{\Lambda_1}{4} \left(\det(\boldsymbol{C}_{e1}) - 1 - 2\ln(J_{e1})\right) \\ & - 3\, K_1\, \alpha_{T1} (\theta - \theta_0) \ln(J_{e1}) \end{aligned} \tag{3.27}$$

$$\Psi_{kin} = \frac{c}{2} \left(\text{tr}(\boldsymbol{C}_{pe}) - 3\right) - c\, \ln(J_{pe}) \tag{3.28}$$

$$\Psi_{iso} = (\sigma_\infty - \sigma_y) \left(\kappa + \frac{\exp(-\beta\, \kappa)}{\beta}\right) + \frac{1}{2}\, H\, \kappa^2 \tag{3.29}$$

Here, $J_{e1} = \det \boldsymbol{F}_{e1}$ and $J_{pe} = \det \boldsymbol{F}_{pe}$ holds. The material parameters $\mu_1(\theta, \chi)$, $\Lambda_1(\theta, \chi)$, $K_1(\theta, \chi)$, $\alpha_{T1}(\theta, \chi)$, $\sigma_\infty(\theta, \chi)$, $\beta(\theta, \chi)$ and $H(\theta, \chi)$ corresponding to the elasto-plastic model are the Lamé constants, bulk modulus, coefficient of thermal expansion and isotropic harden-

ing parameters, respectively, and θ_0 is a reference temperature. Note, that all parameters are assumed to be functions of the temperature and total degree of crystallinity and are provided in chapter 3.7. Finally, $\boldsymbol{S}_1$, $\tilde{\boldsymbol{X}}$ and R can be derived accordingly

$$\boldsymbol{S}_1 = \mu_1 \left(\boldsymbol{C}_p^{-1} - \boldsymbol{C}^{-1}\right) + \frac{\Lambda_1}{2}\left(\frac{\det(\boldsymbol{C})}{\det(\boldsymbol{C}_p)} - 1\right)\boldsymbol{C}^{-1} - 3\,K_1\,\alpha_{T1}\,(\theta - \theta_0)\,\boldsymbol{C}^{-1} \tag{3.30}$$

$$\tilde{\boldsymbol{X}} = c\,\left(\boldsymbol{C}_{pi}^{-1} - \boldsymbol{C}_p^{-1}\right) \tag{3.31}$$

$$R = -(\sigma_\infty - \sigma_y)\,(1 - \exp(-\beta\,\kappa)) - H\,\kappa \tag{3.32}$$

3.4.7.3 Free energy of molecular network resistance

For the elastic energy associated with the molecular network resistance a compressible version of the widely used model of (Arruda and Boyce [1993])

$$\begin{aligned}
\Psi_2 &= \Psi_{vol}(J_{e2}, \theta, \chi) + \Psi_{iso}(\bar{\boldsymbol{C}}_{e2}, \theta) \\
\Psi_{vol} &= K_2\left(\frac{J_{e2}^2 - 1}{4} - \ln(J_{e2})\left(\frac{1}{2} + 3\,\alpha_{T2}(\theta - \theta_0)\right)\right) \\
\Psi_{iso} &= \mu^* \sum_{i=1}^{5} \frac{C_i}{\lambda_m^{2i-2}}\left(\mathrm{tr}(\bar{\boldsymbol{C}}_{e2})^i - 3^i\right)
\end{aligned} \tag{3.33}$$

is chosen. In the latter expression, the volumetric energy Ψ_{vol}, originally proposed by Kaliske and Rothert [1997] is modified by a contribution associated with thermal expansion suggested by e.g. Reese and Govindjee [1998*a*]. The isochoric energy part Ψ_{iso} is a function of the isochoric (volume preserving) part $\bar{\boldsymbol{C}}_{e2} = \bar{\boldsymbol{F}}_{e2}^T \bar{\boldsymbol{F}}_{e2}$ of the elastic right Cauchy-Green tensor, where $\bar{\boldsymbol{F}}_{e2} = J_{e2}^{-\frac{1}{3}} \boldsymbol{F}_{e2}$ (originally suggested by Flory [1961]) and $J_{e2} = \det \boldsymbol{F}_{e2} = \sqrt{\det \boldsymbol{C}_{e2}}$ holds. The constant parameter λ_m relates to the locking stretch of a fully extended chain, $\alpha_{T2}(\theta, \chi)$ is the coefficient of thermal expansion corresponding to the network resistance and θ_0 is a reference temperature. In line with Arruda and Boyce [1993], the parameter μ^* and the tuple C_i are defined as

$$\mu^* = \mu_2\left(1 + \frac{3}{5\lambda_m^2} + \frac{99}{175\lambda_m^4} + \frac{513}{875\lambda_m^6} + \frac{42039}{67375\lambda_m^8}\right)^{-1} \tag{3.34}$$

$$C_i = \left(\tfrac{1}{2} \quad \tfrac{1}{20} \quad \tfrac{11}{1050} \quad \tfrac{19}{7000} \quad \tfrac{519}{67375}\right) \tag{3.35}$$

Based on the decoupled strain energy function the second Piola-Kirchhoff stress $\boldsymbol{S}_2$, corresponding to the molecular network resistance is calculated by

$$\begin{aligned}\boldsymbol{S}_2 = K_2 \left(\frac{1}{2} \left(J_{e2}^2 - 1 \right) - 3\, \alpha_{T2} (\theta - \theta_0) \right) \boldsymbol{C}^{-1} \\ + \operatorname{dev} \left(2\mu^* \sum_{i=1}^{5} \frac{i\, C_i}{\lambda_m^{2i-2}} \operatorname{tr}(\bar{\boldsymbol{C}}_{e2})^{i-1}\, J_{e2}^{-\frac{2}{3}}\, \boldsymbol{I} \right)\end{aligned} \tag{3.36}$$

3.5 Energy balance

Viscous and plastic effects are always accompanied by a loss of the potential energy. This energy causes heat generation due to dissipation. Furthermore, the release of the heat of fusion during crystallization must be accounted for. In order to derive the heat generation terms, the local form of the energy balance with respect to the reference configuration is considered. Concomitant with the previous assumptions the energy balance is treated separately for both considered processes (I. Supercooling of the polymer melt and II. Thermo-mechanical behavior of solidified polymer)

$$\text{I} \quad \rho_0 (\underbrace{\dot{\psi} + \dot{\eta}\, \theta + \eta\, \dot{\theta}}_{\dot{e}}) + \operatorname{Div}(\boldsymbol{q}_0) = 0 \tag{3.37}$$

$$\text{II} \quad \rho_0 (\underbrace{\dot{\psi} + \dot{\eta}\, \theta + \eta\, \dot{\theta}}_{\dot{e}}) + \operatorname{Div}(\boldsymbol{q}_0) - \boldsymbol{S} : \frac{1}{2} \dot{\boldsymbol{C}} = 0 \tag{3.38}$$

Here, the differentiation of the specific internal energy, $e := \psi + \eta\, \theta$, with respect to time $\dot{e}$ is already included. The total time derivative of the Helmholtz free energy (3.4 and 3.5) is inserted in the above expression and equation (3.17) is recalled to formulated the specific entropy time derivative $\dot{\eta} = -\partial \dot{\psi} / \partial \theta$. Subsequently, utilizing the mathematical operations, introduced in Section 3.4.3, in an analogous fashion, it is possible to establish the partial

differential equation for the temperature field with all dissipative terms.

$$\text{I} \quad \rho_0\, c_t\, \dot{\theta} = \rho_0 \left(-\frac{\partial \psi}{\partial \chi} + \frac{\partial^2 \psi}{\partial \chi \partial \theta} \right) \dot{\chi} - \text{Div}(\boldsymbol{q}_0) \tag{3.39}$$

$$\begin{aligned} \text{II} \quad \rho_0\, c_t\, \dot{\theta} = {} & \theta\, \frac{\partial \boldsymbol{S}}{\partial \theta} : \frac{1}{2} \dot{\boldsymbol{C}} + \left(\boldsymbol{M}_2 - \theta\, \frac{\partial \boldsymbol{M}_2}{\partial \theta} \right) : \boldsymbol{D}_i + \left(\boldsymbol{M}_1 - \theta\, \frac{\partial \boldsymbol{M}_1}{\partial \theta} \right) : \boldsymbol{D}_p \\ & - \left(\boldsymbol{X} - \theta\, \frac{\partial \boldsymbol{X}}{\partial \theta} \right) : \boldsymbol{D}_p + \left(\boldsymbol{M}_{kin} - \theta\, \frac{\partial \boldsymbol{M}_{kin}}{\partial \theta} \right) : \boldsymbol{D}_{pi} \\ & + \left(R - \theta\, \frac{\partial R}{\partial \theta} \right) \dot{\kappa} - \text{Div}(\boldsymbol{q}_0) \end{aligned} \tag{3.40}$$

Here, the specific heat capacity $c_T := -\theta\, \partial^2 \psi / \partial \theta^2$ is defined equivalently for both processes. In theory, $c_T = c_T(\chi, \boldsymbol{C}_{e1}, \boldsymbol{C}_{e2}, \boldsymbol{C}_{pe}, \kappa, \theta)$ is a complex function of all internal variables. In order to derive a reasonably general constitutive framework and to imply additional flexibility regarding the nonlinear temperature dependence of the specific heat (cf. e.g. Wunderlich [1960] and Biroli and Garrahan [2013]), a caloric part ψ_c was added to the specific energies (3.4) and (3.5). If these parts were not considered, the specific heat would be already completely defined (via $c_T := -\theta\, \partial^2 \psi / \partial \theta^2$), since the material parameters corresponding to the remaining energy contributions are identified based on the thermo-mechanical response of the material (cf. Section 3.7). In some special cases, for example in the constitutive theory developed by Lion et al. [2017], suitable terms for ψ_c are chosen and the specific heat can be evaluated in closed form. However, in general, much work needs to be done to experimentally characterize these functions. Consequently, in this work, the heat capacity is approximated to depend only on the temperature and degree of crystallinity $c_T \approx c_T(\chi, \theta)$ and the influence of the pressure is neglected, in line with e.g. Ames et al. [2009] and Engel et al. [2013]. Furthermore, the dissipation due to thermo-elastic coupling $\theta(\partial \boldsymbol{S} / \partial \theta) : (1/2\, \dot{\boldsymbol{C}})$ is assumed to be negligibly small and will be omitted (Anand et al. [2009] and Ames et al. [2009]).

With the specific relation for ψ_χ at hand (cf. equation (3.26)), expression (3.39) is reformulated

$$\begin{aligned} \text{I} \quad \rho_0\, c_t\, \dot{\theta} = {} & - \text{Div}(\boldsymbol{q}_0) + r_\chi \\ r_\chi = {} & \rho_0 \left(-\frac{\partial \psi_\chi}{\partial \chi} + \theta\, \frac{\partial^2 \psi_\chi}{\partial \chi\, \partial \theta} \right) \dot{\chi} = \rho_0\, \Delta h_f^{100}\, \dot{\chi} \end{aligned} \tag{3.41}$$

by means of the explicit function of the heat release during crystallization r_χ. Noteworthy, r_χ corresponds indeed to the heat generated by phase change per unit time and reference volume, obtained in conventional DSC experiments $r_\chi = \rho_0\, \Delta h_f^{100}\, \dot{\chi} = \rho_0 \dot{h}$ (cf. equations (3.2) and (3.3)) and is in line with the works of e.g. Zinet et al. [2010] and Kugele et al. [2017].

Table 3.2: Summary of the constitutive equations

Crystallization kinetics

Evolution equation

$$\dot{\chi} = n\, K_c\, (1-\chi_c) \left(\int_{t_{on}}^{t} K_c\, dt \right)^{n-1} \frac{\Delta h_m}{\Delta h_f^{100}}$$

Heat of fusion

$$r_\chi = \rho_0\, \Delta h_f^{100}\, \dot{\chi}$$

Intermolecular resistance

Stresses

$$\boldsymbol{S}_1 = \mu_1 \left(\boldsymbol{C}_p^{-1} - \boldsymbol{C}^{-1} \right) + \frac{\Lambda_1}{2} \left(\frac{\det(\boldsymbol{C})}{\det(\boldsymbol{C}_p)} - 1 \right) \boldsymbol{C}^{-1} - 3\, K_1\, \alpha_{T1}\, (\theta - \theta_0)\, \boldsymbol{C}^{-1},$$

$$\tilde{\boldsymbol{X}} = c \left(\boldsymbol{C}_{pi}^{-1} - \boldsymbol{C}_p^{-1} \right),$$

$$\boldsymbol{Y} = \boldsymbol{C}\boldsymbol{S}_1 - \boldsymbol{C}_p \tilde{\boldsymbol{X}}, \quad \boldsymbol{Y}_{kin} = \boldsymbol{C}_p \tilde{\boldsymbol{X}},$$

$$R = -\left(\sigma_\infty - \sigma_y\right) \left(1 - \exp(-\beta\, \kappa)\right) - H\, \kappa$$

Evolution equations

$$\dot{\boldsymbol{C}}_p = 2\, \dot{\gamma} \frac{\mathrm{dev}(\boldsymbol{Y})\, \boldsymbol{C}_p}{\sqrt{\mathrm{dev}(\boldsymbol{Y}) : \mathrm{dev}(\boldsymbol{Y})^T}},$$

$$\dot{\boldsymbol{C}}_{pi} = 2\, \dot{\gamma}\, \frac{b}{c}\, \mathrm{dev}(\boldsymbol{Y}_{kin})\, \boldsymbol{C}_{pi}, \quad \dot{\kappa} = \sqrt{\frac{2}{3}}\, \dot{\gamma}$$

Yield function

$$\Phi = \sqrt{\mathrm{dev}(\boldsymbol{Y}) : \mathrm{dev}(\boldsymbol{Y})^T} - \sqrt{\frac{2}{3}} (\sigma_y - R)$$

Heat generation due to plastic dissipation

$$r_1 = \frac{1}{2}\, \boldsymbol{C} \left(\boldsymbol{S}_1 - \theta\, \frac{\partial \boldsymbol{S}_1}{\partial \theta} \right) : \boldsymbol{C}_p^{-1} \dot{\boldsymbol{C}}_p - \frac{1}{2} \left(\tilde{\boldsymbol{X}} - \theta\, \frac{\partial \tilde{\boldsymbol{X}}}{\partial \theta} \right) : \dot{\boldsymbol{C}}_p + \frac{1}{2}\, \boldsymbol{C}_p \left(\tilde{\boldsymbol{X}} - \theta\, \frac{\partial \tilde{\boldsymbol{X}}}{\partial \theta} \right) : \boldsymbol{C}_{pi}^{-1} \dot{\boldsymbol{C}}_{pi} + \left(R - \theta\, \frac{\partial R}{\partial \theta} \right) \dot{\kappa}$$

Molecular network resistance

Stress

$$\boldsymbol{S}_2 = K_2 \left(\frac{1}{2} \left(J_{e2}^2 - 1 \right) - 3\, \alpha_{T2}\, (\theta - \theta_0) \right) \boldsymbol{C}^{-1} + \mathrm{dev} \left(2\, \mu^* \sum_{i=1}^{5} \frac{i\, C_i}{\lambda_m^{2i-2}}\, \mathrm{tr}\, (\bar{\boldsymbol{C}}_{e2})^{i-1}\, J_{e2}^{-\frac{2}{3}} \boldsymbol{I} \right)$$

Evolution equation

$$\dot{\boldsymbol{C}}_i = \left(\frac{1}{\tau\, \mu_2}\, \mathrm{dev}(\boldsymbol{C}\boldsymbol{S}_2) + \frac{2}{9\, \tau\, K_2}\, \mathrm{tr}\, (\boldsymbol{C}\boldsymbol{S}_2) \boldsymbol{I} \right) \boldsymbol{C}_i$$

Heat generation due to viscous dissipation

$$r_2 = \frac{1}{2}\, \boldsymbol{C} \left(\boldsymbol{S}_2 - \theta\, \frac{\partial \boldsymbol{S}_2}{\partial \theta} \right) : \boldsymbol{C}_i^{-1} \dot{\boldsymbol{C}}_i$$

Second Piola-Kirchhoff stress

$$\boldsymbol{S} = \boldsymbol{S}_1 + \boldsymbol{S}_2$$

Heat flux

$$\boldsymbol{q}_0 = -J\, \lambda_T\, \boldsymbol{C}^{-1}\, \mathrm{Grad}(\theta)$$

Analogous pull-pack operations, as introduced in Section 3.4.6, are carried out to relate all

stress quantities in equation (3.40) to the reference configuration

$$
\begin{aligned}
\text{II} \quad \rho_0\, c_t\, \dot{\theta} &= -\,\mathrm{Div}(\boldsymbol{q}_0) + r_1 + r_2 \\
r_1 &= \frac{1}{2}\,\boldsymbol{C}\left(\boldsymbol{S}_1 - \theta\,\frac{\partial \boldsymbol{S}_1}{\partial \theta}\right) : \boldsymbol{C}_p^{-1}\dot{\boldsymbol{C}}_p - \frac{1}{2}\left(\tilde{\boldsymbol{X}} - \theta\,\frac{\partial \tilde{\boldsymbol{X}}}{\partial \theta}\right) : \dot{\boldsymbol{C}}_p \\
&\quad + \frac{1}{2}\,\boldsymbol{C}_p\left(\tilde{\boldsymbol{X}} - \theta\,\frac{\partial \tilde{\boldsymbol{X}}}{\partial \theta}\right) : \boldsymbol{C}_{pi}^{-1}\dot{\boldsymbol{C}}_{pi} + \left(R - \theta\,\frac{\partial R}{\partial \theta}\right)\,\dot{\kappa} \\
r_2 &= \frac{1}{2}\,\boldsymbol{C}\left(\boldsymbol{S}_2 - \theta\,\frac{\partial \boldsymbol{S}_2}{\partial \theta}\right) : \boldsymbol{C}_i^{-1}\dot{\boldsymbol{C}}_i
\end{aligned}
\tag{3.42}
$$

where the heat generation due to plastic deformation, kinematic, and isotropic hardening is denoted by r_1 and the dissipation corresponding to viscous processes is defined as r_2.

For convenience, a summary of the proposed constitutive equations is given in Table 3.2.

3.6 Numerical implementation

The presented constitutive framework is implemented as a user material subroutine *UMAT* into the commercial FEM software *ABAQUS/Standard*. In the course of solving a fully thermo-mechanically coupled boundary value problem at finite strains, the routine is called at each Gaussian integration point. Thereby, the deformation gradient $\boldsymbol{F}$, the temperature θ, and the spatial temperature gradient grad(θ), as well as a vector containing all internal variables $\boldsymbol{\xi}_j$ of the last converged time step is passed to the subroutine. At the end of the time increment, the following set of quantities has to be defined within the *UMAT*:

- `STRESS`: Cauchy stress tensor $\boldsymbol{\sigma}$.
- `RPL`: Volumetric heat generation r_t cf. (3.51).
- `FLUX`: Spatial heat flux $\boldsymbol{q}_t = -\lambda_T \mathrm{grad}(\theta)$.
- `DDSDDE`: Material tangent modulus cf. (3.52).
- `DDSDDT`: Variation of the stress increments with respect to the temperature cf. (3.53).
- `DRPLDE`: Variation of heat sources (`RPL`) with respect to the strain increments cf. (3.55).
- `DRPLDT`: Variation of heat sources (`RPL`) with respect to the temperature cf. (3.54).

The algorithmic implementation will be summarized in the following Section, where quantities from the last converged time step are denoted by index j.

3.6.1 Algorithmic implementation

The evolution equation of the total degree of crystallinity (3.19) is discretized by means of the backward Euler method, which yields the following explicit relation for χ

$$\chi = \chi_j + \Delta t \; n \; K_c \underbrace{\exp\left(\left(-\int_{t_{on}}^{t} K_c \; dt\right)^n\right)}_{(1-\chi_c)} \left(\int_{t_{on}}^{t} K_c \; dt\right)^{n-1} \frac{\Delta h_m}{\Delta h_f^{100}} \tag{3.43}$$

The trapezoidal rule is used to numerically approximate the integrals

$$\int_{t_{on}}^{t} K_c(\theta) \; dt = \underbrace{\int_{t_{on}}^{t_j} K_c(\theta) \; dt}_{\mathcal{I}_j} + \int_{t_j}^{t} K_c(\theta) \; dt \approx \mathcal{I}_j + \sum_{i=2}^{N} \frac{K_c(\theta_i) + K_c(\theta_{i-1})}{2}(t_i - t_{i-1}) \tag{3.44}$$

In order to achieve a sufficiently accurate approximation of the integrals, the time step Δt is subdivided into N substeps and the temperature is linearly interpolated in between. The approximated solution of the integral of the last converged time step $\mathcal{I}_j$ is stored as an additional history variable. Furthermore, the beginning of crystallization has to be defined. Therefore, a regression curve for the onset temperature θ_{on} as a function of the cooling rate is derived from experimental data (see chapter 3.7). If the actual temperature at a Gaussian point is lower than the corresponding onset temperature, crystallization is triggered and t_{on} is determined. With the absolute degree of crystallinity and temperature at hand, the material parameters are updated (cf. Table 3.4) and the algorithm for solving the constitutive relations is initiated.

Based on the findings of Vladimirov et al. [2008] the exponential map algorithm is applied for the algorithmic treatment of the described constitutive model corresponding to the intermolecular resistance. The starting point is an alternative representation of the evolution

equations presented above (cf. Table 3.2):

$$\dot{\boldsymbol{C}}_p = \dot{\gamma}\, 2\, \underbrace{\frac{\mathrm{dev}(\boldsymbol{Y})\boldsymbol{C}_p}{\sqrt{\mathrm{dev}(\boldsymbol{Y}) : \mathrm{dev}(\boldsymbol{Y})^T}}}_{\boldsymbol{T}} = \dot{\gamma}\, \boldsymbol{T}(\boldsymbol{C}, \boldsymbol{C}_p, \boldsymbol{C}_{pi})\, \boldsymbol{C}_p^{-1}\, \boldsymbol{C}_p \tag{3.45}$$

$$\dot{\boldsymbol{C}}_{pi} = \dot{\gamma}\, \underbrace{2\, \frac{b}{c}\, \mathrm{dev}(\boldsymbol{Y}_{kin})\, \boldsymbol{C}_{pi}}_{\boldsymbol{T}_{kin}} = \dot{\gamma}\, \boldsymbol{T}_{kin}(\boldsymbol{C}, \boldsymbol{C}_p, \boldsymbol{C}_{pi})\, \boldsymbol{C}_{pi}^{-1}\, \boldsymbol{C}_{pi} \tag{3.46}$$

Since $\dot{\boldsymbol{C}}_p$ and $\dot{\boldsymbol{C}}_{pi}$ are symmetric, the tensor valued functions $\boldsymbol{T}$ and $\boldsymbol{T}_{kin}$ are symmetric as well. This does in general not hold for $\boldsymbol{T}\boldsymbol{C}_p^{-1}$ and $\boldsymbol{T}_{kin}\boldsymbol{C}_{pi}^{-1}$. Consequently, a direct use of the exponential map algorithm to solve the differential equations (3.45) and (3.46) would require a truncated series representation. To overcome this Reese and Christ [2008], Vladimirov et al. [2008], and Pietryga et al. [2012] utilized a modified ansatz originally proposed by Dettmer and Reese [2004]. To this end, equation (3.45) and (3.46) are multiplied from the right by $\boldsymbol{C}_{p,j}^{-1}\boldsymbol{C}_p$ and $\boldsymbol{C}_{pi,j}^{-1}\boldsymbol{C}_{pi}$, respectively and the series representation of the subsequently performed exponential mapping is exploited. This leads to the final form of the discretized evolution equations, here summarized in a residuum format, which need to be solved together with the yield function.

$$\boldsymbol{r}_1 = -\left(\boldsymbol{U}_{p,j}\, \boldsymbol{U}_{p,j}\right)^{-1} + \boldsymbol{U}_p^{-1} \exp\left(\Delta\gamma\, \boldsymbol{U}_p^{-1}\, \boldsymbol{T}\, \boldsymbol{U}_p^{-1}\right) \boldsymbol{U}_p^{-1} = \boldsymbol{0} \tag{3.47}$$

$$\boldsymbol{r}_2 = -\left(\boldsymbol{U}_{pi,j}\, \boldsymbol{U}_{pi,j}\right)^{-1} + \boldsymbol{U}_{pi}^{-1} \exp\left(\Delta\gamma\, \boldsymbol{U}_{pi}^{-1}\, \boldsymbol{T}_{kin}\, \boldsymbol{U}_{pi}^{-1}\right) \boldsymbol{U}_{pi}^{-1} = \boldsymbol{0} \tag{3.48}$$

$$r_3 = \Phi = \sqrt{\mathrm{dev}(\boldsymbol{Y}) : \mathrm{dev}(\boldsymbol{Y})^T} - \sqrt{\frac{2}{3}}\left(\sigma_y - R\left(\kappa\right)\right) = 0 \tag{3.49}$$

Here, the relations $\Delta\gamma = \Delta t\, \dot{\gamma}$, $\boldsymbol{U}_p = \sqrt{\boldsymbol{C}_p}$ and $\boldsymbol{U}_{pi} = \sqrt{\boldsymbol{C}_{pi}}$ are introduced. The scalar evolution equation for the accumulated plastic strain is discretized by means of the classical backward Euler integration algorithm $\kappa = \kappa_j + \sqrt{(2/3)}\, \Delta\gamma$. The latter is already incorporated into the expression of the yield function. Due to the symmetry of the internal variables, a system of only 13 nonlinear scalar equations has to be solved by means of the Newton-Raphson-scheme for $\boldsymbol{U}_p^{-1}$, $\boldsymbol{U}_{pi}^{-1}$ and $\Delta\gamma$. After convergence is achieved, the accumulated plastic strain κ is updated and the required Cauchy stress corresponding to the intermolecular response $\boldsymbol{\sigma}_{\text{I}} = 1/J\boldsymbol{F}\boldsymbol{S}_{\text{I}}\boldsymbol{F}^T$ is computed.

In the case of isotropic elasto-plasticity without kinematic hardening (e.g. Simo [1992]) or visco-elasticity (Reese and Govindjee [1998*b*]), the problem of asymmetric arguments during the exponential mapping procedure does not occur and it can be evaluated in closed form. To this end, one can transform the evolution equation of the inelastic deformation, correspond-

ing to the network resistance, and express it in terms of the elastic left Cauchy-Green tensor $\boldsymbol{B}_{e2} = \boldsymbol{F}_{e2}\boldsymbol{F}_{e2}^T$ and the Kirchhoff stress tensor $\boldsymbol{\tau}_2 = \boldsymbol{F}\boldsymbol{S}_2\boldsymbol{F}^T$ (cf. Reese and Govindjee [1998*b*])

$$\boldsymbol{B}_{e2} = \exp\left(-\Delta t\left(\frac{1}{\tau\,\mu_2}\,\mathrm{dev}(\boldsymbol{\tau}_2) + \frac{2}{9\,\tau\,K_2}\mathrm{tr}\,(\boldsymbol{\tau}_2)\,\boldsymbol{I}\right)\right)\boldsymbol{B}_{e2,trial} \tag{3.50}$$

where $\boldsymbol{B}_{e2,trial} = \boldsymbol{F}\,\boldsymbol{C}_{i,j}^{-1}\,\boldsymbol{F}^T$ results from an initially permitted evolution of the inelastic deformation i.e. $\dot{\boldsymbol{C}}_{i,trial}^{-1} = \boldsymbol{0}$. As shown by Reese and Govindjee [1998*b*], expression (3.50) can be formulated with respect to the principal axes. Consequently, only a system of three scalar valued, implicit, nonlinear equations has to be solved for the eigenvalues of $\boldsymbol{B}_{e2}$, by utilizing the Newton-Raphson-scheme.

Finally, the total Cauchy stress (`STRESS`) is obtained from the contribution of both models $\boldsymbol{\sigma} = \boldsymbol{\sigma}_1 + \boldsymbol{\sigma}_2$.

The heat generation (`RPL`) caused by plastic and viscous dissipation and the heat of fusion is derived from the energy balance with respect to the reference configuration (see equations (3.41) and (3.42)). Since *ABAQUS* requires the heat sources r_t per current volume, the relations obtained from the energy balance are transformed by

$$r_t = \frac{1}{J}\left(r_\chi + r_1 + r_2\right) \tag{3.51}$$

The partial derivatives of the thermodynamic conjugated forces $\boldsymbol{S}_1$, $\boldsymbol{S}_2$, $\tilde{\boldsymbol{X}}$ and R with respect to the temperature are derived analytically (cf. Appendix 3.10.1).

3.6.2 Numerical approximation of tangent moduli

In *ABAQUS*, the material tangent modulus $\mathbb{C}_{\boldsymbol{D}}^{\boldsymbol{\sigma}} = 1/J\,\mathbb{C}_{\boldsymbol{D}}^{\boldsymbol{\tau}}$ (`DDSDDE`) is related to the tangent modulus tensor $\mathbb{C}_{\boldsymbol{D}}^{\boldsymbol{\tau}}$ for the Jaumann rate of the Kirchhoff stress $\boldsymbol{\tau}$ (cf. Stein and Sagar [2008]). The linearized incremental form of the latter can be expressed as

$$\Delta\boldsymbol{\tau} - \Delta\boldsymbol{W}\boldsymbol{\tau} - \boldsymbol{\tau}\Delta\boldsymbol{W}^T = \mathbb{C}_{\boldsymbol{D}}^{\boldsymbol{\tau}}\Delta\boldsymbol{D} \tag{3.52}$$

where $\Delta\boldsymbol{D}$ and $\Delta\boldsymbol{W}$ are the incremental symmetric and antisymmetric parts of the incremental spatial velocity gradient $\Delta\boldsymbol{L}$. In the course of the current work, $\mathbb{C}_{\boldsymbol{D}}^{\boldsymbol{\tau}}$ is obtained by means of an efficient numerical approximation algorithm proposed by Sun et al. [2008], which is based on a more systematic treatment of the topic by Miehe [1996]. The merit of this method lies in 6 successive perturbations of the deformation gradient and thus only six additional stress

computations. The thermal tangent modulus $\boldsymbol{C}_\theta^{\boldsymbol{\sigma}}$ (DDSDDT)

$$\Delta\boldsymbol{\sigma} = \boldsymbol{C}_\theta^{\boldsymbol{\sigma}}\,\Delta\theta \tag{3.53}$$

is defined by means of the temperature derivative of the total Cauchy stress and is approximated by a forward difference quotient. Obviously, from these perturbations (in total 7) and subsequent evaluations of the constitutive model, the temperature derivative of the internal heat source C_θ^r (DRPLDT)

$$\Delta r_t = C_\theta^r\,\Delta\theta \tag{3.54}$$

and the derivative of the heat source with respect to the strain increment $\boldsymbol{C}_{\boldsymbol{D}}^r$ (DRPLDE)

$$\Delta r_t = \boldsymbol{C}_{\boldsymbol{D}}^r : \Delta\boldsymbol{D} \tag{3.55}$$

can be approximated as well by means of a forward difference quotient. It should be emphasized that with this numerical approximation procedures, nearly quadratic convergence of the global Newton-Raphson-scheme was obtained in all considered cases.

3.7 Characterization of material parameters

3.7.1 Crystallization kinetics

In line with e.g. Weng et al. [2003] and Liu and Yang [2010], the temperature independent Avrami exponent n was determined by linear regression from the double logarithmic form of the isothermal and non-isothermal experimental data. Since no large variation was observed, the mean value of $n = 2.375$ was adopted as a constant material parameter (see Appendix 3.10.2).

Table 3.3: Parameters for modified Nakamura-Ziabicki model

$\dot{\theta}$ [K/min]	K_{max} [1/min]	θ_{max} [K]	D [K]	Δh_m [J/g]
5	9.51	348.22	102.27	56.89
10	13.73	348.46	100.48	54.57
20	9.28	351.10	109.52	54.16
40	7.77	355.17	116.97	50.48
60	5.54	362.99	128.31	48.24
100	4.80	359.49	125.64	43.92

Subsequently, nonlinear optimization strategies were utilized to identify the remaining (temperature rate dependent) parameters of the model, based on the non-isothermal DSC results. In order to minimize the uncertainty whether the obtained solution corresponds to a global or local minimum, a combination of the Genetic Algorithm and Levenberg-Marquardt Algorithm was compared with the solution of the Interior-Point method. The procedure was performed with the commercial software *MATLAB*, which provides all algorithms as intrinsic functions. The resulting set of parameters is depicted in Table 3.3 and the non-isothermal experimental data and the corresponding fit of the proposed model is shown in Figure 3.7.

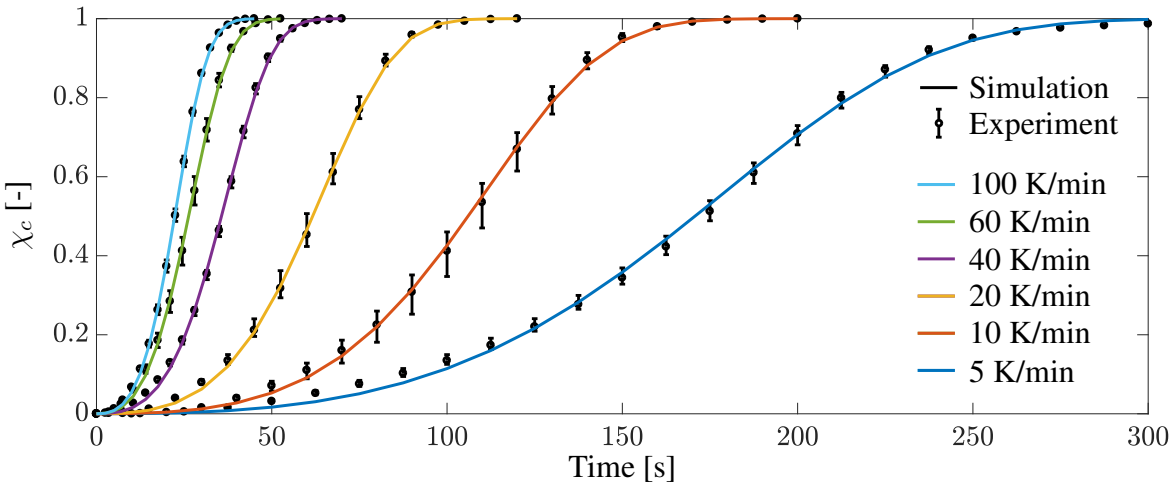

Figure 3.7: Non-isothermal DSC data and corresponding model response.

During the numerical solution procedure, cubic spline interpolation was applied to interpolate the set of parameters based on the actual cooling rate. In order to capture the cooling rate dependent onset temperature of crystallization θ_{on} under non-isothermal conditions, a linear regression was performed, which was based on the non-isothermal DSC data (cf. Appendix 3.10.2)

$$\theta_{on} = -0.2741\,\dot{\theta} + 470.65 \quad [\mathrm{K}] \tag{3.56}$$

3.7.2 Mechanical model parameters

In the recently submitted contribution of Felder, Vu, Reese and Simon [2020], the isothermal version of the proposed model formulation was developed, characterized, and validated. Furthermore, a staggered parameter characterization scheme was developed, to obtain a unique set of mechanical parameters for each considered temperature. The latter is briefly summarized in the following:

1. The Poisson's ratio ν was obtained from the negative ratio of the measured transverse and longitudinal stretch in the elastic regime, where $\nu = \nu_1 = \nu_2$ was assumed. The Young's moduli E_1 and E_2, corresponding to the intermolecular resistance and the molecular network resistance, respectively, were obtained from the initial slopes of the stress-stretch relations for different degrees of crystallinity.

2. From relaxation experiments at different stretch levels it is evident, that the relaxation time τ is a nonlinear function of the overstress $\boldsymbol{\sigma}_2$ and the stretch level. In line with the work of Amin et al. [2006], a post-processing scheme of the relaxation test data was applied, to obtain the fundamental relation between the rate of inelastic deformation $\dot{\boldsymbol{C}}_i$ and the overstress tensor. Based on these relations, a power-law-type function of the relaxation time was proposed $\tau = \tau_0 \|\boldsymbol{B}\|^{\varphi} \exp(\|\boldsymbol{\sigma}_2\|)^{-\delta}$, where the temperature dependent parameters $\tau_0(\theta)$, $\varphi(\theta)$, and $\delta(\theta)$ as well as the left Cauchy-Green deformation tensor $\boldsymbol{B} = \boldsymbol{F}\boldsymbol{F}^T$ were introduced. The latter were fitted by means of a nonlinear multiple curve fitting procedure.

3. The initial yield stress σ_y was directly obtained from cyclic loading-unloading-recovery-tests (cf. Section 3.2) for different degrees of crystallinity.

4. In the final characterization step, the parameters related to isotropic hardening were governed by a nonlinear multiple curve fitting procedure, based on the monotonic tensile test data for different degrees of crystallinity.

The obtained set of parameters is provided in Table 3.4. During the numerical solution procedure of a thermo-mechanically coupled problem, cubic spline interpolation is applied to interpolate the set of parameters based on the actual temperature. The tests were terminated after a stretch of $\lambda_x = 1.20$ was reached, to maintain a constant stretch rate. Thus, no significant increase of strain-hardening was observed at large strains, due to the limited extensibility of the polymer chains. Consequently, the constant locking stretch parameter λ_m, corresponding to the elastic energy contribution of the molecular network resistance, had no influence and was set to an arbitrary large value $\lambda_m = 2.0$.

As alluded above, the objective was to identify a set of material parameter for the considered constant temperatures. However, a significant temperature increase on the surface of the specimen, related to material self-heating, was observed for higher loading rates at stretch levels exceeding $\lambda_x \approx 1.05$ (cf. Section 3.3). Due to this fact, the hardening parameters were only calibrated in the isothermal regime ($\dot{\theta} \approx 0$) i.e. up to a stretch level of $\lambda_x \approx 1.05$ for v_{max}. Consequently, the isothermal model response overestimated the stress response, for $\lambda_x > 1.05$

Table 3.4: Set of mechanical parameters at different temperatures.

Function	Parameter at:	23 °C	50 °C	120 °C	160 °C
$E_1 = \chi\, E_{1,0}(\theta)$	$E_{1,0}$ [MPa]	7610	4398	1051	901
$E_2 = E_2(\theta)$	E_2 [MPa]	1210	703	201	103
$\nu_1 = \nu_2$	ν_1 [-]	0.35	0.35	0.35	0.35
$\sigma_y = \chi\, \sigma_{y,0}(\theta)$	$\sigma_{y,0}$ [MPa]	71	49	30	14
$\beta = \chi\, \beta_0(\theta)$	β_0 [-]	2317	1614	227	240
$H = \chi\, H_0(\theta)$	H_0 [MPa]	333	819	214	150
$\sigma_\infty = \chi^{\alpha(\theta)}\, \sigma_{\infty,0}(\theta)$	$\sigma_{\infty,0}$ [MPa]	68	57	1252	234
	α [-]	0.188	0.575	3.061	2.088
$\tau = \tau_0\, \|\|\boldsymbol{C}\|\|_s^{\varphi} \exp\left(\|\|\boldsymbol{\sigma}_2\|\|_s\right)^{-\delta}$	τ_0 [s]	156	71	48	31
	φ [-]	4.80	2.50	2.38	2.24
	δ [-]	0.211	0.221	0.714	0.517

and v_{max}, as depicted in Figure 3.10. To capture the phenomenon of material-self heating and corresponding thermal-softening, the fully thermo-mechanically coupled model had to be applied, as discussed in Section 3.8. The experimental data for monotonic tensile test at different loading rates and for varying temperatures and degrees of crystallinity is depicted in Figure 3.8, together with the corresponding model response.

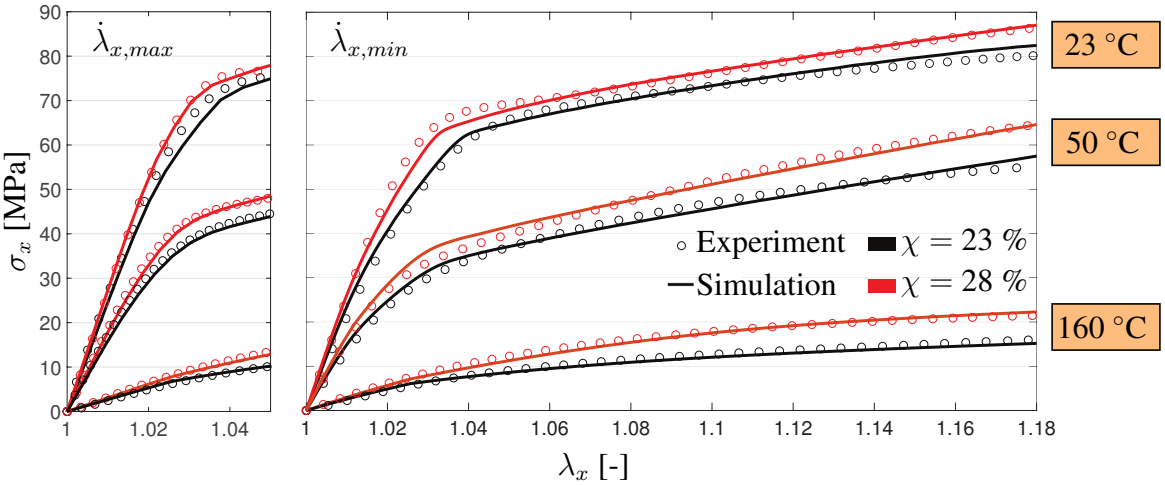

Figure 3.8: Monotonic, uniaxial extension: Experimental data and corresponding model response for different degrees of crystallinity χ, loading rates ($\dot{\lambda}_{x,max} = 0.35$ min^{-1} (left) and $\dot{\lambda}_{x,min} = 0.03$ min^{-1} (right)), and for different temperatures.

Noteworthy, difficulties arise in differentiating between isotropic and kinematic hardening from unloading experiments to zero force only. Due to this fact, only the nonlinear isotropic hardening response was fitted from the monotonic tests, due to the lack of tension-compression data. Consequently, the parameters b and c were set to very small values close to zero. It is important to emphasize that with this choice the nonlinearity upon unloading can be captured, due to the evolution of inelastic deformations within the molecular network branch upon loading (see Figure 3.9). Noteworthy, Krairi and Doghri [2014] proceeded in a similar way and were able to accurately predicted the cyclic loading response of HDPE by considering also only nonlinear isotropic hardening, in a coupled visco-elastic, visco-plastic constitutive framework.

In Figure 3.9, the capabilities of the model to accurately predict the nonlinearities upon loading and unloading, as well as the strain recovery at zero force is shown exemplary for 120 °C and different degrees of crystallinity. These results were obtained, by considering a single-element test where the stress in longitudinal x-direction, was prescribed as a traction boundary condition.

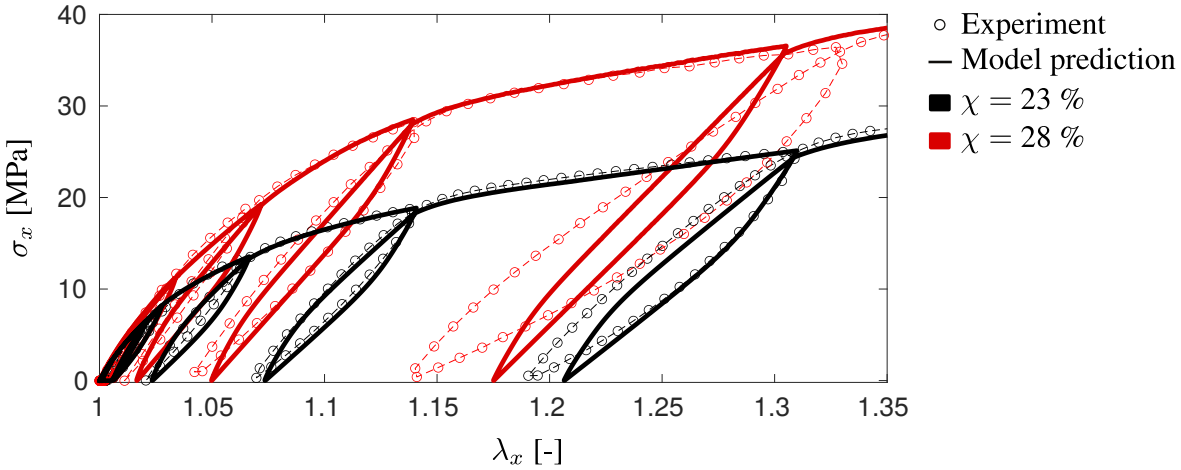

Figure 3.9: Isothermal model predicitions of the cyclic-loading behavior at 120 °C for $\chi = 23$ % and $\chi = 28$ %, with a loading speed of v_{min}.

The remaining parameters (i.e. ρ_0, λ_T, $\alpha_{T_{1/2}}$, and c_T) were obtained from the literature. From the data for the densities of the amorphous ($\rho_a = 1.09$ g/cm^3) and crystalline phases ($\rho_{c,\alpha} = 1.23$ g/cm^3, $\rho_{c,\gamma} = 1.16$ g/cm^3) of Polyamide 6, provided by Fornes and Paul [2003], the following function for the density is proposed

$$\rho_0 = \frac{\rho_{c,\alpha} + \rho_{c,\gamma}}{2}\,\chi + \rho_a(1-\chi) = 0.001195\,\chi + 0.00109\,(1-\chi) \quad \text{g/mm}^3 \tag{3.57}$$

The heat conductivity was set to $\lambda_T = 0.27$ W/Km (Li et al. [2013]) and was assumed to

be constant over the temperature, based on experimental investigations for Polyamide 6 by dos Santos et al. [2013]. For simplicity, the coefficient of thermal expansion was assumed to be constant $\alpha_{T_1} = \alpha_{T_2} = 0.876{\cdot}10^{-4}$ 1/K (cf. Jurkowski et al. [2002]). In addition, the relation for the heat capacity $c_T = 4.502\ \theta{+}138.7$ mJ/gK was assumed, which was proposed by Millot et al. [2015] based on the data provided by Gaur et al. [1983].

3.8 Numerical results

3.8.1 Investigation of material self-heating

As briefly discussed in the previous section, material self-heating was detected for higher loading rates at room temperature 23 °C. Consequently, the (isothermal) hardening parameters were only fitted up to a stretch level of $\lambda_x \approx 1.05$ for v_{max}, for the initial (room) temperature. To investigate the model response regarding the self-heating phenomena, a single element test was considered. The stretch in longitudinal x-direction obtained from the experimental data as a function of time was prescribed as a displacement boundary condition. Lateral contraction was unhindered and no temperature boundary conditions were applied, to account for adiabatic conditions. First, the isothermal model was considered, by setting the heat generation term to zero ($r_t = 0$). Consequently, the temperature remained constant throughout the deformation and the hardening behavior was overestimated for stretches exceeding $\lambda_x > 1.05$, compared to the experimental stress data (see Figure 3.10).

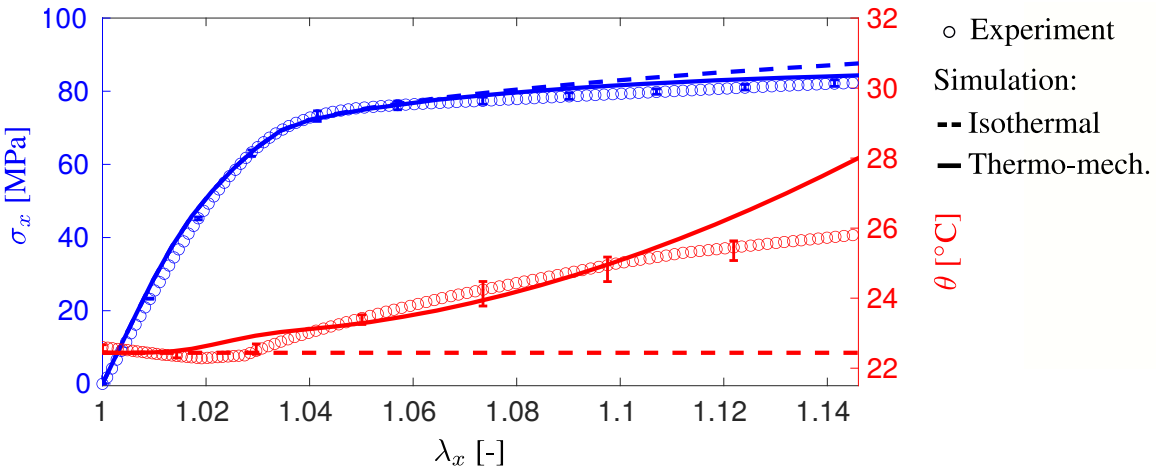

Figure 3.10: Isothermal and thermo-mechanically coupled model response at room temperature for $\chi = 23$ % and v_{max}.

Subsequently, the response of the fully thermo-mechanically coupled constitutive frame-

work was investigated. Due to dissipative processes, a temperature increase was present. The slight, initial temperature drop, due to the thermoelastic effect was not resolved by the model. The following increase of the temperature corresponded with the IR temperature records on the surface of the specimen. With proceeding deformation, the temperature was overestimated and exceeded the recorded data in the end by approximately 2 °C. However, adiabatic conditions were prescribed in the simulation (no heat flux nor convection). This was in contrast to the experimental conditions. Due to the heterogeneous strain field, temperature gradients within the specimen arose and consequently some fraction of the generated heat was transferred within the specimen and to the surrounding environment. This leads to the conclusion, that the simulated temperature increase should indeed be higher than the recorded temperature data - although, the specific discrepancy remains undetermined.

It should be emphasized, that the heat generation due to dissipation (cf. equation (3.42)), was solely derived from the chosen Helmholtz free energy and is consequently only dependent on the set of mechanical parameters (cf. Table 3.4), which was identified from uniaxial tensile tests (no additional parameters were introduced). With rising temperature, thermal softening was reproduced by the model, since the set of parameters was successively interpolated. The resulting stress-stretch response was in good agreement with the experimental data (see Figure 3.10).

To experimentally identify the adiabatic self-heating of the material, tests with higher loading rates should be performed in the future, to minimize the heat flux within the specimen. Based on these results, the model response could be adjusted if necessary. One possible way is to assume that only some fraction ω of the dissipation causes heat (i.e. $r_t^* = \omega\, r_t$). This procedure is widely used in the context of polymers (see e.g. Anand et al. [2009] and Maurel-Pantel et al. [2015]), where the so called Taylor-Quinney coefficient ω is modeled in different ways (e.g. treated as a constant or a function of temperature, strain rate, etc.). However, this approach contradicts the stringent, thermodynamically consistent derivation of the inelastic dissipative terms (r_1 and r_2 see equation (3.42)) from the local form of the energy balance (discussed in Section 3.5). Alternatively, the model could be enhanced by taking energy conversion mechanisms into account which do not generate heat, for example the creation of dislocations within the crystalline structures.

3.8.2 Structural Example

To further investigate the crystallization kinetics and structural response of the model, a thermo-mechanically coupled boundary value problem was considered. To this end, a symmetric plate with hole was subjected to a staggered loading procedure. Due to the symmetry of the consid-

ered problem, only one eighth of the structure was modeled. The prescribed loading procedure and boundary conditions, as well as the geometry of the plate with hole is provided in Figure 3.11. First, the edge of the specimen was cooled down from 200 °C to 120 °C as depicted in Figure 3.11. In two separate computations, the cooling rate was varied between 20 K/min and 80 K/min, by setting the cooling time t_c to 240 s and 80 s, respectively. Subsequently, the temperature boundary conditions were held constant for 180 s, to ensure a homogeneous temperature distribution within the structure. Next, the temperature boundary conditions were removed to investigate heat generation and heat conduction and a displacement was linearly increased over time until a value of 1 mm was prescribed. In the last step, the displacement was held constant for 60 s to allow for stress relaxation and heat transfer.

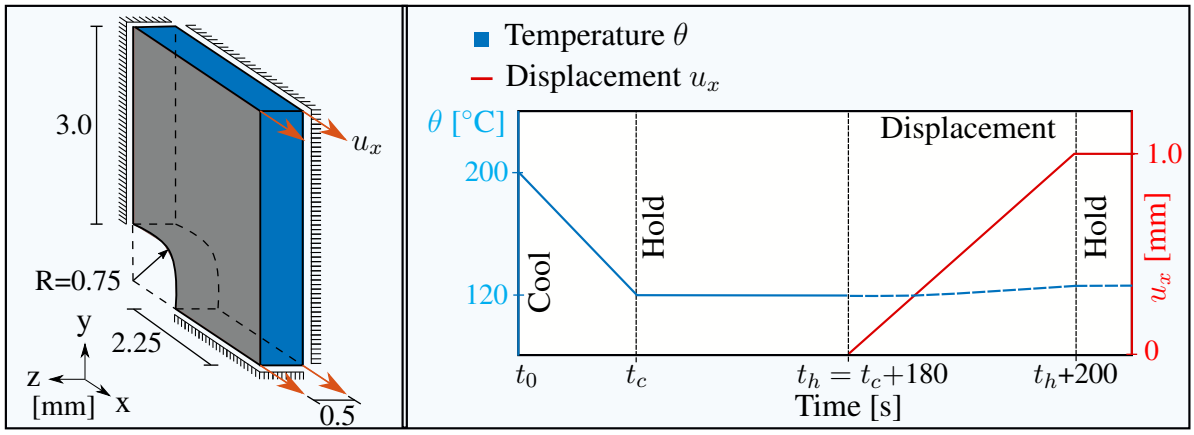

Figure 3.11: Geometry, boundary conditions, and applied loading procedure.

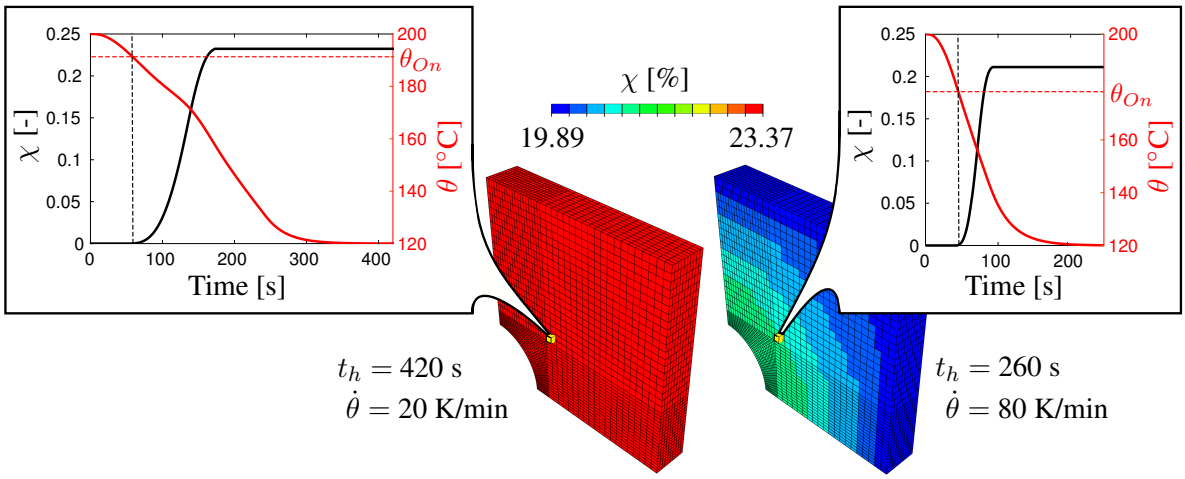

Figure 3.12: Evolution of total degree of crystallinity χ.

The distribution of the total degree of crystallinity χ at the end of the first holding step t_h is

shown in Figure 3.12, for both cooling rates. During the cooling step, temperature gradients and non-constant cooling rates arose, which resulted in locally varying crystallization conditions and thus in a heterogeneous crystallinity of the structure. This variation was more pronounced for the rapid cooling conditions, whereas for $\dot{\theta} = 20$ K/min an almost homogeneous distribution with a higher degree of crystallinity was observed. The depicted temperature and degree of crystallinity over time relations for one Gauss point revealed the typical crystallization kinetics characteristics for different thermal treatments (i.e. lower crystallization onset temperature θ_{On} and lower degree of crystallinity for higher cooling rates). Noteworthy, the heat of fusion during the crystallization process can be detected from a small temperature rise after the crystallization onset (for $\dot{\theta} = 20$ K/min), which is qualitatively in good agreement with the experimental data provided by e.g. Faraj et al. [2015] and Kugele et al. [2017].

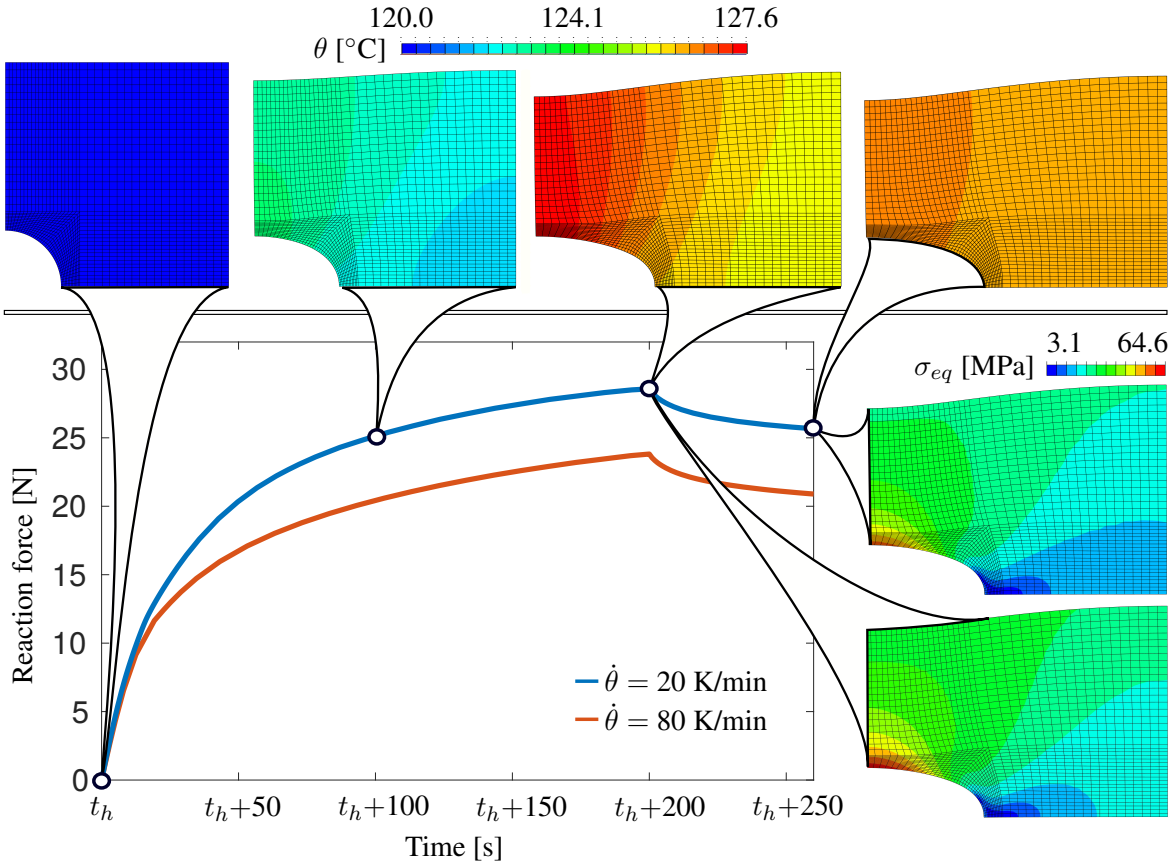

Figure 3.13: Reaction force time relation and temperature (θ) as well as equivalent von Mises stress (σ_{eq}) for selected time steps.

The dependence of the macroscopic mechanical response on the underlying microstructure is clearly visible from the reaction force time relation (i.e. increasing stiffness, hardening and yield stress with increasing degree of crystallinity) in Figure 3.13. In addition, the temperature

field and the distribution of the equivalent von Mises stress σ_{eq} are presented for selected time steps during the deformation and relaxation stages for $\dot{\theta} = 20$ K/min. A heterogeneous temperature field, due to the locally varying (plastic and inelastic) deformation rates, arose. At the end of the deformation step ($t = t_h$+200), stress concentrations were relaxed (leading to a drop of the reaction force) and the temperature distribution strove towards a homogeneous equilibrium state.

3.9 Conclusions

A thermo-mechanically coupled and thermodynamically consistent constitutive framework at finite strains was proposed for analyzing, predicting and optimizing the material and structural response of semi-crystalline polymers during thermoforming processes. To account for the crystallization process of this class of polymers during cooling from a relaxed melt, a non-isothermal modification of the Avrami model was incorporated into the proposed framework. In this new approach, the (evolving) total degree of crystallinity was introduced as an additional internal variable which contributes in an important manner to the macroscopic material properties. To capture the nonlinear material response in the observed elastic, visco-hyperelastic and visco-hyperelastic-plastic deformation regimes, a breakdown of the resistance to deformation into two separate parts was proposed. The intermolecular resistance was modeled by means of an elasto-plastic model, incorporating nonlinear kinematic and isotropic hardening. The molecular network resistance was captured by a visco-hyperelastic model, accounting for nonlinear relaxation behavior. The mechanical material parameters were assumed to be functions of the total degree of crystallinity and the temperature and were identified based on uniaxial tensile tests, spanning a large temperature range, for Polyamide 6 (*Ultramid B40*). DSC data was utilized to characterize the crystallization kinetics model.

The heat sources due to irreversible processes and exothermic crystal growth were derived from the chosen Helmholtz free energy and the energy balance in a thermodynamically consistent manner. In this way, no additional parameters were introduced to predict the material self-heating and accompanied thermal-softening at high loading rates. Therefore it is remarkable, that the model response, regarding adiabatic heating and thermal softening, is in good agreement with the provided experimental data cf. Section 3.8.

Furthermore, the model response was demonstrated in a thermo-mechanically coupled boundary value problem. The phenomenological approach allowed to account for the complex crystallization phenomena on the micro-scale, in a structural example, with sufficient accuracy. The predicted heat release due to the crystallization process is qualitatively in good

agreement with the reported results of Faraj et al. [2015] and Kugele et al. [2017]. To the authors' knowledge, there is no comparable constitutive framework available in the literature, which accounts for the thermal, mechanical and crystallization behavior and the corresponding complex interactions for semi-crystalline polymers. Consequently, the proposed theory provides a promising foundation for further investigations in the future.

However, work needs to be done to fully validate the models response in more complex structural problems. Despite this fact, the validation and analysis of the individual model parts, regarding the prediction of the mechanical (cf. Felder, Vu, Reese and Simon [2020] and Section 3.7) and thermo-mechanical response (cf. Section 3.8), show the promising potential of this new theory to efficiently and accurately predict the material behavior under thermo-mechanical loading conditions. Furthermore, it should be emphasized that the employed modified Nakamura-Ziabicki model (Nakamura et al. [1973]), was successfully utilized in numerous other contributions, to predict the crystallization kinetics of Polyamides on a material point (e.g. Neugebauer et al. [2016] and Zhao et al. [2018]) and on a structural level (cf. Faraj et al. [2015] and Kugele et al. [2017]. In the corresponding experiments, non-constant cooling rates arose and the results in Section 3.8 were qualitatively in good agreement with the reported behavior. Conclusively, it is expected that the employed formulation is suitable to predict the crystallization process from a static relaxed melt, in three-dimensional settings. However, this must be investigated in more detail in the future, on the basis of similar validation experiments.

Furthermore, for simulating real thermoforming processes, a much wider range of cooling rates must be considered. To this end, flash DSC analysis can be applied and the proposed crystallization kinetics model has to be adjusted accordingly. Furthermore, shear-, compression- and combined loading procedures need to be conducted for different loading rates, degrees of crystallinity and temperatures. Based on these results, the energy contributions can be adjusted and, more importantly, a yield criterion, accounting for the underlying microstructure and tension compression asymmetry, can be proposed. To characterize the kinematic hardening response, combined tension-compression experiments are required. Relaxation tests, for different degrees of crystallinity, are needed to capture the dependence of the relaxation time function on this quantity. In addition, the thermal parameters should be obtained from experimental procedures with varying degrees of crystallinity, to investigate and account for the influence of the underlying microstructure. Furthermore, future investigations should focus on the nonlinear thermal contraction behavior during the crystallization process, to accurately capture the formation of residual stresses.

Due to the high flexibility of the proposed model, these modifications can be incorporated in a straight forward manner, without changing the algorithmic solution scheme or the imple-

mented numerical approximation procedures for the required tangent moduli.

Acknowledgments: Financial support of the projects RE 1057/41-1 and RE 1057/46-1 by the German Science Foundation (DFG) is gratefully acknowledged. Furthermore, the authors are grateful for the provision of *Ultramid B40* by BASF SE.

3.10 Appendix

3.10.1

Conversion formula for elastic material parameters:

$$\Lambda_1 = \frac{E_1\,\nu_1}{(1+\nu_1)(1-2\nu_1)}, \quad \mu_{1/2} = \frac{E_{1/2}}{2\,(1+\nu_{1/2})}, \quad K_{1/2} = \frac{E_{1/2}}{3\,(1-2\nu_{1/2})} \tag{3.58}$$

Temperature derivatives of material parameters: Noteworthy, the derivatives of the parameters $E_{1,0}$, $\nu_{1/2,0}$, $\sigma_{y,0}$, β_0, H_0, α, and $\sigma_{\infty,0}$ with respect to the temperature are directly obtained from cubic spline interpolation.

$$\frac{\partial E_1}{\partial \theta} = \chi \frac{\partial E_{1,0}}{\partial \theta} \tag{3.59}$$

$$\frac{\partial \Lambda_1}{\partial \theta} = \frac{\nu_1}{(1+\nu_1)(1-2\,\nu_1)}\frac{\partial E_1}{\partial \theta} + \frac{E_1(2\,\nu_1^2+1)}{(\nu_1+1)^2(2\,\nu_1-1)^2}\frac{\partial \nu_1}{\partial \theta} \tag{3.60}$$

$$\frac{\partial \mu_{1/2}}{\partial \theta} = \frac{1}{2\,(1+\nu_{1/2})}\frac{\partial E_{1/2}}{\partial \theta} - \frac{E_{1/2}}{2\,(\nu_{1/2}+1)^2}\frac{\partial \nu_{1/2}}{\partial \theta} \tag{3.61}$$

$$\frac{\partial K_{1/2}}{\partial \theta} = \frac{1}{3\,(1-2\,\nu_{1/2})}\frac{\partial E_{1/2}}{\partial \theta} + \frac{2E_{1/2}}{3\,(2\,\nu_{1/2}-1)^2}\frac{\partial \nu_{1/2}}{\partial \theta} \tag{3.62}$$

$$\frac{\partial \mu^*}{\partial \theta} = \frac{1}{1+\frac{3}{5\lambda_m^2}+\frac{99}{175\lambda_m^4}+\frac{513}{875\lambda_m^6}+\frac{42039}{67375\lambda_m^8}}\frac{\partial \mu_2}{\partial \theta} \tag{3.63}$$

$$\frac{\partial \sigma_y}{\partial \theta} = \chi \frac{\partial \sigma_{y,0}}{\partial \theta} \tag{3.64}$$

$$\frac{\partial \beta}{\partial \theta} = \chi \frac{\partial \beta_0}{\partial \theta} \tag{3.65}$$

$$\frac{\partial H}{\partial \theta} = \chi \frac{\partial H_0}{\partial \theta} \tag{3.66}$$

$$\frac{\partial \sigma_\infty}{\partial \theta} = \chi^\alpha \ln(\chi)\,\frac{\partial \alpha}{\partial \theta}\,\sigma_{\infty,0} + \chi^\alpha\,\frac{\partial \sigma_{\infty,0}}{\partial \theta} \tag{3.67}$$

Temperature derivatives of driving forces:

$$\begin{aligned}\frac{\partial \boldsymbol{S}_1}{\partial \theta} &= \frac{\partial \mu_1}{\partial \theta}\left(\boldsymbol{C}_p^{-1} - \boldsymbol{C}^{-1}\right) + \frac{1}{2}\frac{\partial \Lambda_1}{\partial \theta}\left(\frac{\det(\boldsymbol{C})}{\det(\boldsymbol{C}_p)} - 1\right)\boldsymbol{C}^{-1} \\ &\quad - 3\left(\frac{\partial K_1}{\partial \theta}\,\alpha_{T1} + K_1\,\frac{\partial \alpha_{T1}}{\partial \theta}\right)(\theta-\theta_0)\,\boldsymbol{C}^{-1} - 3\,K_1\,\alpha_{T1}\,\boldsymbol{C}^{-1}\end{aligned} \tag{3.68}$$

$$\frac{\partial \tilde{\boldsymbol{X}}}{\partial \theta} = \frac{\partial c}{\partial \theta}(\boldsymbol{C}_{pi}^{-1} - \boldsymbol{C}_p^{-1}) \tag{3.69}$$

$$\frac{\partial R}{\partial \theta} = -\left(\frac{\partial \sigma_\infty}{\partial \theta} - \frac{\partial \sigma_y}{\partial \theta}\right)(1 - \exp(-\beta\,\kappa)) - (\sigma_\infty - \sigma_y)\exp(-\beta\,\kappa)\,\frac{\partial \beta}{\partial \theta}\,\kappa - \frac{\partial H}{\partial \theta}\,\kappa \tag{3.70}$$

$$\begin{aligned}\frac{\partial \boldsymbol{S}_2}{\partial \theta} = &\left(\frac{1}{2}\frac{\partial K_2}{\partial \theta}(J_{e2}^2 - 1) - 3\left(\frac{\partial K_2}{\partial \theta}\,\alpha_{T2} + K_2\,\frac{\partial \alpha_{T2}}{\partial \theta}\right)(\theta - \theta_0) - 3\,K_2\,\alpha_{T2}\right)\boldsymbol{C}^{-1} \\ &+ \operatorname{dev}\left(2\,\frac{\partial \mu^*}{\partial \theta}\sum_{i=1}^{5}\frac{i\,C_i}{\lambda_m^{2i-2}}\operatorname{tr}(\bar{\boldsymbol{C}}_{e2})^{i-1}\,J_{e2}^{-\frac{2}{3}}\,\boldsymbol{I}\right)\end{aligned} \tag{3.71}$$

3.10.2

Crystallisation kinetics model characterisation

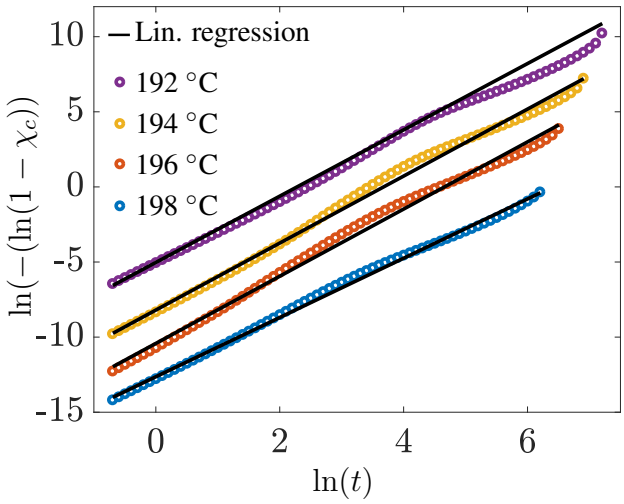

Figure 3.14: Logarithmic plot of isothermal DSC data and linear regression

Table 3.5: Avrami Exponent n from linear regression of the DSC data

Isothermal [°C]				Non-isothermal [K/min]					
192	194	196	198	5	10	20	40	60	100
1.973	2.236	2.230	2.068	2.335	2.847	2.650	2.487	2.391	2.535
Mean Value: 2.3752									

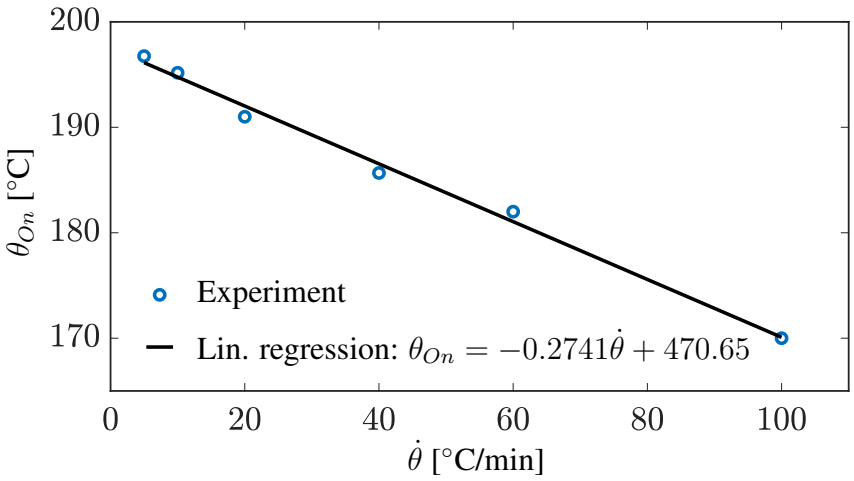

Figure 3.15: Crystallisation onset temperatures for different cooling rates and linear regression

4 Article 3: Thermo-mechanically coupled gradient-extended damage-plasticity modeling of metallic materials at finite strains

This article was accepted for publication and is currently in press:

S. Felder, N. Kopic-Osmanovic, H. Holthusen, T. Brepols, and S. Reese [2021], 'Thermo-mechanically coupled gradient-extended damage-plasticity modeling of metallic materials at finite strains', *International Journal of Plasticity* , Accepted manuscript in press.

Disclosure of the individual authors' contributions to the article:

S. Felder reviewed the relevant existing literature, derived the constitutive framework and implemented the material model and the element routine into the Finite Element software *FEAP*. Furthermore, he carried out the single-element computations and wrote the article. N. Kopic-Osmanovic implemented parts of the element routine, carried out all structural computations and fitted the corresponding parameters. H. Holthusen gave valuable conceptual advice and contributed parts of the material and element routines. T. Brepols and S. Reese gave conceptual advice, contributed to the discussion of the results, read the article and gave valuable suggestions for improvement. All authors approved the publication of the final version of the manuscript.

4.1 Abstract

For various engineering applications, the analysis and prediction of damage onset and propagation within ductile materials under thermo-mechanical loading conditions play a crucial role. However, finite element modeling of the influence of the temperature on plastic flow and damage evolution and the back-coupling of theses dissipative processes on the temperature field remains a challenging task, until today. To this end, a thermo-mechanically coupled two-surface damage-plasticity theory is derived in a thermodynamically consistent manner for large deformations. It can be considered as the thermo-mechanically coupled extension of a corresponding isothermal model, which was proposed recently by Brepols et al. [2020]. In this novel theory, the heat generation associated with thermo-elastic coupling and irreversible processes (i.e. damage and plasticity) is derived from the first law of thermodynamics. To overcome the mesh-dependence of conventional local damage models, a gradient-extension based on the micromorphic approach of Forest [2009, 2016] is employed. Besides the theoretical development, the algorithmic implementation into finite elements is discussed, including the computation of the required tangent operators via automatic differentiation. Finally, the fully coupled multi-physical formulation is verified regarding mesh-insensitive predictions of e.g. strain localization, local heat accumulation, material and thermal-softening, as well as crack propagation and back-coupling effects on the temperature field. Quantitative and qualitative comparisons of the model's predictions to experimental data reveal the promising potential of the numerically robust and flexible theory.

4.2 Introduction

In various engineering applications, metallic materials are subjected to both, large deformations and thermal loadings, e.g. during hot forming processes, where a complex interplay between plastic deformation mechanisms and thermo-mechanical coupling effects arises. Depending on the process parameters, these deformation mechanisms eventually lead to undesired distortions or even crack initiation and propagation. Thus, the influence of the temperature on plastic flow and damage evolution and the back-coupling of theses dissipative processes on the temperature field play a crucial role, in the material and structural behavior. Due to these complex dependencies, a demand for computational models arises to analyze, predict, and optimize the processing of this class of materials.

The cause of damage in ductile materials lies in various physical phenomena, i.e. nucleation, growth and coalescence of microvoids, which are observable on the microlevel (cf.

Hosokawa et al. [2013], Landron et al. [2013], Tekoğlu et al. [2015]). To describe these phenomena, numerous micro-mechanically motivated models (based on the pioneering work of Gurson [1977] and the Gurson-Tvergaard-Needleman (GTN) model (Needleman and Tvergaard [1984])) and models based on the continuum damage mechanics (CDM) concept (cf. Kachanov [1958], Rabotnov [1963, 1969], and Chaboche [1978]) were proposed. Recent improvements of the former group of models incorporate e.g. the void size and the void shearing effect (among others see Malcher and Mamiya [2014], Zhou et al. [2014], Jiang et al. [2016], Wu et al. [2019]). In the class of CDM models, the Lemaitre type (cf. Lemaitre [1984, 1985*a*,*b*]) approach is widely employed until today and was further developed to capture e.g. crack-closure (Desmorat and Cantournet [2008]), finite strains (e.g. Badreddine et al. [2010, 2017]) or the influence of the Lode angle (e.g. Malcher and Mamiya [2014], Yue et al. [2019]). In contrast, in two-surface approaches damage and plasticity are treated as two fully independent dissipative yet strongly interacting mechanisms. This conceptually very different method was applied in more recent works, in the context of small (Voyiadjis et al. [2011, 2012], Zhu et al. [2016]) and finite deformation theories(e.g. Vignjevic et al. [2012], Balieu and Kringos [2015], Brünig et al. [2014, 2018]).

An inherent problem of 'local'damage models (micromechanical and CDM based), implemented into a finite element framework, are strong mesh-dependent results in structural simulations where material softening occurs (see e.g. Bažant et al. [1984], Cervera and Chiumenti [2006], Jirásek and Grassl [2008], de Borst et al. [2012]). In order to solve the aforementioned problems and acquire reliable, mesh-independent results, the local damage variable, at the integration point level, is made dependent on 'nonlocal'quantities, which provide information on the (damage) state of the surrounding points. This can be achieved e.g. through implicit gradient-type formulations, in which the evolution of the global 'nonlocal'variable is governed by an additional partial differential equation and a set of boundary conditions. Based on the CDM approach and previous contributions from Wu et al. [2017], Papadioti et al. [2019] established a theory combining the uncoupled failure criterion by Bai and Wierzbicki [2008] with the implicit gradient damage-plasticity model by Engelen et al. [2002]. The micromorphic approach introduced by Forest [2009, 2016] allows a straight-forward derivation of implicit gradient-type formulations (see e.g. Saanouni and Hamed [2013]). Following this approach, gradient-extended two-surface damage-plasticity models were proposed for small (e.g. Brepols et al. [2017, 2018], Kiefer et al. [2018]) and large Brepols et al. [2020] deformations. More recent models are furthermore concerned with the combination of gradient damage with gradient plasticity, see e.g. Dimitrijevic and Hackl [2011] and Lodygowski et al. [2011], or the works of Miehe, Aldakheel and Raina [2016],Miehe, Teichtmeister and Aldakheel [2016],

and Dittmann et al. [2018], where the phase field of fracture method is employed.

The change in temperature as a result of plastic deformation and corresponding thermal softening motivated numerous scientific works related to the thermo-mechanically coupled modeling of plasticity. In the early works of Simo and Miehe [1992] and Wriggers et al. [1992], the modeling and numerical aspects of classical von Mises thermo-plasticity were investigated. Based on the proposed variational theory of Yang et al. [2006] and Stainier and Ortiz [2010], Canadija and Mosler [2011] developed a thermo-mechanically coupled framework, including kinematic hardening at finite strains. More recent works are concerned with gradient-enhanced thermo-plasticity (cf. Forest and Aifantis [2010], Voyiadjis and Faghihi [2012]), accounting for finite strains (cf. e.g. Wcislo and Pamin [2017]) and incorporating micro-structure based size effects (Aldakheel and Miehe [2017]). A comprehensive review on the latter topic was presented in Voyiadjis and Song [2019]. Furthermore, Russo et al. [2020] proposed an adoption of the Cosserat model in the context of a thermo-elasto-visco-plastic formulation, to obtain mesh-independent results.

When metals undergo large deformations, the local heat accumulation (in particular at high loading rates) leads to temperature-induced softening and, thus, to additional plastic strain localization, which eventually induces fracture. This is particularly the case in most metal manufacturing processes, where the deformation of the material is enforced at relatively high strain rates and is accompanied by the formation of large plastic strains. The corresponding phenomenon of thermal softening was also revealed by several experimental investigations (see e.g. Rusinek and Klepaczko [2009] and Bragov et al. [2019]), where a significant (local) increase in the temperature during mechanical testing at moderate and high deformation rates was reported, for various metals at ambient temperatures. Despite this fact, most of the aforementioned regularized damage-plasticity frameworks were derived for isothermal settings only. Some recent works are concerned with establishing regularized thermo-brittle theories. In this regard, Sicsic et al. [2014] introduced the first phase field based method for modeling thermal failure, which was extended by Miehe et al. [2015]. Sarkar et al. [2020] introduced a thermo-mechanically coupled gradient-damage theory for small strains. However, until today, only a very limited amount of works employ regularization techniques, in order to obtain mesh-insensitive, thermo-mechanically coupled damage and plasticity models. In one of these exclusive contributions by Dittmann et al. [2020], a framework with the aforementioned characteristics, which is based on the phase field method was developed, based on the theory of Dittmann et al. [2019].

Thus, from the literature review above, an ongoing demand for further research regarding regularized thermo-damage-plasticity models becomes evident. Consequently, the objective

of the present study is the derivation of a theory, which allows to evaluate the impact and interplay of all the aforementioned influences (plastic deformations, local heat accumulation, thermal softening, heat conduction as well as damage onset and propagation) collectively. To this end, a thermo-mechanically coupled extension of the isothermal theory presented by Brepols et al. [2020] is proposed. In contrast to the aforementioned isothermal framework, only linear kinematic hardening is considered in this work. To the authors' knowledge, there is no comparable model available in the literature, which comprises all of the following features and novelties:

- Thermodynamically consistent derivation of thermo-mechanically coupled, two-surface damage-plasticity theory at finite strains (see Section 4.3).
- Consistent derivation of the heat generation, associated with thermo-elastic coupling and irreversible processes (i.e. damage and plasticity) from the first law of thermodynamics (cf. Section 4.3.6).
- Employing an implicit gradient-type formulation, based on the micromorphic approach (see Section 4.3).
- Presentation of both, the strong and weak forms and algorithmic solution scheme for the three, fully coupled fields of global unknowns (i.e. displacement $\boldsymbol{u}$, 'nonlocal'damage variable $\bar{D}$, and temperature θ) in Section 4.4.1.
- Introduction of a fully implicit and monolithic approach and the computation of the material tangent operators, required to obtain a quadratic rate of convergence in transient heat transfer problems, via automatic differentiation (cf. Section 4.4.5).

The developed element and material routines are integrated into the finite element software *FEAP*. Computational examples are carried out, to assess and demonstrate the models capabilities regarding mesh-insensitive predictions of e.g. local heat accumulation due to dissipative processes, strain localization and thermal softening, as well as crack propagation and back-coupling effects on the heat conduction (see Section 4.5). Furthermore, the good convergence behavior of the robust and flexible framework is demonstrated in fully-coupled 2D plane strain and 3D transient heat transfer problems. In addition, first comparisons with experimental data from the literature for different metals validate the presented approach.

4.3 Material model formulation

Notational conventions. A direct tensor notation is preferred, where scalars, first-order tensors, second-order tensors, and fourth order tensors are represented by a, $\boldsymbol{a}$, $\boldsymbol{A}$, and $\mathbb{A}$, respectively. The operators grad$(*)$, Grad$(*)$, div$(*)$, and Div$(*)$ denote the gradient and divergence of a quantity $(*)$ with respect to the Eulerian and Lagrangian coordinates, respectively. tr$(\boldsymbol{C})$, sym$(\boldsymbol{C})$, and dev$(\boldsymbol{C})$ represent the trace, the symmetric and deviatoric part of a second order tensor $\boldsymbol{C}$, respectively. Single and double contraction between two tensors are written as $\boldsymbol{A} \cdot \boldsymbol{b}$ and $\mathbb{A} : \boldsymbol{B}$, respectively. To increase the readability, a single contraction of two second-order tensors $\boldsymbol{A}$ and $\boldsymbol{B}$ is implied by $\boldsymbol{AB}$, as an exception. The dyadic product of two first-order tensors $\boldsymbol{a}$ and $\boldsymbol{b}$ is denoted by $\boldsymbol{a} \otimes \boldsymbol{b}$. Furthermore, the norm of a second order tensor $\boldsymbol{A}$ is defined by $||\boldsymbol{A}|| = \sqrt{\text{tr}(\boldsymbol{A}^T \boldsymbol{A})}$.

4.3.1 Micromorphic approach and corresponding balance equations

The constitutive framework, derived in this work, is based on the general micromorphic approach presented by Forest [2009]. In line with this concept, a single scalar micromorphic damage variable $\bar{D}$ is introduced to circumvent mesh-dependent results, as discussed in the introduction. In the unified framework of Forest [2009], the generalized balance equations are derived by applying the principle of virtual work. Assuming a non-isothermal, geometrically nonlinear and quasi-static theory, this leads to the following set of balance equations in the reference configuration of the body B_0:

Balance of linear momentum

$$\begin{aligned} \text{Div}(\boldsymbol{FS}) + \boldsymbol{f}_0 &= \boldsymbol{0} && \text{in } B_0 \\ \boldsymbol{FS} \cdot \boldsymbol{n}_0 &= \boldsymbol{t}_0 && \text{on } \partial B_{0_t} \\ \boldsymbol{u} &= \tilde{\boldsymbol{u}} && \text{on } \partial B_{0_u} \end{aligned} \tag{4.1}$$

Micromorphic balance

$$\begin{aligned} \text{Div}(\boldsymbol{b}_{0_i} - \boldsymbol{b}_{0_e}) - a_{0_i} + a_{0_e} &= 0 && \text{in } B_0 \\ (\boldsymbol{b}_{0_i} - \boldsymbol{b}_{0_e}) \cdot \boldsymbol{n}_0 &= a_{0_c} && \text{on } \partial B_{0_c} \\ \bar{D} &= \tilde{\bar{D}} && \text{on } \partial B_{0_D} \end{aligned} \tag{4.2}$$

Balance of energy

$$
\begin{aligned}
-\dot{e} + \boldsymbol{S} : \frac{1}{2}\dot{\boldsymbol{C}} + a_{0_i}\,\dot{\bar{D}} + \boldsymbol{b}_{0_i} \cdot \text{Grad}\left(\dot{\bar{D}}\right) - \text{Div}(\boldsymbol{q}_0) + r_{\text{ext}} = 0 \qquad & \text{in } B_0 \\
\boldsymbol{q}_0 \cdot \boldsymbol{n}_0 = -q_0 \qquad & \text{on } \partial B_{0_q} \\
\theta = \tilde{\theta} \qquad & \text{on } \partial B_{0_\theta}
\end{aligned}
\tag{4.3}
$$

where the selected 'microvariable' $\bar{D}$ is an additional field variable and an additional micromorphic balance equations is introduced. In the equations above, $\boldsymbol{u}$, $\boldsymbol{F}$, $\boldsymbol{C} = \boldsymbol{F}^T\boldsymbol{F}$, and $\boldsymbol{S}$ are the displacement vector, the deformation gradient, the right Cauchy-Green deformation tensor, and the second Piola-Kirchhoff stress, respectively. Furthermore, the internal forces a_{0_i} and $\boldsymbol{b}_{0_i}$ are related to the micromorphic variable and its gradient. Conventional body forces are denoted by $\boldsymbol{f}_0$, generalized body forces by a_{0_e} and $\boldsymbol{b}_{0_e}$, respectively. The internal energy per reference volume is defined by e, θ is the absolute temperature, $\boldsymbol{q}_0$ the heat flux with respect to the reference configuration and r_{ext} denotes external heat sources per reference volume. The Neumann boundaries are defined at the outer surfaces of the body ∂B_0, where $\boldsymbol{n}_0$ is the outward unit normal vector. Conventional tractions and heat transfer defined on ∂B_{0_t} and ∂B_{0_q} are denoted by $\boldsymbol{t}_0$ and q_0, respectively, whereas a_{0_c} are 'generalized'tractions defined on ∂B_{0_c}. The Dirichlet boundary conditions are imposed on ∂B_{0_u}, ∂B_{0_D}, and ∂B_{0_θ}, where specific values of the displacement $\tilde{\boldsymbol{u}}$, the micromorphic damage variable $\tilde{\bar{D}}$, and the temperature $\tilde{\theta}$ are prescribed, respectively.

4.3.2 Derivation based on the Clausius-Duhem inequality

For the thermo-mechanically coupled damage-plasticity framework, the following dependencies of the free energy density ψ are assumed

$$
\psi = \check{\psi}(\boldsymbol{C}, (\boldsymbol{\zeta}_k, k = 1, ..., n), \bar{D}, \theta) \tag{4.4}
$$

where $\boldsymbol{\zeta}_k$ denotes a set of n internal variables related to damage and plasticity, which shall be specified in the next section.

In order to derive the constitutive equations in a thermodynamically consistent manner, the second law of thermodynamics, expressed by means of the Clausius-Duhem inequality with respect to the reference configuration

$$
\boldsymbol{S} : \frac{1}{2}\dot{\boldsymbol{C}} - \dot{\psi} - \eta\dot{\theta} - \frac{1}{\theta}\,\boldsymbol{q}_0 \cdot \text{Grad}(\theta) + \underbrace{a_{0_i}\,\dot{\bar{D}} + \boldsymbol{b}_{0_i} \cdot \text{Grad}(\dot{\bar{D}})}_{\text{micromorphic extension}} \geq 0 \tag{4.5}
$$

must be fulfilled for arbitrary processes. Here, two additional terms are included, which follow from the micromorphic extension (cf. Forest [2009], Forest [2016]). Furthermore, the entropy defined per unit reference volume η is introduced. Next, the total derivative of the Helmholtz free energy (4.4) is inserted into (4.5), which leads to

$$\begin{aligned}&\left(\boldsymbol{S}-2\,\frac{\partial\psi}{\partial\boldsymbol{C}}\right):\frac{1}{2}\,\dot{\boldsymbol{C}}-\sum_{k=1}^{n}\frac{\partial\psi}{\partial\boldsymbol{\zeta}_k}:\dot{\boldsymbol{\zeta}}_k+\left(\boldsymbol{b}_{0_i}-\frac{\partial\psi_{\bar{d}}}{\partial\,\mathrm{Grad}(\bar{D})}\right)\,\mathrm{Grad}\Big(\dot{\bar{D}}\Big)\\&+\left(a_{0_i}-\frac{\partial\psi_{\bar{d}}}{\partial\bar{D}}\right)\dot{\bar{D}}-\left(\eta+\frac{\partial\psi}{\partial\theta}\right)\dot{\theta}-\frac{1}{\theta}\,\boldsymbol{q}_0\cdot\mathrm{Grad}(\theta)\geq 0.\end{aligned}\tag{4.6}$$

Following the standard arguments by Coleman and Noll [1961] and assuming zero dissipation due to the micromorphic variable (cf. Forest [2016]), the second Piola-Kirchhoff stress as well as the internal forces related to the micromorphic variable and its gradient are defined by

$$\boldsymbol{S}=2\frac{\partial\psi}{\partial\boldsymbol{C}},\quad \boldsymbol{b}_{0_i}=\frac{\partial\psi}{\partial\,\mathrm{Grad}(\bar{D})},\quad a_{0_i}=\frac{\partial\psi}{\partial\bar{D}}\tag{4.7}$$

Analogously, the entropy and heat flux w.r.t. the reference configuration are defined

$$\eta=-\frac{\partial\psi}{\partial\theta},\quad \boldsymbol{q}_0=-\boldsymbol{K}\mathrm{Grad}(\theta)\tag{4.8}$$

In Equation (4.8), $\boldsymbol{K}(\boldsymbol{\zeta}_k)$ denotes the positive semi-definite conductivity tensor, which is also assumed to be affected by the internal state and is defined later (see Equation (4.40)). The remaining inequality $-\sum_{k=1}^{n}(\partial\psi/\partial\boldsymbol{\zeta}_k):\dot{\boldsymbol{\zeta}}_k\geq 0$ must be satisfied by appropriate evolution equations $\dot{\boldsymbol{\zeta}}_k$, which will be discussed later.

4.3.3 Thermodynamic state potential in terms of the Helmholtz free energy

The material behavior is mainly determined by the Helmholtz free energy. In the past, different choices for state potentials were postulated, in order to derive thermo-mechanically coupled constitutive frameworks. In the following, two very common approaches (I. and II.) are briefly discussed.

I. One reasonable starting point is the function for the Helmholtz free energy proposed by Chadwick and Hill [1974]

$$\psi=\psi_0(\boldsymbol{C},\boldsymbol{\zeta}_k,\theta_0)\frac{\theta}{\theta_0}+e_0(\boldsymbol{C},\boldsymbol{\zeta}_k,\theta_0)(1-\frac{\theta}{\theta_0})+\int_{\theta_0}^{\theta}c\,(\boldsymbol{C},\boldsymbol{\zeta}_k,\theta)(1-\frac{\theta}{\tilde{\theta}})d\tilde{\theta}\tag{4.9}$$

which is obtained by integrating the fundamental relation for the volumetric heat capacity

$$c := -\theta \frac{\partial^2 \psi}{\partial \theta^2} \tag{4.10}$$

twice and employing the relation for the internal energy $e = \psi - \theta\,\eta$. In Equation (4.9), ψ_0 and e_0 denote the free energy and internal energy at a reference temperature θ_0. By assuming a heat capacity, which is only dependent on the temperature, this approach furnishes a linear dependence of the stress on the temperature. This motivated e.g. Reese and Govindjee [1998*a*] to consider a deformation and temperature dependent relation for c, which naturally leads to a non-linear stress-temperature relation. In practice, this approach is in particular convenient, if a set of material parameters at one reference temperature θ_0 and the dependencies of c on deformation and temperature are known from experiments.

II. An alternative starting point is to consider a state potential of the format

$$\psi = \psi_m(\boldsymbol{C}, \boldsymbol{\zeta}_k, \theta) + \psi_\theta(\theta) \tag{4.11}$$

where ψ_m is related to the mechanical response (i.e. elastic energy, stored energy due to hardening, etc.) and contains material parameters which are (non-linear) functions of the temperature, in general. The caloric energy ψ_θ is necessary to imply additional flexibility regarding the particular function of the volumetric heat capacity (cf. Equation 4.10)

$$c = -\theta \frac{\partial^2 \psi_m}{\partial \theta^2} - \theta \frac{\partial^2 \psi_\theta}{\partial \theta^2} \tag{4.12}$$

which would otherwise only be defined by the mechanical energy contributions ψ_m. Thus, in general, c is a complex function of all internal variables. In some special cases, appropriate terms for ψ_θ can be specified (see e.g. the constitutive theory by Lion et al. [2017] for polymeric materials) and, thus, the heat capacity is evaluated in closed form. However, for inelastic material behavior, it is in general quite difficult to experimentally assess the heat capacity for different internal states (cf. e.g. Anand et al. [2009] and Ames et al. [2009]). Thus, often a constant heat capacity ($c :=$ const.) is assumed as an approximation and ψ_θ is not further specified. For most metals this leads to sufficiently accurate results (among numerous other contributions see e.g. Canadija and Mosler [2011], Aldakheel and Miehe [2017], and Dittmann et al. [2020]). In this work, the second approach (II.) is followed and an energy of the form (4.11) is considered, which allows the choice of individual functions for the temperature dependent material parameters. In line with the cited literature, a constant heat capacity ($c :=$ const.) is considered for simplicity.

4.3.4 Thermal expansion in the context of CDM

There are different ways to account for thermal expansion of the material within a thermo-mechanically coupled constitutive framework. One possible way is to introduce a multiplicative split of the deformation gradient $\boldsymbol{F} = \boldsymbol{F}_m \boldsymbol{F}_\theta$, into the isothermal deformation gradient $\boldsymbol{F}_m$ and the thermal deformation gradient $\boldsymbol{F}_\theta$ (cf. Stojanović et al. [1964]). In the context of damage modeling, this approach turns out to be in particular convenient, since the damage growth criterion (see Wulfinghoff et al. [2017])

$$\psi(\boldsymbol{C}^*, \theta^*, D + \mathrm{d}D) \leq \psi(\boldsymbol{C}^*, \theta^*, D), \quad \forall\, \boldsymbol{C}^*, \theta^* \tag{4.13}$$

here stated in the context of a thermo-mechanically coupled problem, is a priori fulfilled (for appropriate degradation functions and isotropic damage).

This can be easily demonstrated by considering the simple example of thermo-mechanically coupled brittle damage. When thermal expansion is captured by employing the multiplicative split of $\boldsymbol{F}$, an appropriate choice for the Helmholtz free energy of the second form (II.) (cf. Equation (4.11)) is

$$\psi = f_d(D)\,(\psi_e(\boldsymbol{C}_m)) + \psi_\theta \tag{4.14}$$

where $\boldsymbol{C}_m = \boldsymbol{F}_m^T \boldsymbol{F}_m = \boldsymbol{F}_\theta^{-T} \boldsymbol{C} \boldsymbol{F}_\theta^{-1}$ holds. Noteworthy, in this particular case ψ_m introduced in Equation (4.11) takes the more special form $\psi_m = f_d(D)\psi_e$, where ψ_e denotes the elastic energy. Damage is assumed to affect ψ_e only, by introducing a twice-differentiable positive and monotonically decreasing scalar-valued function $f_d(D)$. Here, $f_d(D) = 1$ holds for an undamaged material, whereas $f_d(D)$ takes on the value 0, if the material is fully damaged. If ψ_e is a convex function and $\boldsymbol{C}_m$ positive-definite, which are natural requirements, the damage growth criterion (cf. Equation (4.13)), here equivalently expressed as

$$\frac{\partial \psi}{\partial D} = \underbrace{\frac{\partial f_d(D)}{\partial D}}_{\leq 0} \underbrace{\psi_e(\boldsymbol{C}_m)}_{\geq 0} \leq 0 \tag{4.15}$$

is fulfilled (noteworthy, $\mathrm{d}D \geq 0$ always holds).

Conclusively, if the thermo-mechanical extension of an isothermal CDM (satisfying condition (4.13)) is desired, introducing the multiplicative split of $\boldsymbol{F}$ is straight forward. In this way, the damage growth criterion remains fulfilled and the form of the term ψ_m within the Helmholtz free energy can be taken over from the mechanical contribution in a purely isothermal case (except for introducing temperature dependent material parameters, if desired).

4.3.5 Constitutive framework

For the discussed reasons above, a multiplicative split of the deformation gradient $\boldsymbol{F} = \boldsymbol{F}_m \boldsymbol{F}_\theta$, into the isothermal deformation gradient $\boldsymbol{F}_m$ and the thermal deformation gradient $\boldsymbol{F}_\theta$ (cf. Stojanović et al. [1964]) is introduced. Depending on the type of material anisotropy, the latter can be specified uniquely as a function of the temperature (cf. e.g. Vujošević and Lubarda [2002], Lubarda [2004]). In the current work, isotropic material behavior and, thus, isotropic thermal expansion is considered. Consequently,

$$\boldsymbol{F}_\theta = \vartheta(\theta)\, \boldsymbol{I} \tag{4.16}$$

holds. Here $\vartheta(\theta) = \exp(\alpha(\theta - \theta_0))$ is the thermal stretch ratio, where a temperature independent coefficient of thermal expansion α is assumed. Consequently, $\boldsymbol{F}_\theta$ is proportional to $\boldsymbol{I}$. Thus, no additional intermediate configuration is introduced and $\boldsymbol{F} = \vartheta(\theta)\boldsymbol{F}_m$ holds. To model elasto-plastic material behavior, it is assumed that $\boldsymbol{F}_m = \boldsymbol{F}_e \boldsymbol{F}_p$ can be multiplicatively decomposed into an elastic ($\boldsymbol{F}_e$) and plastic ($\boldsymbol{F}_p$) part, in addition (cf. e.g. Eckart [1948], Kröner [1959], and Lee [1969]). Conclusively, $\boldsymbol{F} = \vartheta(\theta)\boldsymbol{F}_e \boldsymbol{F}_p$ holds. In this way, $\boldsymbol{F}_p$ maps from the reference configuration rc to the intermediate configuration (ic) and $\boldsymbol{F}_e$ maps from ic to the current configuration (cc), respectively.

Noteworthy, in the anisotropic case, decompositions of the type $\boldsymbol{F} = \boldsymbol{F}_e \boldsymbol{F}_p \boldsymbol{F}_\theta$ (and possibly other permutations) can be found in the literature. However, in the authors' opinion, employing such decompositions ought to be well deliberated, since a clear physical justification remains open. Other approaches, for instance the one suggested by Bertram [2003] based on a combined thermoelastic deformation, seem to be more appropriate.

The state potential is formulated as a function of the elastic and plastic right Cauchy-Green deformation tensors $\boldsymbol{C}_e$ and $\boldsymbol{C}_p$, respectively, which are defined as

$$\boldsymbol{C}_e = \boldsymbol{F}_e^T \boldsymbol{F}_e = \frac{1}{\vartheta^2} \boldsymbol{F}_p^{-T} \boldsymbol{C} \boldsymbol{F}_p^{-1}, \quad \boldsymbol{C}_p = \boldsymbol{F}_p^T \boldsymbol{F}_p \tag{4.17}$$

As alluded above, an additive decomposition of the Helmholtz free energy per unit reference volume

$$\hat{\psi} = f_d(D)(\psi_e(\boldsymbol{C}_e, \theta) + \psi_p(\boldsymbol{C}_p, \xi_p, \theta)) + \psi_d(\xi_d, \theta) + \psi_{\bar{d}}(D, \bar{D}, \mathrm{Grad}(\bar{D}), \theta) + \psi_\theta(\theta) \tag{4.18}$$

is assumed (in line with approach II.). Here, ψ_e denotes the elastic energy. The plastic energy stored due to kinematic and isotropic hardening ψ_p is a function of $\boldsymbol{C}_p$ and the accumulated plastic strain ξ_p. The stored energy due to damage hardening is represented by ψ_d and depends

on the damage hardening variable ξ_d. Furthermore, the energy related to the micromorphic extension ($\psi_{\bar{d}}$) introduces a strong coupling between the local D and micromorphic damage variables $\bar{D}$ and depends on the gradient of $\bar{D}$. To account for a temperature-dependent specific heat of the material, the caloric energy ψ_θ is introduced, in addition. All energy contributions are assumed to be functions of the temperature θ, in order to incorporate the influence of the temperature on the material parameters (cf. discussion above). In line with e.g. Brepols et al. [2020], both the elastic and plastic energies are assumed to be affected by damage, by introducing the scalar valued function $f_d(D)$.

Noteworthy, the invariants of $\boldsymbol{C}_e$ can equivalently be expressed in terms of $\boldsymbol{C}, \boldsymbol{C}_p$, and θ (see Appendix 4.7.1). Thus, $\hat{\psi}(\boldsymbol{C}_e, \boldsymbol{C}_p, \xi_p, D, \xi_d, \bar{D}, \theta) = \check{\psi}(\boldsymbol{C}, \boldsymbol{C}_p, \xi_p, D, \xi_d, \bar{D}, \theta)$ holds and the internal variables (i.e. $\boldsymbol{\zeta}_k$ introduced in Equation (4.4)) are $\boldsymbol{C}_p$, ξ_p, D, and ξ_d, accordingly.

With the Helmholtz free energy at hand, the second law of thermodynamics is exploited to derive the constitutive equations, as alluded above (cf. Section 4.3.2). This longer but otherwise standard derivation (see Appendix 4.7.2) leads to the following expression for the stress

$$\boldsymbol{S} = 2\, f_d(D)\, \frac{1}{\vartheta^2} \boldsymbol{F}_p^{-1} \frac{\partial \psi_e}{\partial \boldsymbol{C}_e} \boldsymbol{F}_p^{-T} \tag{4.19}$$

and the remaining inequality

$$(\boldsymbol{M} - \boldsymbol{\chi}) : \boldsymbol{D}_p - q_p\, \dot{\xi}_p - q_d\, \dot{\xi}_d + Y\, \dot{D} \geq 0 \tag{4.20}$$

Here, $\boldsymbol{D}_p := \mathrm{sym}(\boldsymbol{L}_p)$ denotes the symmetric part of the plastic velocity gradient $\boldsymbol{L}_p := \dot{\boldsymbol{F}}_p \boldsymbol{F}_p^{-1}$. Furthermore, the Mandel-like stress tensor ($\boldsymbol{M}$) and the back-stress tensor ($\boldsymbol{\chi}$)

$$\boldsymbol{M} := f_d(D)\, 2\, \boldsymbol{C}_e \frac{\partial \psi_e}{\partial \boldsymbol{C}_e}, \quad \boldsymbol{\chi} := f_d(D)\, 2\, \boldsymbol{F}_p \frac{\partial \psi_p}{\partial \boldsymbol{C}_p} \boldsymbol{F}_p^T \tag{4.21}$$

in the intermediate configuration ic are introduced. In addition, the thermodynamic conjugated driving forces to damage Y, isotropic hardening q_p, and damage hardening q_d are defined by

$$Y := -\left(\frac{\mathrm{d} f_d}{\mathrm{d} D} (\psi_e + \psi_p) + \frac{\partial \psi_{\bar{d}}}{\partial D} \right), \quad q_p := f_d(D)\, \frac{\partial \psi_p}{\partial \xi_p}, \quad q_d := \frac{\partial \psi_d}{\partial \xi_d} \tag{4.22}$$

4.3.5.1 Evolution equations

The choice of suitable plastic and damage evolution equations, which fulfill condition (4.20), is in line with the isothermal two-surface framework by Brepols et al. [2020].

Plasticity: Without loss of generality, a von Mises-type yield criterion incorporating isotropic and kinematic hardening

$$\Phi_p = \sqrt{\frac{3}{2}}||\text{dev}(\tilde{\boldsymbol{M}}) - \text{dev}(\tilde{\boldsymbol{\chi}})|| - (\sigma_y + \tilde{q}_p) \leq 0 \tag{4.23}$$

is chosen to determine the onset of plasticity, where $\sigma_y\,(\theta)$ is the temperature dependent initial yield stress. The yield function is expressed in terms of effective (i.e. undamaged) quantities $(\tilde{*}) := (*)|_{D=0}$ only, since plastic deformations are assumed to arise on the intact regions of the material only. Associative evolution equations are chosen

$$\boldsymbol{D}_p = \dot{\lambda}_p \frac{\partial \Phi_p}{\partial \boldsymbol{M}} = \dot{\lambda}_p \frac{\sqrt{3/2}}{f_d(D)} \frac{\text{dev}(\tilde{\boldsymbol{M}}) - \text{dev}(\tilde{\boldsymbol{\chi}})}{||\text{dev}(\tilde{\boldsymbol{M}}) - \text{dev}(\tilde{\boldsymbol{\chi}})||} \tag{4.24}$$

$$\dot{\xi}_p = -\dot{\lambda}_p \frac{\partial \Phi_p}{\partial q_p} = \frac{\dot{\lambda}_p}{f_d\,(D)} \tag{4.25}$$

where $\dot{\lambda}_p$ is the plastic multiplier. The standard Karush-Kuhn-Tucker conditions $\Phi_p \leq 0$, $\dot{\lambda}_p \geq 0$, and $\Phi_p\,\dot{\lambda}_p = 0$ complete the set of plastic evolution equations.

Damage: Due to the two-surface character of the presented damage-plasticity framework, the damage behavior is captured by a separate damage criterion

$$\Phi_d = Y - (Y_0 + q_d) \leq 0. \tag{4.26}$$

In the equation above, $Y_0\,(\theta)$ is the temperature dependent damage onset parameter. Analogously to plasticity, associative damage evolution equations are considered, viz.

$$\dot{D} = \dot{\lambda}_d \frac{\partial \Phi_d}{\partial Y} = \dot{\lambda}_d, \quad \dot{\xi}_d = -\dot{\lambda}_d \frac{\partial \Phi_d}{\partial q_d} = \dot{\lambda}_d \tag{4.27}$$

where the damage multiplier $\dot{\lambda}_d$ can be determined from the Karush-Kuhn-Tucker conditions $\Phi_d \leq 0$, $\dot{\lambda}_d \geq 0$, and $\Phi_d\,\dot{\lambda}_d = 0$.

For this set of evolution equations, it can be shown that the remaining parts of the inequality condition (4.74) are fulfilled and, thus, thermodynamic consistency is guaranteed for arbitrary processes. For a detailed proof, the interested reader is referred to the works of Vladimirov et al. [2008] and Brepols et al. [2020].

Up to now, the constitutive equations were derived w.r.t. different configurations, for convenience. However, it has several advantages to represent the tensor valued plastic evolution equation w.r.t the reference configuration. Firstly, an efficient exponential map algorithm can

be employed for the numerical time integration of the evolution equation. In this way, the symmetry of the internal variable, as well as the plastic incompressibility will be preserved. Secondly, in case of an isothermal setting, i.e. $\vartheta(\theta) = 1$ and $\boldsymbol{F}_\theta = \boldsymbol{I}$, the resulting theoretical framework is equivalent to the proposed theory by Brepols et al. [2020], except for the simplification of linear kinematic hardening, in the present work. Noteworthy, in this way, the plastic spin remains undetermined (no assumption must be made) and the model will comprise one symmetric tensorial internal variable (i.e. $\boldsymbol{C}_p$).

The pull-back operations can be equivalently performed as outlined in Brepols et al. [2020] and the resulting constitutive equations with respect to the reference configuration are provided in Table 4.3.7, where the back stress tensor $\boldsymbol{X}$ and the stress-like second order tensor $\boldsymbol{Y} := \boldsymbol{C}\boldsymbol{S} - \boldsymbol{C}_p\boldsymbol{X}$ w.r.t. the reference configuration are introduced. It is instructive to point out that $\boldsymbol{Y}$ is in general unsymmetric. However, the product $\boldsymbol{Y}\boldsymbol{C}_p$ is symmetric.

4.3.6 Derivation of the internal heat generation from the energy balance

In the following section, the heat generation due to thermo-elastic coupling and dissipation, resulting from irreversible processes (i.e. plasticity and damage), is derived in a thermodynamically consistent manner. Starting point is the micromorphic extension of the energy balance (4.3)

$$-\dot{\psi} - \dot{\eta}\,\theta - \eta\,\dot{\theta} + \boldsymbol{S} : \frac{1}{2}\dot{\boldsymbol{C}} + a_{0_i}\,\dot{\bar{D}} + \boldsymbol{b}_{0_i} \cdot \mathrm{Grad}(\dot{\bar{D}}) - \mathrm{Div}(\boldsymbol{q}_0) = 0 \tag{4.28}$$

where the total time derivative of the internal energy per reference volume $\dot{e} = \dot{\psi} + \dot{\eta}\,\theta + \eta\,\dot{\theta}$ was already incorporated. Furthermore, external heat generation is neglected in this work and, thus, r_{ext} vanishes in the balance law above. Subsequently, the total time derivative of the Helmholtz free energy (4.18), as well as the total time derivative of the entropy (4.75) are inserted in Equation (4.28). In this way, the partial differential equation for the temperature field, including internal heat generation r_{int} due to thermo-elastic coupling r_e, plasticity r_p, as

well as damage and the micromorphic extension r_d

$$
\begin{aligned}
& c\,\dot{\theta} = \underbrace{r_e + r_p + r_d}_{r_{\text{int}}} - \text{Div}(\boldsymbol{q}_0) \\
\text{where:} \quad & r_e := \left(\theta\,\frac{1}{2}\,\frac{\partial \boldsymbol{S}}{\partial \theta} - \theta\,\alpha\,\frac{\partial \boldsymbol{S}}{\partial \boldsymbol{C}} : \boldsymbol{C} - \theta\,\boldsymbol{S}\alpha\right) : \dot{\boldsymbol{C}} \\
& r_p := \left(\boldsymbol{M} - \theta\,\frac{\partial \boldsymbol{M}}{\partial \theta} - \boldsymbol{\chi} + \theta\,\frac{\partial \boldsymbol{\chi}}{\partial \theta}\right) : \boldsymbol{D}_p - \left(q_p - \theta\,\frac{\partial q_p}{\partial \theta}\right)\dot{\xi}_p \\
& r_d := \left(Y - \theta\,\frac{\partial Y}{\partial \theta}\right)\dot{D} - \left(q_d - \theta\,\frac{\partial q_d}{\partial \theta}\right)\dot{\xi}_d + \left(\theta\,\frac{\partial a_{0_i}}{\partial \theta} - \theta\,\alpha\,\frac{\partial \boldsymbol{S}}{\partial \bar{D}} : \boldsymbol{C}\right)\dot{\bar{D}} \\
& \qquad + \theta\,\frac{\partial \boldsymbol{b}_{0_i}}{\partial \theta} \cdot \text{Grad}(\dot{\bar{D}})
\end{aligned}
\tag{4.29}
$$

can be established, after several mathematical transformations. In the expression above, the volumetric heat capacity is approximated as a constant ($c := \text{const.}$) for simplicity (see discussion in Section 4.3.3)

Analogous to the plastic constitutive equations, the heat generation due to plastic deformation r_p is expressed in terms of quantities in the reference configuration (i.e. $\boldsymbol{C}_p$, $\boldsymbol{S}$, and $\boldsymbol{X}$) as well

$$
r_p = \frac{1}{2}\boldsymbol{C}\left(\boldsymbol{S} - \theta\,\frac{\partial \boldsymbol{S}}{\partial \theta}\right) : \boldsymbol{C}_p^{-1}\dot{\boldsymbol{C}}_p - \frac{1}{2}\left(\boldsymbol{X} - \theta\,\frac{\partial \boldsymbol{X}}{\partial \theta}\right) : \dot{\boldsymbol{C}}_p - \left(q_p - \theta\,\frac{\partial q_p}{\partial \theta}\right)\dot{\xi}_p \tag{4.30}
$$

For the derivation of the expression above, the interested reader is referred to Appendix 4.7.3.

4.3.7 Summary of constitutive equations

The term $\boldsymbol{F}_p^{-1}(\partial\psi_e/\partial\boldsymbol{C}_e)\boldsymbol{F}_p^{-T}$ can equivalently be expressed as a function of $\boldsymbol{C}$ and $\boldsymbol{C}_p$. Hence, it can be concluded that all constitutive equations introduced above can be expressed in terms of the symmetric tensors $\boldsymbol{C}$ and $\boldsymbol{C}_p$, the temperature θ, the micromorphic damage variable $\bar{D}$, the local damage variable D, as well as the plastic and damage multipliers $\dot{\lambda}_p$ and $\dot{\lambda}_d$. The internal variables are $\boldsymbol{C}_p$, ξ_p, D, ξ_d, accordingly. For convenience, a summary of the constitutive equations is presented below:

- Constitutively dependent quantities:

$$\boldsymbol{S} = 2\, f_d\, \frac{1}{\vartheta^2} \boldsymbol{F}_p^{-1} \frac{\partial \psi_e}{\partial \boldsymbol{C}_e} \boldsymbol{F}_p^{-T}, \quad \boldsymbol{b}_{0_i} = \frac{\partial \psi_{\bar{d}}}{\partial\, \mathrm{Grad}(\bar{D})}, \quad a_{0_i} = \frac{\partial \psi_{\bar{d}}}{\partial \bar{D}}, \quad \boldsymbol{X} = 2\, f_d\, \frac{\partial \psi_p}{\partial \boldsymbol{C}_p}$$

- Referential heat flux:

$$\boldsymbol{q}_0 = -\boldsymbol{K}\, \mathrm{Grad}(\theta)$$

- Thermodynamically conjugated forces:

$$q_p = f_d(D)\, \frac{\partial \psi_p}{\partial \xi_p}, \quad Y = -\left(\frac{\mathrm{d} f_d}{\mathrm{d} D} (\psi_e + \psi_p) + \frac{\partial \psi_{\bar{d}}}{\partial D} \right), \quad q_d = \frac{\partial \psi_d}{\partial \xi_d}$$

- Plastic and damage onset criteria:

$$\Phi_p = \sqrt{\frac{3}{2}} \sqrt{\mathrm{dev}(\tilde{\boldsymbol{Y}}) : \mathrm{dev}(\tilde{\boldsymbol{Y}})^T} - (\sigma_y + \tilde{q}_p), \quad \text{where } \boldsymbol{Y} = \boldsymbol{C}\boldsymbol{S} - \boldsymbol{C}_p \boldsymbol{X}$$

$$\Phi_d = Y - (Y_0 + q_d)$$

- Evolution equations:

$$\dot{\boldsymbol{C}}_p = 2\, \dot{\lambda}_p\, \frac{\sqrt{3/2}}{f_d(D)}\, \frac{\mathrm{dev}(\tilde{\boldsymbol{Y}}) \boldsymbol{C}_p}{\sqrt{\mathrm{dev}(\tilde{\boldsymbol{Y}}) : \mathrm{dev}(\tilde{\boldsymbol{Y}})}}, \quad \dot{\xi}_p = \frac{\dot{\lambda}_p}{f_d\,(D)}, \quad \dot{D} = \dot{\lambda}_d, \quad \dot{\xi}_d = \dot{\lambda}_d$$

- Loading / unloading conditions:

$$\Phi_p \leq 0, \quad \dot{\lambda}_p \geq 0, \quad \Phi_p\, \dot{\lambda}_p = 0 \quad \text{and} \quad \Phi_d \leq 0, \quad \dot{\lambda}_d \geq 0, \quad \Phi_d\, \dot{\lambda}_d = 0$$

- Internal heat generation:

$$r_e = \left(\theta\, \frac{1}{2}\, \frac{\partial \boldsymbol{S}}{\partial \theta} - \theta\, \alpha\, \frac{\partial \boldsymbol{S}}{\partial \boldsymbol{C}} : \boldsymbol{C} - \theta\, \boldsymbol{S} \alpha \right) : \dot{\boldsymbol{C}}$$

$$r_p = \frac{1}{2} \boldsymbol{C} \left(\boldsymbol{S} - \theta\, \frac{\partial \boldsymbol{S}}{\partial \theta} \right) : \boldsymbol{C}_p^{-1} \dot{\boldsymbol{C}}_p - \frac{1}{2} \left(\boldsymbol{X} - \theta\, \frac{\partial \boldsymbol{X}}{\partial \theta} \right) : \dot{\boldsymbol{C}}_p - \left(q_p - \theta\, \frac{\partial q_p}{\partial \theta} \right) \dot{\xi}_p$$

$$r_d = \left(Y - \theta\, \frac{\partial Y}{\partial \theta} \right) \dot{D} - \left(q_d - \theta\, \frac{\partial q_d}{\partial \theta} \right) \dot{\xi}_d + \left(\theta\, \frac{\partial a_{0_i}}{\partial \theta} - \theta\, \alpha\, \frac{\partial \boldsymbol{S}}{\partial \bar{D}} : \boldsymbol{C} \right) \dot{\bar{D}} + \theta\, \frac{\partial \boldsymbol{b}_{0_i}}{\partial \theta} \cdot \mathrm{Grad}(\dot{\bar{D}})$$

4.3.8 Specific choices for energy terms

In the previous sections, the constitutive framework was derived in a general manner, without introducing a specific form of the Helmholtz free energy. However, for the numerical examples

presented in this work, specific energy terms are chosen in the following. To capture the elastic response of the material, a compressible Neo-Hookean-type energy is chosen

$$\psi_e = \frac{\mu}{2}\left(\text{tr}(\boldsymbol{C}_e) - 3 - \ln\left(\det(\boldsymbol{C}_e)\right)\right) + \frac{\Lambda}{4}\left(\det(\boldsymbol{C}_e) - 1 - \ln\left(\det(\boldsymbol{C}_e)\right)\right) \tag{4.31}$$

where $\mu(\theta)$ and $\Lambda(\theta)$ are the temperature dependent Lamé constants. Furthermore, the plastic energy

$$\psi_p = \frac{a}{2}\left(\text{tr}(\boldsymbol{C}_p) - 3 - \ln\left(\det(\boldsymbol{C}_p)\right)\right) + e_p\left(\xi_p + \frac{\exp(-f_p\,\xi_p) - 1}{f_p}\right) + \frac{1}{2}\,P\,\xi_p^2 \tag{4.32}$$

corresponds to linear kinematic hardening and nonlinear isotropic hardening of Voce-type (Voce [1955]) plus an additional linear hardening term, with the corresponding temperature dependent parameters $a(\theta)$, $e_p(\theta)$, $f_p(\theta)$, and $P(\theta)$, respectively. With these functions at hand, the explicit forms of the second Piola-Kirchhoff stress $\boldsymbol{S}$, the back-stress tensor $\boldsymbol{X}$ and the driving force of isotropic hardening q_p can be derived from the Equations provided in Section 4.3.7, accordingly, viz.

$$\boldsymbol{S} = f_d(D)\left(\mu\left(\frac{1}{\vartheta^2}\boldsymbol{C}_p^{-1} - \boldsymbol{C}^{-1}\right) + \frac{\Lambda}{2}\left(\frac{\det(\boldsymbol{C})}{\vartheta^6\det(\boldsymbol{C}_p)} - 1\right)\boldsymbol{C}^{-1}\right) \tag{4.33}$$

$$\boldsymbol{X} = f_d(D)\,a\left(\boldsymbol{I} - \boldsymbol{C}_p^{-1}\right) \tag{4.34}$$

$$q_p = f_d(D)\left(\,e_p\left(1 - \exp(-f_p\,\xi_p)\right) + P\,\xi_p\right) \tag{4.35}$$

Noteworthy, it can be shown that the resulting function for $\boldsymbol{S}$ leads to physically reasonable stress contributions, corresponding to constrained thermal expansion, which might not be obvious from the presented equation above. This fact is discussed in detail in Appendix 4.7.4, where the reduction of the constitutive law to a thermo-elastic theory is presented, which is a natural requirement for any thermo-mechanically coupled framework.

Furthermore, nonlinear damage hardening is considered by choosing

$$\psi_d = e_d\left(\xi_d + \frac{\exp(-f_d\,\xi_d) - 1}{f_d}\right) \tag{4.36}$$

with the corresponding temperature dependent damage hardening parameter $e_d(\theta)$ and $f_d(\theta)$. In addition, the energy related to the micromorphic extension of the model is introduced

$$\psi_{\bar{d}} = \frac{H}{2}(D - \bar{D})^2 + \frac{A}{2}\text{Grad}(\bar{D}) \cdot \text{Grad}(\bar{D}) \tag{4.37}$$

where H serves as a penalty parameter and couples the local and micromorphic damage variables by penalizing the difference between these two. The internal length parameter A controls the influence of the gradient of the micromorphic variable in the formulation. Noteworthy, H and A are assumed to be temperature independent in the present work. Based on these additional energy terms, the remaining state laws as well as the driving forces for damage and damage hardening are derived from Equation (4.7) and (4.22), respectively:

$$a_{0_i} = -H\,(D - \bar{D}), \quad \boldsymbol{b}_{0_i} = A\,\mathrm{Grad}(\bar{D}) \tag{4.38}$$

$$Y = -\frac{\mathrm{d}f_d}{\mathrm{d}D}(\psi_e + \psi_p) - H\,(D - \bar{D}), \quad q_d = e_d\,(1 - \exp(-f_d\,\xi_d)) \tag{4.39}$$

Noteworthy, since Y is a function of the micromorphic variable, a 'nonlocal'character of the damage loading function (4.26) at the constitutive level is introduced.

In line with Dittmann et al. [2020], the conductivity tensor $\boldsymbol{K}$, introduced in Equation (4.8), is chosen to be a function of the local damage variable, viz.

$$\boldsymbol{K} = (f_d(D)\,K_0 + (1 - f_d(D))\,K_\mathrm{c})\boldsymbol{C}^{-1} \tag{4.40}$$

Here, K_0 is the heat conduction parameter in a virgin material ($f_d = 1$), whereas K_c represents a significantly reduced heat conduction in the case of a fully damaged material ($f_d = 0$).

4.4 Algorithmic implementation

4.4.1 Weak form of the problem and its linearization

Due to the presented, thermo-mechanically coupled and gradient extended constitutive theory, three fields $\boldsymbol{u}$, $\bar{D}$, and θ are solved simultaneously. To this end, the strong forms of linear momentum (4.1), the micromorphic balance equation (4.2), and the energy balance (4.29), are transformed to the corresponding weak forms. Hence, in the usual way, the balance laws are multiplied by appropriate test functions $\delta\boldsymbol{u}$, $\delta\bar{D}$, and $\delta\theta$ and are integrated over the domain B_0. At this point, it is assumed that generalized contact and external forces can be neglected (i.e. $a_{0_c} = a_{0_e} = 0$ and $\boldsymbol{b}_{0_e} = \boldsymbol{0}$) and only Neumann boundary conditions are considered for the micromorphic damage (i.e., $\partial B_{0_c} \equiv \partial B_0$, $\partial B_{0_{\bar{D}}} \equiv \varnothing$). By considering the divergence theorem and the boundary conditions, and inserting the relations for a_{0_i} and $\boldsymbol{b}_{0_i}$ (4.38) into the

micromorphic balance law (4.2), the following weak forms can be established.

$$g_u(\boldsymbol{u}, \bar{D}, \theta, \delta\boldsymbol{u}) = \int_{B_0} \boldsymbol{S} : \delta\boldsymbol{E}\,\mathrm{d}V - \int_{B_0} \boldsymbol{f}_0 \cdot \delta\boldsymbol{u}\,\mathrm{d}V - \int_{\partial B_{0_t}} \boldsymbol{t}_0 \cdot \delta\boldsymbol{u}\,\mathrm{d}A = 0 \tag{4.41}$$

$$g_d(\boldsymbol{u}, \bar{D}, \theta, \delta\bar{D}) = \int_{B_0} \left(H\,(D - \bar{D})\delta\bar{D} - A\,\mathrm{Grad}(\bar{D}) \cdot \mathrm{Grad}(\delta\bar{D})\right)\mathrm{d}V = 0 \tag{4.42}$$

$$\begin{aligned}\tilde{g}_\theta(\boldsymbol{u}, \bar{D}, \theta, \dot{\theta}, \delta\theta) = &\int_{B_0} c\,\dot{\theta}\delta\theta\,\mathrm{d}V - \int_{B_0} \boldsymbol{q}_0 \cdot \mathrm{Grad}(\delta\theta)\,\mathrm{d}V - \int_{B_0} r_{\text{int}}\,\delta\theta\,\mathrm{d}V \\ &- \int_{\partial B_{0_q}} q_0\,\delta\theta\,\mathrm{d}A = 0\end{aligned} \tag{4.43}$$

At this point, the weak form corresponding to the energy balance g_θ is discretized in time, by subdividing the total time T into discrete time increments Δt_n, viz.

$$[0, T] \approx \bigcup_{n=1}^{n_{\text{time}}} \Delta t_n \tag{4.44}$$

The approximation $\dot{\theta} \approx (\theta_{n+1} - \theta_n)/(\Delta t)$ is introduced, where θ_{n+1} and θ_n denote the current temperature and the temperature of the last converged time step, respectively. For brevity, the index $n + 1$ is omitted in all following equations. Consequently, the following fully implicit temporal discretization is obtained for g_θ

$$\begin{aligned}g_\theta(\boldsymbol{u}, \bar{D}, \theta, \delta\theta) = &\int_{B_0} c\,\frac{\theta - \theta_n}{\Delta t}\,\delta\theta\,\mathrm{d}V - \int_{B_0} \boldsymbol{q}_0 \cdot \mathrm{Grad}(\delta\theta)\,\mathrm{d}V - \int_{B_0} r_{\text{int}}\,\delta\theta\,\mathrm{d}V \\ &- \int_{\partial B_{0_q}} q_0\,\delta\theta\,\mathrm{d}A = 0\end{aligned} \tag{4.45}$$

The nonlinearity of the problem, stemming from the kinematics and constitutive relations, requires an incremental approach in finding the final solution. To this end, the weak forms above are linearized, with respect to the unknowns $\Delta\boldsymbol{u}$, $\Delta\bar{D}$ and $\Delta\theta$, by utilizing the Gâteaux derivative

$$\Delta g_u = \int_{B_0} \mathrm{Grad}(\delta\boldsymbol{u}) : (\mathrm{Grad}(\Delta\boldsymbol{u})\boldsymbol{S})\,\mathrm{d}V + \int_{B_0} \delta\boldsymbol{E} : \Delta\boldsymbol{S}\,\mathrm{d}V \tag{4.46}$$

$$\Delta g_d = \int_{B_0} H(\Delta D - \Delta\bar{D})\,\delta\bar{D}\,\mathrm{d}V - \int_{B_0} A\,\mathrm{Grad}(\Delta\bar{D}) \cdot \mathrm{Grad}(\delta\bar{D})\,\mathrm{d}V \tag{4.47}$$

$$\Delta g_\theta = -\int_{B_0} \Delta\boldsymbol{q}_0 \cdot \mathrm{Grad}(\delta\theta)\,\mathrm{d}V - \int_{B_0} \Delta r_{\text{int}}\,\delta\theta\,\mathrm{d}V + \int_{B_0} c\,\frac{\Delta\theta}{\Delta t}\,\delta\theta\,\mathrm{d}V \tag{4.48}$$

Here, it was assumed that the body force $\boldsymbol{f}_0$, the surface traction $\boldsymbol{t}_0$, and surface heat transfer

q_0 are independent of the field variables. For a detailed derivation of the increments Δg_u, Δg_d, and Δg_θ, the interested reader is referred to Appendix 4.7.5.

The increments of the constitutive relations in Equations (4.46)-(4.48)

$$\Delta \boldsymbol{S} = \left.\frac{\partial \boldsymbol{S}}{\partial \boldsymbol{E}}\right|_{\substack{\bar{D} \\ \theta}} [\Delta \boldsymbol{E}] + \left.\frac{\partial \boldsymbol{S}}{\partial \bar{D}}\right|_{\substack{\boldsymbol{u} \\ \theta}} \Delta \bar{D} + \left.\frac{\partial \boldsymbol{S}}{\partial \theta}\right|_{\substack{\boldsymbol{u} \\ \bar{D}}} \Delta\theta \tag{4.49}$$

$$\Delta D = \left.\frac{\partial D}{\partial \boldsymbol{E}}\right|_{\substack{\bar{D} \\ \theta}} : \Delta \boldsymbol{E} + \left.\frac{\partial D}{\partial \bar{D}}\right|_{\substack{\boldsymbol{u} \\ \theta}} \Delta \bar{D} + \left.\frac{\partial D}{\partial \theta}\right|_{\substack{\boldsymbol{u} \\ \bar{D}}} \Delta\theta \tag{4.50}$$

$$\Delta \boldsymbol{q}_0 = \left.\frac{\partial \boldsymbol{q}_0}{\partial \boldsymbol{E}}\right|_{\substack{\bar{D} \\ \theta}} : \Delta \boldsymbol{E} + \left.\frac{\partial \boldsymbol{q}_0}{\partial \bar{D}}\right|_{\substack{\boldsymbol{u} \\ \theta}} \Delta \bar{D} + \left.\frac{\partial \boldsymbol{q}_0}{\partial \theta}\right|_{\substack{\boldsymbol{u} \\ \bar{D}}} \Delta\theta \tag{4.51}$$

$$\Delta r_{\text{int}} = \left.\frac{\partial r_{\text{int}}}{\partial \boldsymbol{E}}\right|_{\substack{\bar{D} \\ \theta}} : \Delta \boldsymbol{E} + \left.\frac{\partial r_{\text{int}}}{\partial \bar{D}}\right|_{\substack{\boldsymbol{u} \\ \theta}} \Delta \bar{D} + \left.\frac{\partial r_{\text{int}}}{\partial \theta}\right|_{\substack{\boldsymbol{u} \\ \bar{D}}} \Delta\theta \tag{4.52}$$

are expressed in terms of the primary unknowns $\Delta \boldsymbol{u}$, $\Delta \bar{D}$, and $\Delta\theta$, which are solved for during the iterative solution scheme. In the relations above

$$\Delta \boldsymbol{E} := \frac{1}{2}\left(\boldsymbol{F}^T \text{Grad}(\Delta \boldsymbol{u}) + \text{Grad}(\Delta \boldsymbol{u})^T \boldsymbol{F}\right) \tag{4.53}$$

holds. Noteworthy, the term within Equation (4.51) associated with the temperature derivative of the heat flux can be reformulated, by recalling the chain rule of differentiation viz.

$$\Delta \boldsymbol{q}_0 = \left.\frac{\partial \boldsymbol{q}_0}{\partial \boldsymbol{E}}\right|_{\substack{\bar{D} \\ \theta}} : \Delta \boldsymbol{E} + \left.\frac{\partial \boldsymbol{q}_0}{\partial \bar{D}}\right|_{\substack{\boldsymbol{u} \\ \theta}} \Delta \bar{D} + \left.\frac{\partial \boldsymbol{q}_0}{\partial \theta}\right|_{\substack{\boldsymbol{u} \\ \bar{D} \\ \text{Grad}(\theta)}} \Delta\theta + \left.\frac{\partial \boldsymbol{q}_0}{\partial \text{Grad}(\theta)}\right|_{\substack{\boldsymbol{u} \\ \bar{D} \\ \theta}} \cdot \text{Grad}(\Delta\theta) \tag{4.54}$$

where the relation $(\partial \text{Grad}(\theta)/\partial\theta)\,\Delta\theta = \text{Grad}(\Delta\theta)$ was employed. This alternative representation is beneficial in the finite element discretization, since the remaining derivatives (i.e. $\partial \boldsymbol{q}_0/\partial\theta$ and $\partial \boldsymbol{q}_0/\partial \text{Grad}(\theta)$) can be calculated at the integration point level (cf. Section 4.4.2).

4.4.2 Finite element discretization

By employing the finite element method, the domain of the boundary value problem in the reference configuration B_0 is approximated by n_{el} finite elements B_0^e:

$$B_0 \approx \bigcup_{e=1}^{n_{el}} B_0^e. \tag{4.55}$$

Next, the solution fields (i.e. $\boldsymbol{u}(\boldsymbol{X})$, $\bar{D}(\boldsymbol{X})$, and $\theta(\boldsymbol{X})$) and corresponding test functions in each finite element are approximated

$$\begin{aligned}
\boldsymbol{u}(\boldsymbol{X}) &\approx \boldsymbol{N}_u^e(\boldsymbol{X})\boldsymbol{u}^e, \quad & \delta\boldsymbol{u}(\boldsymbol{X}) &\approx \boldsymbol{N}_u^e(\boldsymbol{X})\delta\boldsymbol{u}^e, \quad & \Delta\boldsymbol{u}(\boldsymbol{X}) &\approx \boldsymbol{N}_u^e(\boldsymbol{X})\Delta\boldsymbol{u}^e, \\
\bar{D}(\boldsymbol{X}) &\approx \boldsymbol{N}_{\bar{D}}^e(\boldsymbol{X})\bar{\boldsymbol{D}}^e, \quad & \delta\bar{D}(\boldsymbol{X}) &\approx \boldsymbol{N}_{\bar{D}}^e(\boldsymbol{X})\delta\bar{\boldsymbol{D}}^e, \quad & \Delta\bar{D}(\boldsymbol{X}) &\approx \boldsymbol{N}_{\bar{D}}^e(\boldsymbol{X})\Delta\bar{\boldsymbol{D}}^e, \\
\theta(\boldsymbol{X}) &\approx \boldsymbol{N}_\theta^e(\boldsymbol{X})\boldsymbol{\theta}^e, \quad & \delta\theta(\boldsymbol{X}) &\approx \boldsymbol{N}_\theta^e(\boldsymbol{X})\delta\boldsymbol{\theta}^e, \quad & \Delta\theta(\boldsymbol{X}) &\approx \boldsymbol{N}_\theta^e(\boldsymbol{X})\Delta\boldsymbol{\theta}^e
\end{aligned} \tag{4.56}$$

where the element nodal values (column vectors) are denoted by $\boldsymbol{u}^e, \bar{\boldsymbol{D}}^e, \boldsymbol{\theta}^e$ and the element shape functions (matrices) by $\boldsymbol{N}_u^e, \boldsymbol{N}_{\bar{D}}^e, \boldsymbol{N}_\theta^e$, respectively. By taking the derivative of the shape functions w.r.t. $\boldsymbol{X}$, the B-operators (matrices) $\boldsymbol{B}_{0u}^e(\boldsymbol{X}), \boldsymbol{B}_{0\bar{D}}^e(\boldsymbol{X}), \boldsymbol{B}_{0\theta}^e(\boldsymbol{X})$ are defined:

$$\begin{aligned}
\mathrm{Grad}(\boldsymbol{u}) &\approx \boldsymbol{B}_{0u}^e\,\boldsymbol{u}^e, \quad & \mathrm{Grad}(\delta\boldsymbol{u}) &\approx \boldsymbol{B}_{0u}^e\,\delta\boldsymbol{u}^e, \quad & \mathrm{Grad}(\Delta\boldsymbol{u}) &\approx \boldsymbol{B}_{0u}^e\,\Delta\boldsymbol{u}^e, \\
\mathrm{Grad}(\bar{D}) &\approx \boldsymbol{B}_{0\bar{D}}^e\,\bar{\boldsymbol{D}}^e, \quad & \mathrm{Grad}(\delta\bar{D}) &\approx \boldsymbol{B}_{0\bar{D}}^e\,\delta\bar{\boldsymbol{D}}^e, \quad & \mathrm{Grad}(\Delta\bar{D}) &\approx \boldsymbol{B}_{0\bar{D}}^e\,\Delta\bar{\boldsymbol{D}}^e, \\
\mathrm{Grad}(\theta) &\approx \boldsymbol{B}_{0\theta}^e\,\boldsymbol{\theta}^e, \quad & \mathrm{Grad}(\delta\theta) &\approx \boldsymbol{B}_{0\theta}^e\,\delta\boldsymbol{\theta}^e, \quad & \mathrm{Grad}(\Delta\theta) &\approx \boldsymbol{B}_{0\theta}^e\,\Delta\boldsymbol{\theta}^e
\end{aligned} \tag{4.57}$$

Subsequently, the Green-Lagrange strain tensor $\boldsymbol{E}$, the test function $\delta\boldsymbol{E}$, and the incremental change of the Green-Lagrange strain tensor $\Delta\boldsymbol{E}$ can be expressed as

$$\boldsymbol{E}(\boldsymbol{X}) \approx \boldsymbol{G}_{0u}^e(\boldsymbol{X})\boldsymbol{u}^e, \qquad \delta\boldsymbol{E}(\boldsymbol{X}) \approx \boldsymbol{G}_{0u}^e(\boldsymbol{X})\delta\boldsymbol{u}^e, \qquad \Delta\boldsymbol{E}(\boldsymbol{X}) \approx \boldsymbol{G}_{0u}^e(\boldsymbol{X})\Delta\boldsymbol{u}^e. \tag{4.58}$$

using matrix $\boldsymbol{G}_{0u}^e$, which is a function of the shape function derivatives and the deformation gradient (details can be found e.g. in Belytschko et al. [2014]).

Next, by introducing the Voigt notation $\hat{(*)}$, the weak forms of the governing Equations (4.41), (4.42), and(4.45) as well as their linearizations (4.46)-(4.48) are expressed in terms of the finite element approximations

$$\begin{aligned}
g_u &\approx \bigcup_{e=1}^{n_{el}} \delta\boldsymbol{u}^{e^T} \Bigg\{ \underbrace{\int_{B_0^e} \boldsymbol{G}_{0u}^{e^T}\,\hat{\boldsymbol{S}}^e \,\mathrm{d}V - \int_{B_0^e} \boldsymbol{N}_u^{e^T}\boldsymbol{f}_0^e \,\mathrm{d}V - \int_{\partial B_{0t}^e} \boldsymbol{N}_u^{e^T}\boldsymbol{t}_0^e \,\mathrm{d}A}_{\boldsymbol{r}_u^e} \Bigg\} \\
\Delta g_u &\approx \bigcup_{e=1}^{n_{el}} \delta\boldsymbol{u}^{e^T} \Bigg\{ \Bigg(\underbrace{\int_{B_0^e} \boldsymbol{B}_{0u}^{e^T}\,\mathbb{D}^e\,\boldsymbol{B}_{0u}^e \,\mathrm{d}V + \int_{B_0^e} \boldsymbol{G}_{0u}^{e^T}\frac{\partial\hat{\boldsymbol{S}}^e}{\partial\hat{\boldsymbol{E}}^e}\boldsymbol{G}_{0u}^e \,\mathrm{d}V}_{\boldsymbol{k}_{uu}^e} \Bigg)\Delta\boldsymbol{u}^e \\
&\quad + \underbrace{\int_{B_0^e} \boldsymbol{G}_{0u}^{e^T}\frac{\partial\hat{\boldsymbol{S}}^e}{\partial\bar{D}^e}\boldsymbol{N}_{\bar{D}}^e \,\mathrm{d}V}_{\boldsymbol{k}_{u\bar{D}}^e}\Delta\bar{\boldsymbol{D}}^e + \underbrace{\int_{B_0^e} \boldsymbol{G}_{0u}^{e^T}\frac{\partial\hat{\boldsymbol{S}}^e}{\partial\theta^e}\boldsymbol{N}_\theta^e \,\mathrm{d}V}_{\boldsymbol{k}_{u\theta}^e}\Delta\boldsymbol{\theta}^e \Bigg\}.
\end{aligned} \tag{4.59}$$

In the expression above, the fourth-order tensor $\mathbb{D}$ can be expressed in index notation, in terms of the Kronecker delta δ_{ik}, as $\mathbb{D}_{ijkl} = S_{jl}\delta_{ik}$ (see e.g. de Souza Neto et al. [2008]). Equivalently, the finite element approximation of the weak form of the micromorphic balance equation

$$
\begin{aligned}
g_d &\approx \bigcup_{e=1}^{n_{el}} \delta\bar{\boldsymbol{D}}^{e^T} \Bigg\{ \underbrace{\int_{B_0^e} H\,\boldsymbol{N}_{\bar{D}}^{e^T}\,(D^e - \boldsymbol{N}_{\bar{D}}^e\bar{\boldsymbol{D}}^e)\,\mathrm{d}V - \int_{B_0^e} A\,\boldsymbol{B}_{0\bar{D}}^{e^T}\,\boldsymbol{B}_{0\bar{D}}^e\,\bar{\boldsymbol{D}}^e\,\mathrm{d}V}_{\boldsymbol{r}_{\bar{D}}^e} \Bigg\} \\
\Delta g_d &\approx \bigcup_{e=1}^{n_{el}} \delta\bar{\boldsymbol{D}}^{e^T} \Bigg\{ \underbrace{\int_{B_0^e} H\,\boldsymbol{N}_{\bar{D}}^{e^T}\,\frac{\partial D^e}{\partial\hat{\boldsymbol{E}}^e}\boldsymbol{G}_{0u}^e\,\mathrm{d}V}_{\boldsymbol{k}_{\bar{D}u}^e}\,\Delta\boldsymbol{u}^e \\
&\quad + \Bigg(\underbrace{\int_{B_0^e} H\,\left(\frac{\partial D^e}{\partial\bar{D}^e} - 1\right)\boldsymbol{N}_{\bar{D}}^{e^T}\,\boldsymbol{N}_{\bar{D}}^e\,\mathrm{d}V - \int_{B_0^e} A\,\boldsymbol{B}_{0\bar{D}}^{e^T}\,\boldsymbol{B}_{0\bar{D}}^e\,\mathrm{d}V}_{\boldsymbol{k}_{\bar{D}\bar{D}}^e}\Bigg)\Delta\bar{\boldsymbol{D}}^e \\
&\quad + \underbrace{\int_{B_0^e} H\,\boldsymbol{N}_{\bar{D}}^{e^T}\,\frac{\partial D^e}{\partial\theta^e}\,\boldsymbol{N}_{\theta}^e\,\mathrm{d}V}_{\boldsymbol{k}_{\bar{D}\theta}^e}\,\Delta\boldsymbol{\theta}^e \Bigg\}
\end{aligned}
\tag{4.60}
$$

as well as the approximation of the weak form corresponding to the energy balance

$$
\begin{aligned}
g_\theta &\approx \bigcup_{e=1}^{n_{el}} \delta\boldsymbol{\theta}^{e^T} \Bigg\{ -\int_{B_0^e} \boldsymbol{B}_{0\theta}^{e^T}\,\boldsymbol{q}_0^e\,\mathrm{d}V - \int_{B_0^e} \boldsymbol{N}_{\theta}^{e^T}\,r_{\text{int}}^e\,\mathrm{d}V - \int_{\partial B_{0q}^e} \boldsymbol{N}_{\theta}^{e^T}\,q_0^e\,\mathrm{d}A \\
&\qquad\qquad + \int_{B_0^e} c\,\boldsymbol{N}_{\theta}^{e^T}\,\boldsymbol{N}_{\theta}^e\frac{1}{\Delta t}\,(\boldsymbol{\theta}^e - \boldsymbol{\theta}_n^e)\,\mathrm{d}V \Bigg\} \\
\Delta g_\theta &\approx \bigcup_{e=1}^{n_{el}} \delta\boldsymbol{\theta}^{e^T} \Bigg\{ \Bigg(\underbrace{-\int_{B_0^e} \boldsymbol{B}_{0\theta}^{e^T}\,\frac{\partial\boldsymbol{q}_0^e}{\partial\hat{\boldsymbol{E}}^e}\,\boldsymbol{G}_{0u}^e\,\mathrm{d}V - \int_{B_0^e} \boldsymbol{N}_{\theta}^{e^T}\,\frac{\partial r_{\text{int}}^e}{\partial\hat{\boldsymbol{E}}^e}\,\boldsymbol{G}_{0u}^e\,\mathrm{d}V}_{\boldsymbol{k}_{\theta u}^e}\Bigg)\Delta\boldsymbol{u}^e \\
&\quad + \Bigg(\underbrace{-\int_{B_0^e} \boldsymbol{B}_{0\theta}^{e^T}\,\frac{\partial\boldsymbol{q}_0^e}{\partial\bar{D}^e}\,\boldsymbol{N}_{\bar{D}}^e\,\mathrm{d}V - \int_{B_0^e} \boldsymbol{N}_{\theta}^{e^T}\,\frac{\partial r_{\text{int}}^e}{\partial\bar{D}^e}\,\boldsymbol{N}_{\bar{D}}^e\,\mathrm{d}V}_{\boldsymbol{k}_{\theta\bar{D}}^e}\Bigg)\Delta\bar{\boldsymbol{D}}^e \\
&\quad + \Bigg(\underbrace{\int_{B_0^e} c\,\boldsymbol{N}_{\theta}^{e^T}\,\boldsymbol{N}_{\theta}^e\frac{1}{\Delta t}\,\mathrm{d}V - \int_{B_0^e} \boldsymbol{B}_{0\theta}^{e^T}\frac{\partial\boldsymbol{q}_0^e}{\partial\theta^e}\boldsymbol{N}_{\theta}^e + \boldsymbol{B}_{0\theta}^{e^T}\frac{\partial\boldsymbol{q}_0^e}{\partial\text{Grad}(\theta)^e}\boldsymbol{B}_{0\theta}^e\,\mathrm{d}V}_{\boldsymbol{k}_{\theta\theta}^e} \\
&\quad \underbrace{- \int_{B_0^e} \boldsymbol{N}_{\theta}^{e^T}\,\frac{\partial r_{\text{int}}^e}{\partial\theta^e}\,\boldsymbol{N}_{\theta}^e\,\mathrm{d}V}_{\boldsymbol{k}_{\theta\theta}^e}\Bigg)\Delta\boldsymbol{\theta}^e \Bigg\}
\end{aligned}
\tag{4.61}
$$

can be derived. In the latter expression, the nodal values of the temperature of the last converged iteration are defined by $\boldsymbol{\theta}_n^e$. Furthermore, the element stiffness matrices $\boldsymbol{k}_{uu}^e$, $\boldsymbol{k}_{u\bar{D}}^e$, $\boldsymbol{k}_{u\theta}^e$, $\boldsymbol{k}_{\bar{D}u}^e$, $\boldsymbol{k}_{\bar{D}\bar{D}}^e$, $\boldsymbol{k}_{\bar{D}\theta}^e$, $\boldsymbol{k}_{\theta u}^e$, $\boldsymbol{k}_{\theta\bar{D}}^e$, and $\boldsymbol{k}_{\theta\theta}^e$ as well as the element residual vectors $\boldsymbol{r}_u^e$, $\boldsymbol{r}_{\bar{D}}^e$, and $\boldsymbol{r}_\theta^e$ were introduced.

Subsequently, the global stiffness matrices $\boldsymbol{K}_{uu}$, $\boldsymbol{K}_{u\bar{D}}$, $\boldsymbol{K}_{u\theta}$, $\boldsymbol{K}_{\bar{D}u}$, $\boldsymbol{K}_{\bar{D}\bar{D}}$, $\boldsymbol{K}_{\bar{D}\theta}$, $\boldsymbol{K}_{\theta u}$, $\boldsymbol{K}_{\theta\bar{D}}$, and $\boldsymbol{K}_{\theta\theta}$ as well as the global residual vectors $\boldsymbol{R}_u$, $\boldsymbol{R}_{\bar{D}}$, $\boldsymbol{R}_\theta$ are assembled from the individual element contributions, in the usual way. Finally, by taking the boundary conditions and the arbitrariness of the test functions into consideration, the following fully coupled set of global nonlinear equations is obtained

$$\begin{bmatrix} \boldsymbol{K}_{uu} & \boldsymbol{K}_{u\bar{D}} & \boldsymbol{K}_{u\theta} \\ \boldsymbol{K}_{\bar{D}u} & \boldsymbol{K}_{\bar{D}\bar{D}} & \boldsymbol{K}_{\bar{D}\theta} \\ \boldsymbol{K}_{\theta u} & \boldsymbol{K}_{\theta\bar{D}} & \boldsymbol{K}_{\theta\theta} \end{bmatrix} \left\{ \begin{array}{c} \Delta\boldsymbol{u} \\ \Delta\bar{\boldsymbol{D}} \\ \Delta\boldsymbol{\theta} \end{array} \right\} = - \left\{ \begin{array}{c} \boldsymbol{R}_u \\ \boldsymbol{R}_{\bar{D}} \\ \boldsymbol{R}_\theta \end{array} \right\} \tag{4.62}$$

which is simultaneously solved for the global nodal increments $\Delta\boldsymbol{u}$, $\Delta\bar{\boldsymbol{D}}$, and $\Delta\boldsymbol{\theta}$, until convergence is achieved.

4.4.3 Time integration of evolution equations

In the following, the time integration schemes for the evolution equations of the internal variables are discussed, where the index n corresponds to quantities of the last converged time step at t_n, whereas the index $n+1$ is omitted for brevity. For the numerical time integration of the plastic evolution Equation (see Section 4.3.7), the exponential map algorithm is employed, which is motivated by the findings of Vladimirov et al. [2008]. This integration scheme results in improved performance, accuracy and robustness for increasing step size. Furthermore, the plastic volume $\det(\boldsymbol{C}_p) = 1$ is preserved.

To circumvent a truncated series representation of the exponential function, due to an asymmetric tensorial argument, Reese and Christ [2008], Vladimirov et al. [2008], and Pietryga et al. [2012] utilized a modified ansatz, originally proposed by Dettmer and Reese [2004]. In the current work, the same modification is employed, which leads to the following form of the discretized evolution equation (for details, see the aforementioned contributions)

$$(\boldsymbol{U}_{p,n}\,\boldsymbol{U}_{p,n})^{-1} = \boldsymbol{U}_p^{-1} \exp\left(\bar{\lambda}_p\, \boldsymbol{U}_p^{-1} \underbrace{2\,\frac{\sqrt{3/2}}{f_d(D)}\,\frac{\mathrm{dev}(\tilde{\boldsymbol{Y}})\boldsymbol{C}_p}{\sqrt{\mathrm{dev}(\tilde{\boldsymbol{Y}}) : \mathrm{dev}(\tilde{\boldsymbol{Y}})^T}}}_{=:\boldsymbol{Z}} \boldsymbol{U}_p^{-1} \right) \boldsymbol{U}_p^{-1} \tag{4.63}$$

where $\bar{\lambda}_p = \Delta t\ \dot{\lambda}_p$ as well as the plastic stretch tensors $\boldsymbol{U}_p = \sqrt{\boldsymbol{C}_p}$ and $\boldsymbol{U}_{p,n} = \sqrt{\boldsymbol{C}_{p,n}}$, corresponding to the current time step and last converged time step, are introduced, respectively. Hence, $\boldsymbol{C}_p^{-1} = \boldsymbol{U}_p^{-1}\boldsymbol{U}_p^{-1}$ holds and Equation (4.63) can be expressed in terms of the unknown quantities $\boldsymbol{U}_p^{-1}$, $\bar{\lambda}_p$ and D only, which must be solved for during the local solution procedure on the integration point level.

For the time integration of the scalar evolution equations, the classical backward Euler algorithm is utilized, viz.

$$\xi_p = \xi_{p,n} + \frac{\bar{\lambda}_p}{f_d(D)}, \qquad D = D_n + \bar{\lambda}_d, \qquad \xi_d = \xi_{d,n} + \bar{\lambda}_d \tag{4.64}$$

where $\bar{\lambda}_d = \Delta t\ \dot{\lambda}_d$ holds.

4.4.4 Numerical implementation at the integration point level

Based on the relations (4.23), (4.63), and (4.26), the following set of equations, here already presented in a residuum format

$$R_1(\boldsymbol{U}_p^{-1}, \bar{\lambda}_p, \bar{\lambda}_d, \boldsymbol{C}, \theta) := \Phi_p = 0 \tag{4.65}$$

$$\boldsymbol{R}_2(\boldsymbol{U}_p^{-1}, \bar{\lambda}_p, \bar{\lambda}_d, \boldsymbol{C}, \theta) := -\left(\boldsymbol{U}_{p,n}\,\boldsymbol{U}_{p,n}\right)^{-1} + \boldsymbol{U}_p^{-1} \exp\left(\bar{\lambda}_p\,\boldsymbol{U}_p^{-1}\,\boldsymbol{Z}\,\boldsymbol{U}_p^{-1}\right)\boldsymbol{U}_p^{-1} = \boldsymbol{0} \tag{4.66}$$

$$R_3(\boldsymbol{U}_p^{-1}, \bar{\lambda}_p, \bar{\lambda}_d, \boldsymbol{C}, \bar{D}, \theta) := \Phi_d = 0 \tag{4.67}$$

must be solved for $\boldsymbol{U}_p^{-1}$, $\bar{\lambda}_p$, and $\bar{\lambda}_d$ at each integration point. Noteworthy, ξ_p, ξ_d, and D can be expressed in terms of $\bar{\lambda}_p$ and $\bar{\lambda}_d$ and the known values of the previous time step t_n (see Equation (4.64)) and are therefore not treated as additional unknowns, during the local iteration.

Due to the employed two-surface framework and the corresponding separate loading / unloading conditions as well as onset criteria (cf. Equations (4.23), (4.26)), four exclusive cases, summarized in Table 4.1, can occur at the integration point level.

Table 4.1: Possible loading scenarios at the integration point level

Loading case	Multiplier		Loading function		Active residuals
	plasticity	damage	plasticity	damage	
elastic loading/unloading	$\bar{\lambda}_p = 0$	$\bar{\lambda}_d = 0$	$\Phi_p \leq 0$	$\Phi_d \leq 0$	none
elasto-plastic loading	$\bar{\lambda}_p > 0$	$\bar{\lambda}_d = 0$	$\Phi_p = 0$	$\Phi_d \leq 0$	R_1, $\boldsymbol{R}_2$
elastic-damage loading	$\bar{\lambda}_p = 0$	$\bar{\lambda}_d > 0$	$\Phi_p \leq 0$	$\Phi_d = 0$	R_3
elastoplastic-damage loading	$\bar{\lambda}_p > 0$	$\bar{\lambda}_d > 0$	$\Phi_p = 0$	$\Phi_d = 0$	R_1, $\boldsymbol{R}_2$, R_3

In this work, a predictor-corrector algorithm in connection with an active set search strategy is utilized, in order to differentiate between the aforementioned cases and compute the actual solution in a monolithic approach. For further details regarding the active set search strategy and its implementation, which is similar to approaches applied in multisurface-plasticity, the interested reader is referred to the work of Brepols et al. [2017].

As an example, the solution procedure for an elastoplastic-damage loading case is briefly discussed, in the following. Due to the symmetry of the internal variables, in total a system of eight nonlinear equations, corresponding to the local residual vector $\boldsymbol{r}_{\text{loc}} := (R_1,\, \hat{\boldsymbol{R}}_2,\, R_3)^T = \boldsymbol{0}$ must be solved for the solution vector $\boldsymbol{x}_{\text{loc}} := (\bar{\lambda}_p,\, \hat{\boldsymbol{U}}_p^{-1},\, \bar{\lambda}_d)^T$. To this end, Newton's method is employed, which requires an additional linearization of the residuals (for constant $\boldsymbol{C}$, $\bar{D}$, and θ) and the calculation of the Jacobian matrix $\boldsymbol{J}_1 := \partial \boldsymbol{r}_{\text{loc}} / \partial \boldsymbol{x}_{\text{loc}}$. The latter is obtained by implementing the residuum as an individual subroutine in *Mathematica*. In this way, the software *AceGen* (cf. Korelc [2002] and Korelc and Wriggers [2016]) can be employed for the automatic differentiation of $\boldsymbol{r}_{\text{loc}}$ w.r.t. $\boldsymbol{x}_{\text{loc}}$ and generating the corresponding *Fortran* routine, comprising the latter.

After the residual is converged, the internal heat generation r_{int} is computed. At this point, two observations are made: First, due to the chosen specific energy $\psi_{\bar{d}}$ (see Equation (4.37)) and the reasonable assumption of temperature independent internal length parameter A and penalty parameter H, the partial derivatives $\partial a_{0i}/\partial\theta$ and $\partial \boldsymbol{b}_{0i}/\partial\theta$ in Equation (4.29) vanish (cf. Equation (4.38)). Secondly, computational examples (see Section 4.5.1) show that the terms in Equation (4.29) multiplied by the thermal expansion coefficient α, which is of the order of 10^{-5} for most metals, are negligibly small compared to the other contributions and can, thus, be neglected. Consequently, the dissipation caused by thermoelastic coupling, plasticity and damage (viz. Equations (4.29) and (4.30)) considered in this work reduces to

$$\begin{aligned} r_{\text{int}} = &\left(\frac{1}{2}\,\theta\,\frac{\partial \boldsymbol{S}}{\partial\theta}\right) : \dot{\boldsymbol{C}} + \frac{1}{2}\boldsymbol{C}\left(\boldsymbol{S} - \theta\,\frac{\partial \boldsymbol{S}}{\partial\theta}\right) : \boldsymbol{C}_p^{-1}\dot{\boldsymbol{C}}_p - \frac{1}{2}\left(\boldsymbol{X} - \theta\,\frac{\partial \boldsymbol{X}}{\partial\theta}\right) : \dot{\boldsymbol{C}}_p \\ &- \left(q_p - \theta\,\frac{\partial q_p}{\partial\theta}\right)\dot{\xi}_p + \left(Y - \theta\,\frac{\partial Y}{\partial\theta}\right)\dot{D} - \left(q_d - \theta\,\frac{\partial q_d}{\partial\theta}\right)\dot{\xi}_d \end{aligned} \tag{4.68}$$

Noteworthy, the rate terms $\dot{\boldsymbol{C}}_p$, $\dot{\xi}_p$, $\dot{D}$, and $\dot{\xi}_d$ required to compute the internal dissipation are obtained from Equations provided in Section 4.3.7, where the plastic multiplier $\dot{\lambda}_p = \bar{\lambda}_p/\Delta t$ and $\dot{\lambda}_d = \bar{\lambda}_d/\Delta t$ are computed from the solution of the local iteration and the corresponding time step size Δt, respectively. The rate of the right Cauchy-Green deformation tensor $\dot{\boldsymbol{C}}$ is approximated by $\dot{\boldsymbol{C}} \approx (\boldsymbol{C}_{n+1} - \boldsymbol{C}_n)/\Delta t$.

4.4.5 Consistent tangent operators

Finally, the 12 material sensitivities, introduced in Equation (4.49)-(4.52) must be implemented consistently with the employed numerical time integration scheme (see e.g. Wriggers [2008]). To this end, a sequential computation is proposed, where segments of the material routine (i.e. the functions for the residuum, the stress and the heat generation) are coded in *Mathematica*. Hence, the software *Acegen* can be used in order to determine the corresponding partial derivatives by means of automatic differentiation and to provide the corresponding computations in separate *Fortran* routines. This approach guarantees a quadratic rate of convergence for the local and global Newton-Raphson schemes, for fully coupled problems (see Section 4.5.2.2). For a more detailed explanation and the derivation of the tangent operators, the interested reader is referred to Appendix 4.7.6.

4.5 Numerical examples

In this section, the model's capabilities to capture the coupling effects between temperature, plasticity, and damage are assessed in both, academic settings as well as in comparison to experimental results for different metals from the literature. In Section 4.5.1, the material self-heating is investigated in single element computations. Subsequently, Section 4.5.2 addresses the model's mesh-insensitivity and convergence behavior in fully-coupled 2D and 3D structural examples.

For all computations, a damage weakening function of $f_d(D) = (1 - D)^2$ was considered. The elastic constants were assumed to be independent of the temperature, whereas the plastic parameters were chosen to degrade linearly with increasing temperature, for simplicity. The saturation-type function $f_\theta(\theta) = (1 - \omega(\theta - \theta_0))$ was chosen, in line with Dittmann et al. [2020], to capture the temperature dependency of the plastic parameters $(*) = f_\theta(\theta)(*)_0$. Here, ω is the softening parameter, as outlined in Simo and Miehe [1992]. Clearly, this choice is only valid for $f_\theta(\theta) > 0$. Some further limitations regarding this thermal softening function are discussed in Appendix 4.7.7. Due to the lack of experimental data, all damage parameters were assumed to be temperature independent, for the time being. Furthermore, the heat conductivity was assumed to be significantly larger in a virgin material than in the fully damaged state and K_c was therefore set to zero, for all computations.

The particular identification procedures or literature sources for the material parameters are discussed for each example separately, in the corresponding sections. An overview is provided in Table 4.2.

Table 4.2: Material parameter sets

Symbol	Numerical Example: Material parameter	4.5.1 Set 1	4.5.1.1 Set 2	4.5.2.1 Set 3	4.5.2.2 Set 4	Unit
Elastic parameters						
Λ	Lamé parameter	50	58.69	101.16	25	GPa
μ	Shear modulus	75	25.15	73.255	55	GPa
Plastic parameters						
σ_0	Yield stress	200	135.7	340	100	MPa
a_0	Kinematic hardening modulus	125	0	0	62.5	MPa
P_0	Isotropic hardening modulus	0	240.3	520	0	MPa
$e_{p,0}$	1st Voce hardening	125	123.41	296	125	MPa
$f_{p,0}$	2nd Voce hardening	8.5	17.1	18.9	5	-
Damage and gradient extension						
Y_0	Damage threshold	10	10^4	750	2.5	MPa
e_d	1st damage hardening	2	-	100	5.0	MPa
f_d	2nd damage hardening	2	-	100	100	-
A	Internal length parameter	-	-	50	75	MPa mm^2
H	Penalty parameter	-	-	10^4	10^6	MPa
Thermal parameters						
c	Volumetric heat capacity	3.59	3.10	3.59	3.59	mJ/(mm^3 K)
α	Thermal expansion coefficient	1.1	2.5	1.1	1.1	10^{-5}/K
K_0	Conductivity	50.2	91.19	50.2	50.2	mW/(mm K)
θ_0	Reference temperature	273.15	293.15	273.15	273.15	K
ω	Thermal softening parameter	0.002	0	0.0005	0.002	1/K

4.5.1 Material self-heating

To study the internal heat generation and material self-heating, a single 3D finite element with unit length was subjected to uniaxial extension, with a loading rate of $\dot{F}_{11} = 0.01$ s^{-1} under adiabatic conditions $\boldsymbol{q}_0 = \mathbf{0}$ at room temperature θ_0 =293 K. The arbitrarily chosen parameters for this academic example are listed in Table 4.2 as Set 1. It should be emphasized that in this example, the micromorphic extension had no influence, due to the homogeneous (i.e. 'gradient-free') deformation state. Noteworthy, a parameter study of the mechanical parameters is not performed in the current manuscript. For a detailed investigation of the influence of the model's plastic parameters, the interested reader is referred to the work of Vladimirov et al. [2008]. The influence of the parameters related to damage onset and hardening are studied in detail in the isothermal finite strain version of the constitutive theory by Brepols et al. [2020].

In Figure 4.1, the corresponding Cauchy stress (top) and the heat generation (middle) are depicted. In the elastic regime, thermo-elastic cooling (with almost constant and negative r_e, see zoom-in in Figure 4.1) arose, leading to a drop in the temperature (see bottom of Figure 4.1).

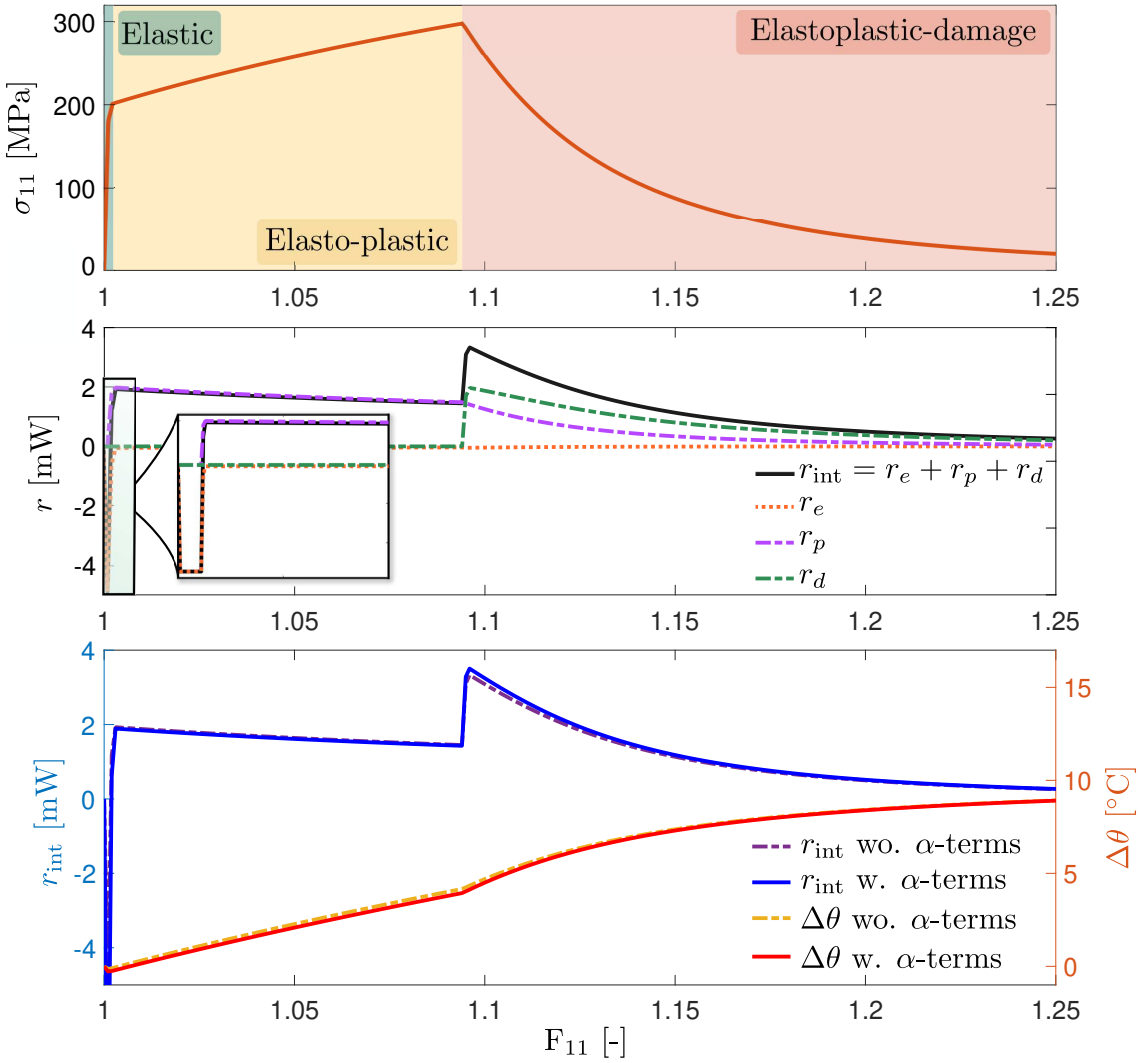

Figure 4.1: Single element subjected to uniaxial extension under adiabatic conditions. Top: Cauchy stress σ_{11} over stretch F_{11} in longitudinal direction. Middle: Corresponding total heat generation r_{int} and decomposition into elastic r_e, plastic r_p, and damage r_d parts. Bottom: Comparison of computation with (w.) and without (wo.) α-terms (cf. Equation (4.29)). Corresponding influence on the heat generation and resulting change in temperature $\Delta\theta$.

Once the initial yield stress was reached, plastic flow occurred, resulting in positive heat generation due to plastic dissipation r_p and a significant decrease in the elastic cooling r_e to almost zero. With increasing deformation, damage occurred, which was accompanied by additional heat generation r_d due to the additional dissipation.

The bottom of Figure 4.1 is concerned with the influence of the terms within the heat generation function (4.29), which are multiplied by the thermal expansion coefficient α. It becomes evident that neglecting these terms, for common thermal expansion coefficients of metals (of

the order of 10^{-5}), leads to a negligibly small deviation in both, the heat generation as well as the corresponding change in temperature. Concomitant with the discussion in Section 4.4.4, these terms are, thus, neglected throughout the following computational examples.

4.5.1.1 Comparison of heat generation with experimental data

Next, the model predictions for the heat generation due to dissipation were quantitatively compared to the experimental findings of Rose and Menzel [2020]. In the aforementioned publication, digital image correlation (DIC) and infrared thermography were employed, to simultaneously measure the temperature and displacement fields of an aluminum alloy (AW6016) under uniaxial extension at room temperature. In this way, the engineering stress-stretch relation in longitudinal 1-direction (First Piola-Kirchhoff P_{11} vs. F_{11}) as well as the temperature rise $\Delta\theta$ in the center of a flat dog bone specimen were obtained (see Figure 4.2). To assess the models' predictions of the heat generation, a single element with dimensions 1 mm x 1 mm x 1.2 mm (capturing the thickness of 1.2 mm of the dogbone specimen) was subjected to uniaxial extension with the same loading rate of $\dot{F}_{11} = 0.00114\ \mathrm{s}^{-1}$ as in the experiment.

The experimentally observed temperature field revealed an almost homogeneous temperature distribution in the center of the gauge length. Thus, by considering a small section of 1 mm x 1 mm in this region of the specimen, it was assumed that the heat conduction within the material to neighboring regions was negligible, due to the small temperature gradient. However, a fraction of the released heat was transferred to the environment via the specimen surface by thermal convection. To account for this heat exchange in the course of the simplified single element model, a corresponding convective heat flux on the two outward surfaces of the element was considered, viz.

$$\dot{q}_c = K_\mathrm{s}\, A\, (\theta - \theta_0). \tag{4.69}$$

In the equation above, K_s is the surface convection coefficient towards air and $A = 1\ \mathrm{mm}^2$ is the considered surface area. As concluded by Rose and Menzel [2020], the literature (e.g. Incropera et al. [2007]) suggests values for K_s between 2 and 25 W/(m^{2}K). Due to the lack of a specific value for the considered experimental setting, 12.5 W/(m^{2}K) was chosen for simplicity in this example. The elastic and thermal parameters were taken from Rose and Menzel [2020], whereas the plastic parameters were fitted to govern the stress-stretch response after the onset of plastic flow (see Figure 4.2 on the top). Noteworthy, since no damage occurred during testing, as stated by Rose and Menzel [2020], the damage onset Y_0 was set to 10^4 MPa. The corresponding parameters are listed as Set 2 in Table 4.2.

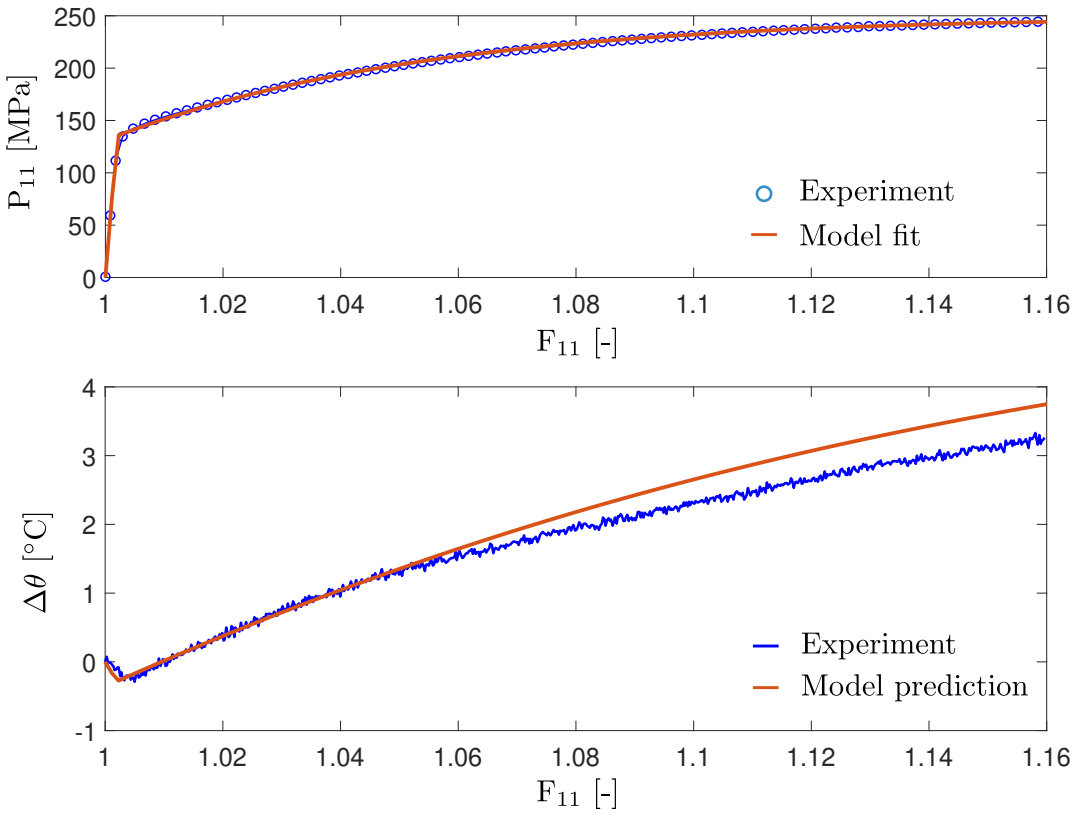

Figure 4.2: Top: Comparison of the engineering stress P_{11} over stretch F_{11} for the aluminium alloy AW6016 under uniaxial tension (Rose and Menzel [2020]) and the model fit. Bottom: Corresponding change in temperature $\Delta\theta$ over stretch F_{11} due to material self-heating. Comparison of experimental data (kindly provided by Rose and Menzel [2020]) and model prediction.

It should be emphasized that with this fixed set of mechanical parameters, the heat generation was completely defined (cf. Equation (4.68)) and no additional parameters were introduced. Consequently, the accurate model predictions of the initial drop in temperature, due to elastic cooling, and subsequent rise in temperature due to plastic heating, depicted in Figure 4.2, are remarkable. For deformations exceeding a stretch level of $F_{11} \approx 1.06$, the model slightly overestimated the rise in temperature. This might be due to the fact that no heat conduction within the specimen was considered (see discussion above). Furthermore, with increasing temperatures, the choice for K_s, in the provided range above, effects this result in addition.

Conclusively, despite this simplified representation of the experiment, it became evident that the thermodynamically consistent derivation of the heat generation, due to thermo-elastic and thermo-plastic coupling effects, led to reliable results. Nevertheless, it must be emphasized

that the investigation of the heat generation due to damage and fracture requires a separate comparison with experimental data, in the future.

4.5.2 Structural examples

4.5.2.1 Flat I-shaped specimen

In this section, a flat I-shaped specimen (steel EN 1.0553) under uniaxial extension was considered, to verify the novel theory in a structural problem by experimental data taken from Ambati et al. [2016]. Due to the symmetry of the considered problem and the evolution of symmetric fields, reported in the aforementioned work, only one eighth of the specimen was modeled, for simplicity. The dimension, boundary conditions and one mesh realization (43848 hexahedral elements with eight integration points) are shown in Figure 4.3. The lower part of the specimen was fixed in y-direction, whereas the upper part was moved in vertical direction with a loading speed of $\dot{\tilde{u}}_y = 0.5$ mm min^{-1}, in accordance with the experimental procedure.

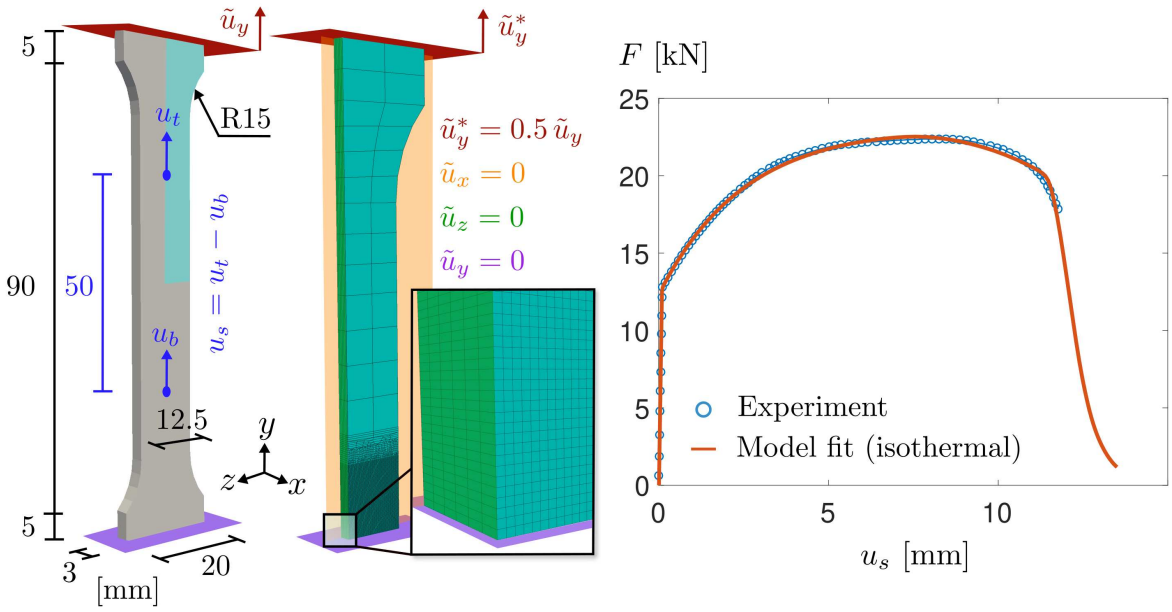

Figure 4.3: Geometry of I-shaped specimen and considered boundary value problem with a mesh realization of 43848 elements (left). Resulting force over displacement u_s for isothermal analysis and comparison with experimental data extracted from Ambati et al. [2016](right).

The elastic parameters were taken from Ambati et al. [2016], whereas the thermal parameters were obtained from Dittmann et al. [2020]. In a first computation, an isothermal problem,

i.e. no heat generation due to dissipation, was considered, in order to fit the remaining plastic and damage parameters. An overview of all material parameters is listed as Set 3 in Table 4.2. The corresponding load displacement curve is depicted in Figure 4.3 and shows good agreement with the experimental data, which was extracted from Ambati et al. [2016] (see also Figure 4.5 and corresponding discussion). Noteworthy, therein and in the following, the presented displacement u_s was measured between two points at ± 25 mm from the center of the specimen, in accordance with the experimental data.

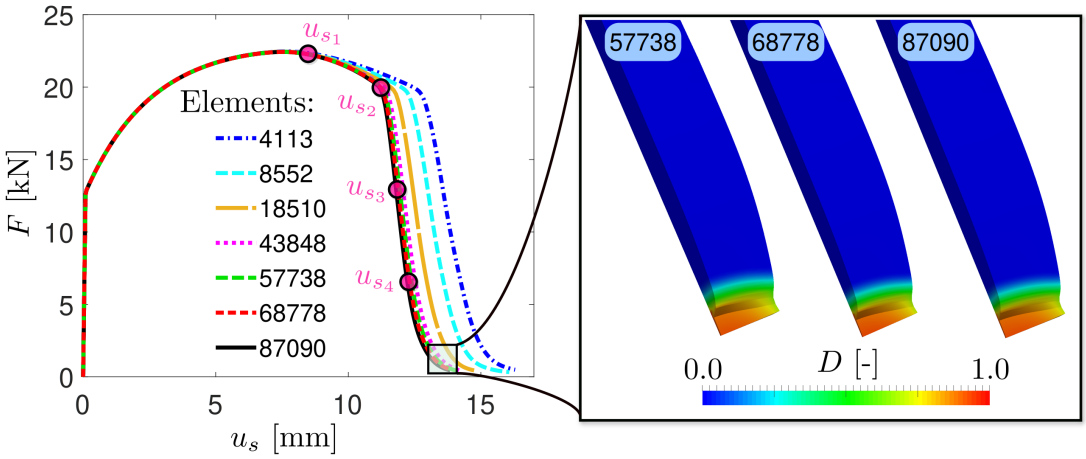

Figure 4.4: Mesh convergence study for a loading rate of 0.5 mm min^{-1}. Force over displacement for different mesh realizations (left) and damage contours for the modeled one eighth of the specimen at $u_s = 13.44$ mm (right).

Subsequently, with the fixed set of material parameters the fully thermo-mechanically coupled model response including internal heat generation was considered for different loading rates. During these simulations, the specimen was assumed to be adiabatically isolated, such that no heat in- nor outflow at the surfaces of the specimen was permitted, for simplicity. A mesh convergence study was performed for the lowest loading speed ($\dot{\bar{u}}_y = 0.5$ mm min^{-1}) and the corresponding reaction force over displacement is shown for different mesh realizations in Figure 4.4. From this study, it became evident that with increasing mesh density the model predictions converged towards one solution with a finite amount of dissipated energy, due to the gradient extension. This fact was deduced from the load displacement data (depicted in Figure 4.4) and the comparison of the contour plots of the damage variable D at the end of the simulation for the three finest meshes (see Figure 4.4). The widths of the damage zones remained finite and were comparable to each other.

The model response was in good agreement with the experimental observations. Plastic strain localization drove the damage evolution within the center of the specimen, which was

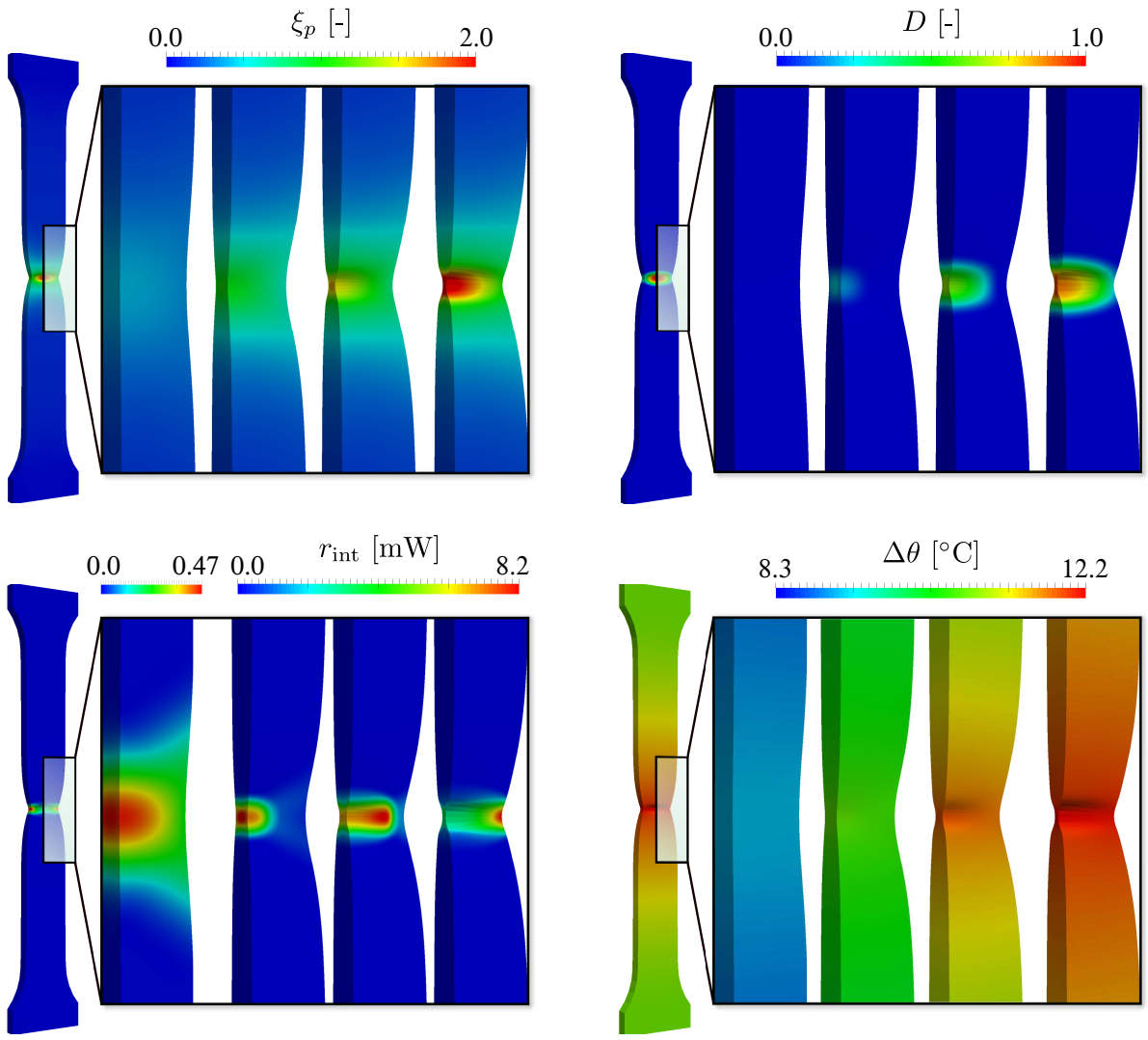

Figure 4.5: Accumulated plastic strain ξ_p, damage D, internal heat generation r_{int}, and change in temperature $\Delta\theta$, at displacement levels of $u_s = \{8.54, 11.23, 11.68, 12.14\}$ (highlighted in Figure 4.4) for a loading rate of 0.5 mm min^{-1}.

followed by a crack propagation towards the edges of the specimen, until complete failure occurred. Due to this localization, the heat generation accompanying plastic and damage evolution led to an increase in the temperature in these very areas. The corresponding fields at displacement levels of $u_s = \{8.54, 11.23, 11.68, 12.14\}$ (highlighted in Figure 4.4), are shown for the finest mesh (87090 elements) in Figure 4.5. It is instructive to point out that the heat generation resulting from the crack propagation was one order of magnitude higher than due to the preceding plastic deformations (note the different scales of the legends before and after the damage onset for r_{int}, in the bottom left in Figure 4.5). Therefore, the local heat generation

after the damage onset clearly indicated the current positions of the crack tip and propagation towards the edges, in addition.

With increasing loading speed, the local rise in temperature increased, due to the limited time for heat conduction within the specimen. Consequently, thermal softening of the material in these regions led to a decrease in yield stress and strain hardening. The latter became also evident from a decrease in the reaction force in the load displacement relations (see Figure 4.6). In addition, with increasing loading rates, the amount of plastic deformations within the center of the specimen increased and, thus, led to a shift of the crack initiation towards smaller displacement levels.

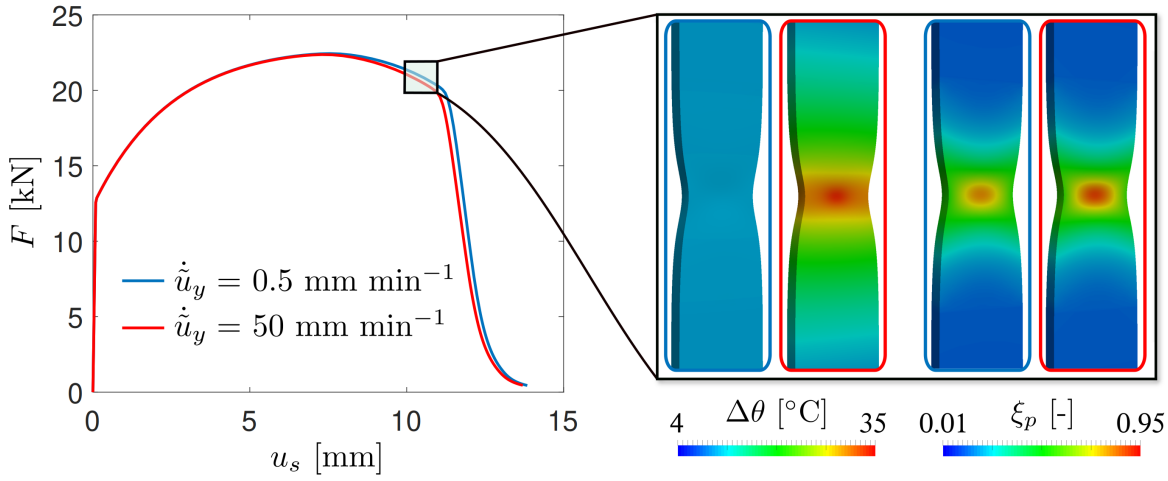

Figure 4.6: Comparison of reaction force for different loading rates (left) and corresponding accumulated plastic strain ξ_p as well as change in temperature $\Delta\theta$ for a displacement level of $u_s = 10.88$ (right).

4.5.2.2 Asymmetrically notched specimen

In this section, a rather academic example is discussed in order to investigate the model predictions regarding thermal expansion and the influence of the damage state on the heat conductivity, in a fully coupled transient heat transfer problem. To this end, a double notched tensile specimen was considered, where the dimensions were taken from Ambati et al. [2016], scaled by a factor of two (cf. Figure 4.7). For simplicity, a 2D plane strain computation with a thickness of 1 mm was conducted. The mechanical material parameter were chosen in line with the proposed values by Brepols et al. [2020]. The latter are listed, along with the thermal parameters (taken from Dittmann et al. [2020]), as Set 4 in Table 4.2.

In a first series of computations, a mesh convergence study was performed, by considering

uniaxial extension of the specimen with a loading speed of $\dot{\tilde{u}}$ =0.114 mm s^{-1}. The boundary conditions and the corresponding reaction force over displacement curves are depicted in Figure 4.7, for different mesh realizations. In all computations, quadrilateral elements with four integration points were employed. A clear convergence trend could be observed, i.e. the amount of dissipated energy strove towards a finite value. Consequently, a mesh consisting of 13955 elements was assumed to be sufficient for the following considered problem.

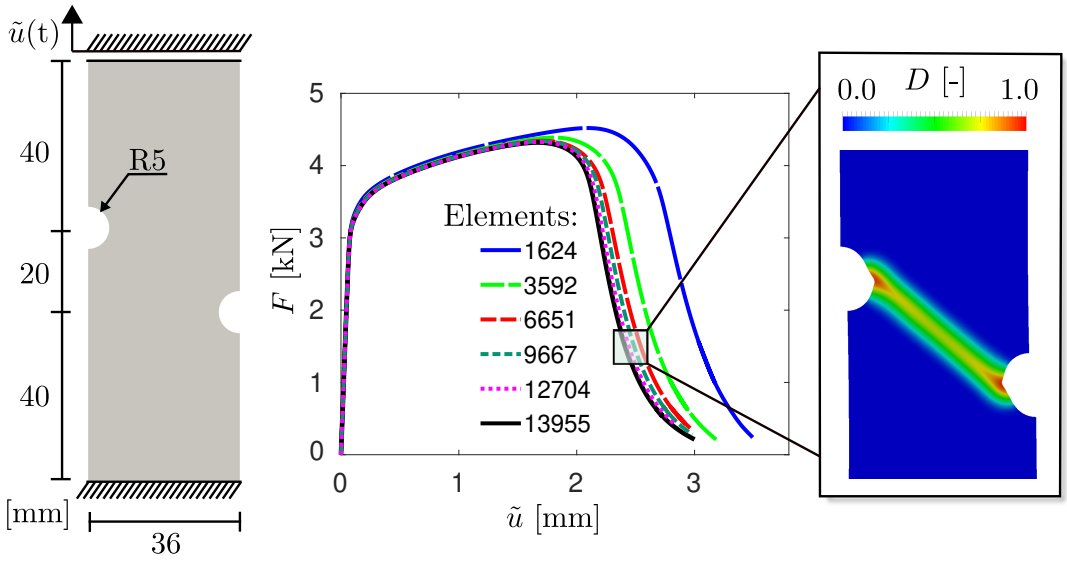

Figure 4.7: Geometry of asymmetrically notched specimen and first considered boundary value problem for the mesh convergence study (left). Resulting force over displacement for different mesh realizations (middle) and predicted deformation and damage evolution (right).

A qualitative comparison with the experimental data published in Ambati et al. [2016] showed good agreement, in terms of the emerging deformation processes and crack pattern (see Figure 4.7). Plastic strain localizations close to the notches and the formation of a plastic strain localization band was resolved. Furthermore, the model predictions regarding the initiation of two cracks at the notches, followed by a crack propagation within the localization branch until their final merging and complete failure, were in agreement with the experimentally observed behavior discussed in Ambati et al. [2016].

Subsequently, a more complex loading scenario was considered (see Figure 4.8). In a first loading step, the specimen with an initial temperature of $\theta(t_0) = 0$ °C was heated up. To this end, the temperature of the nodes at the bottom and top of the specimen were set to different, constant values in time of $\tilde{\theta} = 30$ °C and 15 °C, respectively. This led to a heterogeneous heating of the structure (see temperature field at t_1 in Figure 4.9). When the steady-state solution was reached (at $t \approx 400$ s), a constant temperature gradient in vertical direction was

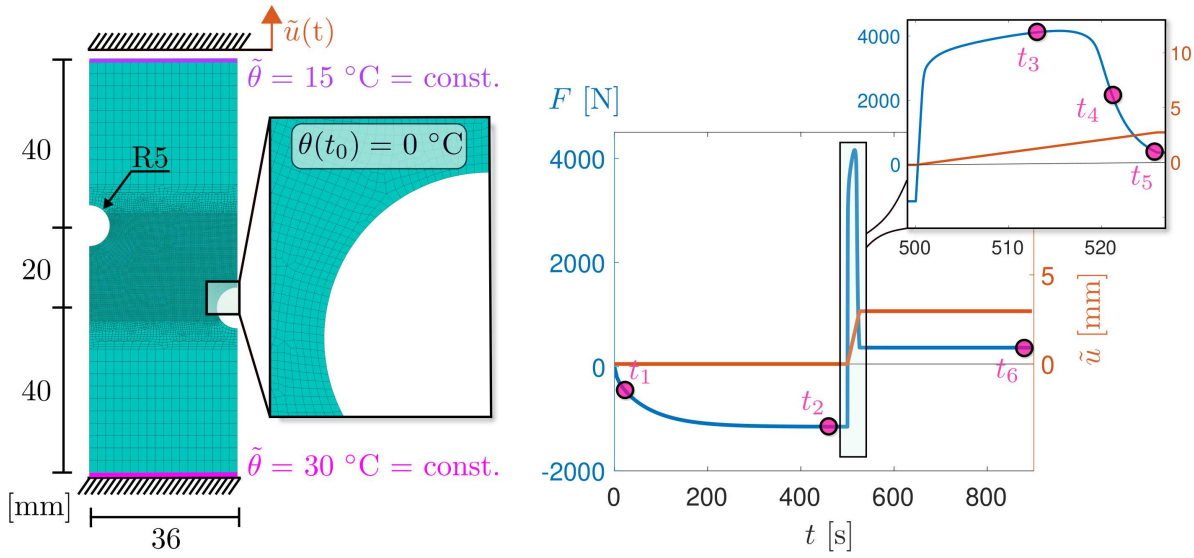

Figure 4.8: Geometry and mesh (13955 elements) of asymmetrically notched specimen and second considered boundary value problem (left). Prescribed displacement loading condition $\tilde{u}$ over time and resulting reaction force F (right).

present (see temperature field at t_2 in Figure 4.9). During this heating phase, the elongation in longitudinal direction was constrained (i.e. $\tilde{u} = 0$) for the first 500 seconds (see right hand side of Figure 4.8). Consequently, the thermal expansion of the material in vertical direction was hindered. This led to the evolution of compressive stresses in vertical direction (and a corresponding negative reaction force), which reached a constant value once the steady state solution was obtained (cf. Figure 4.8).

Next, the specimen was subjected to uniaxial extension with a prescribed loading speed of $\dot{\tilde{u}}$ =0.114 mm s^{-1}. Consequently, a complex interplay between different coupling phenomena arose. First, the temperature field changed as a result of thermo-elastic coupling and plastic deformations. The latter led to local heat sources in the areas with the highest plastic flow rates (see t_2-t_3 in Figure 4.9). At the onset of damage, even more heat was released locally. In addition to the degradation of the stiffness in the damaged regions, the thermal conductivity was reduced (cf. Equation (4.40)). This led to a significant change in the heat flux and the temperature gradient in these areas, due to the insulating effect of the emerging cracks (see t_4-t_5 in Figure 4.9). After the structure had almost completely failed, the displacement was held constant at $\tilde{u} = 3$ mm, for 370 seconds. In this way, the evolution of the temperature field towards a new equilibrium state, resulting from the prescribed thermal boundary conditions and the insulating diagonal crack pattern, was evident (see t_6 in Figure 4.9).

Despite the emerging large gradients within all three solution fields ($\boldsymbol{u}$, $\bar{D}$, and θ) and ob-

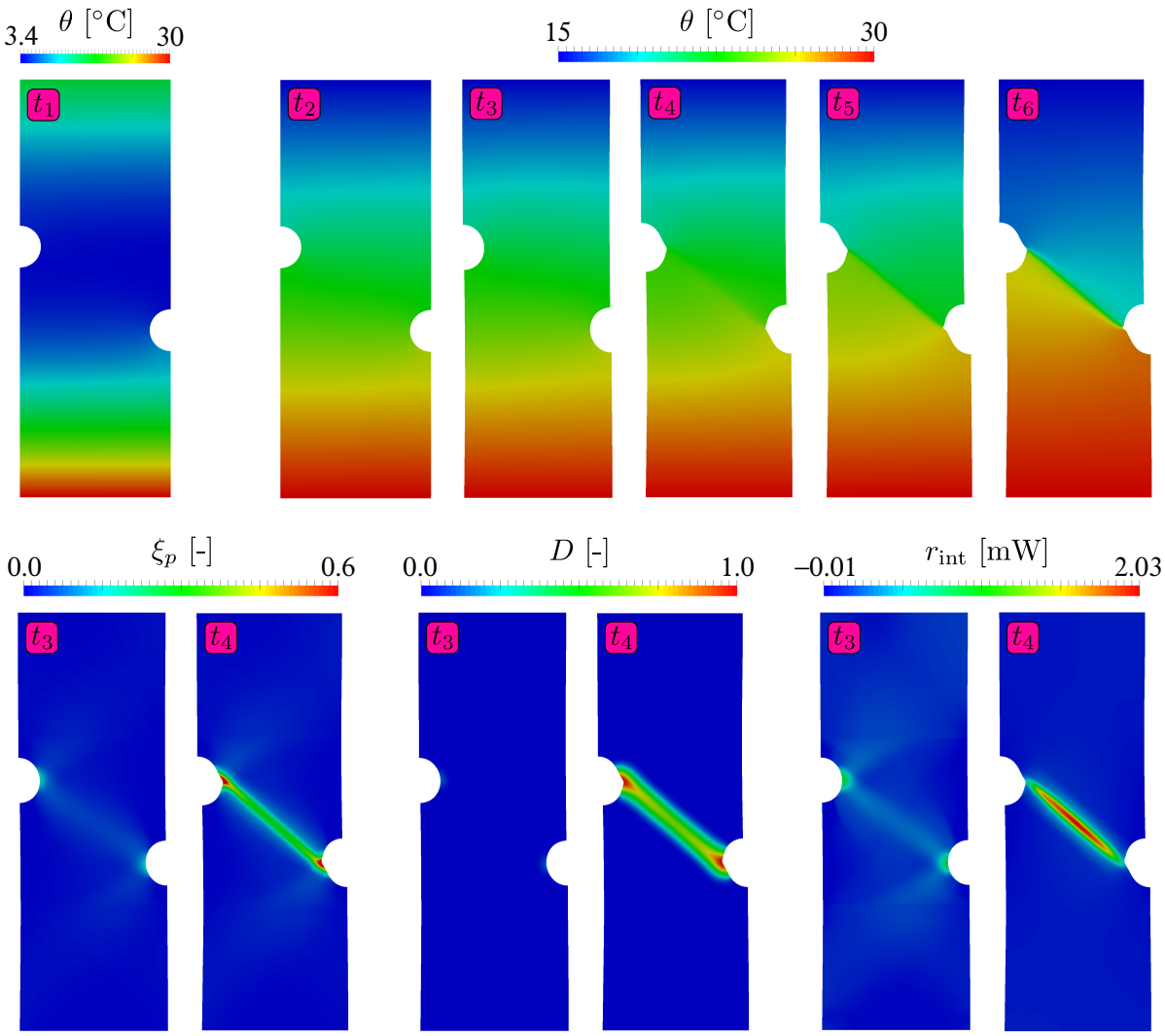

Figure 4.9: Contour plots for: Temperature θ, accumulated plastic strain ξ_p, damage D, and internal heat generation r_{int} for certain points in time ($t_i = \{20, 490, 511.9, 522, 526, 831\}$, highlighted in Figure 4.8).

served strong coupling phenomena, in particular at the end of the considered example, a satisfactory rate of convergence was achieved during all local and global iterations. In Table 4.3, the residual and normalized energy norms are shown for the three time steps t_3-t_5, highlighted in Figure 4.8. A quadratic rate of convergence was observed for purely thermoplastic problems, which is not shown in Table 4.3. With the onset of material softening (t_3-t_5), the rate of convergence was comparatively slow after the first iterations, resulting in a larger number of iterations, which is in line with the reported findings of Brepols et al. [2020] for isothermal computations. However, towards the last iterations a quadratic decrease was observed.

Table 4.3: Global convergence rates for the three time steps t_3-$t_5 = \{511.9, 522, 526\}$ highlighted in Figure 4.8

	Time t_3		Time t_4		Time t_5	
Iteration	Residual	Energy	Residual	Energy	Residual	Energy
0	2.5079E+03	1.0000E+00	4.2461E+03	1.0000E+00	4.2472E+02	1.0000E+00
1	1.0810E+00	4.3104E-04	5.2005E-01	1.2248E-04	1.1104E-02	2.6145E-05
2	6.0611E-02	2.4168E-05	1.2268E-01	2.8893E-05	5.1682E-05	1.2168E-07
3	5.9653E-03	2.3786E-06	2.8108E-02	6.6197E-06	5.2792E-09	1.2430E-11
4	6.4653E-04	2.5779E-07	7.3160E-04	1.7230E-07		
5	6.3801E-09	2.5440E-12	3.5218E-09	8.2943E-13		

4.6 Conclusion

In this work, a novel geometrically nonlinear constitutive framework was proposed for (metallic) materials, to analyze and predict (ductile) fracture and the corresponding thermal coupling effects. The model can be considered as the thermo-mechanical extension of the work by Brepols et al. [2020], with the simplification of a linear kinematic hardening law. This theory was derived in a thermodynamically consistent manner and treats damage and plasticity as truly distinct dissipative mechanisms by employing a two-surface ansatz with individual onset and loading / unloading conditions. The influence of the temperature was considered by temperature dependent material parameters within the Helmholtz free energy. The internal heat generation, associated with thermo-elastic coupling and irreversible processes (i.e. damage and plasticity), was derived from the first law of thermodynamics, in addition.

To ensure mesh-insensitive results, a gradient-extension of the damage variable on the basis of the micromorphic approach by Forest [2009, 2016] was employed. Consequently, a fully coupled problem was obtained, where the balance of linear momentum, the energy balance, and an additional partial differential equation, related to the global ‘nonlocal ’damage variable must be solved. The linearization of the corresponding weak forms and the computation of the 12 material tangent operators via automatic differentiation was discussed. Conclusively, this resulted in a flexible algorithmic framework that, together with the chosen two-surface approach, allows for versatile use and adaptation of the model.

Computational examples were performed, in order to show the model’s mesh regularization properties in fully-coupled transient heat transfer problems. Furthermore, the good convergence behavior of the global Newton-Raphson scheme, in particular in situations where large gradients as well as interactions within and between all physical (solution) fields arose, was highlighted. The predicted local heat accumulation, corresponding to thermo-elastic cooling and plastic deformations, was verified by the experimental data of Rose and Menzel [2020].

From the computation of thermo-mechanically coupled structural problems, corresponding to experimental data by Ambati et al. [2016], it became evident that the model could capture temperature-induced softening as a source of additional plastic strain localization, which influences the onset of damage. Conclusively, the model allowed for a multi-physical analysis and was in accordance with experimental results in terms of the observed phenomena (hardening, necking, crack initiation and propagation).

Despite the demonstrated promising capabilities of the proposed framework, a more comprehensive experimental characterization and validation of the individual model parts is crucial in the future. To this end, an extensive experimental study, investigating cyclic loading, different loading rates and temperatures by employing digital image correlation and infrared thermography (comparable to the setups presented in Felder, Vu, Reese and Simon [2020] and Rose and Menzel [2020]), is planned.

The current model is restricted to rate-independent plasticity and damage, which is a simplification for most metals, even at room temperature. However, the numerical example in Section 4.5.2.1 demonstrates that different loading rates lead to the prediction of varying degrees of thermal softening and thus to a rate-dependent stress response (see Figure 4.6). From the results of the planned experimental study, it must be deduced whether the current rate-independent plasticity and damage formulation, in combination with the modeled back-coupling phenomena related to material self-heating, is suitable to represent the material response for different loading rates. If it turns out that the current formulation is not sufficiently accurate, incorporating rate-dependent plasticity into the model framework is straightforward but leads of course to additional material parameters. Furthermore, related to the findings regarding gradient-enhanced (thermo-)plasticity (cf. Wcislo and Pamin [2017], Dittmann et al. [2018], Aldakheel and Miehe [2017])), the effect of introducing an additional gradient term, related to plastic deformations, would be interesting. Very recently, studies of the authors in the field of reduced integration with hourglass stabilization for gradient-extended damage (Barfusz et al. [2021]), based on the well-established concepts by Reese [2002, 2003*b*, 2005], were published. This special finite element technology cures potential locking effects, leads to a higher efficiency, and should, thus, be also investigated in the context of the presented framework in the future.

Acknowledgments: S. Felder, T. Brepols, and S. Reese gratefully acknowledge the financial support provided by the German Research Foundation (DFG) within the projects RE 1057/48-1 (project number: 440959716) and RE 1057/52-1 (project number: 454873500). Additionally, S. Reese acknowledges the funding which was granted within the subproject M03 of the Transregional Collaborative Research Centre (CRC) Transregio (TRR) 136/2

(project number: 1802283). Furthermore, funding of the DFG project RE 1057/51-1 (project number: 453715964) is gratefully acknowledged by T. Brepols and S. Reese.

Finally, the authors are grateful for the published experimental data by Ambati et al. [2016] and would like to thank the authors of Rose and Menzel [2020] for the fruitful discussions and the provision of the experimental data.

4.7 Appendix

4.7.1

In the following it is shown that the invariants of $\boldsymbol{C}_e$ can be equivalently expressed in terms of $\boldsymbol{C}$, $\boldsymbol{C}_p$, and θ. The three invariants of $\boldsymbol{C}_e$ are

$$\begin{aligned} I_{\boldsymbol{C}_e} &:= \text{tr}(\boldsymbol{C}_e) = \text{tr}\left(\frac{1}{\vartheta^2}\boldsymbol{F}_p^{-T}\boldsymbol{C}\boldsymbol{F}_p^{-1}\right) = \text{tr}\left(\frac{1}{\vartheta^2}\boldsymbol{C}_p^{-1}\boldsymbol{C}\right) \\ II_{\boldsymbol{C}_e} &:= \text{tr}(\boldsymbol{C}_e^2) = \text{tr}\left(\frac{1}{\vartheta^2}\boldsymbol{F}_p^{-T}\boldsymbol{C}\boldsymbol{F}_p^{-1}\frac{1}{\vartheta^2}\boldsymbol{F}_p^{-T}\boldsymbol{C}\boldsymbol{F}_p^{-1}\right) = \text{tr}\left(\left(\frac{1}{\vartheta^2}\boldsymbol{C}_p^{-1}\boldsymbol{C}\right)^2\right) \\ III_{\boldsymbol{C}_e} &:= \det(\boldsymbol{C}_e) = \det\left(\frac{1}{\vartheta^2}\boldsymbol{F}_p^{-T}\boldsymbol{C}\boldsymbol{F}_p^{-1}\right) = \det\left(\frac{1}{\vartheta^2}\boldsymbol{C}_p^{-1}\boldsymbol{C}\right) \end{aligned} \tag{4.70}$$

4.7.2

Starting point is the Clausius-Duhem inequality

$$\boldsymbol{S} : \frac{1}{2}\dot{\boldsymbol{C}} - \dot{\psi} - \eta\dot{\theta} - \frac{1}{\theta}\,\boldsymbol{q}_0 \cdot \text{Grad}(\theta) + \underbrace{a_{0_i}\,\dot{\bar{D}} + \boldsymbol{b}_{0_i} \cdot \text{Grad}(\dot{\bar{D}})}_{\text{micromorphic extension}} \geq 0 \tag{4.71}$$

which must be fulfilled for arbitrary processes. Next, the total derivative of the Helmholtz free energy $\psi = \hat{\psi}(\boldsymbol{C}_e, \boldsymbol{C}_p, \xi_p, D, \xi_d, \bar{D}, \theta)$ (cf. Equation 4.18)) is inserted into (4.71)

$$\begin{aligned} &\boldsymbol{S} : \frac{1}{2}\,\dot{\boldsymbol{C}} - f_d(D)\left(\frac{\partial\psi_e}{\partial\boldsymbol{C}_e} : \dot{\boldsymbol{C}}_e + \frac{\partial\psi_p}{\partial\boldsymbol{C}_p} : \dot{\boldsymbol{C}}_p + \frac{\partial\psi_p}{\partial\xi_p}\,\dot{\xi}_p\right) - \left(\frac{\mathrm{d}f_d}{\mathrm{d}D}(\psi_e + \psi_p) + \frac{\partial\psi_{\bar{d}}}{\partial D}\right)\dot{D} \\ &- \frac{\partial\psi_d}{\partial\xi_d}\,\dot{\xi}_d - \frac{\partial\psi_{\bar{d}}}{\partial\bar{D}}\,\dot{\bar{D}} - \frac{\partial\psi_{\bar{d}}}{\partial\,\text{Grad}\left(\bar{D}\right)}\,\text{Grad}\left(\dot{\bar{D}}\right) - \left(\eta + \frac{\partial\hat{\psi}}{\partial\theta}\right)\dot{\theta} \\ &- \frac{1}{\theta}\,\boldsymbol{q}_0 \cdot \text{Grad}(\theta) + a_{0_i}\,\dot{\bar{D}} + \boldsymbol{b}_{0_i} \cdot \text{Grad}\left(\dot{\bar{D}}\right) \geq 0. \end{aligned} \tag{4.72}$$

To reformulate the relation above, the material time derivative

$$\dot{\boldsymbol{C}}_e = -\boldsymbol{L}_p^T\boldsymbol{C}_e + \frac{1}{\vartheta^2}\boldsymbol{F}_p^{-T}\dot{\boldsymbol{C}}\boldsymbol{F}_p^{-1} - \boldsymbol{C}_e\boldsymbol{L}_p - \frac{2}{\vartheta^2}\boldsymbol{F}_p^{-T}\boldsymbol{C}\boldsymbol{F}_p^{-1}\,\alpha\,\dot{\theta} \tag{4.73}$$

is derived from (4.17), by employing the product rule of differentiation and considering the identities $\dot{\boldsymbol{F}}_p^{-1} = -\boldsymbol{F}_p^{-1}\dot{\boldsymbol{F}}_p\boldsymbol{F}_p^{-1}$, $\dot{\boldsymbol{F}}_p^{-T} = -\boldsymbol{F}_p^{-T}\dot{\boldsymbol{F}}_p^T\boldsymbol{F}_p^{-T}$, and $\dot{\vartheta} = \mathrm{d}/\mathrm{d}t\,(\exp(\alpha(\theta - \theta_0))) = \vartheta\,\alpha\,\dot{\theta}$. In addition, the plastic velocity gradient $\boldsymbol{L}_p = \dot{\boldsymbol{F}}_p\boldsymbol{F}_p^{-1}$ is defined. Inserting (4.73) into

(4.72) and assuming that ψ_e and ψ_p are isotropic functions of $\boldsymbol{C}_e$ and $\boldsymbol{C}_p$, respectively, yields the following inequality

$$\begin{aligned}
&\left(\boldsymbol{S} - 2\, f_d(D)\, \frac{1}{\vartheta^2} \boldsymbol{F}_p^{-1} \frac{\partial \psi_e}{\partial \boldsymbol{C}_e} \boldsymbol{F}_p^{-T}\right) : \frac{1}{2} \dot{\boldsymbol{C}} + \left(\boldsymbol{b}_{0_i} - \frac{\partial \psi_{\bar{d}}}{\partial\, \mathrm{Grad}(\bar{D})}\right) \mathrm{Grad}\left(\dot{\bar{D}}\right) \\
&+ \left(a_{0_i} - \frac{\partial \psi_{\bar{d}}}{\partial \bar{D}}\right) \dot{\bar{D}} - \left(\eta + \frac{\partial \hat{\psi}}{\partial \theta} - \boldsymbol{C}\, \alpha\, 2\, f_d(D)\, \frac{1}{\vartheta^2} \boldsymbol{F}_p^{-1} \frac{\partial \psi_e}{\partial \boldsymbol{C}_e} \boldsymbol{F}_p^{-T} : \boldsymbol{I}\right) \dot{\theta} - \frac{1}{\theta}\, \boldsymbol{q}_0 \cdot \mathrm{Grad}(\theta) \\
&+ f_d(D) \left(2\, \boldsymbol{C}_e \frac{\partial \psi_e}{\partial \boldsymbol{C}_e} - 2\, \boldsymbol{F}_p \frac{\partial \psi_p}{\partial \boldsymbol{C}_p} \boldsymbol{F}_p^T\right) : \boldsymbol{D}_p - f_d(D)\, \frac{\partial \psi_p}{\partial \xi_p}\, \dot{\xi}_p - \frac{\partial \psi_d}{\partial \xi_d}\, \dot{\xi}_d \\
&- \left(\frac{\mathrm{d} f_d}{\mathrm{d} D}(\psi_e + \psi_p) + \frac{\partial \psi_{\bar{d}}}{\partial D}\right) \dot{D} \geq 0
\end{aligned} \tag{4.74}$$

Here, the relation $\dot{\boldsymbol{C}}_p = 2\, \boldsymbol{F}_p^T \boldsymbol{D}_p \boldsymbol{F}_p$ is employed and $\boldsymbol{D}_p := \mathrm{sym}(\boldsymbol{L}_p)$ holds.

Following the standard arguments by Coleman and Noll [1961] the following alternative representations for the second Piola-Kirchhoff stress as well as the entropy

$$\boldsymbol{S} = 2\, f_d(D)\, \frac{1}{\vartheta^2} \boldsymbol{F}_p^{-1} \frac{\partial \psi_e}{\partial \boldsymbol{C}_e} \boldsymbol{F}_p^{-T}, \quad \eta = -\frac{\partial \hat{\psi}}{\partial \theta} + \mathrm{tr}(\boldsymbol{C}\boldsymbol{S})\alpha, \tag{4.75}$$

can be established. Together with the relations for the internal forces related to the micromorphic variable and its gradient (4.7) and the heat flux (4.8), the first two lines of inequality (4.74) are always larger than or equal to zero.

For the sake of a more compact format of the constitutive equations, the following quantities are defined in addition

$$\boldsymbol{M} := f_d(D)\, 2\, \boldsymbol{C}_e \frac{\partial \psi_e}{\partial \boldsymbol{C}_e}, \quad \boldsymbol{\chi} := f_d(D)\, 2\, \boldsymbol{F}_p \frac{\partial \psi_p}{\partial \boldsymbol{C}_p} \boldsymbol{F}_p^T \tag{4.76}$$

representing the Mandel-like stress tensor and the back-stress tensor in the intermediate configuration ic, respectively. Furthermore, the thermodynamic conjugated driving forces to damage Y, isotropic hardening q_p, and damage hardening q_d are defined by

$$Y := -\left(\frac{\mathrm{d} f_d}{\mathrm{d} D}(\psi_e + \psi_p) + \frac{\partial \psi_{\bar{d}}}{\partial D}\right), \quad q_p := f_d(D)\, \frac{\partial \psi_p}{\partial \xi_p}, \quad q_d := \frac{\partial \psi_d}{\partial \xi_d} \tag{4.77}$$

Hence, the remaining inequality can be rewritten as

$$(\boldsymbol{M} - \boldsymbol{\chi}) : \boldsymbol{D}_p - q_p\, \dot{\xi}_p - q_d\, \dot{\xi}_d + Y\, \dot{D} \geq 0 \tag{4.78}$$

4.7.3

To express the heat generation related to plasticity (4.30) in terms of $\boldsymbol{C}_p$, $\boldsymbol{S}$, and $\boldsymbol{X}$, the relation $\boldsymbol{D}_p = \frac{1}{2}\boldsymbol{F}_p^{-T}\dot{\boldsymbol{C}}_p\boldsymbol{F}_p^{-1}$ must be recalled. Furthermore, recall

$$\boldsymbol{M} = 2\, f_d\, \boldsymbol{C}_e \frac{\partial \psi}{\partial \boldsymbol{C}_e} = 2\, f_d\, \frac{1}{\vartheta^2}\boldsymbol{F}_p^{-T}\boldsymbol{C}\boldsymbol{F}_p^{-1}\frac{\partial \psi}{\partial \boldsymbol{C}_e} = \boldsymbol{F}_p^{-T}\boldsymbol{C}\boldsymbol{S}\boldsymbol{F}_p^{T} \tag{4.79}$$

Thus,

$$\begin{aligned} \boldsymbol{M} : \boldsymbol{D}_p &= \frac{1}{2}\,\mathrm{tr}(\boldsymbol{F}_p^{-T}\boldsymbol{C}\boldsymbol{S}\boldsymbol{F}_p^{T}\boldsymbol{F}_p^{-T}\dot{\boldsymbol{C}}_p\boldsymbol{F}_p^{-1}) \\ &= \frac{1}{2}\,\boldsymbol{C}\boldsymbol{S} : (\dot{\boldsymbol{C}}_p\boldsymbol{C}_p^{-1})^T = \frac{1}{2}\,\boldsymbol{C}\boldsymbol{S} : \boldsymbol{C}_p^{-1}\dot{\boldsymbol{C}}_p \end{aligned} \tag{4.80}$$

follows. Analogously,

$$\theta\,\frac{\partial \boldsymbol{M}}{\partial \theta} : \boldsymbol{D}_p = \frac{1}{2}\,\theta\,\boldsymbol{C}\frac{\partial \boldsymbol{S}}{\partial \theta} : \boldsymbol{C}_p^{-1}\dot{\boldsymbol{C}}_p \tag{4.81}$$

holds. Conclusively, the following transformations are considered

$$\boldsymbol{\chi} : \boldsymbol{D}_p = \frac{1}{2}\,\mathrm{tr}(\boldsymbol{F}_p\boldsymbol{X}\boldsymbol{F}_p^{T}\boldsymbol{F}_p^{-T}\dot{\boldsymbol{C}}_p\boldsymbol{F}_p^{-1}) = \frac{1}{2}\boldsymbol{X} : \dot{\boldsymbol{C}}_p \tag{4.82}$$

$$\theta\,\frac{\partial \boldsymbol{\chi}}{\theta} : \boldsymbol{D}_p = \frac{1}{2}\,\theta\,\frac{\partial \boldsymbol{X}}{\partial \theta} : \dot{\boldsymbol{C}}_p \tag{4.83}$$

4.7.4

In the following the reduction of the derived relation for the stress to a thermo-elastic theory is discussed. To this end, the Cauchy stress tensor $\boldsymbol{\sigma} = 1/(\mathrm{det}\boldsymbol{F})\boldsymbol{F}\boldsymbol{S}\boldsymbol{F}^T$ is obtained by a push-forward of the second Piola-Kirchhoff stress tensor, viz.

$$\begin{aligned} \boldsymbol{\sigma} =& \frac{1}{\mathrm{det}(\boldsymbol{F})}\, f_d(D)\, \boldsymbol{F}\left(\mu\left(\frac{1}{\vartheta^2}\boldsymbol{C}_p^{-1} - \boldsymbol{C}^{-1}\right) + \frac{\Lambda}{2}\left(\frac{\mathrm{det}(\boldsymbol{C})}{\vartheta^6\,\mathrm{det}(\boldsymbol{C}_p)} - 1\right)\boldsymbol{C}^{-1}\right)\boldsymbol{F}^T \\ =& \frac{1}{\mathrm{det}(\boldsymbol{F})}\, f_d(D)\, \left(\mu\,(\boldsymbol{B}_e - \boldsymbol{I}) + \frac{\Lambda}{2}\,(\mathrm{det}(\boldsymbol{B}_e) - 1)\,\boldsymbol{I}\right) \end{aligned} \tag{4.84}$$

where the elastic left Cauchy-Green tensor $\boldsymbol{B}_e = \boldsymbol{F}_e\boldsymbol{F}_e^T = 1/\vartheta^2\,\boldsymbol{F}\boldsymbol{C}_p^{-1}\boldsymbol{F}^T$ was introduced. Next, assuming no damage $\dot{D} = 0$, nor plastic evolution $\dot{\boldsymbol{C}}_p = \boldsymbol{0}$ and hence $f_d = 1$ and $\boldsymbol{C}_p = \boldsymbol{I}$, respectively, a thermo-elastic theory is obtained

$$\boldsymbol{\sigma} = \frac{1}{\mathrm{det}(\boldsymbol{F})}\,\left(\mu\left(\frac{1}{\vartheta^2}\boldsymbol{B} - \boldsymbol{I}\right) + \frac{\Lambda}{2}\left(\frac{1}{\vartheta^6}\mathrm{det}(\boldsymbol{B}) - 1\right)\boldsymbol{I}\right) \tag{4.85}$$

Finally, the resulting thermal stresses for a fully constrained thermal expansion (i.e. $\boldsymbol{B} = \boldsymbol{I}$) are examined:

$$\boldsymbol{\sigma} = \left(\mu \left(\frac{1}{\vartheta^2} - 1 \right) \boldsymbol{I} + \frac{\Lambda}{2} \left(\frac{1}{\vartheta^6} - 1 \right) \boldsymbol{I} \right) \tag{4.86}$$

Subsequently, the first two terms of a Taylor-series approximation of $1/\vartheta^2$ and $1/\vartheta^6$ around the point $\Delta\theta = 0$ are considered

$$\begin{aligned} 1/\vartheta^2 &= 1/(\exp(2\,\alpha\,\Delta\theta)) \approx 1 - 2\,\alpha\,\Delta\theta \\ 1/\vartheta^6 &= 1/(\exp(6\,\alpha\,\Delta\theta)) \approx 1 - 6\,\alpha\,\Delta\theta \end{aligned} \tag{4.87}$$

By inserting these approximations into (4.86), the known thermal Cauchy stress tensor is obtained

$$\boldsymbol{\sigma} = -\alpha\,(2\,\mu + 3\,\Lambda)\Delta\theta\,\boldsymbol{I} = -3\,\alpha\,K\,\Delta\theta\,\boldsymbol{I} \tag{4.88}$$

where the bulk modulus $K = 2/3\,\mu + \Lambda$ was introduced.

4.7.5

In the following, the linearization of the weak forms (4.41)-(4.45) is discussed.

Linearization of g_u:

The linearization of g_u around a known state $(\boldsymbol{u}^*, \bar{D}^*, \theta^*)$ is defined as

$$\begin{aligned} \mathcal{L}g_u(\Delta\boldsymbol{u}, \Delta\bar{D}, \Delta\theta, \delta\boldsymbol{u}) &= g_u(\boldsymbol{u}^*, \bar{D}^*, \theta^*, \delta\boldsymbol{u}) + \mathcal{D}_u g_u(\boldsymbol{u}^*, \bar{D}^*, \theta^*, \delta\boldsymbol{u})[\Delta\boldsymbol{u}] \\ &+ \mathcal{D}_{\bar{D}} g_u(\boldsymbol{u}^*, \bar{D}^*, \theta^*, \delta\boldsymbol{u})[\Delta\bar{D}] + \mathcal{D}_\theta g_u(\boldsymbol{u}^*, \bar{D}^*, \theta^*, \delta\boldsymbol{u})[\Delta\theta] \end{aligned} \tag{4.89}$$

The first Gâteaux derivative $\mathcal{D}_u g_u(\boldsymbol{u}^*, \bar{D}^*, \theta^*, \delta\boldsymbol{u})[\Delta\boldsymbol{u}]$ is given as

$$
\begin{aligned}
&\mathcal{D}_u g_u(\boldsymbol{u}^*, \bar{D}^*, \theta^*, \delta\boldsymbol{u})[\Delta\boldsymbol{u}] = \left.\frac{\mathrm{d}}{\mathrm{d}\epsilon}\right|_{\epsilon=0} g_u(\boldsymbol{u}^* + \epsilon\,\Delta\boldsymbol{u}, \bar{D}^*, \theta^*, \delta\boldsymbol{u}) \\
&= \left.\frac{\mathrm{d}}{\mathrm{d}\epsilon}\right|_{\epsilon=0} \left(\int_{B_0} \left((\boldsymbol{F}(\epsilon)\boldsymbol{S}(\boldsymbol{E}(\boldsymbol{F}(\epsilon)), \bar{D}^*, \theta^*) \right) : \mathrm{Grad}(\delta\boldsymbol{u}) - \boldsymbol{f}_0 \cdot \delta\boldsymbol{u} \right) \mathrm{d}V - \int_{\partial B_{0_t}} \boldsymbol{t}_0 \cdot \delta\boldsymbol{u}\,\mathrm{d}A \right) \\
&= \left.\frac{\mathrm{d}}{\mathrm{d}\epsilon}\right|_{\epsilon=0} \int_{B_0} \left((\boldsymbol{F}(\epsilon)\,\boldsymbol{S}(\boldsymbol{E}(\boldsymbol{F}(\epsilon)), \bar{D}^*, \theta^*) \right) : \mathrm{Grad}(\delta\boldsymbol{u}))\,\mathrm{d}V \\
&= \int_{B_0} \left(\frac{\partial \boldsymbol{F}}{\partial \epsilon}\,\boldsymbol{S}(\boldsymbol{E}(\boldsymbol{F}(\epsilon)), \bar{D}^*, \theta^*) + \boldsymbol{F}(\epsilon) \left(\frac{\partial \boldsymbol{S}}{\partial \boldsymbol{E}} \left[\frac{\partial \boldsymbol{E}}{\partial \boldsymbol{F}} \left[\frac{\partial \boldsymbol{F}}{\partial \epsilon} \right] \right] \right) \right) \Bigg|_{\epsilon=0} : \mathrm{Grad}(\delta\boldsymbol{u}))\,\mathrm{d}V \\
&= \int_{B_0} \left(\mathrm{Grad}(\Delta\boldsymbol{u})\, \underbrace{\boldsymbol{S}(\boldsymbol{E}(\boldsymbol{F}^*, \bar{D}^*, \theta^*)}_{\boldsymbol{S}^*} \right) : \mathrm{Grad}(\delta\boldsymbol{u})\,\mathrm{d}V \\
&\qquad + \int_{B_0} \boldsymbol{F}^* \left(\frac{\partial \boldsymbol{S}}{\partial \boldsymbol{E}} \left[\underbrace{\frac{1}{2} \left(\mathrm{Grad}(\Delta\boldsymbol{u})^T \boldsymbol{F}^* + \boldsymbol{F}^{*T} \mathrm{Grad}(\Delta\boldsymbol{u}) \right)}_{\Delta\boldsymbol{E}^*} \right] \right) : \mathrm{Grad}(\delta\boldsymbol{u})\,\mathrm{d}V \\
&= \int_{B_0} \left(\mathrm{Grad}(\Delta\boldsymbol{u})\,\boldsymbol{S}^* \right) : \mathrm{Grad}(\delta\boldsymbol{u})\,\mathrm{d}V + \int_{B_0} \frac{\partial \boldsymbol{S}}{\partial \boldsymbol{E}} \left[\Delta\boldsymbol{E}^* \right] : \left(\mathrm{Grad}(\delta\boldsymbol{u})^T \boldsymbol{F}^* \right)\,\mathrm{d}V \\
&= \int_{B_0} \left(\mathrm{Grad}(\Delta\boldsymbol{u})\,\boldsymbol{S}^* \right) : \mathrm{Grad}(\delta\boldsymbol{u})\,\mathrm{d}V \\
&\qquad + \int_{B_0} \frac{\partial \boldsymbol{S}}{\partial \boldsymbol{E}} \left[\Delta\boldsymbol{E}^* \right] : \left(\underbrace{\frac{1}{2} \left(\mathrm{Grad}(\delta\boldsymbol{u})^T \boldsymbol{F}^* + \boldsymbol{F}^{*T} \mathrm{Grad}(\delta\boldsymbol{u}) \right)}_{\delta\boldsymbol{E}^*} \right) \mathrm{d}V \\
&= \int_{B_0} \left(\mathrm{Grad}(\Delta\boldsymbol{u})\,\boldsymbol{S}^* \right) : \mathrm{Grad}(\delta\boldsymbol{u})\,\mathrm{d}V + \int_{B_0} \frac{\partial \boldsymbol{S}}{\partial \boldsymbol{E}} \left[\Delta\boldsymbol{E}^* \right] : \delta\boldsymbol{E}^* \mathrm{d}V
\end{aligned}
\tag{4.90}
$$

where

$$
\boldsymbol{F}(\epsilon) = \boldsymbol{I} + \mathrm{Grad}(\boldsymbol{u}^* + \epsilon\Delta\boldsymbol{u}) = \boldsymbol{F}^* + \epsilon\,\mathrm{Grad}(\Delta\boldsymbol{u}) \tag{4.91}
$$

The second Gâteaux derivative $\mathcal{D}_{\bar{D}} g_u(\boldsymbol{u}^*, \bar{D}^*, \theta^*, \delta\boldsymbol{u})[\Delta\bar{D}]$ is given as

$$\begin{aligned}
&\mathcal{D}_{\bar{D}} g_u(\boldsymbol{u}^*, \bar{D}^*, \theta^*, \delta\boldsymbol{u})[\Delta\bar{D}] = \left.\frac{\mathrm{d}}{\mathrm{d}\epsilon}\right|_{\epsilon=0} g_u(\boldsymbol{u}^*, \bar{D}^* + \epsilon\,\Delta\bar{D}, \theta^*, \delta\boldsymbol{u}) \\
&= \left.\frac{\mathrm{d}}{\mathrm{d}\epsilon}\right|_{\epsilon=0} \left(\int_{B_0} \left(\boldsymbol{F}^*\,\boldsymbol{S}(\boldsymbol{F}^*, \bar{D}(\epsilon), \theta^*) : \mathrm{Grad}(\delta\boldsymbol{u}) - \boldsymbol{f}_0 \cdot \delta\boldsymbol{u}\right) \mathrm{d}V - \int_{\partial B_{0_t}} \boldsymbol{t}_0 \cdot \delta\boldsymbol{u}\,\mathrm{d}A \right) \\
&= \left.\frac{\mathrm{d}}{\mathrm{d}\epsilon}\right|_{\epsilon=0} \int_{B_0} \left(\boldsymbol{F}^*\,\boldsymbol{S}(\boldsymbol{F}^*, \bar{D}(\epsilon), \theta^*)\right) : \mathrm{Grad}(\delta\boldsymbol{u}))\,\mathrm{d}V \\
&= \int_{B_0} \left(\boldsymbol{F}^* \frac{\partial \boldsymbol{S}}{\partial \bar{D}} \frac{\partial \bar{D}}{\partial \epsilon} \right)\Bigg|_{\epsilon=0} : \mathrm{Grad}(\delta\boldsymbol{u}))\,\mathrm{d}V \\
&= \int_{B_0} \left(\frac{\partial \boldsymbol{S}}{\partial \bar{D}}\,\Delta\bar{D} \right) : \left(\mathrm{Grad}(\delta\boldsymbol{u})^T \boldsymbol{F}^*\right)\,\mathrm{d}V \\
&= \int_{B_0} \left(\frac{\partial \boldsymbol{S}}{\partial \bar{D}}\,\Delta\bar{D} \right) : \Bigg(\underbrace{\frac{1}{2}\left(\mathrm{Grad}(\delta\boldsymbol{u})^T \boldsymbol{F}^* + \boldsymbol{F}^{*T} \mathrm{Grad}(\delta\boldsymbol{u})\right)}_{\delta\boldsymbol{E}^*} \Bigg)\,\mathrm{d}V \\
&= \int_{B_0} \left(\frac{\partial \boldsymbol{S}}{\partial \bar{D}}\,\Delta\bar{D} \right) : \delta\boldsymbol{E}^*\,\mathrm{d}V
\end{aligned} \tag{4.92}$$

where

$$\bar{D}(\epsilon) = \bar{D}^* + \epsilon\,\Delta\bar{D} \tag{4.93}$$

The third Gâteaux derivative $\mathcal{D}_{\theta} g_u(\boldsymbol{u}^*, \bar{D}^*, \theta^*, \delta\boldsymbol{u})[\Delta\theta]$ is computed analogously viz.

$$\begin{aligned}
&\mathcal{D}_{\theta} g_u(\boldsymbol{u}^*, \bar{D}^*, \theta^*, \delta\boldsymbol{u})[\Delta\theta] = \left.\frac{\mathrm{d}}{\mathrm{d}\epsilon}\right|_{\epsilon=0} g_u(\boldsymbol{u}^*, \bar{D}^*, \theta^* + \epsilon\,\Delta\theta, \delta\boldsymbol{u}) \\
&= \left.\frac{\mathrm{d}}{\mathrm{d}\epsilon}\right|_{\epsilon=0} \left(\int_{B_0} \left(\boldsymbol{F}^*\,\boldsymbol{S}(\boldsymbol{F}^*, \bar{D}^*, \theta(\epsilon)) : \mathrm{Grad}(\delta\boldsymbol{u}) - \boldsymbol{f}_0 \cdot \delta\boldsymbol{u}\right) \mathrm{d}V - \int_{\partial B_{0_t}} \boldsymbol{t}_0 \cdot \delta\boldsymbol{u}\,\mathrm{d}A \right) \\
&= \int_{B_0} \left(\frac{\partial \boldsymbol{S}}{\partial \theta}\,\Delta\theta \right) : \delta\boldsymbol{E}^*\,\mathrm{d}V
\end{aligned} \tag{4.94}$$

where

$$\theta(\epsilon) = \theta^* + \epsilon\,\Delta\theta \tag{4.95}$$

The increment Δg_u is therefore defined as

$$\begin{aligned}
\Delta g_u &= \mathcal{D}_u g_u(\boldsymbol{u}, \bar{D}^*, \theta^*, \delta\boldsymbol{u})[\Delta\boldsymbol{u}] + \mathcal{D}_{\bar{D}} g_u(\boldsymbol{u}^*, \bar{D}^*, \theta^*, \delta\boldsymbol{u})[\Delta\bar{D}] + \mathcal{D}_\theta g_u(\boldsymbol{u}^*, \bar{D}^*, \theta^*, \delta\boldsymbol{u})[\Delta\theta] \\
&= \int_{B_0} \left(\mathrm{Grad}(\Delta\boldsymbol{u})\, \boldsymbol{S}^*\right) : \mathrm{Grad}(\delta\boldsymbol{u})\, \mathrm{d}V \\
&+ \int_{B_0} \Bigg(\underbrace{\frac{\partial \boldsymbol{S}}{\partial \boldsymbol{E}}\,[\Delta\boldsymbol{E}^*] + \frac{\partial \boldsymbol{S}}{\partial \bar{D}}\,\Delta\bar{D} + \frac{\partial \boldsymbol{S}}{\partial \theta}\,\Delta\theta}_{\Delta\boldsymbol{S}} \Bigg) : \delta\boldsymbol{E}^* \mathrm{d}V \\
&= \int_{B_0} \left(\mathrm{Grad}(\Delta\boldsymbol{u})\, \boldsymbol{S}^*\right) : \mathrm{Grad}(\delta\boldsymbol{u})\, \mathrm{d}V + \int_{B_0} \Delta\boldsymbol{S} : \delta\boldsymbol{E}^* \mathrm{d}V
\end{aligned} \tag{4.96}$$

Linearization of g_d:

The linearization of g_d around a known state $(\boldsymbol{u}^*, \bar{D}^*, \theta^*)$ is defined in the same manner as

$$\begin{aligned}
\mathcal{L} g_d(\Delta\boldsymbol{u}, \Delta\bar{D}, \Delta\theta, \delta\bar{D}) = g_d(\boldsymbol{u}^*, \bar{D}^*, \theta^*, \delta\bar{D}) + \mathcal{D}_u g_d(\boldsymbol{u}^*, \bar{D}^*, \theta^*, \delta\bar{D})[\Delta\boldsymbol{u}] \\
+ \mathcal{D}_{\bar{D}} g_d(\boldsymbol{u}^*, \bar{D}^*, \theta^*, \delta\bar{D})[\Delta\bar{D}] + \mathcal{D}_\theta g_d(\boldsymbol{u}^*, \bar{D}^*, \theta^*, \delta\bar{D})[\Delta\theta]
\end{aligned} \tag{4.97}$$

The first Gâteaux derivative $\mathcal{D}_u g_d(\boldsymbol{u}^*, \bar{D}^*, \theta^*, \delta\bar{D})[\Delta\boldsymbol{u}]$ is given as

$$\begin{aligned}
\mathcal{D}_u g_d(\boldsymbol{u}^*, \bar{D}^*, \theta^*, \delta\bar{D})[\Delta\boldsymbol{u}] &= \left.\frac{\mathrm{d}}{\mathrm{d}\epsilon}\right|_{\epsilon=0} g_d(\boldsymbol{u}^* + \epsilon\,\Delta\boldsymbol{u}, \bar{D}^*, \theta^*, \delta\bar{D}) \\
&= \left.\frac{\mathrm{d}}{\mathrm{d}\epsilon}\right|_{\epsilon=0} \left(\int_{B_0} \left(H\left(D(\boldsymbol{E}(\boldsymbol{F}(\epsilon)), \bar{D}^*, \theta^*) - \bar{D}^*\right) \delta\bar{D} - A\,\mathrm{Grad}(\bar{D}^*) \cdot \mathrm{Grad}(\delta\bar{D}) \right) \mathrm{d}V \right) \\
&= \left.\frac{\mathrm{d}}{\mathrm{d}\epsilon}\right|_{\epsilon=0} \int_{B_0} H\, D(\boldsymbol{E}(\boldsymbol{F}(\epsilon)), \bar{D}^*, \theta^*)\, \delta\bar{D}\, \mathrm{d}V \\
&= \int_{B_0} H \left(\frac{\partial D}{\partial \boldsymbol{E}} : \frac{\partial \boldsymbol{E}}{\partial \boldsymbol{F}} \left[\frac{\partial \boldsymbol{F}}{\partial \epsilon} \right] \right) \Bigg|_{\epsilon=0} \delta\bar{D}\, \mathrm{d}V \\
&= \int_{B_0} H\, \frac{\partial D}{\partial \boldsymbol{E}} : \Bigg(\underbrace{\frac{1}{2} \left(\mathrm{Grad}(\Delta\boldsymbol{u})^T \boldsymbol{F}^* + \boldsymbol{F}^{*T} \mathrm{Grad}(\Delta\boldsymbol{u}) \right)}_{\Delta\boldsymbol{E}^*} \Bigg) \delta\bar{D}\, \mathrm{d}V \\
&= \int_{B_0} H \left(\frac{\partial D}{\partial \boldsymbol{E}} : \Delta\boldsymbol{E}^* \right) \delta\bar{D}\, \mathrm{d}V
\end{aligned} \tag{4.98}$$

The second Gâteaux derivative $\mathcal{D}_{\bar{D}} g_d(\boldsymbol{u}^*, \bar{D}^*, \theta^*, \delta\bar{D})[\Delta\bar{D}]$ is given as

$$\begin{aligned}
&\mathcal{D}_{\bar{D}} g_d(\boldsymbol{u}^*, \bar{D}^*, \theta^*, \delta\bar{D})[\Delta\bar{D}] = \left.\frac{\mathrm{d}}{\mathrm{d}\epsilon}\right|_{\epsilon=0} g_d(\boldsymbol{u}^*, \bar{D}^* + \epsilon\,\Delta\bar{D}, \theta^*, \delta\bar{D}) \\
&= \left.\frac{\mathrm{d}}{\mathrm{d}\epsilon}\right|_{\epsilon=0} \left(\int_{B_0} \left(H\left(D(\boldsymbol{E}^*, \bar{D}(\epsilon), \theta^*) - \bar{D}(\epsilon)\right) \delta\bar{D} - A\,\mathrm{Grad}(\bar{D}(\epsilon)) \cdot \mathrm{Grad}(\delta\bar{D}) \right) \mathrm{d}V \right) \\
&= \int_{B_0} \left(H \left(\frac{\partial D}{\partial \bar{D}} \frac{\partial \bar{D}}{\partial \epsilon} - \frac{\partial \bar{D}}{\partial \epsilon} \right) \Big|_{\epsilon=0} \delta\bar{D} - A \left. \frac{\partial \mathrm{Grad}(\bar{D})}{\partial \epsilon} \right|_{\epsilon=0} \cdot \mathrm{Grad}(\delta\bar{D}) \right) \mathrm{d}V \\
&= \int_{B_0} \left(H \left(\frac{\partial D}{\partial \bar{D}}\,\Delta\bar{D} - \Delta\bar{D} \right) \delta\bar{D} - A\,\mathrm{Grad}(\Delta\bar{D}) \cdot \mathrm{Grad}(\delta\bar{D}) \right) \mathrm{d}V
\end{aligned} \tag{4.99}$$

The third Gâteaux derivative $\mathcal{D}_{\theta} g_u(\boldsymbol{u}, \bar{D}^*, \theta^*, \delta\boldsymbol{u})[\Delta\theta]$ is given as

$$\begin{aligned}
&\mathcal{D}_{\theta} g_d(\boldsymbol{u}^*, \bar{D}^*, \theta^*, \delta\bar{D})[\Delta\theta] = \left.\frac{\mathrm{d}}{\mathrm{d}\epsilon}\right|_{\epsilon=0} g_d(\boldsymbol{u}^*, \bar{D}^*, \theta^* + \epsilon\,\Delta\theta, \delta\bar{D}) \\
&= \left.\frac{\mathrm{d}}{\mathrm{d}\epsilon}\right|_{\epsilon=0} \left(\int_{B_0} \left(H\left(D(\boldsymbol{E}^*, \bar{D}^*, \theta(\epsilon)) - \bar{D}^*\right) \delta\bar{D} - A\,\mathrm{Grad}(\bar{D}^*) \cdot \mathrm{Grad}(\delta\bar{D}) \right) \mathrm{d}V \right) \\
&= \left.\frac{\mathrm{d}}{\mathrm{d}\epsilon}\right|_{\epsilon=0} \int_{B_0} H\, D(\boldsymbol{E}^*, \bar{D}^*, \theta(\epsilon))\, \delta\bar{D}\, \mathrm{d}V \\
&= \int_{B_0} H \left(\frac{\partial D}{\partial \theta} \frac{\partial \theta}{\partial \epsilon} \right) \Big|_{\epsilon=0} \delta\bar{D}\, \mathrm{d}V \\
&= \int_{B_0} H \left(\frac{\partial D}{\partial \theta}\,\Delta\theta \right) \delta\bar{D}\, \mathrm{d}V
\end{aligned} \tag{4.100}$$

The increment Δg_d is therefore defined as follows

$$\begin{aligned}
&\Delta g_d = \mathcal{D}_u g_d(\boldsymbol{u}^*, \bar{D}^*, \theta^*, \delta\bar{D})[\Delta\boldsymbol{u}] + \mathcal{D}_{\bar{D}} g_d(\boldsymbol{u}^*, \bar{D}^*, \theta^*, \delta\bar{D})[\Delta\bar{D}] + \mathcal{D}_{\theta} g_d(\boldsymbol{u}^*, \bar{D}^*, \theta^*, \delta\bar{D})[\Delta\theta] \\
&= \int_{B_0} H \left(\underbrace{\left(\frac{\partial D}{\partial \boldsymbol{E}} : \Delta\boldsymbol{E}^* + \frac{\partial D}{\partial \bar{D}}\,\Delta\bar{D} + \frac{\partial D}{\partial \theta}\,\Delta\theta \right)}_{\Delta D} - \Delta\bar{D} \right) \delta\bar{D}\, \mathrm{d}V \\
&\quad - \int_{B_0} A\,\mathrm{Grad}(\Delta\bar{D}) \cdot \mathrm{Grad}(\delta\bar{D}) \Big) \mathrm{d}V \\
&= \int_{B_0} H\left(\Delta D - \Delta\bar{D}\right) \delta\bar{D}\, \mathrm{d}V - \int_{B_0} A\,\mathrm{Grad}(\Delta\bar{D}) \cdot \mathrm{Grad}(\delta\bar{D}) \Big) \mathrm{d}V
\end{aligned} \tag{4.101}$$

Linearization of g_θ:

Lastly, the linearization of g_θ around a known state $(\boldsymbol{u}^*, \bar{D}^*, \theta^*)$ is defined as

$$\begin{aligned}\mathcal{L}g_\theta(\Delta\boldsymbol{u}, \Delta\bar{D}, \Delta\theta, \delta\theta) = g_\theta(\boldsymbol{u}^*, \bar{D}^*, \theta^*, \delta\theta) + \mathcal{D}_u g_\theta(\boldsymbol{u}^*, \bar{D}^*, \theta^*, \delta\theta)[\Delta\boldsymbol{u}] \\ + \mathcal{D}_{\bar{D}} g_\theta(\boldsymbol{u}^*, \bar{D}^*, \theta^*, \delta\theta)[\Delta\bar{D}] + \mathcal{D}_\theta g_\theta(\boldsymbol{u}^*, \bar{D}^*, \theta^*, \delta\theta)[\Delta\theta]\end{aligned} \tag{4.102}$$

The first Gâteaux derivative $\mathcal{D}_u g_\theta(\boldsymbol{u}, \bar{D}^*, \theta^*, \delta\theta)[\Delta\boldsymbol{u}]$ is given as

$$\begin{aligned}
&\mathcal{D}_u g_\theta(\boldsymbol{u}, \bar{D}^*, \theta^*, \delta\theta)[\Delta\boldsymbol{u}] = \frac{\mathrm{d}}{\mathrm{d}\epsilon}\bigg|_{\epsilon=0} g_\theta(\boldsymbol{u}^* + \epsilon\,\Delta\boldsymbol{u}, \bar{D}^*, \theta^*, \delta\theta) \\
&= \frac{\mathrm{d}}{\mathrm{d}\epsilon}\bigg|_{\epsilon=0} \left(\int_{B_0} c\,\frac{\theta^* - \theta_n}{\Delta t}\,\delta\theta\,\mathrm{d}V - \int_{B_0} \boldsymbol{q}_0(\boldsymbol{E}(\boldsymbol{F}(\epsilon)), \bar{D}^*, \theta^*) \cdot \mathrm{Grad}(\delta\theta)\,\mathrm{d}V \right. \\
&\qquad \left. - \int_{B_0} r_{\text{int}}(\boldsymbol{E}(\boldsymbol{F}(\epsilon)), \bar{D}^*, \theta^*)\,\delta\theta\,\mathrm{d}V - \int_{\partial B_{0_q}} q_0\,\delta\theta\,\mathrm{d}A \right) \\
&= \frac{\mathrm{d}}{\mathrm{d}\epsilon}\bigg|_{\epsilon=0} \left(- \int_{B_0} \boldsymbol{q}_0(\boldsymbol{E}(\boldsymbol{F}(\epsilon)), \bar{D}^*, \theta^*) \cdot \mathrm{Grad}(\delta\theta)\,\mathrm{d}V - \int_{B_0} r_{\text{int}}(\boldsymbol{E}(\boldsymbol{F}(\epsilon)), \bar{D}^*, \theta^*)\,\delta\theta\,\mathrm{d}V \right) \\
&= -\int_{B_0} \frac{\partial \boldsymbol{q}_0}{\partial \boldsymbol{E}} : \frac{\partial \boldsymbol{E}}{\partial \boldsymbol{F}} \left[\frac{\partial \boldsymbol{F}}{\partial \epsilon} \right] \bigg|_{\epsilon=0} \cdot \mathrm{Grad}(\delta\theta)\,\mathrm{d}V - \int_{B_0} \frac{\partial r_{\text{int}}}{\partial \boldsymbol{E}} : \frac{\partial \boldsymbol{E}}{\partial \boldsymbol{F}} \left[\frac{\partial \boldsymbol{F}}{\partial \epsilon} \right] \bigg|_{\epsilon=0} \delta\theta\,\mathrm{d}V \\
&= -\int_{B_0} \frac{\partial \boldsymbol{q}_0}{\partial \boldsymbol{E}} : \Bigg(\underbrace{\frac{1}{2}\left(\mathrm{Grad}(\Delta\boldsymbol{u})^T \boldsymbol{F}^* + \boldsymbol{F}^{*T} \mathrm{Grad}(\Delta\boldsymbol{u}) \right)}_{\Delta \boldsymbol{E}^*} \Bigg) \cdot \mathrm{Grad}(\delta\theta)\,\mathrm{d}V \\
&\qquad - \int_{B_0} \frac{\partial r_{\text{int}}}{\partial \boldsymbol{E}} : \Bigg(\underbrace{\frac{1}{2}\left(\mathrm{Grad}(\Delta\boldsymbol{u})^T \boldsymbol{F}^* + \boldsymbol{F}^{*T} \mathrm{Grad}(\Delta\boldsymbol{u}) \right)}_{\Delta \boldsymbol{E}^*} \Bigg) \delta\theta\,\mathrm{d}V \\
&= -\int_{B_0} \left(\frac{\partial \boldsymbol{q}_0}{\partial \boldsymbol{E}} : \Delta\boldsymbol{E}^* \right) \cdot \mathrm{Grad}(\delta\theta)\,\mathrm{d}V - \int_{B_0} \left(\frac{\partial r_{\text{int}}}{\partial \boldsymbol{E}} : \Delta\boldsymbol{E}^* \right) \delta\theta\,\mathrm{d}V
\end{aligned} \tag{4.103}$$

The second Gâteaux derivative $\mathcal{D}_{\bar{D}} g_\theta(\boldsymbol{u}^*, \bar{D}^*, \theta^*, \delta\theta)[\Delta\bar{D}]$ is given as

$$
\begin{aligned}
&\mathcal{D}_{\bar{D}} g_\theta(\boldsymbol{u}^*, \bar{D}^*, \theta^*, \delta\theta)[\Delta\bar{D}] = \left.\frac{\mathrm{d}}{\mathrm{d}\epsilon}\right|_{\epsilon=0} g_\theta(\boldsymbol{u}^*, \bar{D}^* + \epsilon\,\Delta\bar{D}, \theta^*, \delta\theta) \\
&= \left.\frac{\mathrm{d}}{\mathrm{d}\epsilon}\right|_{\epsilon=0} \Bigg(\int_{B_0} c\,\frac{\theta^* - \theta_n}{\Delta t}\,\delta\theta\,\mathrm{d}V - \int_{B_0} \boldsymbol{q}_0(\boldsymbol{E}^*, \bar{D}(\epsilon), \theta^*) \cdot \mathrm{Grad}(\delta\theta)\,\mathrm{d}V \\
&\qquad - \int_{B_0} r_{\text{int}}(\boldsymbol{E}^*, \bar{D}(\epsilon), \theta^*)\,\delta\theta\,\mathrm{d}V - \int_{\partial B_{0_q}} q_0\,\delta\theta\,\mathrm{d}A \Bigg) \\
&= \left.\frac{\mathrm{d}}{\mathrm{d}\epsilon}\right|_{\epsilon=0} \Bigg(- \int_{B_0} \boldsymbol{q}_0(\boldsymbol{E}^*, \bar{D}(\epsilon), \theta^*) \cdot \mathrm{Grad}(\delta\theta)\,\mathrm{d}V - \int_{B_0} r_{\text{int}}(\boldsymbol{E}^*, \bar{D}(\epsilon), \theta^*)\,\delta\theta\,\mathrm{d}V \Bigg) \\
&= - \int_{B_0} \left.\frac{\partial \boldsymbol{q}_0}{\partial \bar{D}}\,\frac{\partial \bar{D}}{\partial \epsilon}\right|_{\epsilon=0} \cdot \mathrm{Grad}(\delta\theta)\,\mathrm{d}V - \int_{B_0} \left.\frac{\partial r_{\text{int}}}{\partial \bar{D}}\,\frac{\partial \bar{D}}{\partial \epsilon}\right|_{\epsilon=0} \delta\theta\,\mathrm{d}V \\
&= - \int_{B_0} \left(\frac{\partial \boldsymbol{q}_0}{\partial \bar{D}}\,\Delta\bar{D}\right) \cdot \mathrm{Grad}(\delta\theta)\,\mathrm{d}V - \int_{B_0} \left(\frac{\partial r_{\text{int}}}{\partial \bar{D}}\,\Delta\bar{D}\right) \delta\theta\,\mathrm{d}V
\end{aligned}
\tag{4.104}
$$

The third Gâteaux derivative $\mathcal{D}_\theta g_\theta(\boldsymbol{u}^*, \bar{D}^*, \theta^*, \delta\theta)[\Delta\theta]$ is given as

$$
\begin{aligned}
&\mathcal{D}_\theta g_\theta(\boldsymbol{u}, \bar{D}^*, \theta^*, \delta\theta)[\Delta\theta] = \left.\frac{\mathrm{d}}{\mathrm{d}\epsilon}\right|_{\epsilon=0} g_\theta(\boldsymbol{u}^*, \bar{D}^*, \theta^* + \epsilon\,\Delta\theta, \delta\theta) \\
&= \left.\frac{\mathrm{d}}{\mathrm{d}\epsilon}\right|_{\epsilon=0} \Bigg(\int_{B_0} c\,\frac{\theta(\epsilon) - \theta_n}{\Delta t}\,\delta\theta\,\mathrm{d}V - \int_{B_0} \boldsymbol{q}_0(\boldsymbol{E}^*, \bar{D}^*, \theta(\epsilon)) \cdot \mathrm{Grad}(\delta\theta)\,\mathrm{d}V \\
&\qquad - \int_{B_0} r_{\text{int}}(\boldsymbol{E}^*, \bar{D}^*, \theta(\epsilon))\,\delta\theta\,\mathrm{d}V - \int_{\partial B_{0_q}} q_0\,\delta\theta\,\mathrm{d}A \Bigg) \\
&= \left.\frac{\mathrm{d}}{\mathrm{d}\epsilon}\right|_{\epsilon=0} \Bigg(\int_{B_0} c\,\frac{\theta(\epsilon) - \theta_n}{\Delta t}\,\delta\theta\,\mathrm{d}V - \int_{B_0} \boldsymbol{q}_0(\boldsymbol{E}^*, \bar{D}^*, \theta(\epsilon)) \cdot \mathrm{Grad}(\delta\theta)\,\mathrm{d}V \\
&\qquad - \int_{B_0} r_{\text{int}}(\boldsymbol{E}^*, \bar{D}^*, \theta(\epsilon))\,\delta\theta\,\mathrm{d}V \Bigg) \\
&= \int_{B_0} c\,\frac{\partial\theta}{\partial\epsilon}\,\frac{1}{\Delta t}\bigg|_{\epsilon=0} \delta\theta\,\mathrm{d}V - \int_{B_0} \left.\frac{\partial \boldsymbol{q}_0}{\partial\theta}\,\frac{\partial\theta}{\partial\epsilon}\right|_{\epsilon=0} \cdot \mathrm{Grad}(\delta\theta)\,\mathrm{d}V - \int_{B_0} \left.\frac{\partial r_{\text{int}}}{\partial\theta}\,\frac{\partial\theta}{\partial\epsilon}\right|_{\epsilon=0} \delta\theta\,\mathrm{d}V \\
&= \int_{B_0} c\,\frac{\Delta\theta}{\Delta t}\,\delta\theta\,\mathrm{d}V - \int_{B_0} \left(\frac{\partial \boldsymbol{q}_0}{\partial\theta}\,\Delta\theta\right) \cdot \mathrm{Grad}(\delta\theta)\,\mathrm{d}V - \int_{B_0} \left(\frac{\partial r_{\text{int}}}{\partial\theta}\Delta\theta\right) \delta\theta\,\mathrm{d}V
\end{aligned}
\tag{4.105}
$$

The increment Δg_θ is therefore defined as follows

$$\begin{aligned}
\Delta g_\theta &= \mathcal{D}_u g_\theta(\boldsymbol{u}^*, \bar{D}^*, \theta^*, \delta\theta)[\Delta \boldsymbol{u}] + \mathcal{D}_{\bar{D}} g_\theta(\boldsymbol{u}^*, \bar{D}^*, \theta^*, \delta\theta)[\Delta \bar{D}] + \mathcal{D}_\theta g_\theta(\boldsymbol{u}^*, \bar{D}^*, \theta^*, \delta\theta)[\Delta\theta] \\
&= \int_{B_0} c\,\frac{\Delta\theta}{\Delta t}\,\delta\theta\,\mathrm{d}V - \int_{B_0} \Bigg(\underbrace{\frac{\partial \boldsymbol{q}_0}{\partial \boldsymbol{E}} : \Delta \boldsymbol{E}^* + \frac{\partial \boldsymbol{q}_0}{\partial \bar{D}}\,\Delta\bar{D} + \frac{\partial \boldsymbol{q}_0}{\partial \theta}\,\Delta\theta}_{\Delta \boldsymbol{q}_0} \Bigg) \cdot \mathrm{Grad}(\delta\theta)\,\mathrm{d}V \\
&\quad - \int_{B_0} \Bigg(\underbrace{\frac{\partial r_{\text{int}}}{\partial \boldsymbol{E}} : \Delta \boldsymbol{E}^* + \frac{\partial r_{\text{int}}}{\partial \bar{D}}\,\Delta\bar{D} + \frac{\partial r_{\text{int}}}{\partial \theta}\,\Delta\theta}_{\Delta r_{\text{int}}} \Bigg) \delta\theta\,\mathrm{d}V \\
&= \int_{B_0} c\,\frac{\Delta\theta}{\Delta t}\,\delta\theta\,\mathrm{d}V - \int_{B_0} \Delta \boldsymbol{q}_0 \cdot \mathrm{Grad}(\delta\theta)\,\mathrm{d}V - \int_{B_0} \Delta r_{\text{int}}\,\delta\theta\,\mathrm{d}V
\end{aligned} \tag{4.106}$$

4.7.6

In this section, the sequential approach to compute the 12 material tangents, introduced in (4.49)-(4.52) is discussed in more detail.

Since the stress is a function of $\boldsymbol{C}$, $\boldsymbol{U}_p^{-1}$, D, and θ, the algorithmic tangents corresponding to the stress increment $\Delta \boldsymbol{S}$ (4.49) can be expressed by

$$\left.\frac{\partial \boldsymbol{S}}{\partial \boldsymbol{E}}\right|_{\substack{\bar{D} \\ \theta}} = 2 \left(\left.\frac{\partial \boldsymbol{S}}{\partial \boldsymbol{C}}\right|_{\Gamma\setminus\boldsymbol{C}} + \left.\frac{\partial \boldsymbol{S}}{\partial \boldsymbol{U}_p^{-1}}\right|_{\Gamma\setminus\boldsymbol{U}_p^{-1}} : \left.\frac{\partial \boldsymbol{U}_p^{-1}}{\partial \boldsymbol{C}}\right|_{\substack{\bar{D} \\ \theta}} + \left.\frac{\partial \boldsymbol{S}}{\partial D}\right|_{\Gamma\setminus D} \otimes \left.\frac{\partial D}{\partial \boldsymbol{C}}\right|_{\substack{\bar{D} \\ \theta}} \right) \tag{4.107}$$

$$\left.\frac{\partial \boldsymbol{S}}{\partial \bar{D}}\right|_{\substack{\boldsymbol{C} \\ \theta}} = \left.\frac{\partial \boldsymbol{S}}{\partial \boldsymbol{U}_p^{-1}}\right|_{\Gamma\setminus\boldsymbol{U}_p^{-1}} : \left.\frac{\partial \boldsymbol{U}_p^{-1}}{\partial \bar{D}}\right|_{\substack{\boldsymbol{C} \\ \theta}} + \left.\frac{\partial \boldsymbol{S}}{\partial D}\right|_{\Gamma\setminus D} \left.\frac{\partial D}{\partial \bar{D}}\right|_{\substack{\boldsymbol{C} \\ \theta}} \tag{4.108}$$

$$\left.\frac{\partial \boldsymbol{S}}{\partial \theta}\right|_{\substack{\boldsymbol{C} \\ \bar{D}}} = \left.\frac{\partial \boldsymbol{S}}{\partial \theta}\right|_{\Gamma\setminus\theta} + \left.\frac{\partial \boldsymbol{S}}{\partial \boldsymbol{U}_p^{-1}}\right|_{\Gamma\setminus\boldsymbol{U}_p^{-1}} : \left.\frac{\partial \boldsymbol{U}_p^{-1}}{\partial \theta}\right|_{\substack{\boldsymbol{C} \\ \bar{D}}} + \left.\frac{\partial \boldsymbol{S}}{\partial D}\right|_{\Gamma\setminus D} \left.\frac{\partial D}{\partial \theta}\right|_{\substack{\boldsymbol{C} \\ \bar{D}}} \tag{4.109}$$

where the set $\Gamma := \{\boldsymbol{C}, \bar{D}, \theta, \boldsymbol{U}_p^{-1}, D\}$ was introduced, for the sake of brevity, to indicate which variables are held constant in the partial derivatives.

In addition, the derivatives related to the increment of the internal heat generation Δr_{int} must be computed (see Equation (4.52)). From Equation (4.68) and the corresponding discussion, it can be deduced that r_{int} can be expressed as a function of $\boldsymbol{C}$, θ, $\bar{D}$, $\boldsymbol{U}_p^{-1}$, $\bar{\lambda}_p$, and $\bar{\lambda}_d$. Thus,

the following relations hold

$$\begin{aligned}\left.\frac{\partial r_{\text{int}}}{\partial \boldsymbol{E}}\right|_{\substack{\bar{D}\\ \theta}} =& 2\left(\left.\frac{\partial r_{\text{int}}}{\partial \boldsymbol{C}}\right|_{\Upsilon\setminus\boldsymbol{C}} + \left.\frac{\partial r_{\text{int}}}{\partial \boldsymbol{U}_p^{-1}}\right|_{\Upsilon\setminus\boldsymbol{U}_p^{-1}} : \left.\frac{\partial \boldsymbol{U}_p^{-1}}{\partial \boldsymbol{C}}\right|_{\substack{\bar{D}\\ \theta}} + \left.\frac{\partial r_{\text{int}}}{\partial \bar{\lambda}_p}\right|_{\Upsilon\setminus\bar{\lambda}_p} \left.\frac{\partial \bar{\lambda}_p}{\partial \boldsymbol{C}}\right|_{\substack{\bar{D}\\ \theta}}\right)\\ &+ 2\left(\left.\frac{\partial r_{\text{int}}}{\partial \bar{\lambda}_d}\right|_{\Upsilon\setminus\bar{\lambda}_d} \left.\frac{\partial \bar{\lambda}_d}{\partial \boldsymbol{C}}\right|_{\substack{\bar{D}\\ \theta}}\right)\end{aligned} \tag{4.110}$$

$$\left.\frac{\partial r_{\text{int}}}{\partial \bar{D}}\right|_{\substack{\boldsymbol{C}\\ \theta}} = \left.\frac{\partial r_{\text{int}}}{\partial \bar{D}}\right|_{\Upsilon\setminus\bar{D}} + \left.\frac{\partial r_{\text{int}}}{\partial \boldsymbol{U}_p^{-1}}\right|_{\Upsilon\setminus\boldsymbol{U}_p^{-1}} : \left.\frac{\partial \boldsymbol{U}_p^{-1}}{\partial \bar{D}}\right|_{\substack{\boldsymbol{C}\\ \theta}} + \left.\frac{\partial r_{\text{int}}}{\partial \bar{\lambda}_p}\right|_{\Upsilon\setminus\bar{\lambda}_p} \left.\frac{\partial \bar{\lambda}_p}{\partial \bar{D}}\right|_{\substack{\boldsymbol{C}\\ \theta}} + \left.\frac{\partial r_{\text{int}}}{\partial \bar{\lambda}_d}\right|_{\Upsilon\setminus\bar{\lambda}_d} \left.\frac{\partial \bar{\lambda}_d}{\partial \bar{D}}\right|_{\substack{\boldsymbol{C}\\ \theta}} \tag{4.111}$$

$$\left.\frac{\partial r_{\text{int}}}{\partial \theta}\right|_{\substack{\boldsymbol{C}\\ \bar{D}}} = \left.\frac{\partial r_{\text{int}}}{\partial \theta}\right|_{\Upsilon\setminus\theta} + \left.\frac{\partial r_{\text{int}}}{\partial \boldsymbol{U}_p^{-1}}\right|_{\Upsilon\setminus\boldsymbol{U}_p^{-1}} : \left.\frac{\partial \boldsymbol{U}_p^{-1}}{\partial \theta}\right|_{\substack{\boldsymbol{C}\\ \bar{D}}} + \left.\frac{\partial r_{\text{int}}}{\partial \bar{\lambda}_p}\right|_{\Upsilon\setminus\bar{\lambda}_p} \left.\frac{\partial \bar{\lambda}_p}{\partial \theta}\right|_{\substack{\boldsymbol{C}\\ \bar{D}}} + \left.\frac{\partial r_{\text{int}}}{\partial \bar{\lambda}_d}\right|_{\Upsilon\setminus\bar{\lambda}_d} \left.\frac{\partial \bar{\lambda}_d}{\partial \theta}\right|_{\substack{\boldsymbol{C}\\ \bar{D}}} \tag{4.112}$$

where the set $\Upsilon := \{\boldsymbol{C}, \theta, \bar{D}, \boldsymbol{U}_p^{-1}, \bar{\lambda}_p, \bar{\lambda}_d\}$ was introduced, for a clearer representation of the partial derivatives. In this context, it is instructive to point out that $\partial\bar{\lambda}_d/\partial(*) = \partial D/\partial(*)$ holds.

In order to determine these complex derivatives (4.107)-(4.112), a sequential approach is developed. First, the functions for the stress as well as for the internal heat generation are implemented in *AceGen*, where $\boldsymbol{C}$, θ, $\bar{D}$, $\boldsymbol{U}_p^{-1}$, $\bar{\lambda}_p$, and $\bar{\lambda}_d$, as well as the internal variables from the last converged time step, serve as input variables. Consequently, the partial derivatives of $\boldsymbol{S}$ and r_{int} with respect to the aforementioned input quantities (see Equations (4.107)-(4.112)) can be computed by automatic differentiation via *AceGen*. Next, the remaining derivatives of the solution vector $\boldsymbol{x}_{\text{loc}} := (\bar{\lambda}_p,\, \hat{\boldsymbol{U}}_p^{-1},\, \bar{\lambda}_d)^T$ with respect to the 'global unknowns ', i.e. $\boldsymbol{C}$, θ, $\bar{D}$ must be computed, such that all terms in (4.107)-(4.112) are known. To this end, an additional linearization of the converged local residual vector (i.e. $\boldsymbol{r}_{\text{loc}} := (R_1,\, \hat{\boldsymbol{R}}_2,\, R_3)^T = \boldsymbol{0}$) is considered, viz.

$$\begin{aligned}\boldsymbol{0} =& \underbrace{\boldsymbol{r}_{\text{loc}}}_{=\boldsymbol{0}} + \left.\frac{\partial \boldsymbol{r}_{\text{loc}}}{\partial \boldsymbol{x}_{\text{loc}}}\right|_{\substack{\boldsymbol{C}\\ \bar{D}\\ \theta}} \cdot \Delta\boldsymbol{x}_{\text{loc}} + \left.\frac{\partial \boldsymbol{r}_{\text{loc}}}{\partial \hat{\boldsymbol{C}}}\right|_{\substack{\bar{D}\\ \theta\\ \boldsymbol{x}_{\text{loc}}}} : \Delta\hat{\boldsymbol{C}} + \left.\frac{\partial \boldsymbol{r}_{\text{loc}}}{\partial \bar{D}}\right|_{\substack{\boldsymbol{C}\\ \theta\\ \boldsymbol{x}_{\text{loc}}}} \Delta\bar{D} + \left.\frac{\partial \boldsymbol{r}_{\text{loc}}}{\partial \theta}\right|_{\substack{\boldsymbol{C}\\ \bar{D}\\ \boldsymbol{x}_{\text{loc}}}} \Delta\theta\\ =& \left.\frac{\partial \boldsymbol{r}_{\text{loc}}}{\partial \boldsymbol{x}_{\text{loc}}}\right|_{\boldsymbol{x}_{\text{glo}}} \cdot \Delta\boldsymbol{x}_{\text{loc}} + \left.\frac{\partial \boldsymbol{r}_{\text{loc}}}{\partial \boldsymbol{x}_{\text{glo}}}\right|_{\boldsymbol{x}_{\text{loc}}} \cdot \Delta\boldsymbol{x}_{\text{glo}} =: \boldsymbol{J}_1\, \Delta\boldsymbol{x}_{\text{loc}} + \boldsymbol{J}_2\, \Delta\boldsymbol{x}_{\text{glo}}\end{aligned} \tag{4.113}$$

where $\boldsymbol{x}_{\text{glo}} := (\hat{\boldsymbol{C}},\, \theta,\, \bar{D})^T$ was introduced. From the relation above, it follows that the in-

cremental change of the local variables $\Delta\boldsymbol{x}_{\text{loc}}$ with respect to an incremental change of the global ones $\Delta\boldsymbol{x}_{\text{glo}}$ can be expressed by the matrix $\boldsymbol{J}^* = -\boldsymbol{J}_1^{-1}\boldsymbol{J}_2$. As alluded above, the residual function $\boldsymbol{r}_{\text{loc}}$ is implemented in *Mathematica* and *AceGen* is employed to provide the derivatives comprised in $\boldsymbol{J}_2$. The remaining derivatives ($\bar{\lambda}_p$, $\hat{\boldsymbol{U}}_p^{-1}$, $\bar{\lambda}_d$ with respect to $\hat{\boldsymbol{C}}$, θ, $\bar{D}$, respectively) can, thus, be extracted from $\boldsymbol{J}^*$. In this way, the tangent operators related to the increment of the local damage variable ΔD (see Equation (4.50)) are directly obtained as well.

Finally, the derivatives related to the increment of the heat flux vector $\Delta\boldsymbol{q}_0$ (4.51), which is expressed as a function of $\boldsymbol{C}$, D, Grad(θ), and θ (cf. Equation (4.8)), can be derived:

$$\left.\frac{\partial \boldsymbol{q}_0}{\partial \boldsymbol{E}}\right|_{\substack{\bar{D}\\ \theta}} = 2\left(\left.\frac{\partial \boldsymbol{q}_0}{\partial \boldsymbol{C}}\right|_{\substack{\bar{D}\\ \theta\\ D}} + \left.\frac{\partial \boldsymbol{q}_0}{\partial D}\right|_{\substack{\boldsymbol{C}\\ \bar{D}\\ \theta}} \otimes \left.\frac{\partial D}{\partial \boldsymbol{C}}\right|_{\substack{\bar{D}\\ \theta}}\right) \tag{4.114}$$

$$\left.\frac{\partial \boldsymbol{q}_0}{\partial \bar{D}}\right|_{\substack{\boldsymbol{C}\\ \theta}} = \left.\frac{\partial \boldsymbol{q}_0}{\partial D}\right|_{\substack{\boldsymbol{C}\\ \bar{D}\\ \theta}} \left.\frac{\partial D}{\partial \bar{D}}\right|_{\substack{\boldsymbol{C}\\ \theta}} \tag{4.115}$$

$$\left.\frac{\partial \boldsymbol{q}_0}{\partial \theta}\right|_{\substack{\boldsymbol{C}\\ \bar{D}\\ \text{Grad}(\theta)}} = \left.\frac{\partial \boldsymbol{q}_0}{\partial \theta}\right|_{\substack{\boldsymbol{C}\\ \bar{D}\\ D\\ \text{Grad}(\theta)}} + \left.\frac{\partial \boldsymbol{q}_0}{\partial D}\right|_{\substack{\boldsymbol{C}\\ \bar{D}\\ \theta}} \left.\frac{\partial D}{\partial \theta}\right|_{\substack{\boldsymbol{C}\\ \bar{D}}} \tag{4.116}$$

$$\left.\frac{\partial \boldsymbol{q}_0}{\partial \text{Grad}(\theta)}\right|_{\substack{\boldsymbol{C}\\ \bar{D}\\ \theta}} = -\boldsymbol{K} \tag{4.117}$$

The derivatives of the local damage variable with respect to global ones, in the expressions above, are extracted from $\boldsymbol{J}^*$. Due to the much simpler functional dependencies, the partial derivatives of the heat flux with respect to $\boldsymbol{C}$, D, and θ are established analytically:

$$\left.\frac{\partial q_{0,i}}{\partial C_{kl}}\right|_{\substack{\bar{D}\\ \theta\\ D}} = -\left(f_d(D)\,K_0 + (1-f_d(D))\,K_{\text{c}}\right)\frac{1}{2}\left(C_{ik}^{-1}C_{lj}^{-1} + C_{il}^{-1}C_{kj}^{-1}\right)\text{Grad}(\theta)_j \tag{4.118}$$

$$\left.\frac{\partial \boldsymbol{q}_0}{\partial D}\right|_{\substack{\boldsymbol{C}\\ \bar{D}\\ \theta}} = -\left(\frac{\text{d}f_d}{\text{d}D}K_0 - \frac{\text{d}f_d}{\text{d}D}K_c\right)\boldsymbol{C}^{-1}\,\text{Grad}(\theta) \tag{4.119}$$

$$\left.\frac{\partial \boldsymbol{q}_0}{\partial \theta}\right|_{\substack{\boldsymbol{C}\\ \bar{D}\\ D\\ \text{Grad}(\theta)}} = -\left(f_d(D)\,\frac{\text{d}K_0}{\text{d}\theta} + (1-f_d(D))\,\frac{\text{d}K_c}{\text{d}\theta}\right)\boldsymbol{C}^{-1}\,\text{Grad}(\theta) \tag{4.120}$$

4.7.7

In the following, the constitutive framework is reduced, to discuss a simplified expression for the heat generation due to plastic processes and the corresponding influence of the ther-

mal softening function f_θ. To this end, damage is suppressed ($f_d = 1$), thermal expansion is neglected ($\alpha = 0.0$), no kinematic hardening ($a = 0$) and only linear isotropic hardening ($P_0 > 0$, $e_p = 0$) are considered. Furthermore, thermal softening is assumed to affect the hardening modulus ($P = f_\theta(\theta)\, P_0$) and the yield stress ($\sigma_y = f_\theta(\theta)\, \sigma_0$) only, where a linear softening function ($f_\theta = 1 - \omega(\theta - \theta_0)$) is chosen.

With the aforementioned choices, the heat generation (4.29) reduces to the following form in the case of plastic flow, i.e. $\Phi_p = 0$ and $\dot{\lambda}_p > 0$:

$$\begin{aligned} r_{\text{int}} =& \boldsymbol{M} : \boldsymbol{D}_p - \left(q_p - \theta \frac{\partial q_p}{\partial \theta} \right) \dot{\xi}_p \\ =& \boldsymbol{M} : \dot{\lambda}_p \sqrt{3/2} \frac{\text{dev}(\boldsymbol{M})}{||\text{dev}(\boldsymbol{M})||} - \left(q_p - \theta \frac{\partial q_p}{\partial \theta} \right) \dot{\lambda}_p \\ =& \dot{\lambda}_p \Big(|| \underbrace{\text{dev}(\boldsymbol{M})||}_{=\sigma_y} - q_p + \theta \frac{\partial q_p}{\partial \theta} \Big) \\ =& \dot{\lambda}_p \Big(f_\theta\, \sigma_0 + \theta \frac{\partial f_\theta}{\partial \theta}\, P_0\, \xi_p \Big) = \dot{\lambda}_p (\sigma_0 - \sigma_0\, \omega\, (\theta - \theta_0) - \omega\, \theta\, P_0\, \xi_p) \end{aligned} \tag{4.121}$$

where the evolution equation for $\boldsymbol{D}_p$ (4.24) and $\dot{\xi}_p$ (4.25) were incorporated. Thus, for this simple choice of f_θ, it becomes evident that negative heat generation occurs eventually for increasing plastic deformation ξ_p and temperatures θ, depending on the chosen material parameters ω, σ_0, and P_0. It must be emphasized that this a mere consequence of the chosen softening function and the assumption that linear hardening and yield stress are affected equivalently by the temperature. Noteworthy, the Clausius-Duhem inequality (4.74) is always fulfilled, as long as the material parameters are positive, which is a natural requirement, in any case.

Clearly, in less academic settings, the procedure regarding the determination of appropriate softening functions is fundamentally different. In this case, the temperature dependent parameters would be calibrated based on isothermal experiments at different temperatures and individual softening functions for each parameter would be proposed, subsequently (see e.g. Felder, Holthusen, Hesseler, Pohlkemper, Gries, Simon and Reese [2020]). Noteworthy, in the present work, careful attention was paid, when choosing ω, to ensure positive plastic heat generation only, in all considered numerical examples, where thermal softening is involved.

5 Conclusions and Outlook

The present cumulative dissertation was concerned with the development of multiphysics modeling approaches for polymers and metals, in order to capture important coupling effects, which arise e.g. during (non-isothermal) forming processes of these materials.

The first two articles within this dissertation dealt with the modeling of semi-crystalline polymers. It was in particular aimed to investigate the temperature dependent effect of the degree of the crystallinity on the macroscopic response and to incorporate this into continuum mechanical models. To this end, in Chapter 2, an extensive experimental study was performed, where various tensile experiments under monotonic and cyclic loading conditions as well as relaxation tests were conducted for Polyamide 6. Three degrees of crystallinity (ranging from $\chi = 0.23$ to $\chi = 0.28$) were investigated and the considered strain rates were limited to one decade. To obtain 'true'stress-stretch data and well defined loading rates, digital image correlation (DIC) measurements were performed.

The experimental results provided important insights into the complex dependencies of the effective material properties on the aforementioned factors. Based on these findings, a continuum mechanical phenomenological approach was proposed, which relied on a combined nonlinear visco-elastic and elasto-plastic theory. The latter incorporated nonlinear isotropic and kinematic hardening, as well as nonlinear relaxation behavior. In addition, infrared thermography was employed during the tensile tests at room temperature, which revealed significant material self-heating at higher loading rates. Conclusively, the isothermal model was only fitted in the deformation range of approximately constant temperatures, which is an important requirement for future characterization studies for this class of polymers. The material parameters were assumed to be functions of the temperature as well as the degree of crystallinity, which served as constant input quantities. These individual functions were fitted during a staggered identification procedure, in order to minimize the uncertainty during the employed nonlinear optimization strategies.

Finally, the effect of the aforementioned factors on the loading-rate dependent plastic deformations, strain hardening, strain recovery, stress relaxation, and loading-unloading hysteresis loops were accurately predicted.

In Chapter 3, the model was further developed towards a fully thermo-mechanically coupled theory. To account for the microstructural formation of crystalline regimes during the solidification of the melt during processing, a non-isothermal modification of the Avrami model was included in the proposed framework. In this way, the (evolving) overall degree of crystallinity served as an additional internal variable which influenced the macroscopic behavior, by effecting the material parameters, as discussed above. Differential scanning calorimetry (DSC) experiments were utilized to characterize the corresponding crystallization kinetics parameters.

The free energy storage was taken into account and the relations for the heat release due to irreversible processes and exothermic crystal growth were derived from the energy balance. This is in contrast to other approaches, where a Taylor-Quinney factor is frequently proposed instead. Consequently, no additional parameters related to the material self-heating were proposed. Despite this fact, the model predictions of adiabatic heating and thermal softening were in good agreement with the experimental infrared thermography data.

Furthermore, academic thermo-mechanically coupled boundary value problems revealed the capabilities of the model to account for the complex crystallization phenomena and back-coupling effects on the temperature and mechanical behavior, in structural examples. Conclusively, the proposed theory provided a promising foundation for further investigations in the future.

Further research in this field is beyond doubt necessary. First of all, the experimental studies of the mechanical behavior must be extended to investigate different loading conditions (e.g. shear-, compression- and combined loading procedures). Clearly, the studies in Chapter 2 will help to reduce the number of experiments, by indicating which effects (e.g. loading rate and degree of crystallinity) have the highest impact at different temperatures (below and above the glass transition). Based on these results, a more accurate formulation of the yield criterion, accounting for the degree of crystallinity and temperature might be proposed.

Furthermore, in the current modification of the Avrami theory, the influence of the pressure on the crystallization was neglected, which is a big assumption considering the predominant processing conditions during thermoforming. Consequently, the model should be enhanced to account for this, in the future. In addition, the creation of the so-called rigid amorphous phase was not addressed at all (neither in the experimental study nor in the numerical modeling) and would thus be of interest for future investigations as well. Most crucial, two decoupled processes (I. supercooling of the polymer melt and II. thermo-mechanical behavior of solidified polymer) were considered, up to now. The crystallinity field was computed in a preceding step, where a purely thermo-chemically coupled problem was solved under the assumption of

a relaxed static melt. Subsequently, the computed crystallinity distribution served as a constant input parameter for the thermo-mechanically coupled model formulation, which was a considerable simplification. Thus, the derivation of a thermodynamically consistent and fully coupled theory remains an intriguingly challenging task, which the author (and his co-authors) aim to tackle in the near future.

The second part of this dissertation was concerned with the modeling of the coupled interplay and evolution of plasticity, damage, and temperature within metals. Thus, in Chapter 3 a general nonlinear theory of elasto-plasticity and damage coupled with heat conduction and heat generation was derived consistently from the second law of thermodynamics. To this end, a previously developed two-surface damage-plasticity framework was combined with the energy conservation law, including thermal dilatation, temperature dependent material parameters, thermal softening, and damage-dependent heat conduction. In order to obtain mesh-insensitive results, a gradient-extension based on the micromorphic approach was included. A monolithic finite element implementation was proposed, where the tangent operators were obtained using automatic differentiation. Three numerical examples (material self-heating at the material point level and two structural problems) confirmed the proposed theory. Mesh independent localization of strain, damage, and temperature was demonstrated, which was quantitatively and qualitatively in good agreement with experimental data from the literature.

Despite these promising capabilities of the proposed framework, a comprehensive experimental study is necessary, in order to fully characterize and validate the individual model parts. To this end, the author's workgroup currently plans extensive experimental investigations, where cyclic loading, different loading rates, and temperatures will be considered. In order to obtain 'true'stress-strain data and to resolve the evolution of the temperature field, due to material self-heating, digital image correlation and infrared thermography (comparable to the setup presented in Chapter 2) will be incorporated. From the planned experimental study, it must be judged whether the current simplification of a rate-independent plasticity and damage formulation is sufficiently accurate or if rate-dependent plasticity ought to be incorporated. Noteworthy, such further developments are straightforward and should be, in principle, 'easily'achievable.

It is instructive to point out that the onset and evolution of damage as well as plasticity in most metal forming processes are in general strongly direction-dependent, which can be traced back to the manufacturing process of the sheet metals. Consequently, the modeling of anisotropic damage and plasticity, by introducing higher-order damage tensors and more sophisticated yield criteria are of particular interest for future works. Furthermore, an additional gradient-enhancement of the plastic deformations, in line with the numerous contributions in

the field of regularized plasticity, would be of interest. Thus, plastic size effects could be captured due to a separate internal length scale, which might be a valuable improvement of the current formulation. One other crucial aspect is related to the incorporation of finite element technology, in order to circumvent potential locking effects during the evolution of large deviatoric plastic strains. To this end, reduced integration with hourglass stabilization could be employed. This would also lead to a higher efficiency, since the (computationally costly) material model would need to be evaluated in a single integration point per element only.

Finally, the thermo-mechanically coupled modeling of damage and irreversible deformations within semi-crystalline polymers could be tackled in a straightforward manner, by combining the contributions presented in this dissertation. To this end, the proposed theories within Chapter 2 and 3 for Polyamide 6 could be extended by a conceptually similar two-surface damage-plasticity ansatz and micromorphic extension, as presented in Chapter 4. In this way, the complex interactions between irreversible deformations, damage, temperature, and degree of crystallinity might be resolved, in the future. For example, the less ductile behavior for higher degrees of crystallinity (see Chapter 2) could be captured, by considering the damage onset parameter as a function of degree of crystallinity and temperature.

List of Figures

List of Tables

Bibliography

Abdul-Hameed, H., Messager, T., Zaïri, F. and Naït-Abdelaziz, M. [2014], 'Large-strain viscoelastic-viscoplastic constitutive modeling of semi-crystalline polymers and model identification by deterministic/evolutionary approach', *Computational Materials Science* **9**0, 241 – 252.

Ahzi, S., Makradi, A., Gregory, R. and Edie, D. [2003], 'Modeling of deformation behavior and strain-induced crystallization in poly(ethylene terephthalate) above the glass transition temperature', *Mechanics of Materials* **3**5(12), 1139 – 1148.

Aldakheel, F. and Miehe, C. [2017], 'Coupled thermomechanical response of gradient plasticity', *International Journal of Plasticity* **9**1, 1 – 24.

Aldakheel, F., Wriggers, P. and Miehe, C. [2018], 'A modified Gurson-type plasticity model at finite strains: formulation, numerical analysis and phase-field coupling', *Computational Mechanics* **6**2, 815 – 833.

Alisafaei, F., Han, C.-S. and Garg, N. [2016], 'On couple-stress elasto-plastic constitutive frameworks for glassy polymers', *International Journal of Plasticity* **7**7, 30 – 53.

Ambati, M., Kruse, R. and Lorenzis, L. D. [2016], 'A phase-field model for ductile fracture at finite strains and its experimental verification', *Computational Mechanics* **5**7(1), 149 – 167.

Ames, N. M., Srivastava, V., Chester, S. A. and Anand, L. [2009], 'A thermo-mechanically coupled theory for large deformations of amorphous polymers. part ii: Applications', *International Journal of Plasticity* **2**5(8), 1495 – 1539.

Amin, A. F. M. S., Lion, A., Sekita, S. and Okui, Y. [2006], 'Nonlinear dependence of viscosity in modeling the rate-dependent response of natural and high damping rubbers in compression and shear: Experimental identification and numerical verification', *International Journal of Plasticity* **2**2(9), 1610 – 1657.

Anand, L. and Ames, N. M. [2006], 'On modeling the micro-indentation response of an amorphous polymer', *International Journal of Plasticity* **2**2(6), 1123 – 1170.

Anand, L., Ames, N. M., Srivastava, V. and Chester, S. A. [2009], 'A thermo-mechanically coupled theory for large deformations of amorphous polymers. part i: Formulation', *International Journal of Plasticity* **2**5(8), 1474 – 1494.

Argyris, J. H. and Doltsinis, J. S. [1981], 'On the natural formulation and analysis of large deformation coupled thermomechanical problems', *Computer Methods in Applied Mechanics and Engineering* **2**5(2), 195 – 253.

Argyris, J. H., Doltsinis, J. S., Pimenta, P. M. and Wüstenberg, H. [1982], 'Thermomechanical response of solids at high strains - natural approach', *Computer Methods in Applied Mechanics and Engineering* **3**2(1), 3 – 57.

Armstrong, P. J. and Frederick, C. O. [1966], *A mathematical representation of the multiaxial Bauschinger effect*, CEGB Report RD/B/N731, Central Electricity Generating Board and Berkeley Nuclear Laboratories, Research & Development Department.

Arruda, E. M. and Boyce, M. C. [1993], 'A three-dimensional constitutive model for the large stretch behavior of rubber elastic materials', *Journal of the Mechanics and Physics of Solids* **4**1(2), 389 – 412.

Arruda, E. M., Boyce, M. C. and Jayachandran, R. [1995], 'Effects of strain rate, temperature and thermomechanical coupling on the finite strain deformation of glassy polymers', *Mechanics of Materials* **1**9(2), 193 – 212.

Aslan, O., Cordero, N. M., Gaubert, A. and Forest, S. [2011], 'Micromorphic approach to single crystal plasticity and damage', *International Journal of Engineering Science* **4**9(12), 1311 – 1325.

Aslan, O., Quilici, S. and Forest, S. [2011], 'Numerical modeling of fatigue crack growth in single crystals based on microdamage theory', *International Journal of Damage Mechanics* **2**0(5), 681 – 705.

Avrami, M. [1939], 'Kinetics of phase change. i general theory', *The Journal of Chemical Physics* **7**(12), 1103 – 1112.

Avrami, M. [1940], 'Kinetics of phase change. ii transformation - time relations for random distribution of nuclei', *The Journal of Chemical Physics* **8**(2), 212 – 224.

Ayoub, G., Zaïri, F., Fréderix, C., Gloaguen, J., Naït-Abdelaziz, M., Seguela, R. and Lefebvre, J. [2011], 'Effects of crystal content on the mechanical behaviour of polyethylene under finite strains: Experiments and constitutive modelling', *International Journal of Plasticity* **2**7(4), 492 – 511.

Ayoub, G., Zaïri, F., Naït-Abdelaziz, M. and Gloaguen, J. M. [2010], 'Modelling large deformation behaviour under loading - unloading of semicrystalline polymers: Application to a high density polyethylene', *International Journal of Plasticity* **2**6(3), 329 – 347.

Badreddine, H., Saanouni, K. and Dogui, A. [2010], 'On non-associative anisotropic finite plasticity fully coupled with isotropic ductile damage for metal forming', *International Journal of Plasticity* **2**6(11), 1541 – 1575.

Badreddine, H., Yue, Z. M. and Saanouni, K. [2017], 'Modeling of the induced plastic anisotropy fully coupled with ductile damage under finite strains', *International Journal of Solids and Structures* **1**08, 49 – 62.

Bai, Y. and Wierzbicki, T. [2008], 'A new model of metal plasticity and fracture with pressure and Lode dependence', *International Journal of Plasticity* **2**4(6), 1071 – 1096.

Balieu, R. and Kringos, N. [2015], 'A new thermodynamical framework for finite strain multiplicative elastoplasticity coupled to anisotropic damage', *International Journal of Plasticity* **7**0, 126 – 150.

Barfusz, O., Brepols, T., van der Velden, T., Frischkorn, J. and Reese, S. [2021], 'A single gauss point continuum finite element formulation for gradient-extended damage at large deformations', *Computer Methods in Applied Mechanics and Engineering* **3**73, 113440.

Barriere, T., Gabrion, X. and Holopainen, S. [2019], 'A compact constitutive model to describe the viscoelastic-plastic behaviour of glassy polymers: Comparison with monotonic and cyclic experiments and state-of-the-art models', *International Journal of Plasticity* **1**22, 31–48.

Bažant, Z. P., Belytschko, T. and Chang, T.-P. [1984], 'Continuum theory for strain-softening', *Journal of Engineering Mechanics* **1**10(12), 1666 – 1692.

Bažant, Z. P. and Jirásek, M. [2002], 'Nonlocal integral formulations of plasticity and damage: Survey of progress', *Journal of Engineering Mechanics* **1**28(11), 1119 – 1149.

Belytschko, T., Liu, W. K., Moran, B. and Elkhodary, K. [2014], *Nonlinear Finite Elements for Continua and Structures*, 2nd edn, Wiley.

Bergström, J. S., Rimnac, C. M. and Kurtz, S. M. [2003], 'Prediction of multiaxial mechanical behavior for conventional and highly crosslinked uhmwpe using a hybrid constitutive model', *Biomaterials* **2**4(8), 1365 – 1380.

Bertram, A. [2003], 'Finite thermoplasticity based on isomorphisms', *International Journal of Plasticity* **1**9(11), 2027 – 2050.

Biroli, G. and Garrahan, J. P. [2013], 'Perspective: The glass transition', *The Journal of Chemical Physics* **1**38(12), 12A301.

Boyce, M., Socrate, S. and Llana, P. [2000], 'Constitutive model for the finite deformation stress-strain behavior of poly(ethylene terephthalate) above the glass transition', *Polymer* **4**1(6), 2183 – 2201.

Bragov, A., Igumnov, L., Konstantinov, A., Lomunov, A. and Rusin, E. [2019], 'Effects of high strain rate and self-heating on plastic deformation of metal materials under fast compression loading', *Journal of Dynamic Behavior of Materials* **5**, 309 – 319.

Brepols, T., Wulfinghoff, S. and Reese, S. [2017], 'Gradient-extended two-surface damage-plasticity: Micromorphic formulation and numerical aspects', *International Journal of Plasticity* **9**7, 64 – 106.

Brepols, T., Wulfinghoff, S. and Reese, S. [2018], A Micromorphic Damage-Plasticity Model to Counteract Mesh Dependence in Finite Element Simulations Involving Material Softening, *in* J. Sorić, P. Wriggers and O. Allix, eds, 'Multiscale Modeling of Heterogeneous Structures', Vol. 86 of *Lecture Notes in Applied and Computational Mechanics*, Springer International Publishing, Cham, pp. 235 – 255.

Brepols, T., Wulfinghoff, S. and Reese, S. [2020], 'A gradient-extended two-surface damage-plasticity model for large deformations', *International Journal of Plasticity* **1**29, 102635.

Brünig, M., Gerke, S. and Hagenbrock, V. [2014], 'Stress-state-dependence of damage strain rate tensors caused by growth and coalescence of micro-defects', *International Journal of Plasticity* **6**3, 49 – 63.

Brünig, M., Gerke, S. and Schmidt, M. [2018], 'Damage and failure at negative stress triaxialities: Experiments, modeling and numerical simulations', *International Journal of Plasticity* **1**02, 70 – 82.

Canadija, M. and Mosler, J. [2011], 'On the thermomechanical coupling in finite strain plasticity theory with non-linear kinematic hardening by means of incremental energy minimization', *International Journal of Solids and Structures* **4**8(7), 1120 – 1129.

Cavallo, D., Gardella, L., Alfonso, G. C., Portale, G., Balzano, L. and Androsch, R. [2011], 'Effect of cooling rate on the crystal/mesophase polymorphism of polyamide 6', *Colloid and Polymer Science* **2**89(9), 1073–1079.

Cervera, M. and Chiumenti, M. [2006], 'Mesh objective tensile cracking via a local continuum damage model and a crack tracking technique', *Computer Methods in Applied Mechanics and Engineering* **1**96(1 – 3), 304 – 320.

Chaboche, J.-L. [1978], Description thermodynamique et phénoménologique de la viscoplasticité cyclique avec endommagement, PhD thesis, University Pierre and Marie Curie (Paris VI).

Chadwick, P. and Creasy, C. F. M. [1984], 'Modified entropic elasticity of rubberlike materials', *Journal of the Mechanics and Physics of Solids* **3**2(5), 337 – 357.

Chadwick, P. and Hill, R. [1974], 'Thermo-mechanics of rubberlike materials', *Philosophical Transactions of the Royal Society of London. Series A, Mathematical and Physical Sciences* **2**76(1260), 371–403.

Chen, H. and Cebe, P. [2007], 'Investigation of the rigid amorphous fraction in nylon-6', *Journal of Thermal Analysis and Calorimetry* **8**9(2), 417 – 425.

Chen, K., Kang, G., Yu, C. and Jiang, H. [2019], 'Effect of crystalline content on ratchetting of ultra-high molecular weight polyethylene polymers: Experimental investigation and constitutive model', *Mechanics of Materials* **1**33, 37 – 54.

Chevalier, J., Brassart, L., Lani, F., Bailly, C., Pardoen, T. and Morelle, X. P. [2018], 'Unveiling the nanoscale heterogeneity controlled deformation of thermosets', *Journal of the Mechanics and Physics of Solids* **1**21, 432 – 446.

Coleman, B. D. and Noll, W. [1961], 'Foundations of linear viscoelasticity', *Reviews of Modern Physics* **3**3, 239 – 249.

Comi, C. [1999], 'Computational modelling of gradient-enhanced damage in quasi-brittle materials', *Mechanics of Cohesive-frictional Materials* **4**(1), 17 – 36.

Şerban, D. A., Weber, G., Marşavina, L., Silberschmidt, V. V. and Hufenbach, W. [2013], 'Tensile properties of semi-crystalline thermoplastic polymers: Effects of temperature and strain rates', *Polymer Testing* **3**2(2), 413 – 425.

Cui, J., Lei, C., Xing, Z. and Li, C. [2012], 'Microstructure distribution and mechanical properties prediction of boron alloy during hot forming using fe simulation', *Materials Science and Engineering: A* **5**35, 241 – 251.

de Borst, R., Crisfield, M., Remmers, J. and Verhiisel, C. [2012], *Nonlinear finite element analysis of solids and structures*, John Wiley & Sons Ltd.

de Borst, R., Sluys, L. J., Mühlhaus, H.-B. and Pamin, J. [1993], 'Fundamental issues in finite element analyses of localization of deformation', *Engineering Computations* **1**0(2), 99 – 121.

de Souza Neto, E. A., Perić, D. and Owen, D. R. J. [2008], *Computational Methods for Plasticity: Theory and Applications*, John Wiley & Sons, Ltd.

Desmorat, R. and Cantournet, S. [2008], 'Modeling microdefects closure effect with isotropic/anisotropic damage', *International Journal of Damage Mechanics* **1**7(1), 65 – 96.

Dettmer, W. and Reese, S. [2004], 'On the theoretical and numerical modelling of Armstrong-Frederick kinematic hardening in the finite strain regime', *Computer Methods in Applied Mechanics and Engineering* **1**93(1 – 2), 87 – 116.

Dimitrijevic, B. J. and Hackl, K. [2011], 'A regularization framework for damage-plasticity models via gradient enhancement of the free energy', *International Journal for Numerical Methods in Biomedical Engineering* **2**7(8), 1199 – 1210.

Dittmann, M., Aldakheel, F., Schulte, J., Schmidt, F., Krüger, M., Wriggers, P. and Hesch, C. [2020], 'Phase-field modeling of porous-ductile fracture in non-linear thermo-elasto-plastic solids', *Computer Methods in Applied Mechanics and Engineering* **3**61, 112730.

Dittmann, M., Aldakheel, F., Schulte, J., Wriggers, P. and Hesch, C. [2018], 'Variational phase-field formulation of non-linear ductile fracture', *Computer Methods in Applied Mechanics and Engineering* **3**42, 71 – 94.

Dittmann, M., Krüger, M., Schmidt, F., Schuß, S. and Hesch, C. [2019], 'Variational modeling of thermomechanical fracture and anisotropic frictional mortar contact problems with adhesion', *Computational Mechanics* **6**3, 571 – 591.

dos Santos, W. N., de Sousa, J. A. and Gregorio, R. [2013], 'Thermal conductivity behaviour of polymers around glass transition and crystalline melting temperatures', *Polymer Testing* **3**2(5), 987 – 994.

Drozdov, A. D. [2011], 'Cyclic strengthening of polypropylene under strain-controlled loading', *Materials Science and Engineering: A* **5**28(29), 8781 – 8789.

Drozdov, A. D. and Gupta, R. K. [2003], 'Constitutive equations in finite viscoplasticity of semicrystalline polymers', *International Journal of Solids and Structures* **4**0(23), 6217 – 6243.

Dusunceli, N. and Colak, O. U. [2008], 'Modelling effects of degree of crystallinity on mechanical behavior of semicrystalline polymers', *International Journal of Plasticity* **2**4(7), 1224 – 1242.

Eckart, C. [1948], 'The Thermodynamics of Irreversible Processes. IV. The Theory of Elasticity and Anelasticity', *Physical Review* **7**3(4), 373 – 382.

El-Qoubaa, Z. and Othman, R. [2016], 'Strain rate sensitivity of polyetheretherketone's compressive yield stress at low and high temperatures', *Mechanics of Materials* **9**5, 15 – 27.

Engel, T., Drobny, G. and Reid, P. [2013], *Physical Chemistry: Pearson New International Edition*, Pearson Education Limited.

Engelen, R. A. B., Geers, M. G. D. and Baaijens, F. P. T. [2002], 'Nonlocal implicit gradient-enhanced elasto-plasticity for the modelling of softening behaviour', *International Journal of Plasticity* **1**9, 403 – 433.

Faraj, J., Pignon, B., Bailleul, J. L., Boyard, N., Delaunay, D. and Orange, G. [2015], 'Heat transfer and crystallization modeling during compression molding of thermoplastic composite parts', *Key Engineering Materials* **6**51 - 653, 1507 – 1512.

Felder, S., Holthusen, H., Hesseler, S., Pohlkemper, F., Gries, T., Simon, J.-W. and Reese, S. [2020], 'Incorporating crystallinity distributions into a thermo-mechanically coupled constitutive model for semi-crystalline polymers', *International Journal of Plasticity* **1**35, 102751.

Felder, S., Vu, N. A., Reese, S. and Simon, J.-W. [2020], 'Modeling the effect of temperature and degree of crystallinity on the mechanical response of polyamide 6', *Mechanics of Materials* **1**48, 103476.

Fleck, N. A. and Willis, J. R. [2009], 'A mathematical basis for strain-gradient plasticity theory - part i: Scalar plastic multiplier', *Journal of the Mechanics and Physics of Solids* **5**7(1), 161 – 177.

Flory, P. J. [1961], 'Thermodynamic relations for high elastic materials', *Transaction of the Faraday Society* **5**7, 829–838.

Forest, S. [2009], 'Micromorphic approach for gradient elasticity, viscoplasticity, and damage', *Journal of Engineering Mechanics* **1**35(3), 117 – 131.

Forest, S. [2016], 'Nonlinear regularization operators as derived from the micromorphic approach to gradient elasticity, viscoplasticity and damage', *Proceedings of the Royal Society of London A: Mathematical, Physical and Engineering Sciences* **4**72(2188).

Forest, S. and Aifantis, E. C. [2010], 'Some links between recent gradient thermo-elastoplasticity theories and the thermomechanics of generalized continua', *International Journal of Solids and Structures* **4**7(25), 3367 – 3376.

Fornes, T. and Paul, D. [2003], 'Crystallization behavior of nylon 6 nanocomposites', *Polymer* **4**4(14), 3945 – 3961.

Fujiyama, M., Awaya, H. and Kimura, S. [1977], 'Mechanical anisotropy in injection-molded polypropylene', *Journal of Applied Polymer Science* **2**1(12), 3291 – 3309.

Garcia-Gonzalez, D., Garzon-Hernandez, S. and Arias, A. [2018], 'A new constitutive model for polymeric matrices: Application to biomedical materials', *Composites Part B: Engineering* **1**39, 117 – 129.

Gaur, U., Lau, S., Wunderlich, B. B. and Wunderlich, B. [1983], 'Heat capacity and other thermodynamic properties of linear macromolecules. viii. polyesters and polyamides', *Journal of Physical and Chemical Reference Data* **1**2(1), 65 – 89.

Goff, R. L., Poutot, G., Delaunay, D., Fulchiron, R. and Koscher, E. [2005], 'Study and modeling of heat transfer during the solidification of semi-crystalline polymers', *International Journal of Heat and Mass Transfer* **4**8(25), 5417 – 5430.

Gudimetla, M. R. and Doghri, I. [2017], 'A finite strain thermodynamically-based constitutive framework coupling viscoelasticity and viscoplasticity with application to glassy polymers', *International Journal of Plasticity* **9**8, 197 – 216.

Gudmundson, P. [2004], 'A unified treatment of strain gradient plasticity', *Journal of the Mechanics and Physics of Solids* **5**2(6), 1379 – 1406.

Gueguen, O., Ahzi, S., Makradi, A. and Belouettar, S. [2010], 'A new three-phase model to estimate the effective elastic properties of semi-crystalline polymers: Application to pet', *Mechanics of Materials* **4**2(1), 1 – 10.

Gurato, G., Fichera, A., Grandi, F. Z., Zannetti, R. and Canal, P. [1974], 'Crystallinity and polymorphism of 6-polyamide', *Die Makromolekulare Chemie* **1**75(3), 953 – 975.

Gurson, A. L. [1977], 'Continuum theory of ductile rupture by void nucleation and growth: Part I – Yield criteria and flow rules for porous ductile media', *Journal of Engineering Materials and Technology* **9**9(1), 2 – 15.

Gurtin, M. E. [2008], 'A finite-deformation, gradient theory of single-crystal plasticity with free energy dependent on densities of geometrically necessary dislocations', *International Journal of Plasticity* **2**4(4), 702 – 725.

Hansen, N. R. and Schreyer, H. L. [1994], 'A thermodynamically consistent framework for theories of elastoplasticity coupled with damage', *International Journal of Solids and Structures* **3**1(3), 359 – 389.

Hasan, O. A. and Boyce, M. C. [1995], 'A constitutive model for the nonlinear viscoelastic viscoplastic behavior of glassy polymers', *Polymer Engineering & Science* **3**5(4), 331 – 344.

Haward, R. N., Thackray, G. and Sugden, T. M. [1968], 'The use of a mathematical model to describe isothermal stress-strain curves in glassy thermoplastics', *Proceedings of the Royal Society of London. Series A. Mathematical and Physical Sciences* **3**02(1471), 453 – 472.

Hirth, J. P. and Lothe, J. [1982], *Theory of Dislocations*, New York: Wiley.

Holzapfel, G. A. and Simo, J. C. [1996], 'A new viscoelastic constitutive model for continuous media at finite thermomechanical changes', *International Journal of Solids and Structures* **3**3(20), 3019 – 3034.

Hosokawa, A., Wilkinson, D. S., Kang, J., Kobayashi, M. and Toda, H. [2013], 'Void growth and coalescence in model materials investigated by high-resolution X-ray microtomography', *International Journal of Fracture* **1**81(1), 51 – 66.

Illers, K. H. [1978], 'Polymorphie, kristallinität und schmelzwärme von poly(ϵ-caprolactam), 2. kalorimetrische untersuchungen', *Die Makromolekulare Chemie* **1**79(2), 497 – 507.

Illers, K. H., Haberkorn, H. and Simák, P. [1972], 'Untersuchungen über die γ-struktur in unverstrecktem und verstrecktem 6-polyamid', *Die Makromolekulare Chemie* **1**58(1), 285 – 311.

Incropera, F. P., Lavine, A. S., Bergman, T. L. and DeWitt, D. [2007], *Fundamentals of Heat and Mass Transfer*, Wiley.

Ishisaka, A. and Kawagoe, M. [2004], 'Examination of the time-water content superposition on the dynamic viscoelasticity of moistened polyamide 6 and epoxy', *Journal of Applied Polymer Science* **9**3(2), 560 – 567.

Jabbari-Farouji, S., Lame, O., Perez, M., Rottler, J. and Barrat, J.-L. [2017], 'Role of the intercrystalline tie chains network in the mechanical response of semicrystalline polymers', *Physical Review Letters* **1**18, 217802.

Jatin, Sudarkodi, V. and Basu, S. [2014], 'Investigations into the origins of plastic flow and strain hardening in amorphous glassy polymers', *International Journal of Plasticity* **5**6, 139 – 155.

Jenkins, A. D. [1992], *Polymers: chemistry & physics of modern materials*, Vol. 28, J. M. G. Cowie Blackie & Son Ltd, Glasgow & London Chapman & Hall, New York, 1991.

Jeziorny, A. [1978], 'Parameters characterizing the kinetics of the non-isothermal crystallization of poly(ethylene terephthalate) determined by d.s.c.', *Polymer* **1**9(10), 1142 – 1144.

Jiang, W., Li, Y. and Su, J. [2016], 'Modified gtn model for a broad range of stress states and application to ductile fracture', *European Journal of Mechanics - A/Solids* **5**7, 132 – 148.

Jirásek, M. and Grassl, P. [2008], 'Evaluation of directional mesh bias in concrete fracture simulations using continuum damage models', *Engineering Fracture Mechanics* **7**5(8), 1921 – 1943.

Jurkowski, B., Olkhov, Y. A., Kelar, K. and Olkhova, O. M. [2002], 'Thermomechanical study of low-density polyethylene, polyamide 6 and its blends', *European Polymer Journal* **3**8(6), 1229 – 1236.

Kachanov, L. M. [1958], 'Time of the rupture process under creep conditions', *Izvestiya Akademii Nauk SSSR. Otdelenie Tekhnicheskikh Nauk* **8**, 26 – 31.

Kaliske, M. and Rothert, H. [1997], 'On the finite element implementation of rubber-like materials at finite strains', *Engineering Computations* **1**4, 216 – 232.

Kästner, M., Obst, M., Brummund, J., Thielsch, K. and Ulbricht, V. [2012], 'Inelastic material behavior of polymers - experimental characterization, formulation and implementation of a material model', *Mechanics of Materials* **5**2, 40 – 57.

Katunin, A. [2019], 'Criticality of the self-heating effect in polymers and polymer matrix composites during fatigue, and their application in non-destructive testing', *Polymers* **1**1(1).

Kelly, A., Stebner, A. P. and Bhattacharya, K. [2016], 'A micromechanics-inspired constitutive model for shape-memory alloys that accounts for initiation and saturation of phase transformation', *Journal of the Mechanics and Physics of Solids* **9**7, 197 – 224.

Khan, A. S., Lopez-Pamies, O. and Kazmi, R. [2006], 'Thermo-mechanical large deformation response and constitutive modeling of viscoelastic polymers over a wide range of strain rates and temperatures', *International Journal of Plasticity* **2**2(4), 581 – 601.

Khan, F. and Yeakle, C. [2011], 'Experimental investigation and modeling of non-monotonic creep behavior in polymers', *International Journal of Plasticity* **2**7(4), 512 – 521.

Khanna, Y. P. and Kuhn, W. P. [1997], 'Measurement of crystalline index in nylons by dsc: Complexities and recommendations', *Journal of Polymer Science Part B: Polymer Physics* **3**5(14), 2219 – 2231.

Kiefer, B., Waffenschmidt, T., Sprave, L. and Menzel, A. [2018], 'A gradient-enhanced damage model coupled to plasticity – multi-surface formulation and algorithmic concepts', *International Journal of Damage Mechanics* **2**7(2), 253 – 295.

Klusemann, B. and Yalçinkaya, T. [2013], 'Plastic deformation induced microstructure evolution through gradient enhanced crystal plasticity based on a non-convex helmholtz energy', *International Journal of Plasticity* **4**8, 168 – 188.

Knysh, P. and Korkolis, Y. P. [2015], 'Determination of the fraction of plastic work converted into heat in metals', *Mechanics of Materials* **8**6, 71 – 80.

Korelc, J. [2002], 'Multi-language and multi-environment generation of nonlinear finite element codes', *Engineering with Computers* **1**8, 312 – 327.

Korelc, J. and Wriggers, P. [2016], *Automation of Finite Element Methods*, Springer.

Krairi, A. and Doghri, I. [2014], 'A thermodynamically-based constitutive model for thermoplastic polymers coupling viscoelasticity, viscoplasticity and ductile damage', *International Journal of Plasticity* **6**0, 163 – 181.

Krairi, A., Doghri, I., Schalnat, J., Robert, G. and Paepegem, W. V. [2019], 'Thermomechanical coupling of a viscoelastic-viscoplastic model for thermoplastic polymers: Thermodynamical derivation and experimental assessment', *International Journal of Plasticity* **1**15, 154 – 177.

Kröner, E. [1959], 'Allgemeine Kontinuumstheorie der Versetzungen und Eigenspannungen', *Archive for Rational Mechanics and Analysis* **4**(1), 273 – 334.

Kugele, D., Dörr, D., Wittemann, F., Hangs, B., Rausch, J., Kärger, L. and Henning, F. [2017], 'Modeling of the non-isothermal crystallization kinetics of polyamide 6 composites during thermoforming', *AIP Conference Proceedings* **1**896(1), 030005 – 030005 – 6.

Kyotani, M. and Mitsuhashi, S. [1972], 'Studies on crystalline forms of nylon 6. ii. crystallization from the melt', *Journal of Polymer Science Part A-2: Polymer Physics* **1**0(8), 1497 – 1508.

Lai, D., Yakimets, I. and Guigon, M. [2005], 'A non-linear viscoelastic model developed for semi-crystalline polymer deformed at small strains with loading and unloading paths', *Materials Science and Engineering: A* **4**05(1), 266 – 271.

Landron, C., Bouaziz, O., Maire, E. and Adrien, J. [2013], 'Experimental investigation of void coalescence in a dual phase steel using X-ray tomography', *Acta Materialia* **6**1(18), 6821 – 6829.

Lee, E. H. [1969], 'Elastic-plastic deformation at finite strains', *Journal of Applied Mechanics* **3**6(1), 1 – 6.

Lei, M., Hamel, C. M., Chen, K., Zhao, Z., Lu, H., Yu, K. and Qi, H. J. [2021], 'Thermomechanical behaviors of polyether ether ketone (peek) with stretch-induced anisotropy', *Journal of the Mechanics and Physics of Solids* **1**48, 104271.

Lemaitre, J. [1984], A three-dimensional ductile damage model applied to deep-drawing forming limits, *in* J. Carlsson and N. G. Ohlson, eds, 'Mechanical Behaviour of Materials', Pergamon, pp. 1047 – 1053.

Lemaitre, J. [1985*a*], 'A continuous damage mechanics model for ductile fracture', *Journal of Engineering Materials and Technology* **1**07(1), 83 – 89.

Lemaitre, J. [1985*b*], 'Coupled elasto-plasticity and damage constitutive equations', *Computer Methods in Applied Mechanics and Engineering* **5**1(1), 31 – 49.

Li, G. and Shojaei, A. [2012], 'A viscoplastic theory of shape memory polymer fibres with application to self-healing materials', *Proceedings of the Royal Society A: Mathematical, Physical and Engineering Sciences* **4**68(2144), 2319 – 2346.

Li, M., Wan, Y., Gao, Z., Xiong, G., Wang, X., Wan, C. and Luo, H. [2013], 'Preparation and properties of polyamide 6 thermal conductive composites reinforced with fibers', *Materials & Design* **5**1, 257 – 261.

Li, W., Gazonas, G., Brown, E. N., Rae, P. J. and Negahban, M. [2019], 'Thermomechanical model for monotonic and cyclic loading of peek', *Mechanics of Materials* **1**29, 113 – 138.

Lion, A. [1997*a*], 'On the large deformation behaviour of reinforced rubber at different temperatures', *Journal of the Mechanics and Physics of Solids* **4**5(11), 1805 – 1834.

Lion, A. [1997*b*], 'A physically based method to represent the thermo-mechanical behaviour of elastomers', *Mechanica* **1**23, 1 – 25.

Lion, A. [2000], 'Constitutive modelling in finite thermoviscoplasticity: a physical approach based on nonlinear rheological models', *International Journal of Plasticity* **1**6(5), 469 – 494.

Lion, A., Dippel, B. and Liebl, C. [2014], 'Thermomechanical material modelling based on a hybrid free energy density depending on pressure, isochoric deformation and temperature', *International Journal of Solids and Structures* **5**1(3), 729 – 739.

Lion, A. and Johlitz, M. [2016], 'A thermodynamic approach to model the caloric properties of semicrystalline polymers', *Continuum Mechanics and Thermodynamics* **2**8, 799 – 819.

Lion, A., Liebl, C., Kolmeder, S. and Peters, J. [2010], 'Representation of the glass-transition in mechanical and thermal properties of glass-forming materials: A three-dimensional theory based on thermodynamics with internal state variables', *Journal of the Mechanics and Physics of Solids* **5**8(9), 1338 – 1360.

Lion, A., Mittermeier, C. and Johlitz, M. [2017], 'Heat capacities and volumetric changes in the glass transition range: a constitutive approach based on the standard linear solid', *Continuum Mechanics and Thermodynamics* **2**9, 1061 – 1079.

Lion, A., Peters, J. and Kolmeder, S. [2011], 'Simulation of temperature history-dependent phenomena of glass-forming materials based on thermodynamics with internal state variables', *Thermochimica Acta* **5**22(1), 182 – 193. Special Issue: Interplay between Nucleation, Crystallization, and the Glass Transition.

Liu, Y. and Yang, G. [2010], 'Non-isothermal crystallization kinetics of polyamide-6/graphite oxide nanocomposites', *Thermochimica Acta* **5**00(1), 13 – 20.

Lodygowski, A., Voyiadjis, G. Z., Deliktas, B. and Palazotto, A. [2011], 'Non-local and numerical formulations for dry sliding friction and wear at high velocities', *International Journal of Plasticity* **2**7(7), 1004 – 1024.

Lubarda, V. A. [2004], 'Constitutive theories based on the multiplicative decomposition of deformation gradient: Thermoelasticity, elastoplasticity, and biomechanics', *Applied Mechanics Reviews* **5**7(2), 95 – 108.

Lubliner, J. [1985], 'A model of rubber viscoelasticity', *Mechanics Research Communications* **1**2(2), 93 – 99.

Malcher, L. and Mamiya, E. N. [2014], 'An improved damage evolution law based on continuum damage mechanics and its dependence on both stress triaxiality and the third invariant', *International Journal of Plasticity* **5**6, 232 – 261.

Mandelkern, L., Quinn, F. A. and Flory, P. J. [1954], 'Crystallization kinetics in high polymers. i. bulk polymers', *Journal of Applied Physics* **2**5(7), 830 – 839.

Maurel-Pantel, A., Baquet, E., Bikard, J., Bouvard, J. L. and Billon, N. [2015], 'A thermo-mechanical large deformation constitutive model for polymers based on material network description: Application to a semi-crystalline polyamide 66', *International Journal of Plasticity* **6**7, 102 – 126.

Merklein, M. and Lechler, J. [2006], 'Investigation of the thermo-mechanical properties of hot stamping steels', *Journal of Materials Processing Technology* **1**77(1), 452 – 455. Proceedings of the 11th International Conference on Metal Forming 2006.

Miehe, C. [1996], 'Numerical computation of algorithmic (consistent) tangent moduli in large-strain computational inelasticity', *Computer Methods in Applied Mechanics and Engineering* **1**34(3 – 4), 223 – 240.

Miehe, C. [2014], 'Variational gradient plasticity at finite strains. Part I: Mixed potentials for the evolution and update problems of gradient-extended dissipative solids', *Computer Methods in Applied Mechanics and Engineering* **2**68, 677 – 703.

Miehe, C., Aldakheel, F. and Raina, A. [2016], 'Phase field modeling of ductile fracture at finite strains: A variational gradient-extended plasticity-damage theory', *International Journal of Plasticity* **8**4, 1 – 32.

Miehe, C., Kienle, D., Aldakheel, F. and Teichtmeister, S. [2016], 'Phase field modeling of fracture in porous plasticity: A variational gradient-extended Eulerian framework for the macroscopic analysis of ductile failure', *Computer Methods in Applied Mechanics and Engineering* **3**12, 3 – 50.

Miehe, C., Schänzel, L.-M. and Ulmer, H. [2015], 'Phase field modeling of fracture in multi-physics problems. part i. balance of crack surface and failure criteria for brittle crack propagation in thermo-elastic solids', *Computer Methods in Applied Mechanics and Engineering* **2**94, 449–485.

Miehe, C., Teichtmeister, S. and Aldakheel, F. [2016], 'Phase-field modelling of ductile fracture: a variational gradient-extended plasticity-damage theory and its micromorphic regularization', *Philosophical Transactions of the Royal Society of London A: Mathematical, Physical and Engineering Sciences* **3**74(2066).

Miehe, C., Welschinger, F. and Aldakheel, F. [2014], 'Variational gradient plasticity at finite strains. part ii: Local–global updates and mixed finite elements for additive plasticity in the logarithmic strain space', *Computer Methods in Applied Mechanics and Engineering* **2**68, 704 – 734.

Miled, B., Doghri, I. and Delannay, L. [2011], 'Coupled viscoelastic-viscoplastic modeling of homogeneous and isotropic polymers: Numerical algorithm and analytical solutions', *Computer Methods in Applied Mechanics and Engineering* **2**00(47), 3381 – 3394.

Miller, P. J., Coffey, C. S. and DeVost, V. F. [1986], 'Heating in crystalline solids due to rapid deformation', *Journal of Applied Physics* **5**9(3), 913 – 916.

Millot, C., Fillot, L.-A., Lame, O., Sotta, P. and Seguela, R. [2015], 'Assessment of polyamide-6 crystallinity by dsc', *Journal of Thermal Analysis and Calorimetry* **1**22(1), 307 – 314.

Miri, V., Persyn, O., Lefebvre, J. M. and Seguela, R. [2009], 'Effect of water absorption on the plastic deformation behavior of nylon 6', *European Polymer Journal* **4**5(3), 757 – 762.

Mittermeier, C. and Lion, A. [2020], 'Challenges in the experimental investigation of the caloric and thermomechanical behaviour of semi-crystalline polymers: A study on the example of polyethylene terephthalate (pet)', *Polymer Testing* **8**1, 106252.

Mohagheghian, I., McShane, G. J. and Stronge, W. J. [2015], 'Impact perforation of monolithic polyethylene plates: Projectile nose shape dependence', *International Journal of Impact Engineering* **8**0, 162 – 176.

Moreau, S., Chrysochoos, A., Muracciole, J.-M. and Wattrisse, B. [2005], 'Analysis of thermoelastic effects accompanying the deformation of pmma and pc polymers', *Comptes Rendus Mécanique* **3**33(8), 648 – 653.

Mubarak, Y., Harkin-Jones, E. M. A., Martin, P. J. and Ahmad, M. [2001], 'Modeling of non-isothermal crystallization kinetics of isotactic polypropylene', *Polymer* **4**2(7), 3171 – 3182.

Nakamura, K., Katayama, K. and Amano, T. [1973], 'Some aspects of nonisothermal crystallization of polymers. ii. consideration of the isokinetic condition', *Journal of Applied Polymer Science* **1**7(4), 1031 – 1041.

Needleman, A. and Tvergaard, V. [1984], Limits to formability in rate-sensitive metal sheets, *in* J. Carlsson and N. G. Ohlson, eds, 'Mechanical Behaviour of Materials', Pergamon, pp. 51 – 65.

Neugebauer, F., Ploshikhin, V., Ambrosy, J. and G., W. [2016], 'Isothermal and non-isothermal crystallization kinetics of polyamide 12 used in laser sintering', *Journal of Thermal Analysis and Calorimetry* **1**24, 925 – 933.

Ozawa, T. [1971], 'Kinetics of non-isothermal crystallization', *Polymer* **1**2(3), 150 – 158.

Papadioti, I., Aravas, N., Lian, J. and Münstermann, S. [2019], 'A strain-gradient isotropic elastoplastic damage model with j3 dependence', *International Journal of Solids and Structures* **1**74-175, 98 – 127.

Parodi, E., Gerrit, P. W. M. and Govaert, L. E. [2018], 'Prediction of plasticity-controlled failure in polyamide 6: Influence of temperature and relative humidity', *Journal of Applied Polymer Science* **1**35(11), 45942.

Pietryga, M. P., Vladimirov, I. N. and Reese, S. [2012], 'A finite deformation model for evolving flow anisotropy with distortional hardening including experimental validation', *Mechanics of Materials* **4**4, 163 – 173. Microstructures and Anisotropies.

Pokharel, R., Lind, J., Kanjarla, A., Lebensohn, R. A., Li, S. F., Kenesei, P., Suter, R. M. and Rollett, A. D. [2014], 'Polycrystal plasticity: Comparison between grain - scale observations of deformation and simulations', *Annual Review of Condensed Matter Physics* **5**(1), 317 – 346.

Polizzotto, C. [2009], 'A nonlocal strain gradient plasticity theory for finite deformations', *International Journal of Plasticity* **2**5(7), 1280 – 1300.

Polizzotto, C. [2014], 'Surface effects, boundary conditions and evolution laws within second strain gradient plasticity', *International Journal of Plasticity* **6**0, 197 – 216.

Ponçot, M., Addiego, F. and Dahoun, A. [2013], 'True intrinsic mechanical behaviour of semicrystalline and amorphous polymers: Influences of volume deformation and cavities shape', *International Journal of Plasticity* **4**0, 126 – 139.

Popa, C. M., Fleischhauer, R., Schneider, K. and Kaliske, M. [2014], 'Formulation and implementation of a constitutive model for semicrystalline polymers', *International Journal of Plasticity* **6**1, 128 – 156.

Praud, F., Chatzigeorgiou, G., Bikard, J. and Meraghni, F. [2017], 'Phenomenological multimechanisms constitutive modelling for thermoplastic polymers, implicit implementation and experimental validation', *Mechanics of Materials* **1**14, 9 – 29.

Qi, Z., Hu, N., Li, G., Zeng, D. and Su, X. [2019], 'Constitutive modeling for the elastic-viscoplastic behavior of high density polyethylene under cyclic loading', *International Journal of Plasticity* **1**13, 125 – 144.

Rabotnov, Y. N. [1963], 'Paper 68: On the equation of state of creep', *Proceedings of the Institution of Mechanical Engineers, Conference Proceedings* **1**78(1), 117 – 122.

Rabotnov, Y. N. [1969], Creep rupture, *in* M. Hetényi and W. G. Vincenti, eds, 'Applied Mechanics', Springer Berlin Heidelberg, Berlin, Heidelberg, pp. 342 – 349.

Rae, P. J., Brown, E. N. and Orler, E. B. [2007], 'The mechanical properties of poly(ether-ether-ketone) (peek) with emphasis on the large compressive strain response', *Polymer* **4**8(2), 598 – 615.

Reddy, B. D., Ebobisse, F. and McBride, A. [2008], 'Well-posedness of a model of strain gradient plasticity for plastically irrotational materials', *International Journal of Plasticity* **2**4(1), 55 – 73.

Reese, S. [2002], 'On the equivalent of mixed element formulations and the concept of reduced integration in large deformation problems', *International Journal of Nonlinear Sciences and Numerical Simulation* **3**(1), 1 – 34.

Reese, S. [2003*a*], 'A micromechanically motivated material model for the thermo-viscoelastic material behaviour of rubber-like polymers', *International Journal of Plasticity* **1**9(7), 909 – 940.

Reese, S. [2003*b*], 'On a consistent hourglass stabilization technique to treat large inelastic deformations and thermo-mechanical coupling in plane strain problems', *International Journal for Numerical Methods in Engineering* **5**7(8), 1095 – 1127.

Reese, S. [2005], 'On a physically stabilized one point finite element formulation for three-dimensional finite elasto-plasticity', *Computer Methods in Applied Mechanics and Engineering* **1**94(45), 4685 – 4715.

Reese, S. and Christ, D. [2008], 'Finite deformation pseudo-elasticity of shape memory alloys – constitutive modelling and finite element implementation', *International Journal of Plasticity* **2**4(3), 455 – 482.

Reese, S. and Govindjee, S. [1998*a*], 'Theoretical and numerical aspects in the thermo-viscoelastic material behaviour of rubber-like polymers', *Mechanics of Time-Dependent Materials* **1**(4), 357 – 396.

Reese, S. and Govindjee, S. [1998*b*], 'A theory of finite viscoelasticity and numerical aspects', *International Journal of Solids and Structures* **3**5(26), 3455 – 3482.

Rosakis, P., Rosakis, A. J., Ravichandran, G. and Hodowany, J. [2000], 'A thermodynamic internal variable model for the partition of plastic work into heat and stored energy in metals', *Journal of the Mechanics and Physics of Solids* **4**8(3), 581 – 607.

Rose, L. and Menzel, A. [2020], 'Optimisation based material parameter identification using full field displacement and temperature measurements', *Mechanics of Materials* **1**45, 103292.

Rottler, J. [2009], 'Fracture in glassy polymers: a molecular modeling perspective', *Journal of Physics: Condensed Matter* **2**1(46), 463101.

Rozanski, A. and Galeski, A. [2013], 'Plastic yielding of semicrystalline polymers affected by amorphous phase', *International Journal of Plasticity* **4**1, 14 – 29.

Rusinek, A. and Klepaczko, J. R. [2009], 'Experiments on heat generated during plastic deformation and stored energy for trip steels', *Materials & Design* **3**0(1), 35 – 48.

Russo, R., Forest, S. and Mata, F. A. G. [2020], 'Thermomechanics of cosserat medium: modeling adiabatic shear bands in metals', *Continuum Mechanics and Thermodynamics* .

Saanouni, K. and Hamed, M. [2013], 'Micromorphic approach for finite gradient-elastoplasticity fully coupled with ductile damage: Formulation and computational aspects', *International Journal of Solids and Structures* **5**0(14 – 15), 2289 – 2309.

Sarkar, S., Singh, I. V. and Mishra, B. K. [2020], 'A thermo-mechanical gradient enhanced damage method for fracture', *Computational Mechanics* **6**6, 1399 – 1426.

Shan, G., Yang, W., Yang, M., Xie, B., Feng, J. and Fu, Q. [2007], 'Effect of temperature and strain rate on the tensile deformation of polyamide 6', *Polymer* **4**8(10), 2958 – 2968.

Shen, F., Kang, G., Lam, Y. C., Liu, Y. and Zhou, K. [2019], 'Thermo-elastic-viscoplastic-damage model for self-heating and mechanical behavior of thermoplastic polymers', *International Journal of Plasticity* **1**21, 227 – 243.

Shojaei, A. K. and Volgers, P. [2017], 'Fatigue damage assessment of unfilled polymers including self-heating effects', *International Journal of Fatigue* **1**00, 367 – 376.

Sicsic, P., Marigo, J.-J. and Maurini, C. [2014], 'Initiation of a periodic array of cracks in the thermal shock problem: A gradient damage modeling', *Journal of the Mechanics and Physics of Solids* **6**3, 256 – 284.

Sidoroff, F. [1974], 'Un modèle viscoélastique non linéaire avec configuration intermédiaire', *Journal de mécanique* **1**3, 679 – 713.

Sierra, J. D., Noriega, M. P., Gomez, J. F. and Pastor, J. M. [2006], 'Isothermal and non-isothermal crystallization kinetics for blends of polyamide 6 and polypropylene', *Journal of Plastics Technology* **5**, 1 – 21.

Simo, J. C. [1992], 'Algorithms for static and dynamic multiplicative plasticity that preserve the classical return mapping schemes of the infinitesimal theory', *Computer Methods in Applied Mechanics and Engineering* **99**(1), 61 – 112.

Simo, J. and Miehe, C. [1992], 'Associative coupled thermoplasticity at finite strains: Formulation, numerical analysis and implementation', *Computer Methods in Applied Mechanics and Engineering* **98**(1), 41 – 104.

Srivastava, V., Chester, S. A., Ames, N. M. and Anand, L. [2010], 'A thermo-mechanically-coupled large-deformation theory for amorphous polymers in a temperature range which spans their glass transition', *International Journal of Plasticity* **26**(8), 1138 – 1182. Special Issue In Honor of Lallit Anand.

Stainier, L. and Ortiz, M. [2010], 'Study and validation of a variational theory of thermo-mechanical coupling in finite visco-plasticity', *International Journal of Solids and Structures* **47**(5), 705 – 715.

Stein, E. and Sagar, G. [2008], 'Convergence behavior of 3D finite elements for Neo-Hookean material', *Engineering Computations* **25**(3), 220 – 232.

Stojanović, R., Djurić, S. and Vujošević, L. [1964], 'On finite thermal deformations', *Archives of Mechanics* **16**, 103 – 108.

Sun, W., Chaikof, E. L. and Levenston, M. E. [2008], 'Numerical approximation of tangent moduli for finite element implementations of nonlinear hyperelastic material models', *Journal of Biomechanical Engineering* **130**(6), 061003 – 061003 – 7.

Sutton, M. A., Orteu, J. and Schreier, H. W. [2009], *Image correlation for shape, motion and deformation measurements: Basic concepts, theory and applications*, Springer, Boston, MA.

Svendsen, B. and Bargmann, S. [2010], 'On the continuum thermodynamic rate variational formulation of models for extended crystal plasticity at large deformation', *Journal of the Mechanics and Physics of Solids* **58**(9), 1253 – 1271.

Tekoğlu, C., Hutchinson, J. W. and Pardoen, T. [2015], 'On localization and void coalescence as a precursor to ductile fracture', *Philosophical Transactions of the Royal Society of London A: Mathematical, Physical and Engineering Sciences* **3**73(2038).

Turnbull, D. and Fisher, J. C. [1949], 'Rate of nucleation in condensed systems', *The Journal of Chemical Physics* **1**7(1), 71–73.

Uchida, M. and Tada, N. [2013], 'Micro-, meso- to macroscopic modeling of deformation behavior of semi-crystalline polymer', *International Journal of Plasticity* **4**9, 164 – 184.

van Dommelen, J. A. W., Parks, D. M., Boyce, M. C., Brekelmans, W. A. M. and Baaijens, F. P. T. [2003], 'Micromechanical modeling of the elasto-viscoplastic behavior of semi-crystalline polymers', *Journal of the Mechanics and Physics of Solids* **5**1(3), 519 – 541.

Vázquez, J., López-Alemany, P., Villares, P. and Jiménez-Garay, R. [2000], 'Generalization of the avrami equation for the analysis of non-isothermal transformation kinetics. application to the crystallization of the cu0.20as0.30se0.50 alloy', *Journal of Physics and Chemistry of Solids* **6**1(4), 493 – 500.

Vignjevic, R., Djordjevic, N. and Panov, V. [2012], 'Modelling of dynamic behaviour of orthotropic metals including damage and failure', *International Journal of Plasticity* **3**8, 47 – 85.

Vladimirov, I. N., Pietryga, M. P. and Reese, S. [2008], 'On the modelling of non-linear kinematic hardening at finite strains with application to springback – comparison of time integration algorithms', *International Journal for Numerical Methods in Engineering* **7**5(1), 1 – 28.

Voce, E. [1955], 'A practical strain-hardening function', *Metallurgia* **5**1(307), 219 – 226.

Voyiadjis, G. Z. and Faghihi, D. [2012], 'Thermo-mechanical strain gradient plasticity with energetic and dissipative length scales', *International Journal of Plasticity* **3**0-31, 218 – 247.

Voyiadjis, G. Z., Pekmezi, G. and Deliktas, B. [2010], 'Nonlocal gradient-dependent modeling of plasticity with anisotropic hardening', *International Journal of Plasticity* **2**6(9), 1335 – 1356. Special Issue In Honor of David L. McDowell.

Voyiadjis, G. Z., Shojaei, A. and Li, G. [2011], 'A thermodynamic consistent damage and healing model for self healing materials', *International Journal of Plasticity* **2**7(7), 1025 – 1044.

Voyiadjis, G. Z., Shojaei, A. and Li, G. [2012], 'A generalized coupled viscoplastic-viscodamage-viscohealing theory for glassy polymers', *International Journal of Plasticity* **2**8(1), 21 – 45.

Voyiadjis, G. Z. and Song, Y. [2019], 'Strain gradient continuum plasticity theories: Theoretical, numerical and experimental investigations', *International Journal of Plasticity* **1**21, 21 – 75.

Vujošević, L. and Lubarda, V. A. [2002], 'Finite-strain thermoelasticity based on multiplicative decomposition of deformation gradient', *Theoretical and Applied Mechanics* **2**8 – 29, 379 – 399.

Wang, J., Peng, L. F., Deng, Y. J., Lai, X. M., Fu, M. W. and Ni, J. [2019], 'A finite strain thermodynamically-based constitutive modeling and analysis of viscoelastic-viscoplastic deformation behavior of glassy polymers', *International Journal of Plasticity* .

Wcislo, B. and Pamin, J. [2017], 'Local and non-local thermomechanical modeling of elastic-plastic materials undergoing large strains', *International Journal for Numerical Methods in Engineering* **1**09(1), 102 – 124.

Weng, W., Chen, G. and Wu, D. [2003], 'Crystallization kinetics and melting behaviors of nylon 6/foliated graphite nanocomposites', *Polymer* **4**4(26), 8119 – 8132.

Wriggers, P. [2008], *Nonlinear Finite Element Methods*, Springer-Verlag Berlin Heidelberg.

Wriggers, P., Miehe, C., Kleiber, M. and Simo, J. C. [1992], 'On the coupled thermomechanical treatment of necking problems via finite element methods', *International Journal for Numerical Methods in Engineering* **3**3(4), 869 – 883.

Wu, B., Li, X., Di, Y., Brinnel, V., Lian, J. and Münstermann, S. [2017], 'Extension of the modified bai-wierzbicki model for predicting ductile fracture under complex loading conditions', *Fatigue & Fracture of Engineering Materials & Structures* **4**0(12), 2152 – 2168.

Wu, H., Xu, W., Shan, D. and Jin, B. C. [2019], 'An extended gtn model for low stress triaxiality and application in spinning forming', *Journal of Materials Processing Technology* **2**63, 112 – 128.

Wulfinghoff, S. and Böhlke, T. [2012], 'Equivalent plastic strain gradient enhancement of single crystal plasticity: theory and numerics', *Proceedings of the Royal Society of London A: Mathematical, Physical and Engineering Sciences* **4**68(2145), 2682 – 2703.

Wulfinghoff, S., Fassin, M. and Reese, S. [2017], 'A damage growth criterion for anisotropic damage models motivated from micromechanics', *International Journal of Solids and Structures* **1**21, 21 – 32.

Wunderlich, B. [1960], 'Study of the change in specific heat of monomeric and polymeric glasses during the glass transition', *The Journal of Physical Chemistry* **6**4(8), 1052–1056.

Wunderlich, B. [1976], 'Crystal nucleation, growth, annealing', *Macromolecular Physics* **2**.

Wunderlich, B. [2003], 'Reversible crystallization and the rigid-amorphous phase in semicrystalline macromolecules', *Progress in Polymer Science* **2**8(3), 383 – 450.

Xie, S., Séguéla, R., Lefebvre, J.-M. and Gloaguen, J.-M. [2009], 'A re-examination of the sub-tm exotherm in polyamide 6: The roles of thermal history, water and clay', *Journal of Polymer Science Part B: Polymer Physics* **4**7(23), 2385 – 2393.

Yang, Q., Stainier, L. and Ortiz, M. [2006], 'A variational formulation of the coupled thermo-mechanical boundary-value problem for general dissipative solids', *Journal of the Mechanics and Physics of Solids* **5**4(2), 401 – 424.

Yu, C., Kang, G., Lu, F., Zhu, Y. and Chen, K. [2016], 'Viscoelastic-viscoplastic cyclic deformation of polycarbonate polymer: Experiment and constitutive model', *Journal of Applied Mechanics* **8**3(4). 041002.

Yue, Z., Cao, K., Badreddine, H., Saanouni, K. and Gao, J. [2019], 'Failure prediction on steel sheet under different loading paths based on fully coupled ductile damage model', *International Journal of Mechanical Sciences* **1**53-154, 1 – 9.

Zeng, F., Grognec, P. L., Lacrampe, M.-F. and Krawczak, P. [2010], 'A constitutive model for semi-crystalline polymers at high temperature and finite plastic strain: Application to pa6 and pe biaxial stretching', *Mechanics of Materials* **4**2(7), 686 – 697.

Zhao, M., Wudy, K. and Drummer, D. [2018], 'Crystallization kinetics of polyamide 12 during selective laser sintering', *Polymers* **1**0, 168.

Zhou, J., Gao, X., Sobotka, J. C., Webler, B. A. and Cockeram, B. V. [2014], 'On the extension of the gurson-type porous plasticity models for prediction of ductile fracture under shear-dominated conditions', *International Journal of Solids and Structures* **5**1(18), 3273 – 3291.

Zhu, Q. Z., Zhao, L. Y. and Shao, J. F. [2016], 'Analytical and numerical analysis of frictional damage in quasi brittle materials', *Journal of the Mechanics and Physics of Solids* **9**2, 137 – 163.

Zhu, Y. Y. and Cescotto, S. [1995], 'A fully coupled elasto-visco-plastic damage theory for anisotropic materials', *International Journal of Solids and Structures* **3**2(11), 1607 – 1641.

Ziabicki, A. [1976], *Fundamentals of Fibre Formation: The Science of Fibre Spinning and Drawing*, John Wiley & Sons Ltd.

Zinet, M., Otmani, R. E., Boutaous, M. and Chantrenne, P. [2010], 'Numerical modeling of nonisothermal polymer crystallization kinetics: Flow and thermal effects', *Polymer Engineering & Science* **5**0(10), 2044 – 2059.